ELECTROACTIVE LIGHT METAL NANOSTRUCTURES FOR CORROSION PROTECTION AND ELECTROCHEMICAL ENERGY STORAGE

A Dissertation

by

RACHEL D. DAVIDSON

Submitted to the Office of Graduate and Professional Studies of
Texas A&M University
in partial fulfillment of the requirements for the degree of

DOCTOR OF PHILOSOPHY

Chair of Committee,	Sarbajit Banerjee
Committee Members,	Lei Fang
	Matthew Sheldon
	Homero Castaneda
Head of Department,	Simon North

December 2020

Major Subject: Chemistry

ABSTRACT

Stability in electrochemical systems is governed by interactions at the local scale where isolated inhomogeneities can define system performance. This concept plays a key role in failure of battery systems and corrosion of materials. For rechargeable batteries, replacement of graphite with metal anodes provides considerable promise for sizable gains in gravimetric and volumetric energy densities. However, out of equilibrium processes guide formation of anisotropic, dendritic growths which are capable of short circuiting the cell and causing catastrophic failure of the system. Magnesium-based batteries have garnered significant interest as an alternative to lithium-ion largely due to its designation as a ‘dendrite free’ system.

This would allow for the use of metal anodes providing significant improvements in capacity compared to graphite but requires controlled and consistent plating and stripping of the active metal over hundreds of cycles. Here, we detail our investigations into the electrodeposition of magnesium in varying electric fields, electrolyte concentrations, and with the addition of growth-directing ligands, providing understanding of mechanisms of deposition across a wide range of deposit morphologies. Through combining in situ video microscopy studies of electrodeposition of Mg in symmetric cells with 3D tomographic characterization and mesoscale modeling we demonstrate some of the first definitive examples of dendritic growth on magnesium anodes and elucidate mechanisms of formation.

In corroding systems, local inhomogeneities often serve as key sites in failure, often dominating electrochemical activity. For corrosion inhibition, our approach has involved modular design of nanocomposite coatings enabling multiple modes of corrosion protection. Here we outline our efforts in design of magnesium nanoparticle and exfoliated graphite-based nanocomposites for protection of high-strength aluminum alloys. Mechanisms of corrosion inhibition have been elucidated through extended submersion testing coupled with electrochemical impedance spectroscopy measurements.

DEDICATION

This dissertation is dedicated to Prof. David Nikles who introduced me to materials chemistry.

ACKNOWLEDGEMENTS

I would like to thank Prof. Banerjee for seeing the potential of every student he mentors regardless of the work and time it will take to get them where they want to go and for advocating for his students in every battle where they need his help. I would also like to acknowledge my committee members, Professor Lei Fang, Professor Matthew Sheldon, and Professor Homero Castaneda for helping me throughout my time at Texas A&M. I would like to thank our collaborators in the labs of Professors Homero Castaneda, Partha Mukherjee, Matt Pharr, Raymundo Arróyave, Kelvin Xie, and Bai-Xiang Xu, who have each greatly expanded the scope of understanding of the systems explored in each of our projects. I would like to thank Professors Gary Gray, Jacqueline Nikles, and David Nikles for preparing me for graduate school. Finally, I would like to thank my family and friends for their support.

CONTRIBUTORS AND FUNDING SOURCES

Contributors

This work was supervised by a dissertation committee consisting of Professor Sarbajit Banerjee, Professor Lei Fang, and Professor Matthew Sheldon of the Department of Chemistry and Professor Homero Castaneda of the Department of Materials Science and Engineering.

Mesoscale modeling and Sand's time calculations in Chapters 2 and 3 were performed by Dr. Ankit Verma and Dr. Feng Hao under the advisement of Prof. Partha Mukherjee. David Santos performed X-ray tomography in Chapter 2 under the advisement of Prof. Sarbajit Banerjee. Transmission electron microscopy in Chapter 2 and Chapter 3 was performed by Dr. Sisi Xiang and Dr. Dexin Zhao working under the advisement of Prof. Kelvin Xie. Phase field modeling in Chapter 3 was performed by Dr. Vahid Attari under the advisement of Raymundo Arróyave. Mechanical testing in Chapters 2, 3 and 5 was performed by Cole Fincher under the advisement of Prof. Matt Pharr. Finite element modeling in Chapter 5 was performed by Dr. Peter Stein under the advisement of Bai-Xiang Xu. Electrochemical impedance spectroscopy, open circuit potential testing, and AC conductivity measurements in Chapters 3 and 4 were performed by Yenny Cubides under the advisement of Prof. Homero Castaneda. Justin Andrews performed Rietveld refinement in Chapter 4. X-ray photoelectron spectroscopy in Chapter 3 was performed by Parker Scofield and Dr. Theodore Alivio under the advisement of Prof. Sarbajit Banerjee. Chelsea McLain, Jonathan Van Buskirk, and

Antonio Fraticelli performed various experiments as part of their undergraduate research experiences throughout Chapters 2-5. All other work conducted for the dissertation was completed by the student independently.

Funding Sources

Graduate study was supported by a fellowship from the National Science Foundation Research Traineeship (NRT) Program under Grant Number DGE-1545403. This work was also made possible in part by the NSF under DMR 1809866 as well as Sigma Xi under GIAR G20191001105943152. Its contents are solely the responsibility of the authors and do not necessarily represent the official views of the NSF. 3D tomography using STXM was performed at the Canadian Light Source, which is supported by the Natural Sciences and Engineering Research Council of Canada, the National Research Council Canada, the Canadian Institutes of Health Research, the Province of Saskatchewan, Western Economic Diversification Canada, and the University of Saskatchewan. Authors also acknowledge the Materials Characterization Facility at Texas A&M for work using SEM and XPS.

TABLE OF CONTENTS

Page

LIST OF FIGURES

Page

LIST OF TABLES

Page

1. INTRODUCTION*

1.1. Overview

Electrochemical reactions are inherently heterogeneous and driven by local electric fields. This simple idea underpins the challenges in design of metal anodes for batteries and the design of coatings for inhibiting corrosion. The replacement of graphitic anodes with metallic Li would bring about substantial gains in capacity as compared to current carbon anodes (3,860 mAh·g^{-1} versus ca. 372 mAh g^{-1})[1]. However, this would require precise control over the reversible electroplating and stripping of Li over hundreds of cycles. Electrodeposition encompasses several processes spanning the range from transport of electroactive species to the electrode, dissociation of ion pairs, adsorption of electrostatically attracted ions on the electrode surface, and surface diffusion of the adsorbate to a thermodynamically favored location.[2] When these processes are disrupted or in the presence of kinetic traps, inhomogeneous deposition morphologies are observed. For lithium anodes, inhomogeneous electroplating has catastrophic consequences, resulting in dendrite formation wherein the incipient dendrites are capable of penetrating the battery separator, ultimately resulting in short circuiting and thermal runaway. Combined with the flammability of solvent-based electrolytes, thermal runaway reactions pose a major fire hazard. The economic consequences of battery fires has been enormous spanning from grounding of the Boeing 787 Dreamliner to a recall of the Samsung Galaxy Note 7, and most recently, a massive

*Part of this chapter is reprinted with permission from R. V. Dennis, N. A. Fleer, R. D. Davidson, S. Banerjee, in *Graphene Technol. From Lab. to Fabr.*, Wiley-VCH Verlag GmbH & Co. KGaA, Weinheim, Germany, **2016**, pp. 155–176.

explosion in McMicken, AZ, which has brought into question the viability of Li-ion batteries for grid-level storage. Devising routes to obtain planar deposition of light metals remains a seminal challenge in the discipline and requires precise control of electrochemical reactions as well as mass and charge transport phenomena across multiple length scales. The first section of this dissertation will focus on examining the electrodeposition of Mg evidencing the vastly distinct regimes that are accessible "far from equilibrium" and placing in perspective the consequences of inhomogeneous metal deposition for the utilization of metal anodes.

There is great interest in moving beyond lithium-ion towards magnesium-based electrochemical energy systems driven in large measure by the alleged imperviousness of metallic magnesium to dendrite formation, which would allow for the use of metal anodes affording much higher capacities than graphite. Initial reports noted that Mg could be plated as relatively smooth deposits under charging conditions that resulted in dendritic growth for lithium.[4] Since these reports, there has been substantial progress in development of cathodes and electrolytes, however, there has been little to no further vetting of the notion of metallic magnesium anodes. We have demonstrated the remarkable formation of Mg dendrites upon the electrodeposition of Grignard reagents in ethereal solvents under galvanostatic conditions monitored using *in situ* videomicroscopy. Mechanisms of formation are understood by examining effects of applied current density and concentration of the electrolyte.

From the perspective of corrosion inhibition, a coating should ideally serve as a physical barrier isolating the metal from its environment, thereby serving as a kinetic

impediment to thermodynamically favored corrosion reactions. However, barrier protection alone is insufficient given the inevitability of damage under abrasive conditions. Upon exposure of a protected metal to corrosive media, a concentration gradient is established, and the corrosion kinetics are dominated by the tortuosity and diffusion lengths of the pathways for mass transport of corrodant species through the coating. In polymeric coatings, the corrosion kinetics are typically governed by the diffusion of neutral corrosive species such as oxygen and water through pores, thinned sections, or defects, resulting in anodic corrosion of the underlying substrate.[3] In other words, the kinetics of a given system are dominated by local effects caused by imperfections. Mechanistic understanding and enhancing the tortuosity and ion transport resistance of coatings is thus of pivotal importance to obtain prolonged corrosion protection. The second part of this dissertation focuses on elucidation of design principles for nanocomposite coatings incorporating electroactive fillers that imbue corrosion protection through increased tortuosity and sacrificial anodic protection.

The second half of this dissertation research involves the design of nanocomposite coatings for the corrosion protection of high-strength aluminum alloys. Despite several decades having passed since chrome and chromium-based coatings were subject to strict regulations owing to their carcinogenic properties (the most stringent of which being the European Registry of Hazardous Substances (ROHS), few alternatives have emerged that can match these coatings in terms of their ability to provide prolonged corrosion inhibition.[5] Nanocomposite coatings containing unfunctionalized exfoliated graphite (UFG) immersed in polyetherimide have been designed and evaluated as a

function of UFG loading. Graphene-related systems have gained significant interest owing to their excellent barrier protection. However, reports on their utility for corrosion inhibition have been decidedly mixed. While in theory, the impermeability of 2D graphene is anticipated to provide excellent barrier protection, acceleration of corrosion has also been observed as a result of galvanic coupling with substrates. UFG composite coatings demonstrate this transition from corrosion inhibition to corrosion promoting with increased particle loading beyond the percolation threshold. An alternative approach involves design of nanostructured magnesium-based composite coatings, which provide sacrificial, cathodic protection for aluminum. Mechanisms of corrosion inhibition have been elucidated through extended submersion testing coupled with electrochemical impedance spectroscopy measurements.

1.1.1. Electro-crystallization of light metal nanostructures

The process of electrocrystallization and non-equilibrium growth products can be broken down into discrete processes, which provide understanding of the mechanisms of formation for various deposit structures. Here, these processes and models of these processes will be briefly overviewed looking at interfacial reaction kinetics, nucleation, and growth. The effect of various contributions will be related to the observed morphology of deposits.

1.1.1.1. Interfacial reaction kinetics

When electrodes are submerged in electrolytes, an interfacial double layer forms creating a gradient in distribution of ions throughout the electrolyte. The Debye length defines the approximate length of this electrostatic effect. Guyer developed a phase field

model to describe the nature of these diffuse interfaces in which a charge buildup on either side of the interface is created and drives the chemical reactions occurring at the interface.[6,7] The electrode and electrolyte can be considered as wells on a reaction coordinate diagram. The interfacial kinetics can be described through the Butler-Volmer equation shown below and approximated through Tafel kinetics.

$$\boldsymbol{j = j_0 \left\{ exp \left[\frac{\alpha_a z F \eta}{RT} \right] - exp \left[\frac{\alpha_c z F \eta}{RT} \right] \right\}} \quad \textbf{1.1}$$

Where j is the electrode current density, j_0 is the exchange current density describing the current in absence of net electrolysis and applied overpotential, α_a and α_c are the anodic and cathodic charge transference coefficients, z is the number of electrons involved in the reaction at the electrode, F is Faraday's constant, and η is the activation overpotential. This describes the reaction at the electrode interface in terms of a forward and backwards flux and how the current is dependent on the overpotential applied which acts to effectively lower the energy of the electrode well during electrodeposition.

1.1.1.2. Heterogeneous nucleation

Electrocrystallization involves heterogeneous nucleation and subsequent growth of the resulting deposit driven by application of an overpotential. Thermodynamically, heterogeneous nucleation can be described, similarly to homogeneous nucleation, in terms of a competition between a volume term relating to the promotion of nucleation through energy released during solidification and a surface area term relating to the inhibition of nucleation through interfacial energy costs. Homogeneous nucleation will typically result in growth of spherical particles due to the reduction in the interfacial

energy costs given the low surface area to volume ratio. Gibb's energy of nucleation for a spherical particle can be considered to follow:

$$\Delta G_{hom} = \left[\frac{4}{3}\pi r^3 \Delta G_V + 4\pi r^2 \gamma_{sl}\right] \quad \textbf{1.2}$$

Here ΔG_V is the Gibb's free energy of solidification and γ_{sl} representes the interfacial energy between the solid nuclei and liquid electrolyte. With heterogeneous nucleation, the nucleation site can be considered as a spherical cap forming on the substrate and an additional term can be added to describe the interfacial interaction of the growth with the substrate surface using the idea of wettability and contact angle on the surface.

$$\Delta G_{het} = \left[\frac{4}{3}\pi r^3 \Delta G_V + 4\pi r^2 \gamma_{sl}\right]\left[\frac{2-3\cos\theta+\cos^3\theta}{4}\right] \quad \textbf{1.3}$$

The second term varies between zero and one and thus provides a reduction in the energy for nucleation relative to homogenous nucleation. A critical radius and overpotential balancing the contributions of these energetic parameters can be defined for the stabilization of a nucleus, beyond which the nucleus would be expected to be thermodynamically stable. Many nuclei may form during electrocrystallization and often the energy of nucleation is lowered at defect sites of inhomogeneities in the electrode surface.[8,9]

1.1.1.3. Stability of nuclei and growth

While many nuclei may form during electrocrystallization, not all nuclei survive to enter the growth stage. If it is assumed that the nucleus grows following Butler-Volmer kinetics, then a critical size for growth of a nucleus can be predicted as well as the rate of that growth or disappearance of the resulting dendrite.[10] The critical radius

for growth is different and often larger than the critical radius for the thermodynamic stabilization of the nucleus creating the possibility for an ‘incubation’ period. Within this intermediate regime, the duration of anticipated incubation period can be predicted based on and driven by expected thermal fluctuations distributions in the system and growth is promoted through local interactions among nuclei through coarsening kinetics.

1.1.1.4. What does morphology tell us about mechanism?

Conditions for formation of deposits varying in morphology are described here. It is critical to emphasize that the factors relevant to growth are those at the local scale, which may vary drastically from the globally applied conditions. Dense planar deposits are typical in regions with lower reaction rates and low self-diffusion barrier allowing the deposit to densely pack.[11] In this regime, reduction events become the rate limiting step and the deposit takes on the lowest surface energy form. This can similarly be anticipated in regions below the thermodynamic limit for stable nuclei formation. In this regime, protruding nuclei due to thermal fluctuations are not anticipated to persist to form anisotropic deposits. This regime has also been described as a balance between tip induced growth which is smoothed through plastic flow.[10]

A generally planar but porous morphology would be expected if low reaction rates were maintained but the self-diffusion barrier was lowered.[11] An alternative explanation for a more porous layer of growth is that the surface passivation due to the rapid breakdown of the electrolyte and the inevitable formation of solid electrolyte interfaces (SEI) in lithium systems causes stress due to its inhomogeneous nature.[12] Growth under these passivating films creates stress leading to cracks in the SEI which

result in base-controlled growth of dendrites. This is anticipated in regimes with larger electrodeposit size and lower overpotential; the plasticity of the system thus controls the mechanism of growth.[10] This type of mossy or whisker growth is common in lithium systems but is not generally observed for magnesium, as the self-diffusion barrier is higher in magnesium than in lithium and passivation does not occur quite as readily due to its lower activity in comparison to lithium. It is also anticipated to cause fewer safety concerns due to the low elastic moduli of the mossy deposits.[13]

Higher reaction rates promote dendritic growth *via* a few different possible mechanisms resulting in different deposit morphologies. In each case, systems would have had to surpass the nucleation phase with the surviving nuclei entering a growth phase. Dense, rounded needle like growths, are anticipated at high reaction rates with low self-diffusion barriers.[11] Similarly this would correspond to higher overpotential regimes and larger initial deposit sizes.[10] Branching in these linear deposits can be induced due to localization of elastic energy at the growth tip, thus promoting development of branches rather than continued growth of the tip front.[10] Branching in this regime has also been proposed to result from distributions in the chemical potential based on historical understanding from the growth of dendrites in alloy melt solidification caused by undercooling gradients.[14,15] These deposits are more likely to have larger grains and even produce large single crystals with preferential growth axis based on the relative stability of different growth fronts.

Diffusion-limited aggregation mechanisms are observed when long range diffusion limitations occur limiting the rate of growth based on the diffusion of

electrolyte species to the electrode. Resulting dendrites are fractal in nature with highly branched deposits with seemingly random growth directions due to the random walk arising from Brownian motion of incoming ions. In this limit, wherever ions interact with the growth surface they deposit almost immediately.[13] This regime is associated with high self-diffusion barriers coupled with high reaction rates.[11] This would similarly be anticipated at the highest overpotentials. The onset of diffusion limitations can also result from eventual depletion of electrolyte through extended charge or discharge cycles. The onset of diffusion limitations is described by Sand's time which predicts the onset of diffusion limited growth for systems beyond a limiting current density.

The factors delineating these regimes of growth provide insight into the fundamental descriptors that can promote planar growth and limit anisotropic growth in battery systems. In subsequent chapters factors influencing electrocrystallization of magnesium will be explored in order to gain broader understanding of the potential use of metal anodes.[16,17]

1.2. Composite coatings for corrosion inhibition

The unfortunate and relentless problem of corrosion of base metals has plagued mankind for thousands of years. In industrialized societies, the massive costs of maintaining and repairing infrastructure can be attributed in large measure to the weathering and corrosion of structural components.[18–21] The complexity of corrosion processes makes estimation of the true costs of such degradation phenomena rather difficult; however, several studies have attempted to provide some accounting of the

financial impact of corrosion on the economy. An influential report from the United States Federal Highway Administration, published in 2002, estimated that the direct cost of corrosion to the United States economy in 1998 was $276B (amounting to as much as 3.1% of the nation's gross domestic product).[18] This staggeringly high monetary cost has likely only escalated over the last two decades with diminished spending on infrastructure and furthermore this number does not include indirect costs associated with the inhibition and control of corrosion, which are likely just as high, if not higher, than the direct costs.[18–20]

Fundamentally, corrosion of a metal is based on a series of electrochemical reactions where concurrent metal dissolution (oxidation) and the reduction of oxygen in the presence of water result in the loss of metal and the reformation of a more thermodynamically stable metal oxide. The generalized anodic and cathodic reactions can be written as follows:

$$\boldsymbol{M_{(s)} \rightarrow M^{+}_{(aq.)} + e^{-}} \qquad \textbf{1.4}$$

$$\boldsymbol{O_{2\,(g)} + 2H_2O_{(l)} + 4e^{-} \rightarrow 4OH^{-}_{(aq.)}} \qquad \textbf{1.5}$$

eventually yielding a metal oxide upon further reaction. The metal substrate itself serves as the conduit for the electrons and charge compensation between the anodic and cathodic half-cells is further facilitated by ion transport through an external medium. Mitigating corrosion thus fundamentally comes down to inhibiting this sequence of half-cell reactions by either impeding electron or ion transport, providing a barrier precluding oxygen and water diffusion, or incorporating a sacrificial layer that reacts preferentially instead of the metal surface. While detailed mechanistic understanding is not yet

available, graphene coatings that exhibit promise for corrosion inhibition and will be discussed in Chapter 5 are thought to mobilize a combination of these modes.

As a good first approximation, all coatings that are designed to inhibit corrosion of metals can be classified according to the following four mechanisms: (1) cathodic protection; (2) anodic passivation; (3) electrolytic inhibition; and (4) active corrosion inhibition.[22–26] Several particularly effective coatings incorporate multiple modes of action. **Figure 1.1** schematically represents the four main modes of corrosion inhibition as well as an additional mode, "self-healing", which is a broader concept that has been differentiated from active corrosion inhibition for the purposes of this discussion. The concept of cathodic protection is based around the idea that deposition of a more electropositive metal will polarize the substrate metal with the coating thus serving as a sacrificial anode that is preferentially oxidized. The most common example of this mode of action is galvanization of steel or other metal substrates by hot-dip or electroplating processes. Other metals such as aluminum and magnesium have also commonly been alloyed with zinc *via* interdiffusion or used independently as sacrificial barrier coatings.[27] It is of utmost importance that the sacrificial metal and the substrate be properly coupled so that the polarization of the substrate is sufficient to prevent pitting corrosion while also avoiding "overprotection" that can lead to hydrogen embrittlement or alkaline attack.[22] In Chapter 4 , we describe the design of nanocomposite coatings incorporating metallic Mg nanoparticles that provide a means of imbuing sacrificial cathodic protection. Embedding Mg nanoparticles within a barrier coating provides a

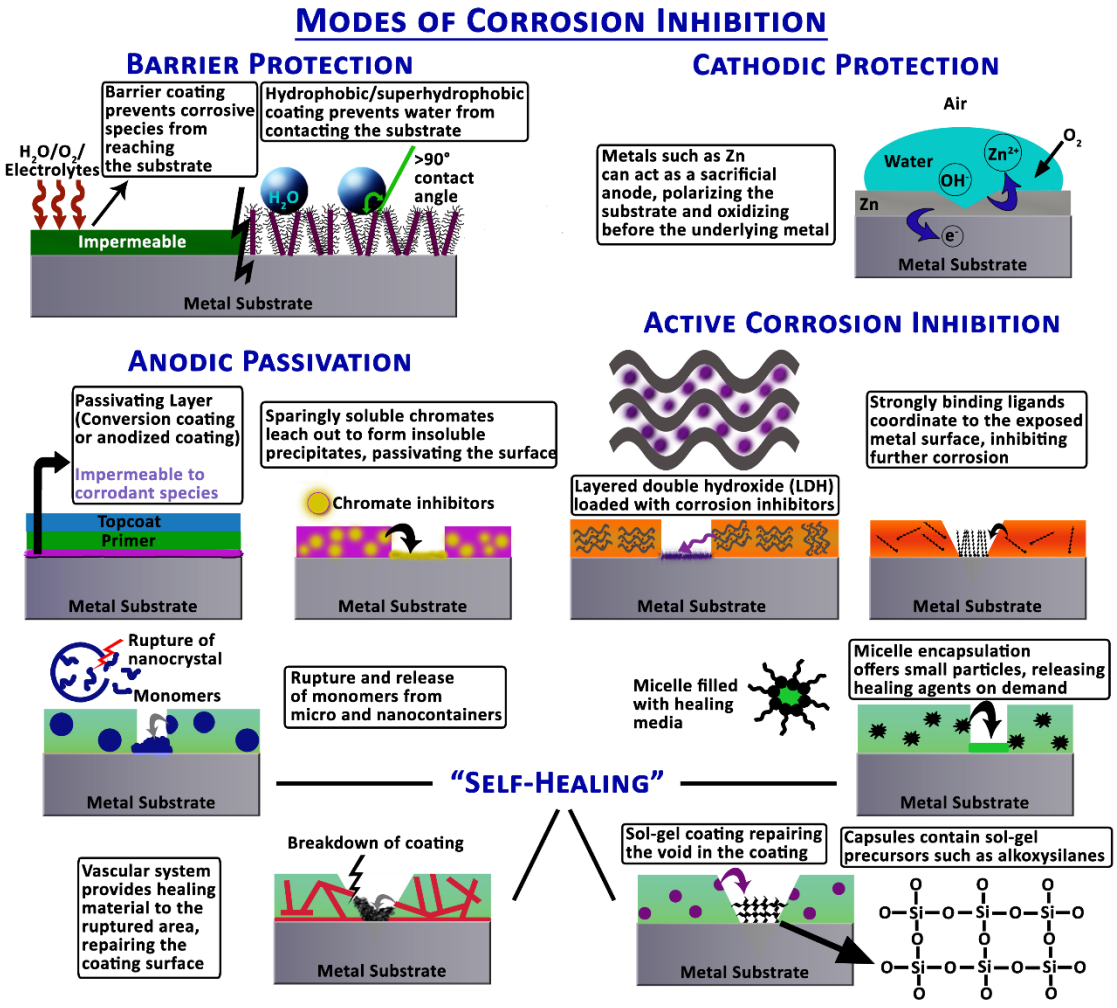

Figure 1.1. Schematic depiction of different modes of corrosion inhibition, including barrier protection, cathodic protection, anodic passivation, active corrosion inhibition, and "self-healing". Dennis R V, Patil V, Andrews J L, Aldinger J P, Yadav G D and Banerjee S 2015 Mater. Res. Express 2 032001. © IOP Publishing. Reproduced with permission. All rights reserved.

viable means of protecting Al substrates which cannot be protected by galvanization given the differential in the redox potentials of Al and Zn.

Anodic passivation of a metal substrate inhibits corrosion by using a passivating layer to coat the metal surface, which has the effect of suppressing the redox reactions

listed in equations 1.4 and 1.5. This mode essentially involves deposition of a barrier film on the metal surface that is either impervious to ion diffusion or only allows the selective diffusion of specific ions.[23,28] This approach has been commonly used for a number of decades in the form of chromate conversion coatings and anodized aluminum. In this approach, a natural oxide layer is typically combined with some sort of passivation layer, which together create a bipolar precipitate that strongly reduces ion transport through the barrier. Additionally, closely aligned or alternating layers of densely packed oxides and porous oxides deposited during an anodization or conversion coating step redirect ion transport between the anodic and cathodic sites.[23,29,30]

A third mode of corrosion resistance, electrolytic inhibition, also involves shutting down ion transport pathways between the anodic and cathodic sites of the metal by using a low-ionic-conductivity matrix or diffusion barrier. These coatings are typically barriers that attempt to limit the transport of corrodant electrolyte species to the metal by increasing the tortuosity of the conduction pathways and reducing the movement of charge. The use of high molecular weight polytherimide coatings with dense crosslinking provides a means to greatly inhibit corrodant transport; embedding nanosheets such as graphene and layered double hydroxides with poor ionic permeability further provides a means to greatly enhance the effective tortuosity of the nanocomposites.

Finally, active corrosion inhibition addresses the inevitable scenario of coating failure. Active corrosion inhibition involves the incorporation of components that can be selectively released upon failure or in response to external stimuli, thereby reconstituting

a protective barrier at the metal interface.[22,23,31,32] Some examples of these active corrosion inhibitors include strongly binding ligands (with high binding constants for formation of dative bonds at metal surfaces) or sparingly soluble oxide precursors (with low solubility product, K_{sp}, values) that can precipitate, even at very low concentrations, to form barrier layers. Typically, such active species are encapsulated within appropriate polymeric or porous inorganic containers that in turn are embedded within the coating; the active inhibitors are released upon coating failure or the initiation of corrosion.[22,32–35] The broad umbrella of "self-healing" coatings also includes the incorporation of monomers and catalyst particles that can help to actually reconstruct the existing coating upon failure without necessarily addressing corrosion inhibition. Figure 1.1 schematically depicts the main modes of corrosion inhibition with examples of each.

During the last couple of decades there has been a renewed push towards the development of novel coating systems spurred by several critical imperatives. An ever aging global infrastructure requires a reevaluation of current coating technologies with increasing realization that many conventional coating materials represent a hazard to human health and the environment. One of the single most important forces driving the development of new coating technologies is the stringent regulatory environment addressing the potent carcinogenicity and environmental concerns of hexavalent chromium, which has been used extensively in chromate conversion coatings and hard-chrome electroplating processes for a number of decades. Hexavalent chromium-based coatings have been commonly used in the industry owing to their excellent corrosion resistance and self-healing properties (depicted in Fig. 1.1); such coatings also providing

the excellent sheen and metallic luster that gives it its distinctive aesthetic.[22,36–42] The exceptional mobility of hexavalent chromium ions that make it ideal for corrosion inhibition also allow for the facile environmental transport of these species.[36,39,43,44] Given the increasing realization of the long-term environmental legacy of hexavalent chromium, its use is stringently regulated around the globe.[36,39,40,42,45,46] Similar to hexavalent chromium, volatile organic compounds (VOCs) found in most polymer and paint coatings (as organic solvents and sometimes toxic curing agents) represent a major occupational safety hazard, particularly during application of the coatings.[47–49] Consequently, there is a global push towards sustainable technologies that incorporate earth-abundant and non-toxic components while at the same time providing protection over protracted periods of operation.

Sacrificial coatings such as galvanized zinc have been the "gold standard" for corrosion resistant coatings for more than a century due to the ease of plating and the excellent barrier and sacrificial coating properties that they bestow upon the underlying base metal substrate.[50,51] Sacrificial coatings such as zinc owe their corrosion inhibition properties to the difference in reduction potentials between the sacrificial metal and the substrate metal, whereby the coated metal is oxidized preferentially, preventing oxidation of the substrate (as schematically illustrated in Fig. 1.1).[50] Unfortunately, the longevity of the corrosion inhibition is directly proportional to the coating thickness and in a sense these coatings function on the basis of continuous dissolution or failure over their operational lifetime. In other words, ensuring longevity of protection often requires considerable cost and weight penalties with the latter being particularly consequential for

aerospace and transportation applications since increased weight oftentimes correlates to increased fuel consumption.[26,52] Since base metals are for the most part a commodity business with small margins, the recent market unpredictability and the dramatic fluctuations in the price of zinc have been cause for serious concern in the steel industry and have substantially cut into profit margins.[26] On the other end of the spectrum, high-performance coatings are more critical than ever for advanced lightweight alloys that are increasingly finding use in aerospace and transportation applications. The highly heterogeneous nature of these alloys, oftentimes characterized by intermetallic or elemental precipitates, make them particularly susceptible to corrosion by establishing surface domains with distinctive reduction potentials that can each serve as the cathodic and anodic halves of corrosion cells. To compound this problem, zinc does not have the ability to protect aluminum and aluminum alloys from corrosion since aluminum lies lower in the galvanic series than zinc and thus new, more electroactive, coating systems are urgently required.[53]

Given the inadequacies of current technologies, the exploration of entirely new coating paradigms has become of utmost importance. Two distinctive approaches will be reviewed; inclusion of electroactive magnesium offers potential to cathodically protect more electroactive metals such as aluminum while graphene is an attractive non-metallurgical candidate for protecting base metals either by itself or as the active element of polymer, metal matrix, or ceramic composites.[21,54] In the sections to follow, the current mechanistic understanding of how magnesium and graphene inhibit corrosion is reviewed. For graphene-based coatings illustrative examples of the use of graphene as a

component in- or as a stand-alone- coating for the corrosion inhibition of base metals are provided. The objective of this contribution is to contrast approaches for corrosion protection based on the use of graphene, explore the mechanistic underpinnings of the protection bestowed by graphene coatings, capture a snapshot of this rapidly developing area of research, and to examine the potential of this material as an alternative to conventional metallurgical films or polymeric coatings. Additionally, perspective on the outlook for magnesium and graphene-based corrosion resistant coatings has been included with a focus on the obstacles to commercialization.

1.2.1. Magnesium in corrosion inhibition

Magnesium offers the opportunity to cathodically protect aluminum and aluminum alloys given its high electrochemical activity and rapid self-passivation under atmospheric conditions. Bierwagen and co. workers have extensively explored inclusion of bulk magnesium particles in epoxy primers for protection of high-strength aluminum alloys targeting application in the aerospace industry.[55,56] Their work demonstrates that a careful balance must be struck between inclusion of sufficient quantities of Mg to surpass the critical pigment volume concentration enabling contact between the underlying substrate and the active Mg particles thus activating the cathodic protection mechanisms while also providing protection of magnesium to limit its rate of exposure to ensure that it is not rapidly depleted.[57] Bierwagen has also suggested however, that in situations where a percolative network is not established, oxygen sequestration may still occur offering some protection. The protection afforded and the nature of the chemical reactions that take place are highly dependent on the environment surrounding the

reactive Mg species. Activation of a deleterious pathway producing hydrogen can occur following:

$$\mathbf{Mg_{(s)} + 2H_2O_{(l)} \rightarrow Mg(OH)_{2(s)} + H_{2(g)}\uparrow} \quad \mathbf{1.6}$$

In environments with limited CO_2 or submersion in water this reaction causes blistering of coatings due to the formation of hydrogen gas. In the presence of sufficient CO_2 a magnesium carbonate biproduct forms subsequently due to the instability of the $Mg(OH)_2$, passivating the surface and avoiding further hydrogen evolution. [58,59] The magnesium carbonate layer is more well adhered to the metal surface and dense than the magnesium hydroxide byproducts. Magnesium carbonate formation is observed under mild atmospheric exposure conditions but can be promoted through inclusion of $Mg(NO_3)_2$ and Li_2CO_3 which increase the availability of both Mg^{2+} and CO_3^{+}, respectively, promoting the following reactions:[60]

$$\mathbf{2H_2O_{(l)} + O_{2(g)} + 4e^- \rightarrow 4OH^-_{(aq.)}} \quad \mathbf{1.7}$$

$$\mathbf{Mg^{2+}_{(aq.)} + 2OH^-_{(aq.)} \rightarrow Mg(OH)_{2(s)}} \quad \mathbf{1.8}$$

$$\mathbf{Mg(OH)_{2(s)} + CO_{2(g)} \leftrightarrow MgCO_{3(s)} + H_2O_{(l)}} \quad \mathbf{1.9}$$

Use of accelerated testing is commonplace in corrosion engineering and typically involves exposure of samples to more harsh environments than would be experienced in their intended application in order to rapidly understand the relative performance of coatings, however, more extreme conditions can also alter the mechanism of protection and modes of failure. For magnesium systems it is thus critical to track not only relative performance but also the modes of failure and protection.[61]

1.2.2. Bare Graphene as a Protective Barrier

1.2.2.1. Some Electronic Structure Considerations at Graphene/Metal Interfaces

The conduction and valence bands of graphene, derived from p_z orbitals, adopt a conical configuration and intersect at the Fermi level (E_F).[62,63] Remarkably, the bands show a linear dispersion as a function of energy ± 1 eV from the point of intersection (the Dirac point). Such a "slim hourglass" electronic structure has some peculiarities that render it particularly useful for protecting metal surfaces. The low density of states near E_F imply that metals (amongst other species) can readily participate in charge transfer interactions with graphene depending on the relative alignment of their work functions and the extent of overlap of the graphene π-cloud with metal orbitals of the appropriate symmetry.[62,64] Extensive details of electronic structure consequences of interfacing graphene with metals and dielectrics have been reviewed elsewhere and are summarized here only to provide a perspective of mechanisms for mitigating corrosion.[62,65–67] As a first approximation, charge transfer between metal surfaces and graphene induces a potential barrier at the graphene/metal interface and the resulting polarization impedes the electron transfer processes necessary for corrosion depicted in Equations 1 and 2. Unlike in a bulk solid, charge transfer and other perturbations propagate across the 2D geometric structure and can profoundly alter the electronic structure of graphene.[62] The nature of the metal/graphene interface is thus of paramount importance in determining the extent of polarization and consequently the degree of protection afforded to the metal substrate by graphene.

Several different types of graphene/metal interactions can be distinguished. For low work-function and highly electropositive metals such as Li, Na, K, and Cs, graphene serves as an electron acceptor and a rigid shift of the band structure is observed as a result of electron doping.[26,62] In contrast, a broad class of transition- and post-transition metals such as Cu, Ag, Au, and Pt exhibit interactions reminiscent of physisorption accompanied by charge transfer and development of an interfacial dipole as illustrated in Figure 1.2. For these metals, *ab initio* density functional calculations predict that whereas at distant separations, the directionality of charge transfer and the magnitude of the interfacial dipole are well predicted by the relative alignments of work functions, at closer separations, exchange repulsion terms assume greater significance.[68,69] At a Cu/graphene interface, the direction of charge transfer flips from *n* to *p*-type doping with increasing separation between graphene and the underlying Cu(111) surface.[70] In other words, the repulsion between the itinerant electrons in the π-cloud of graphene and the electron gas of the metal contribute significantly to the surface potential difference (denoted as Δv in Fig. 1.2) that develops at the interface This potential difference can thus impede redox processes involved in corrosion.

As a third type of metal/graphene interface, for metals such as Ni, Co, Pd, and Ti, the high degree of epitaxial matching of crystal lattices with graphene as well as the strong hybridization of the transition metal d_{z2} orbitals with the graphene π-cloud profoundly reshapes the electronic structure of graphene, opening up a bandgap at the Fermi level and removing spin degeneracy.[69–71] The interfaced graphene layer thus acquires some carbidic character and is rendered a semiconductor.[26,62] A potential

difference now exists between the surficial (and sub-surficial) metal layers that are hybridized with the graphene and constitute a semiconductor and the underlying metallic layers that are relatively unperturbed by interfacing with graphene. The semiconductor/metal interface thus established within the metal gives rise to a Schottky barrier to the tunneling of electrons and this potential barrier can further impede electron transfer at the metal/graphene interface. The height of the barrier depends on the pinning of the Fermi level of the carbide-like semiconductor formed at the graphene/metal interface.[72] Indeed, the Schottky barrier represents a major challenge with making ohmic contacts to semiconducting carbon nanotubes. In other words, both physisorption and covalent hybridization of graphene on metal surface give rise to interfacial potential barriers that serve to protect against oxidation of the metal. Notably, this mechanism is operational primarily when graphene is directly interfaced with the metal but is ineffective at providing corrosion protection within nanocomposite coatings that do not have continuous graphene coverage of metal layers.

Another potential mechanism, illustrated in **Figure 1.2**., derives from the high electrical conductivity of graphene where room-temperature mobilities can readily surpass 10,000 $cm^2\ V^{-1}\ s^{-1}$. The much higher electrical conductivity of graphene as compared to the underlying metal substrate provides an alternative conduit for transporting electrons generated at the anode away from cathodic sites thereby disrupting

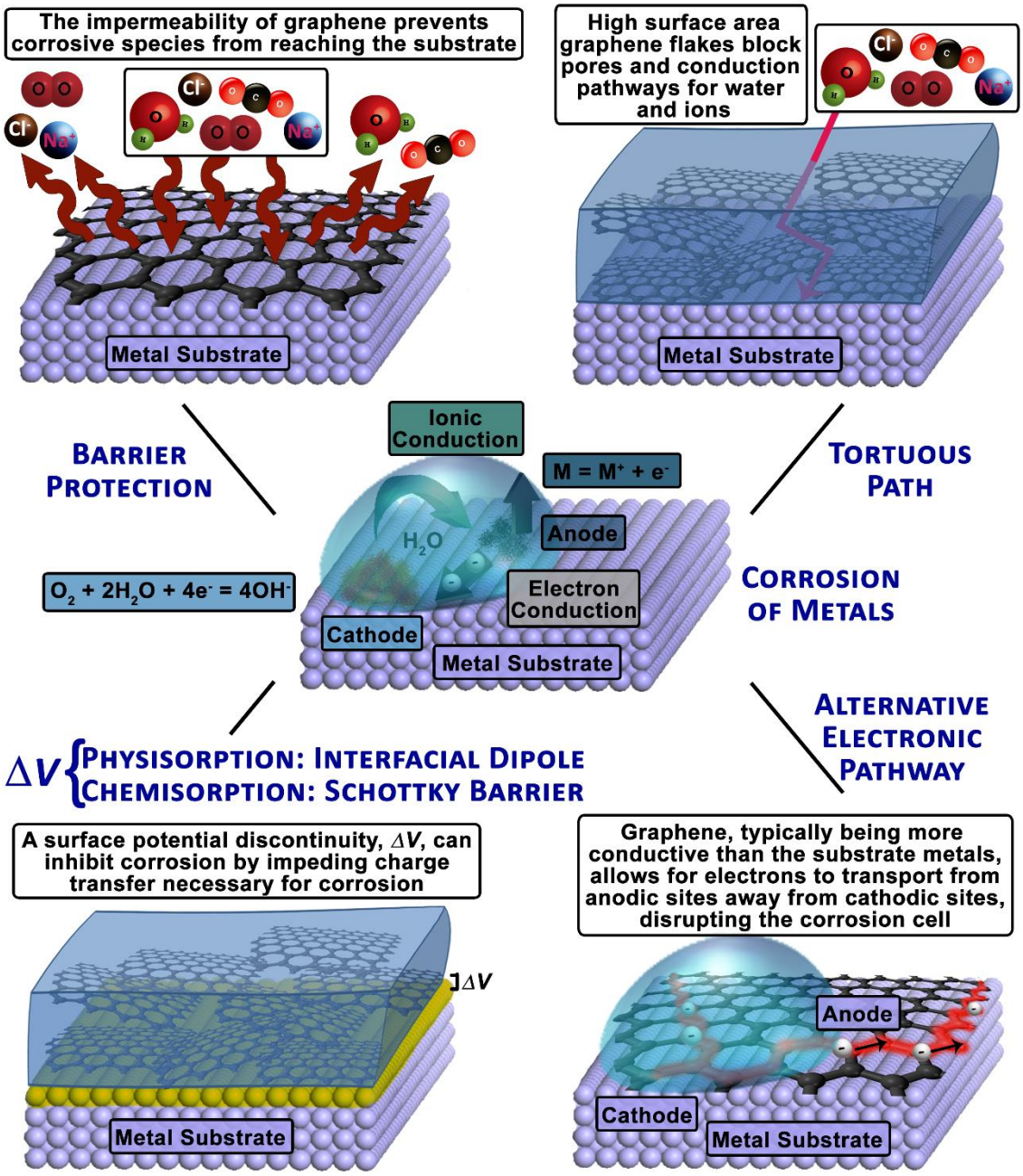

Figure 1.2. Schematic depiction of the four main modes of corrosion inhibition by graphene. This graphic depicts the ways that graphene can help to impede or entirely shut down the electrochemical processes related to corrosion: (a) by providing barrier protection; (b) by requiring a tortuous path for ion permeation; (c) by formation of a potential barrier at the graphene/metal interface (either a Schottky barrier or interfacial dipole); and (d) providing an alternative electronic pathway.

the corrosion reactions.[21] Notably, a mechanism predicated on electrical conductivity is not confined to being an interfacial phenomenon as in the case of direct physisorption or covalent hybridization of graphene on metal surfaces. Indeed, the formation of percolative networks within composite coatings could have much the same effect but as will be discussed in Chapter 5 can have a deleterious effect by enabling the formation of corrosion cells across the cross-section of the coating

Beyond the electronic structure considerations, it is also primarily the hexagonal honeycomb-like structure of graphene that gives rise to a highly efficient and impervious barrier to diffusion of gaseous and vapor-phase species.[73–75] For instance, Herman and co-workers have shown that CdSe quantum dots with a graphene overlayer show prolonged resistance to photodegradation (and retain their bright luminescence) as a result of limited diffusion of oxygen and water vapor.[73] Preventing diffusion of water vapor and oxygen blocks the cathodic reactions and thus prevents oxidation of metal surfaces. However, even the highest quality graphene layers are characterized by point defects, grain boundaries, and extended cracks inevitable from their growth on polycrystalline metal foils that themselves have a highly heterogeneous surface structure. The extended defects allow pathways for gaseous and liquid diffusion and thus barrier properties by themselves are not expected to provide protection over prolonger operational lifetimes.

1.2.2.2. Graphene and as a standalone corrosion resistant coating and some mechanistic considerations

The degree of protection provided by graphene to a copper substrate has been examined for graphene samples grown directly onto polycrystalline copper foils by chemical vapor deposition (CVD).[76,77] Extensive electrochemical studies and Tafel analysis of potentiodynamic plots allow for derivation of corrosion rates from the measured corrosion current density in various corrosive environments, including aqueous solutions of Na_2SO_4 and NaCl.[76,78] The open circuit potential of graphene-coated Cu is characterized by a slightly lower value (decreased by ca. 25 mV) and furthermore this sample shows a much lower corrosion current density relative to its uncoated counterpart.[76] A corrosion rate of 5.76×10^{-13} m/s has been deduced for bare copper, and is diminished by a factor of about seven to 7.85×10^{-14} m/s upon coating with graphene when exposed to a 0.1 M Na_2SO_4 electrolyte.[76]

Analogous tests have been performed for nickel substrates with and without graphene overlayers.[76,79] Graphene has been applied onto nickel foils through two distinct methods: (a) direct growth onto the nickel surfaces by CVD from hydrocarbon precursors and (b) mechanical transfer of graphene grown by CVD onto Cu foils using poly(methyl methacrylate) (PMMA) as the transfer medium.[76,79] The graphene film grown directly *via* CVD is observed to provide a higher degree of protection, which is attributed to the high degree of uniformity, relatively pinhole-free coverage, and improved adhesion obtained for these films as compared to mechanically transferred coatings.[76,79] The latter approach allows for deposition of multilayered films but does

not appear to be as effective. The corrosion rate of bare nickel has been determined by Tafel plot analysis to be 2.99×10^{-14} m/s,[76] and is reduced by almost 20-fold to 1.71×10^{-15} m/s for graphene grown directly on a nickel substrate.[76,79] Graphene that is mechanically transferred to a nickel substrate provides a substantially reduced degree of protection (only a four-fold reduction); the corrosion rate is 1.83×10^{-14} m/s for two transferred graphene layers and 7.62×10^{-15} m/s for four layers of transferred graphene.[76,79] Interestingly, the graphene coatings do not substantially alter the negative current potentials corresponding to cathodic reduction of oxygen for either the Cu or Ni samples.[76] This is due in part to graphene being impervious to gas and demonstrates one mechanism by which it can slow the corrosion process.[76] These authors do observe corrosion is initiated in unprotected regions beneath extended defects in graphene. Researchers at Tata Steel have reported that the graphene protection of stainless steel 304L and 316 L substrates greatly decreases the corrosion rates from 0.7 and 0.5 mm yr^{-1}, respectively, to 1.96×10^{-4} and 8.59×10^{-4} mm yr^{-1}, respectively, in a harsh fuel cell environment.[21]

Despite the promising results noted above, several researchers have pointed out that due caution is warranted in extrapolating short-term corrosion protection observed in electrochemical tests to prolonged operational lifetimes. In particular, Zettl and co-workers have suggested that even though graphene excels in corrosion tests that capture a snapshot of the ongoing processes (such as cyclic voltammetry and potentiodynamic testing), failure is inevitable over prolonged periods of operation under ambient conditions. Indeed, these researchers suggest that graphene coatings eventually

accelerate corrosion and that graphene-coated samples fare much worse under ambient conditions as compared to even bare metal substrates.[54,76,80] These authors claim that the impermeability of graphene to gas diffusion along with the inevitable defects results in local concentration of corrodant species at the metal interface (through seepage), thereby exacerbating corrosion.[80] In contrast to bare copper, where a native oxide forms uniformly and homogeneously across the surface and affords some degree of protection, upon coating with graphene, corrosion is initiated at specific defect sites. The inhomogeneous surface oxide generates stress, resulting in crack formation and generating fresh sites for surface oxidation. The high conductivity of graphene further implies that electrons can be transported across large distances where they can further facilitate cathodic reactions, once again initiating the cycle of surficial and eventually bulk corrosion upon crack formation and propagation.[79–81]

It is apparent that at the present time, a single, defect-free graphene layer is difficult to grow, and virtually impossible to mechanically transfer while still retaining uniform and pinhole-free characteristics.[62,76,80] Consequently, coatings relying solely on barrier properties of monolayer or few-layered graphene are unlikely to yield corrosion inhibition over prolonged periods of time even under ambient conditions. It is important to note that the challenges here are not *per se* derived from the properties of graphene but instead arise from the inevitable presence of defects, which allows the electrochemistry required for wet corrosion to run rampant, yielding an outcome much worse than for bare copper where the native oxide provides some degree of passivation.[80,81] These findings suggest that practical coatings must be significantly

thicker and must mitigate the accumulation of corrodant species at defect sites. Indeed, coatings developed at Tata Steel as well as in our laboratories either make use of significantly thicker coatings wherein the high surface area of graphene establishes a highly tortuous path for transport of corrodant species or deploy an additional ion impervious matrix.[21,26,54,82] Thicker films of graphene oxide, obtained by oxidation of natural flake graphite with strong oxidizing agents, can be electrophoretically deposited onto metal substrates upon the application of DC fields. The ionized functional groups on graphene oxide provides a surface charge that enables their manipulation and deposition using electric fields.[83,84] The resulting graphene oxide coating can be reduced (using a suitable reducing agent such as hydrazine or $NaBH_4$) to reduced graphene oxide and initial reports indicate that such coatings provide excellent protection against oxidizing agents.[54,83,85] In Chapter 5, we provide a detailed mechanistic evaluation of corrosion mechanisms afforded by graphene and reconcile the seemingly disparate observations based on whether graphene is able to form a percolative network in contact with the underlying metal substrate.

1.2.2.3. Graphene Nanocomposites for Corrosion Inhibition

In recent years, polymer based nanocomposites, wherein an inorganic filler is incorporated within a continuous polymer matrix, have attracted interest for a number of different applications including corrosion resistant coatings.[24,26,34,86] A particular advantage that these materials offer (subject to overcoming challenges with dispersion and interfacial bonding) is the ability to incorporate modular function wherein the desired properties of both the polymeric matrix and the inorganic filler can be deployed

towards some functional purpose. Furthermore, such hybrid composites can often be applied onto surfaces through continuous phase liquid coating or roll-to-roll printing methods, allowing for largescale industrial deployment.[87]

Given the remarkable properties of graphene, both electronic and mechanical, the incorporation of graphene within polymer matrices has emerged as a means to utilize this material within coatings as an alternative to the direct deposition of graphene onto metal substrates discussed in the preceding section. Furthermore, the need for lightweight and strong composite materials has led to a flurry of research on bulk graphene nanocomposites.[88] Two primary and related challenges with fabricating nanocomposite coating formulations are: (a) the dispersion of graphene within the polymeric matrix and (b) designing the best possible interface between graphene and the polymer matrix to facilitate not just dispersion but also strong interfacial bonding. A properly engineered interface is imperative to avoid mechanical slippage and aggregation of the graphene within the composite.[26] Graphene has indeed been successfully integrated into a number of polymers over the last decade; a representative (but not exhaustive) list of polymer matrices includes polyaniline (PANI), PMMA, polyetherimide (PEI), various epoxy resins, and polysiloxanes (**Figure 1.3**).[54,82,89–95] In many cases these nanocomposites have then been applied to metal substrates for corrosion protection and several orders of magnitude improvements in longevity have been observed. While this specific area of research is relatively new, it holds tremendous promise as a sustainable approach for the inhibition of corrosion.[21] In this section, we overview several types of nanocomposites that show exceptional promise.

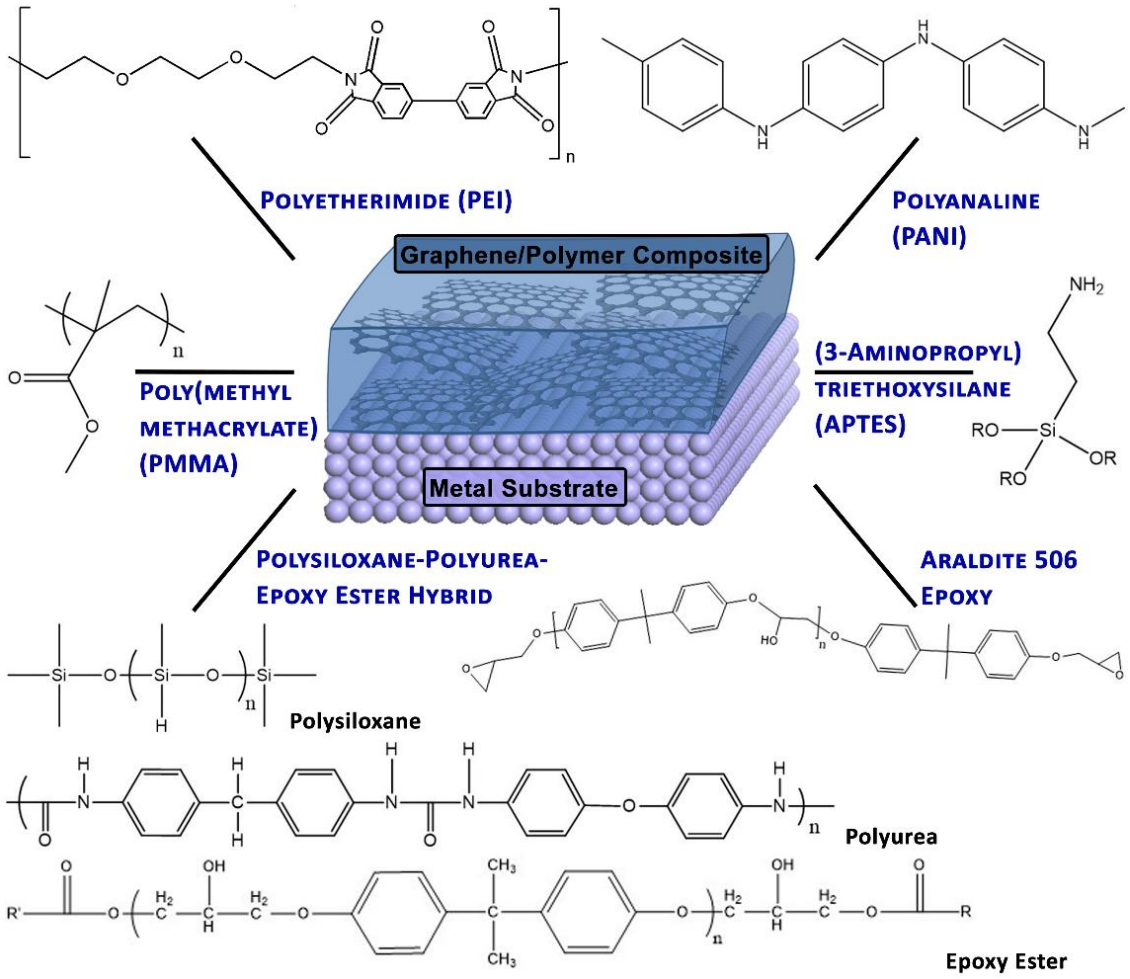

Figure 1.3. Schematic depiction and overview of selected polymers and that graphene has been incorporated in for use as a corrosion-resistant coating.

A notable example of a graphene nanocomposite coating that provides excellent corrosion inhibition to low-alloy steel under salt water exposure was reported previously by out group, is further investigated in Chapter 5, and involves the incorporation of graphene within a PEI matrix.[54] In this work, graphene is exfoliated from graphite using *N*-methylpyrrolidone (NMP) as the solvent; subsequently, polyamic acid (PAA) is also prepared in NMP and graphene is dispersed in PAA. The final coating is obtained

by wire-bar deposition of the graphene/PAA nanocomposite onto a freshly degreased low-alloy steel surface followed by imidization at 250°C to obtain PEI. A 20 wt.% graphene (UFG)/PEI coating showed a significant drop in corrosion current density of approximately seven orders of magnitude from the blank steel as well as the formation of a passivation band in the Tafel analysis of potentiodynamic polarization data (Fig. 1.4). Based on the data presented in **Figure 1.4** and summarized in Table 1.1., the estimated corrosion rate for a low alloy steel is decreased by six orders of magnitude as compared to the blank low-alloy steel and about an order of magnitude as compared to

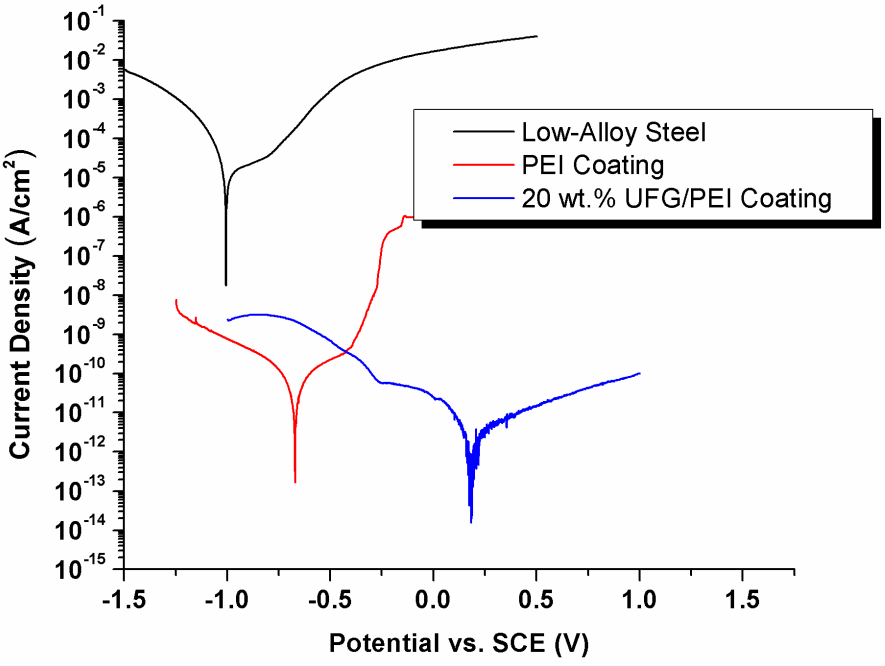

Figure 1.4. Tafel plot showing enhanced corrosion resistance afforded by the 20 wt.% UFG/PEI coating as compared to a PEI coating and uncoated low-alloy steel.

the PEI coating alone.[54] Extended exposure tests (more than 3100 h in 3.5% NaCl) of this coating system on cold-rolled steel showed qualitatively that the lifetime of the graphene coating was significantly greater than that of the PEI alone (**Fig. 1.5**). As a result of the excellent dispersion of the graphene within the PEI, likely owing to favorable π—π stacking interactions, a percolative network of graphene appears to be established within the coating that provides an alternative electronic pathway to prevent electrons from flowing from the anodic to cathodic half cells. In addition, the well-dispersed high-surface-area graphene platelets impose a tortuous path for ion permeation and further likely yield a potential barrier at the metal interface (Figure 1.2).[54]

In an alternative approach developed by the authors of this work, graphene oxide was used both as the active filler material and as the curing agent and covalently linked

Table 1.1. Corrosion Potential (E_{corr}), Corrosion Current Density (I_{corr}), and Extrapolated Corrosion Rate in mm/y from Electrochemical Testing of Low-Alloy Steel, PEI Coating, and 20 wt.% UFG/PEI Coating

Sample	E_{corr} **(V)**	I_{corr} **(A/cm^2)**	**Corrosion Rate (mm/yr.)**
Low-Alloy Steel	-1.01	1.29×10^{-5}	9.53×10^{-3}
PEI Coating	-0.67	7.00×10^{-11}	5.19×10^{-8}
20 wt.% UFG/PEI Coating	0.19	3.00×10^{-12}	2.22×10^{-9}

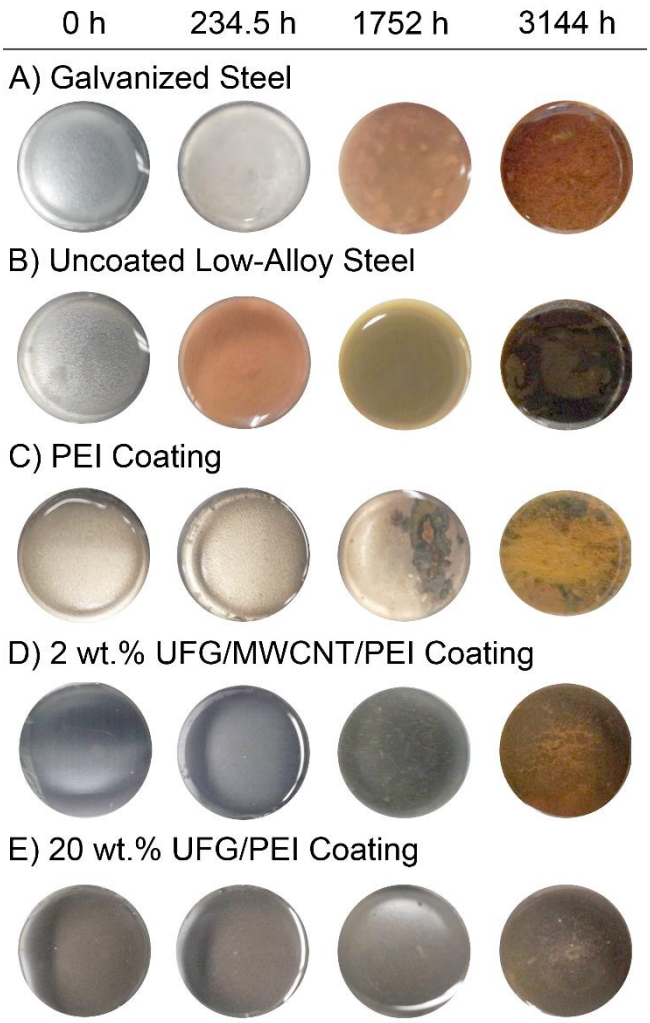

Figure 1.5. Digital photographs of salt-water immersion measurements on uncoated low-alloy steel, a PEI coating, and a 20 wt.% UFG/PEI coating.[37] Dennis R V, Viyannalage L T, Gaikwad A V, Rout T K and Banerjee S 2013 Am. Ceram. Soc. Bull. 92 18–24. Credit: *American Ceramic Society Bulletin*. Used with permission.

to the host polymer matrix, thereby achieving excellent dispersion at high loading levels.[92] A commercially available epoxy resin, Araldite 506, was used as the matrix. This resin typically requires a curing agent and/or elevated temperatures to initiate the reaction; however, the hydroxyl and carboxylic acid groups of graphene

oxide can react with the epoxide groups of the Araldite, thereby constituting a cross-linked network. This approach enabled the incorporation of graphene loadings up to 50 wt.% within the epoxy matrix. Samples with high loading levels of graphene oxide exhibited excellent corrosion resistance upon exposure to 3.5 wt.% aqueous solutions of NaCl even after the 2160 h of exposure. Lower loading levels (e.g., 5 wt.%) did not perform as well in the extended exposure tests, likely as a result of the lower cross-linking density (which renders the matrix more permeable to water and corrodant species) as well as the relatively low amount of the electro-active filler material.[92]

Several analogous approaches have been developed to improve the interfacial chemistry between graphene and the polymer matrix including that of Chang *et al.*, who demonstrated that functionalizing graphene sheets with 4-aminobenzoic acid allows for facile incorporation within PANI.[96] PANI by itself is one of most promising polymeric systems used for corrosion protection of steels as a result of its high electroactivity and facile charge transfer with steel substrates.[97] Unfortunately, it can be difficult to achieve good dispersion of graphene within PANI; however, excellent dispersion was achieved with the mediation of 4-aminobenzoic acid and authors report excellent corrosion-resistant barrier properties. Tafel analysis for this system showed a significant drop in corrosion current density and a shift to a more positive potential from the bare steel or that of the PANI coating alone (from 3.70 $\mu A/cm^2$ and -647 mV for PANI to 0.38 $\mu A/cm^2$ and -537 mV for a 0.5 wt.% graphene/PANI coating), which in turn also decreased the estimated corrosion rate by approximately two orders of magnitude.[89] The incorporation of graphene within PMMA has been achieved using a “grafting from”

approach by first binding an initiator for atom-transfer radical polymerization, (*N*-(2-aminoethyl)-2-bromo-2-methylpropanamide, NABM), and subsequently polymerizing methyl methacrylate (MMA) from the surface of graphene.[93] Graphene oxide loadings of up to 81 wt.% within PMMA are achieved by this method; the corrosion current density of a coated copper sheet decreased by ca. three to four orders of magnitude upon coating with the graphene/PMMA composite. The coating was able to provide corrosion protection to the copper surface even up to 100 h of exposure to the 3.5% NaCl solution.[93] As a concluding example, Okafor *et al.* found that graphene that was incorporated within a hybrid polymer of epoxy ester, siloxane, and urea afforded excellent corrosion protection properties for Al coupons.[91] Even at concentrations as low as 1-2 wt.% of graphene it was possible to achieve a significant diminution in corrosion, as corroborated by electrochemical impedance spectroscopy (EIS) and Tafel analysis of potentiodynamic polarization experiments. Tafel analysis of polarization data indicates a drop in the corrosion current density of about two orders of magnitude as compared to the neat hybrid polymer coating.[91] From a practical perspective, graphene/polymer nanocomposites likely represent the most viable option for large-scale applications given the drawbacks of single- and few-layered graphene as stand-alone coatings summarized in the preceding section. The widespread use of nanocomposites incorporating carbon black, microstructured carbon, carbon fibers, and increasingly carbon nanotubes, renders the incorporation of graphene within polymers a relatively facile “drop-in” solution for a diverse range of paints and coatings. The static dissipation

properties arising from formation of a percolative network are an added bonus, particularly for packaging applications in the semiconductor industry.

1.2.2.4. Graphene/Metal Nanocomposites for Corrosion Inhibition

The incorporation of graphene within metallurgical thin films yields interesting metal matrix composites some of which hold promise for corrosion protection.[98] Metallurgical films and alloys are extremely effective at preventing corrosion of various metal substrates and can serve as sacrificial anodes when used as coatings. Alternatively, metals that lie higher in the reductive potential series can also serve to protect substrates by creating a barrier that requires an increased potential to initiate oxidation. Incorporation of graphene (or carbon nanotubes) can increase the formability of the metal coating and potentially offer enhanced electrical conductivity. The primary drawback is that dispersion of graphene within metals remains a formidable challenge and the dissimilar graphene/metal interface is prone to debonding, which in turn can lead to incipient porosity and serve as the nucleation point for initiation of corrosion.[98] This drawback limits the amount of graphene that can be incorporated within such composites.

Corrosion studies have been performed on several graphene/metal composite materials including Ni/graphene[99,100], Zn/graphene[101], and Sn/graphene[102]. These coatings were all synthesized *via* combined electrophoretic deposition and electroplating from dispersions of chemically modified graphene or exfoliated graphene in plating baths. The substrate used in all cases was mild steel. Based on analysis of X-ray diffraction data, the incorporation of graphene brings about a substantial change in the

texture and grain size of the electrodeposited films. Table 1.2 collates the percentage decrease in grain size reported by various authors.[99–102] While the values for each trial cannot be compared directly, the general trends suggests a pronounced decrease of grain size upon incorporation of graphene. The decrease in grain size can be attributed to an increased density of nucleation sites on the metal surface as a result of the presence of graphene, which could potentially inhibit grain growth. Changes in texture could also potentially result from changes of the preferred crystallographic growth planes during deposition as a result of deposition onto graphene and not metal surfaces. Kumar and Berlia have postulated that graphene could limit access of solution phase metal to the substrate surface, thereby limiting particle growth.[101,102] Several of these studies also indicate that the surfaces of the coatings exhibit protrusions of hillock structures upon

Table 1.2. Average grain size calculated using the Scherrer equation and the reduction in grain size upon incorporation of graphene[99–102]

	Grain size (nm)		**Reduction in grain size (%)**
	Metal	Composite	
Ni [74]	30	20	33
Ni [75]	35	~19	46
Ni [75]	35	~16	54
Zn [76]	70	62	11
Sn [77]	79.46	75	5.6

the incorporation of graphene. These protrusions suggest the partial segregation of graphene domains and can potentially be sites for initiation of failure.

The metal matrix composites show an appreciable increase of microhardness, which can be attributed to the high strength of graphene as well as the small grain size achieved in the electrodeposited films. The diminution in grain size prevents the build-up and movement of dislocations.[100] Kumar and co-workers suggest that despite the presence of hillocks, the overall density of pits is reduced in Zn/graphene coatings upon graphene incorporation, likely as a result of the ability of graphene to bridge or fill gaps.[101] The reduced density of pits is thought to favorable for protection of the underlying metal substrates since such defects can serve to initiate corrosion. In each study, Tafel analysis was performed on electrodeposited bare metal and the metal/graphene composite films. The results of these studies are summarized in Table 1.3. In all cases, the corrosion current (I_{corr}) was observed to substantially decrease for the composite material and the corrosion potential (E_{corr}) became more positive. The corrosion rate for the Zn/graphene composite decreased four-fold as compared to the bare metal; similarly, the corrosion rate for the Sn/graphene composite was about 60% of the value for the bare Sn film.

Graphene oxide has also been instead of reduced graphene oxide within cobalt/graphene oxide composite coatings deposited by electrodeposition onto mild steel.[103] Graphene oxide can be used with a wider variety of solvents when compared to reduced graphene oxide and the oxygen groups present on the surface allow for a greater range of coordinative interactions with a metal substrate. Analogous to the results

Table 1.3. Summary of Tafel analysis results for Ni/graphene, Zn/graphene, and Sn/graphene composite coatings.[99–102]

	$\underline{I}_{corr}$ (μA/cm^2)		E_{corr} (V)	
	Metal	Composite	Metal	Composite
Ni [74]	15.8	6.687	-0.492	-0.398
Ni [75]	19.1	3.02	-0.2665	-0.2512
Ni [75]	19.1	.398	-0.2665	-0.2346
Zn [76]	19.86	6.82	0.915	0.920
Sn [77]	1.365	0.815	-0.573	-0.537

summarized in Table 1.2, the grain size of cobalt was reduced to 20 ± 2 nm for a cobalt/graphene oxide composite coating compared to a value of 50 ± 5 nm for the bare cobalt film.[103] These authors also observed a change in the preferred growth orientation of the cobalt films upon incorporation of graphene. Tafel plot analysis indicated corrosion potentials of -0.3149 V and -0.3597 V for the bare cobalt and cobalt/graphene oxide composite coatings, respectively. The corrosion current decreased from 9.70×10^{-6} A/cm^2 for the bare cobalt films to 3.04×10^{-6} A/cm^2 for the cobalt/graphene oxide coatings. The corrosion rate also similarly decreased for the composite, going from 4.98×10^{-2} mm yr^{-1} for the bare metal coating to 1.56×10^{-2} mm yr^{-1} for the cobalt/graphene oxide coating.[103]

Graphene/metal nanocomposites thus show promising performance for corrosion inhibition. Graphene is observed to decrease the grain size of electroplated metal films

and to increase their hardness. By providing more nucleation sites and enabling homogeneous deposition with reduced pit density, the nanocomposite coatings increase the resistance of the electrodeposited films to corrosive attack. Further optimization of graphene/metal interfaces is clearly required to mitigate a major probable reason for failure.

1.2.2.5. Graphene/Ceramic Nanocomposites for Corrosion Inhibition

Several reports in the literature suggest the attachment of silica or alumina prior to incorporation within an epoxy resin to not only more readily disperse the material, but also in some cases prevent the graphene from having any deleterious effects on the corrosion resistance.[82,90,94,95] Some research has suggested that because graphene is so electro-active it could actually increase the degree of corrosion for the underlying metal by increasing the number of active cathode sites throughout the coating matrix, essentially setting up a graphene/metal couple that causes galvanic corrosion.[80,94,104] Consequently, a number of different approaches have been developed to incorporate graphene within a number of commercially available epoxy resins wherein the graphene is first encapsulated by an insulating ceramic layer.[90,94,95,104,105] The enhancement in corrosion resistance that is observed for such composites is predicated entirely on the high surface area and aspect ratio of the graphene, which implies that any corrosive species must take a tortuous path to reach the metal surface (Figure 1.2). As a representative example of this approach, Sun *et al.* showed that graphene encapsulated by a nanometer-sized layer of SiO_2 created an effective barrier type coating when

dispersed within a polymer matrix, thereby significantly increasing the corrosion protection afforded to underlying copper substrates.[94]

Alternatively, Aneja *et al.* recently described an approach where they used silica not as an electrically insulating barrier but instead as a means to attach the graphene to a steel surface.[82] In this work, the authors used (3-aminopropyl)triethoxysilane (APTES) to create a functionalized graphene surface that could then be reacted with the steel surface to create a graphene/silica composite that was bonded to hydroxyl groups on the steel substrate. The subsequent deposition of an epoxy layer further enhances the corrosion resistant properties through its barrier characteristics. Remarkably, potentiodynamic polarization measurements indicate that these silica-functionalized graphene coatings are superior even to samples that have undergone conventional pretreatment with chrome. The corrosion current density for the silica/graphene coating was approximately three orders of magnitude lower than that of bare steel alone and an order of magnitude lower than the chromium-pretreated sample. In addition, a pronounced to more positive corrosion potentials was observed for the silica/graphene/epoxy composites. Salt fog testing of these samples as well as EIS data corroborate the results of Tafel analysis, confirming the formation of an excellent corrosion resistant coating.[82]

Another study by Khalil and co-workers examined the corrosion inhibition afforded by a nickel/graphene/anatase-TiO_2 coating on mild steel.[106] This coating design seeks to combine the desirable properties of graphene/metal composites discussed in the preceding section with the possibility for a further increase of stability and

increase in hardness through the incorporation of ceramic materials. Graphene/TiO_2 composites were prepared separately prior to being electrodeposited from a plating bath onto mild steel alongside metallic nickel. A coating thickness of 20 μm was achieved with a concentration of 0.4 g/L graphene-TiO_2 particles in the plating bath at a current density of 10 mA/cm^2. X-ray diffraction analysis indicates an average particle size of 24 nm for a bare nickel coating and 20 nm for the nickel/graphene/TiO_2 composite deposited under the same conditions. No major changes in the preferred orientation of growth was observed in the diffraction data. Tafel analysis showed a decrease in corrosion current density and corrosion rate with an increase in coating thickness. When comparing films of the maximum thickness, the corrosion current density decreased from 1.53×10^{-6} A/cm^2 for the nickel/graphene composite to 3.46×10^{-8} A/cm^2 for the nickel/graphene/TiO_2 composite. The corrosion rate also decreased from 0.0183 mm yr^{-1} for nickel/graphene to 0.0004 mm yr^{-1} for the nickel/graphene/TiO_2 coating. Nyquist plots showed an increase in polarization resistance from 3.90×10^3 Ω for nickel/graphene on mild steel to 3.31×10^4 Ω for nickel/graphene/TiO_2.

The inclusion of ceramic components can thus enhance the corrosion resistance of the first two classes of coatings discussed in this chapter. For graphene/polymer composites, ceramic components can facilitate the immobilization of graphene to SiO_2 surfaces or mitigate graphene/steel galvanic couples. For graphene/metal composites, the inclusion of ceramic components can further increase the hardness of the coatings and tortuosity of the ion permeation pathways.

1.2.3. Summary and future outlooks for nanocomposite design

In this section, we have attempted to capture a snapshot of a rapidly emerging discipline that could potentially yield some of the first largescale commercial products incorporating magnesium or graphene. Protecting base metals is an urgent imperative not just to prolong the longevity of infrastructure but also to facilitate the use of base metals in many emerging applications related to clean energy. Concerns regarding ecological toxicity of conventional coating materials have created interesting opportunities for the adoption of new technologies. For magnesium-bases systems, sacrificial protection can be achieved however, design of composite coatings requires understanding of the modes of corrosion inhibition and as well as failure. The interesting results obtained for graphene composites suggests that this material could be ideally poised for widespread industrial deployment. It is clear that the use of graphene by itself is unlikely to be practical over prolonged periods of operation given the inevitable presence of extended defects and thus the rational design of polymer, ceramic, and metal composites remains a critical imperative.

Mechanistic understanding of how graphene reacts with metal substrates remains incomplete, particularly with regards to the influence of additional polymeric, metal, or ceramic matrices. In this work, we have discussed several mechanistic possibilities including the development of interfacial potential barriers as a result of exchange repulsions or covalent hybridization, imposition of a highly tortuous path for ion permeation as a result of its high surface area, disruption of electron transport from the anode to the cathode as a result of its high electrical conductivity, and the establishment

of an impermeable barrier as a result of its tightly packed covalently bonded structure (Fig. 1.2). It is noteworthy that several graphene/polymer and graphene/metal matrix composites show excellent corrosion inhibition not just under potentiodynamic and EIS testing but over prolonged exposure to accelerated testing environments.

A major challenge in the discipline is the wide diversity of materials that are designated as being graphene, spanning a broad range of thicknesses, lateral dimensions, and extent of functionalization. The inconsistencies noted in the literature possibly derive in large measure from the widely heterogeneous materials used within coatings. With increased quality and consistency of available graphene materials, it is expected that more definitive answers will become available regarding the modes of action. The availability of higher quality and consistent graphene materials will also facilitate the development of systematic structure—function correlations (including through high-throughput experimental methods coupled with the appropriate data analytics), which will subsequently inform optimization of coating formulations much in the same way that integrated computational materials engineering approaches are currently being used for the development of new alloys.

A second major problem pertains to the mode of application. Most studies thus far use laboratory equipment and testing under controlled conditions. For deployment on an industrial scale, methods such as wet casting, electrodeposition, and roll-to-roll printing will need to be developed (which further requires the availability of large amounts of high-quality samples). The results of field testing are yet to become publicly available although it is clear that several companies have now advanced graphene

coatings to pilot-plant and field-testing scales. As with other areas of coatings research, the development of multifunctional and "self-healing" coatings is a particularly attractive frontier. The authors hope that this contribution will provide further impetus to this nascent discipline that shows exceptional promise for rapid commercialization. In the subsequent chapters we will explore design of graphene nanocomposite coatings with sub-30 μm thickness dispersed within a polyetherimide (PEI) matrix which show excellent corrosion inhibition of Al 7075 substrates upon prolonged exposure to saline environments.[107] and incorporate magnesium nanocrystals within such composite coatings to endow an additional mode of corrosion protection.[108] A detailed mechanistic elucidation of the origins of corrosion protection afforded by such coatings has been performed using open circuit potential measurements (OCP), electrochemical impedance spectroscopy (EIS), salt fog exposure testing, and post-mortem analysis of interfacial layers between the coating and substrate. The measurements suggest the excellent ability of graphene to enhance the resistance to transport of corrosive species through barrier protection and increased tortuosity, but emphasize the need to prevent galvanic corrosion, which can be activated when a percolative network of graphene is constituted within the polymeric matrix. Magnesium nanoparticle composite coatings are further shown to provide cathodic protection which is combined with the barrier properties of the polymer.

1.3. References

[1] Y. Liu, Y. Cui, *Joule* **2017**, *1*, 649.

[2] J. W. Evans, in *Encycl. Mater. Sci. Technol.*, **2004**, pp. 1–12.

[3] V. A. Goldade, L. S. Pinchuk, A. V. Makarevich, N. Kestelman, V, *Plastics for Corrosion Inhibition*, Springer-Verlag Berlin Heidelberg, **2005**.

[4] M. Matsui, *J. Power Sources* **2011**, *196*, 7048.

[5] O. Gharbi, S. Thomas, C. Smith, N. Birbilis, *npj Mater. Degrad.* **2018**, *2*, 12.

[6] J. E. Guyer, W. J. Boettinger, J. A. Warren, G. B. McFadden, *Phys. Rev. E* **2004**, *69*, 021603.

[7] J. E. Guyer, W. J. Boettinger, J. A. Warren, G. B. McFadden, *Phys. Rev. E* **2004**, *69*, 021604.

[8] K. F. Kelton, A. L. Greer, in *Pergamon Mater. Ser.*, **2010**, pp. 165–226.

[9] D. D. Vvedensky, *Transformations of Materials*, IOP Publishing, **2019**.

[10] A. Jana, S. I. Woo, K. S. N. Vikrant, R. E. García, *Energy Environ. Sci.* **2019**, *12*, 3595.

[11] F. Hao, A. Verma, P. P. Mukherjee, *ACS Appl. Mater. Interfaces* **2018**, *10*, 26320.

[12] J. I. Yamaki, S. I. Tobishima, K. Hayashi, K. Saito, Y. Nemoto, M. Arakawa, *J. Power Sources* **1998**, *74*, 219.

[13] P. Bai, J. Li, F. R. Brushett, M. Z. Bazant, *Energy Environ. Sci.* **2016**, *9*, 3221.

[14] R. A. Huggins, *Advanced Batteries: Materials Science Aspects*, **2009**.

[15] R. A. Huggins, D. Elwell, *J. Cryst. Growth* **1977**, *37*, 159.

[16] R. D. Davidson, A. Verma, D. Santos, F. Hao, C. D. Fincher, D. Zhao, V. Attari, P. Schofield, J. Van Buskirk, A. Fraticelli-Cartagena, T. E. G. G. Alivio, R. Arroyave, K. Xie, M. Pharr, P. P. Mukherjee, S. Banerjee, *Mater. Horizons* **2019**,

DOI 10.1039/c9mh01367a.

[17] R. Davidson, A. Verma, D. Santos, F. Hao, C. Fincher, S. Xiang, J. Van Buskirk, K. Xie, M. Pharr, P. P. Mukherjee, S. Banerjee, *ACS Energy Lett.* **2019**, *4*, 375.

[18] G. H. Koch, M. P. H. Brongers, N. G. Thompson, Y. P. Virmani, J. H. Payer, *Corrosion Costs and Preventive Strategies in the United States*, Washington D.C. FHWA, **2002**.

[19] National Research Council, *Research Opportunities in Corrosion Science and Engineering*, The National Academies Press, Washington, DC, **2011**.

[20] A. Winkleman, E. B. Svedberg, R. E. Schafrik, D. J. Duquette, *Adv. Mater. Process.* **2011**, *169*, 26.

[21] S. Böhm, *Nat. Nanotechnol.* **2014**, *9*, 741.

[22] F. Presuel-Moreno, M. A. Jakab, N. Tailleart, M. Goldman, J. R. Scully, *Mater. Today* **2008**, *11*, 14.

[23] A. E. Hughes, I. S. Cole, T. H. Muster, R. J. Varley, *NPG Asia Mater.* **2010**, *2*, 143.

[24] R. B. Figueira, C. J. R. Silva, E. V. Pereira, *J. Coatings Technol. Res.* **2014**, *12*, 1.

[25] M. L. Zheludkevich, I. M. Salvado, M. G. S. Ferreira, *J. Mater. Chem.* **2005**, *15*, 5099.

[26] R. V. Dennis, V. Patil, J. L. Andrews, J. P. Aldinger, G. D. Yadav, S. Banerjee, *Mater. Res. Express* **2015**, *2*, 032001.

[27] T. Prosek, A. Nazarov, U. Bexell, D. Thierry, J. Serak, *Corros. Sci.* **2008**, *50*, 2216.

[28] B. C. Worley, W. A. Ricks, M. P. Prendergast, B. W. Gregory, R. Collins, J. J. Cassimus, R. G. Thompson, *Langmuir* **2013**, *29*, 12969.

[29] I. S. Cole, T. H. Muster, D. Lau, N. Wright, N. S. Azmat, *J. Electrochem. Soc.* **2010**, *157*, C213.

[30] N. Sato, *Corrosion* **1989**, *45*, 354.

[31] W. J. Clark, J. D. Ramsey, R. L. McCreery, G. S. Frankel, *J. Electrochem. Soc.* **2002**, *149*, B179.

[32] D. Grigoriev, D. Akcakayiran, M. Schenderlein, D. Shchukin, *Corrosion* **2014**, *70*, 446.

[33] D. G. Shchukin, M. Zheludkevich, H. Möhwald, *J. Mater. Chem.* **2006**, *16*, 4561.

[34] S. V. Lamaka, M. L. Zheludkevich, K. A. Yasakau, R. Serra, S. K. Poznyak, M. G. S. Ferreira, *Prog. Org. Coatings* **2007**, *58*, 127.

[35] M. L. Zheludkevich, D. G. Shchukin, K. A. Yasakau, H. Möhwald, M. G. S. Ferreira, *Chem. Mater.* **2007**, *19*, 402.

[36] M. W. Kendig, R. G. Buchheit, *Corrosion* **2003**, *59*, 379.

[37] E. Groshart, *Met. Finish.* **1997**, *95*, 70.

[38] J. W. Bibber, *J. Appl. Surf. Finish.* **2007**, *2*, 273.

[39] J. W. Bibber, *Met. Finish.* **2008**, *106*, 41.

[40] J. W. Bibber, in *Manag. Hazard. Residues Contain. Cr* (Ed.: M.J. Balart Murria), Nova Science Publishers, Inc., Hauppauge, NY USA, **2011**, pp. 37–49.

[41] T. Chen, W. Li, J. Cai, *RSC Adv.* **2011**, *1*, 607.

[42] J. H. Osborne, *Prog. Org. Coatings* **2001**, *41*, 280.

[43] D. G. Shchukin, M. Zheludkevich, K. Yasakau, S. Lamaka, M. G. S. Ferreira, H. Möhwald, *Adv. Mater.* **2006**, *18*, 1672.

[44] S. A. Katz, H. Salem, *J. Appl. Toxicol.* **1993**, *13*, 217.

[45] S. Wilbur, H. Abadin, M. Fay, D. Yu, B. Tencza, L. Ingerman, J. Klotzbach, S. James, *Toxilogical Profile for Chromium*, Atlanta, Georgia, **2012**.

[46] A. Baral, R. D. Engelken, *Environ. Sci. Policy* **2002**, *5*, 121.

[47] S. D. Jagtap, S. P. Tambe, R. N. Choudhari, B. P. Mallik, *Prog. Org. Coatings* **2014**, *77*, 395.

[48] Y. Kou, J. Wang, M. Lv, X. Jian, *Polym. Int.* **2010**, *59*, 107.

[49] J. D. Elmore, D. S. Kincaid, P. C. Komar, J. E. Nielsen, *J. Coatings Technol.* **2002**, *74*, 63.

[50] A. R. Marder, *Prog. Mater. Sci.* **2000**, *45*, 191.

[51] N. C. Hosking, M. A. Ström, P. H. Shipway, C. D. Rudd, *Corros. Sci.* **2007**, *49*, 3669.

[52] T. K. Rout, A. V. Gaikwad, T. Dingemans, *A Method of Preparing a Polyetherimide Coating on a Metallic Substrate*, **2011**, World Intellectual Property Organization, Patent number WO 2011035920 A1.

[53] R. V. Dennis, L. T. Viyannalage, J. P. Aldinger, T. K. Rout, S. Banerjee, *Ind. Eng. Chem. Res.* **2014**, *53*, 18873.

[54] R. V Dennis, L. T. Viyannalage, A. V. Gaikwad, T. K. Rout, S. Banerjee, *Am. Ceram. Soc. Bull.* **2013**, *92*, 18.

[55] A. Simões, D. Battocchi, D. Tallman, G. Bierwagen, *Prog. Org. Coatings* **2008**,

63, 260.

[56] S. S. Pathak, S. K. Mendon, M. D. Blanton, J. W. Rawlins, S. S. Pathak, S. K. Mendon, M. D. Blanton, J. W. Rawlins, *Metals (Basel).* **2012**, *2*, 353.

[57] M. E. Nanna, G. P. Bierwagen-North, P. A. Philadelphia, *JCT Res.* **2004**, *1*, 69.

[58] R. Lindström, J.-E. Svensson, L.-G. Johansson, *J. Electrochem. Soc.* **2002**, *149*, B103.

[59] R. Lindström, L. G. Johansson, G. E. Thompson, P. Skeldon, J. E. Svensson, *Corros. Sci.* **2004**, *46*, 1141.

[60] B. J. E. Merten, D. Battocchi, G. P. Bierwagen, *Prog. Org. Coatings* **2015**, *78*, 446.

[61] G. Bierwagen, R. Brown, D. Battocchi, S. Hayes, *Prog. Org. Coatings* **2010**, *67*, 195.

[62] B. J. Schultz, R. V. Dennis, V. Lee, S. Banerjee, *Nanoscale* **2014**, *6*, 3444.

[63] K. S. Novoselov, A. K. Geim, S. V Morozov, D. Jiang, M. I. Katsnelson, I. V Grigorieva, S. V Dubonos, A. A. Firsov, *Nature* **2005**, *438*, 197.

[64] S. Sarkar, M. L. Moser, X. Tian, X. Zhang, Y. F. Al-Hadeethi, R. C. Haddon, *Chem. Mater.* **2014**, *26*, 184.

[65] M. Batzill, *Surf. Sci. Rep.* **2012**, *67*, 83.

[66] E. Bekyarova, S. Sarkar, F. Wang, M. E. Itkis, I. Kalinina, X. Tian, R. C. Haddon, *Acc. Chem. Res.* **2013**, *46*, 65.

[67] A. Dahal, M. Batzill, *Nanoscale* **2014**, *6*, 2548.

[68] V. Lee, C. Park, C. Jaye, D. A. Fischer, Q. Yu, W. Wu, Z. Liu, J. Bao, S.-S. Pei,

C. Smith, P. Lysaght, S. Banerjee, *J. Phys. Chem. Lett.* **2010**, *1*, 1247.

[69] G. Giovannetti, P. A. Khomyakov, G. Brocks, V. M. Karpan, J. van den Brink, P. J. Kelly, *Phys. Rev. Lett.* **2008**, *101*, 026803.

[70] P. A. Khomyakov, G. Giovannetti, P. C. Rusu, G. Brocks, J. van den Brink, P. J. Kelly, *Phys. Rev. B* **2009**, *79*, 195425.

[71] T. Abtew, B.-C. Shih, S. Banerjee, P. Zhang, *Nanoscale* **2013**, *5*, 1902.

[72] J. Tersoff, *Phys. Rev. Lett.* **1984**, *52*, 465.

[73] D. Zhang, D. Z.-R. Wang, R. Creswell, C. Lu, J. Liou, I. P. Herman, *Chem. Mater.* **2015**, *27*, 5032.

[74] O. Leenaerts, B. Partoens, F. M. Peeters, *Appl. Phys. Lett.* **2008**, *93*, 193107.

[75] J. S. Bunch, S. S. Verbridge, J. S. Alden, A. M. van der Zande, J. M. Parpia, H. G. Craighead, P. L. McEuen, *Nano Lett.* **2008**, *8*, 2458.

[76] D. Prasai, J. C. Tuberquia, R. R. Harl, G. K. Jennings, K. I. Bolotin, *ACS Nano* **2012**, *6*, 1102.

[77] R. K. Singh Raman, P. Chakraborty Banerjee, D. E. Lobo, H. Gullapalli, M. Sumandasa, A. Kumar, L. Choudhary, R. Tkacz, P. M. Ajayan, M. Majumder, *Carbon* **2012**, *50*, 4040.

[78] N. T. Kirkland, T. Schiller, N. Medhekar, N. Birbilis, *Corros. Sci.* **2012**, *56*, 1.

[79] R. K. Singh Raman, A. Tiwari, *JOM* **2014**, *66*, 637.

[80] M. Schriver, W. Regan, W. J. Gannett, A. M. Zaniewski, M. F. Crommie, A. Zettl, *ACS Nano* **2013**, *7*, 5763.

[81] P. Keil, R. Frahm, D. Lützenkirchen-Hecht, *Corros. Sci.* **2010**, *52*, 1305.

[82] K. S. Aneja, S. Bohm, A. Khanna, M. Bohm, *Nanoscale* **2015**, *7*, 17879.

[83] S. C. Sahu, A. K. Samantara, M. Seth, S. Parwaiz, B. P. Singh, P. C. Rath, B. K. Jena, *Electrochem. commun.* **2013**, *32*, 22.

[84] V. Lee, L. Whittaker, C. Jaye, K. M. Baroudi, D. A. Fischer, S. Banerjee, *Chem. Mater.* **2009**, *21*, 3905.

[85] E. T. Y. Lih, R. bt M. Zaid, T. L. Ling, K. F. Chong, *Int. J. Chem. Eng. Appl.* **2012**, *3*, 453.

[86] G. Bierwagen, R. Brown, D. Battocchi, S. Hayes, *Prog. Org. Coatings* **2010**, *67*, 195.

[87] N. D. Orloff, C. J. Long, J. Obrzut, L. Maillaud, F. Mirri, T. P. Kole, R. D. McMichael, M. Pasquali, S. J. Stranick, J. Alexander Liddle, *Sci. Rep.* **2015**, *5*, 17019.

[88] H. Kim, A. A. Abdala, C. W. MacOsko, *Macromolecules* **2010**, *43*, 6515.

[89] C.-H. Chang, T.-C. Huang, C.-W. Peng, T.-C. Yeh, H.-I. Lu, W.-I. Hung, C.-J. Weng, T.-I. Yang, J.-M. Yeh, *Carbon* **2012**, *50*, 5044.

[90] Y. Ma, H. Di, Z. Yu, L. Liang, L. Lv, Y. Pan, Y. Zhang, D. Yin, *Appl. Surf. Sci.* **2015**.

[91] P. A. Okafor, J. Singh-Beemat, J. O. Iroh, *Prog. Org. Coatings* **2015**, *88*, 237.

[92] V. Patil, R. V. Dennis, T. K. Rout, S. Banerjee, G. D. Yadav, *RSC Adv.* **2014**, *4*, 49264.

[93] K. Qi, Y. Sun, H. Duan, X. Guo, *Corros. Sci.* **2015**, *98*, 500.

[94] W. Sun, L. Wang, T. Wu, Y. Pan, G. Liu, *J. Mater. Chem. A* **2015**, *3*, 16843.

[95] Z. Yu, H. Di, Y. Ma, L. Lv, Y. Pan, C. Zhang, Y. He, *Appl. Surf. Sci.* **2015**, *351*, 986.

[96] C.-H. Chang, T.-C. Huang, C.-W. Peng, T.-C. Yeh, H.-I. Lu, W.-I. Hung, C.-J. Weng, T.-I. Yang, J.-M. Yeh, *Carbon* **2012**, *50*, 5044.

[97] T. K. Rout, G. Jha, A. K. Singh, N. Bandyopadhyay, O. N. Mohanty, *Surf. Coatings Technol.* **2003**, *167*, 16.

[98] L.-Y. Chen, H. Konishi, A. Fehrenbacher, C. Ma, J.-Q. Xu, H. Choi, H.-F. Xu, F. E. Pfefferkorn, X.-C. Li, *Scr. Mater.* **2012**, *67*, 29.

[99] C. M. P. Kumar, T. V Venkatesha, R. Shabadi, *Mater. Res. Bull.* **2013**, *48*, 1477.

[100] K. Jiang, J. Li, J. Liu, *RSC Adv.* **2014**, *4*, 36245.

[101] M. K. P. Kumar, M. P. Singh, C. Srivastava, *RSC Adv.* **2015**, *5*, 25603.

[102] R. Berlia, M. K. P. Kumar, C. Srivastava, *RSC Adv.* **2015**, *5*, 71413.

[103] C. Liu, F. Su, J. Liang, *Appl. Surf. Sci.* **2015**, *351*, 889.

[104] Z. Yang, W. Sun, L. Wang, S. Li, T. Zhu, G. Liu, *Corros. Sci.* **2015**.

[105] W. Sun, L. Wang, T. Wu, Y. Pan, G. Liu, *Carbon* **2014**, *79*, 605.

[106] M. W. Khalil, T. A. Salah Eldin, H. B. Hassan, K. El-Sayed, Z. Abdel Hamid, *Surf. Coatings Technol.* **2015**, *275*, 98.

[107] R. D. Davidson, Y. Cubides, C. Fincher, P. Stein, C. McLain, B.-X. Xu, M. Pharr, H. Castaneda, S. Banerjee, *ACS Appl. Nano Mater.* **2019**, *2*, 3100.

[108] R. D. Davidson, Y. Cubides, J. L. Andrews, C. M. McLain, H. Castaneda, S. Banerjee, *Phys. status solidi* **2019**, *216*, 1800817.

2. FORMATION OF MAGNESIUM DENDRITES DURING ELECTRODEPOSITION*

2.1. Overview

We demonstrate the growth of dendritic magnesium deposits with fractal morphologies exhibiting shear moduli in excess of values for polymeric separators upon the galvanostatic electrodeposition of metallic Mg from Grignard reagents in symmetric Mg—Mg cells. Dendritic growth is understood based on the competing influences of reaction rate, electrolyte transport rate, and self-diffusion barrier evaluated using a dimensionless Damköhler ratio as further corroborated by mesoscale simulations.

2.2. Introduction

The use of lithium-ion batteries (LIBs) as a means of energy storage is pervasive across most types of consumer electronics and is on the ascent for large-area formats such as electric vehicles. Current commercial LIBs pair transition metal oxide cathodes with graphite anodes. A substantial enhancement of performance metrics is conceptually possible through the use of lithium metal anodes.[1] However, Li metal has a high propensity for dendrite formation. Numerous high-profile incidents have led to safety concerns emerging as a paramount consideration. Furthermore, such incidents have underscored the importance of understanding the accumulative impact of low-probability stochastic processes.

Magnesium batteries have attracted considerable attention as a potential alternative to lithium owing to the divalent nature of Mg-ions, which has been proposed

*Reprinted (adapted) with permission from (R. Davidson, A. Verma, D. Santos, F. Hao, C. Fincher, S. Xiang, J. Van Buskirk, K. Xie, M. Pharr, P. P. Mukherjee, S. Banerjee, ACS Energy Lett. 2019, 4, 375.). Copyright (2019) American Chemical Society.

as a means of achieving higher energy densities. The higher crustal abundance of magnesium as compared to lithium, its resilience to criticality constraints, and the apparent “non-dendrite” forming nature of this metal upon electroplating (which holds promise for enabling the use of metal anodes) has focused considerable attention on this alternative energy storage vector.[2–9] Despite considerable focus on electrolyte development, the intrinsic electrodeposition process remains relatively scarcely explored.[10–13] The idea of a lower propensity towards dendrite formation has been uncritically accepted across a vast swath of the literature, even though most studies are limited in their exploration of deposition conditions. In this work, we demonstrate the electrochemical growth of fractal Mg dendrites from Grignard reagents[5] in symmetric cells under galvanostatic conditions as described in the experimental section.

2.3. Results and Discussion

Figure A.1 shows SEM images of the surfaces of Mg ribbon electrodes attesting to their smooth initial topographies. **Videos A.1—A.3** illustrates time-lapse images of Mg deposition monitored in situ with applied current densities of 0.307, 0.921, and 1.54 mA/cm^2 and average measured overpotentials of 0.278, 0.432, 0.668 V/mm respectively. **Figure 2.1A** shows images of fractal deposits formed from the electrodeposition of Mg from a 0.5 M solution of MeMgCl in THF at a constant current density of 0.921 mA/cm^2. **Video A.4** shows a tomographic reconstruction of a dendrite. The deposits span several millimeters in length, are highly branched, and grow from the edges of the Mg ribbon. SEM images indicate aggregated hexagonal platelets that are crystallized in the intrinsic habit of hcp Mg (angles of 118—121° between adjacent faces as shown in

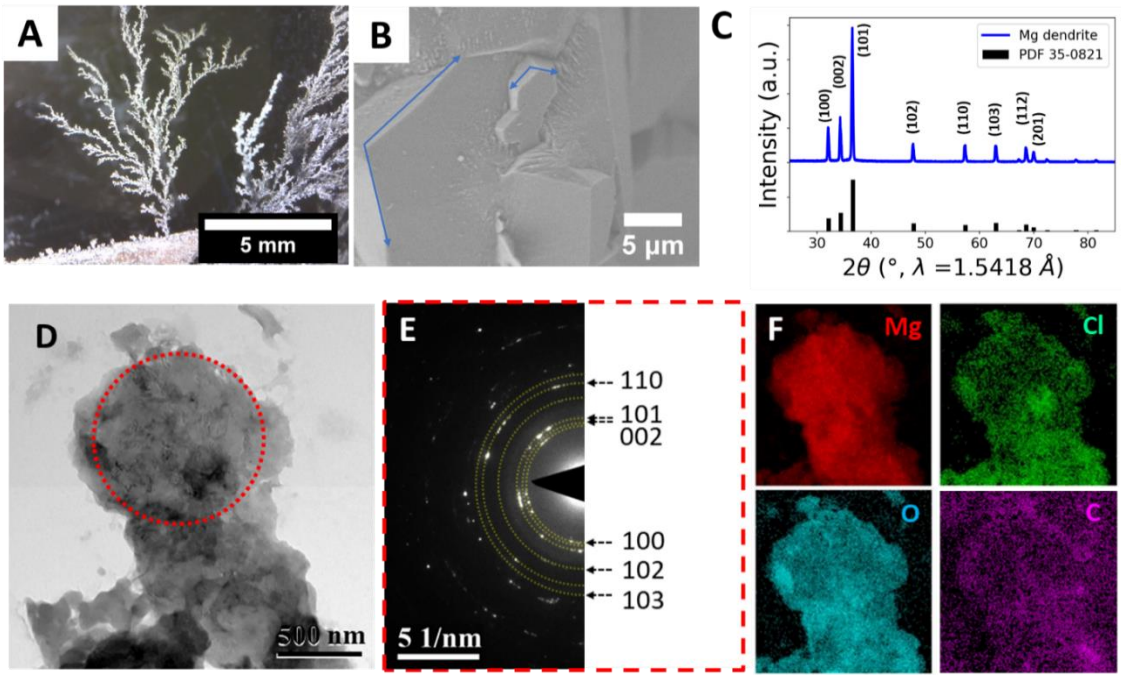

Figure 2.1. Characterization of Fractal Mg deposits. A) Digital photograph of fractal Mg structure; B) SEM image of a section of the structure; C) powder XRD pattern measured for detached Mg fractal structure D) TEM image of a region of polycrystalline Mg dendrites; E) SAED pattern acquired from the region delineated by the red circle. F) EDS maps of the region imaged in (D).

Figure 2.1B). A powder XRD pattern of the deposits can be indexed to PDF 35-0821, corresponding to hcp magnesium. Figure 2.1D shows a representative transmission electron microscopy (TEM) image. A selected area electron diffraction (SAED) pattern (Figure 2.1E) shows diffraction spots indicative of a well-developed polycrystalline structure. Energy dispersive spectroscopy (EDS) mapping indicated that the Mg dendrite is rich in Mg with trace amounts of Cl (Figure 2.1F). Based on nanoindentation measurements, dendritic Mg exhibits an elastic modulus of 27.1±2.8 GPa as shown in Figures 2.2A-B. Following the Newman and Monroe criterion,[14] this translates to the

need for a separator or solid state electrolyte with a shear modulus of greater than ca. 24 GPa indicating that Mg dendrites will readily puncture commonly used polymeric separators. This is much greater than the estimated requirement of around 6.8 GPa for lithium anodes.[14] Similar results would likely be observed when considering other "beyond-Li" systems which have much greater elastic moduli than lithium.

In order to examine the balance between the surface diffusion and the electrochemical reaction rate, a non-dimensional electrochemical Damköhler number, *Da*, can be defined as the ratio of the electrochemical reaction rate, k_e to the surface diffusion rate, k_d as per:[15]

$$\boldsymbol{Da = \frac{k_e}{k_d}} \qquad \textbf{2.1}$$

Values of *Da* >>1 imply that the electrochemical reaction occurs at a much faster rate as compared to surface self-diffusion (see experimental section). In this limit, dendritic structures are expected, as observed in Figure 2.1, since despite the low calculated surface diffusion barriers for Mg[6], the large monomer flux shifts the system to a reaction-dominated growth regime.[6,15] For $Da \sim 1$, the formation of discrete Mg islands is anticipated. Finally, for *Da* <<1, Mg self-diffusion eclipses the reaction rate and homogeneous thin film morphologies are expected. **Figure 2.2C** plots the aforementioned regimes in terms of the predicted morphologies of electroplated Mg deposits as a function of the electrochemical reaction and surface diffusion rates. The operating regime is delineated by white lines based on electrochemical reaction and surface diffusion rates noted in **Tables A.1 and A.2**.

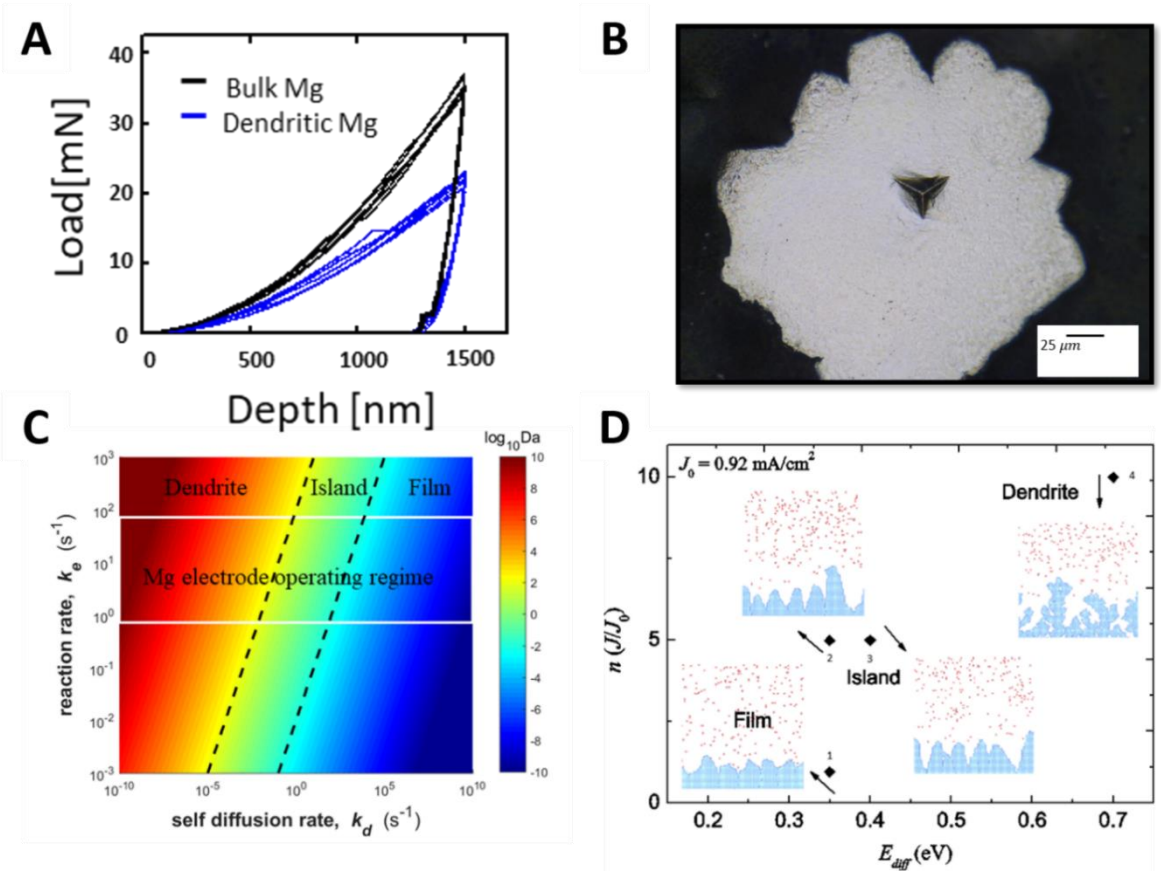

Figure 2.2. A) Representative load-depth curves for dendritic and bulk Mg and B) optical image of an indentation site. C) Predicted deposition morphology phase plotted as a function of Damköhler number. D) Deposition morphology predicted by kinetic Monte Carlo simulations for different values of current density and diffusion barriers.

Figure 2.2D shows the deposition morphologies obtained from mesoscale Kinetic Monte Carlo (KMC) simulations upon varying the current density and self-diffusion activation barrier. High current densities lead to high electrochemical reaction rates, whereas high self-diffusion activation barriers correlate to low magnitudes of self-diffusion rates. Under conditions of high current densities and high self-diffusion energy barriers (top-right of Figure 2.2B), a strong propensity to form dendritic structures is

clearly observed (marker 4 corresponds to J = 9.2 mA/cm^2, E_{diff} = 0.7 eV). Intermediate values of reaction current density and diffusion energy barrier (markers 2 and 3) give rise to island-type Mg deposits owing to the comparable weighting of both parameters. Finally, for low current densities and diffusion energy barriers (marker 1), the growth of continuous thin films is predicted as a result of the primacy of the self-diffusion rates.

In conjunction to the relative dominance of electrochemical growth over surface diffusion, edge/curvature effects at the corners of the magnesium electrode contribute to preferential dendritic growth at the edges. Strongest electric fields and consequently electrolyte potential gradients occur at locations along the surface where the electrode is most curved. Consequently, the Mg ribbon corners form high current density and preferential magnesium deposition sites. This phenomenon is also observed at dendrite tips and electrode surface protrusions.[16]

The promise of magnesium batteries derives in large measure from claims that they are immune to dendrite formation. Galvanostatic electrodeposition of metallic Mg from Grignard reagents in symmetric Mg-Mg cells demonstrates growth of highly anisotropic fractal deposits that are predominantly zero-valent magnesium. While experimental conditions employed here, such as the lower operational temperatures, localization of overpotential at the anode edges, and fast charge rates likely exacerbate dendritic growth and the generalizability of the observed phenomena to other electrolytes and full cells remains to be established, it is worth noting that electrochemical reaction rates can quite readily surpass self-diffusion rates as a result of local inhomogeneities and reactivity. Furthermore, the possibility for formation of “dead

magnesium" caused by stripping at the base from high aspect ratio structures during discharge and the resulting issues with capacity fading will require future consideration.[17] Though considerable effort has been invested in the development of Mg and other "beyond Li" such as Zn and Ca intercalation systems that derive a considerable portion of their promise from the potential to utilize their respective metallic anodes, further study is clearly required and the term "dendrite-free" must be used with caution.

2.4. Experimental

2.4.1. Electrodeposition Conditions and Videomicroscopy

Three-neck round bottom flasks (100 mL) were equipped with two electrical leads threaded through a septum, which allowed for Mg ribbon electrodes (Alfa Aesar, purity of 99.5 % Mg) to be held at a constant separation to form a symmetric cell. Solutions of MeMgCl (3 M in anhydrous tetrahydrofuran (THF), Alfa Aesar) were further diluted with anhydrous THF (EMD Millipore Co.) to obtain 0.5 M solutions. The electrodeposition assemblies were assembled within an argon-filled glove box (< 0.1 ppm O_2) and operated under Schlenk conditions in an Ar ambient.

The leads were connected to a programmable power supply (FB1000, Fisher Scientific), and a constant current was applied for specified durations. Plating of Mg onto the ribbon electrodes was monitored *in situ* with the help of a videomicroscope (Plugable Technologies).

2.4.2. Structural Characterization of Deposits

The electrodeposited residues were removed from the substrates through gentle washing with THF. Phase identification was performed using powder X-ray diffraction (XRD) in Bragg—Brentano geometry using a Bruker D8-Focus diffractometer (Cu Kα: λ = 1.5418Å; 40 kV voltage; 25 mA current).

2.4.3. Electron Microscopy

The deposits were examined by scanning electron microscopy (SEM) using a JEOL JSM-7500F instrument operating at an accelerating voltage of 10 kV, emission current of 5 μA, and a probe current of 10 μA. Bright-field transmission electron microscopy (TEM), high-angle annular dark-field scanning TEM (HAADF-STEM), and energy dispersive X-ray spectroscopy (EDS) were employed to investigate the morphology, crystal structure, and compositional distribution using a FEI Tecnai G2 F20 Super-Twin FE-TEM operated at 200 kV.

2.4.4. Nanomechanical Characterization of Deposits

Two samples, one of dendritic Mg electroplated deposits and one of bulk Mg (Mg ribbon Alfa Aesar, purity of 99.5% Mg), were cast into Buehler EpoKwik cold-mounting epoxy and consecutively polished using 9, 6, and 1 μm diamond suspensions (Metallurgical Supplies) followed by Buehler MasterPrep 0.05 μm diamond suspensions. After polishing, the elastic modulus and hardness of the samples were measured using a Nanomechanics iMicro indenter with an InForce 50 actuator and a diamond Berkovich tip. Estimation of the elastic modulus and hardness follows the standard approach of Oliver and Pharr.[18] Both the frame stiffness and the depth—area relationship were

empirically determined based upon the indentation response of a standard fused silica sample. Indentation was implemented at a constant strain rate test of $\frac{\dot{P}}{P} = 0.2\frac{1}{s}$, with a continuous stiffness oscillation of 2 nm. Ten tests were conducted on the bulk magnesium sample to a depth of 1.5 μm. For the dendritic Mg deposits, ten tests were conducted to a depth of 600 nm, and ten more tests were conducted to a depth of 1 μm. For both samples, the modulus and hardness measurements were acquired by averaging the continuous stiffness measurements at depths of 500—600 nm, a depth chosen to minimize the effects of any potential frame stiffness or surface roughness issues. As observed in the tomographic reconstruction shown in Video A.4, the dendrites span several millimeters in thickness, which are several orders of magnitude larger than the probe depths, thereby eliminating the role of substrate effects.

2.4.5. Model Formulation

The deposition morphology on a substrate is determined based on the relative magnitudes of the electrochemical reaction rate and the surface diffusion rate.[15] For Mg deposition on Mg substrates, these parameters can be related to the magnitude of the experimental current density and the self-diffusion coefficient of Mg.[6] The electrochemical reaction rate, k_e can be obtained from the experimental current density, J as per:

$$\boldsymbol{k_e = \frac{Jd^2}{2F} N_A} \qquad \textbf{2.2}$$

where d is the mean diffusion distance between lattice sites of magnesium, F is Faraday's constant, and N_A is Avogadro's constant. The values of these parameters have

been enumerated in Table A.1. The average current density magnitude utilized for our experiments is, J_0 = 9.2 A/m^2. Since, the formation of Mg deposits can vary the interface morphology and consequently affect the local current density at the substrate, an order of magnitude variation, $n = \frac{J}{J_0}$ = 0.1 – 10, relative to the current density magnitude has been evaluated, i.e., from 0.92 A/m^2 to 92 A/m^2, when defining the electrode operating conditions. Given that Mg adopts a hcp structure with lattice constants of a = 3.21Å and c = 5.21Å, an average lattice cell dimension of d = 5Å is used in the model.

The surface diffusion rate, k_d, is computed using Equation 2.3 and depends on the activation energy barrier for self-diffusion, E_{diff}, temperature, T and jump frequency for Mg diffusion, ν. Literature reports of average values of jump frequency range between ca. 10^{12}—10^{13} s^{-1}.[19] Consequently, a value of $\nu = 5\times10^{12}$ s^{-1} has been utilized where k_B represents the Boltzmann constant.

$$\boldsymbol{k_d = \nu\, exp\left(\frac{-E_{diff}}{k_B T}\right)} \qquad \textbf{2.3}$$

The self-diffusion energy barrier, E_{diff}, determines the magnitude of the diffusion rate, and thus, needs to be determined accurately to capture the underlying dynamics of the Mg system. In the literature, values of the diffusion energy barrier, E_{diff} [13] or diffusion coefficients, D, have been disparately reported.[20–23] When the E_{diff} value is reported, equation 2.3 can be directly used to compute the self-diffusion rate. Alternatively, the

diffusion coefficient can be related to the diffusion rate via the Einstein—Smoluchowski relation as per:[19]

$$\boldsymbol{D = \frac{1}{2} k_d d^2} \qquad \textbf{2.4}$$

Experimental and theoretical values of diffusion coefficients, self-diffusion energy barriers, and diffusion rates from the literature have been computed at $T = 300$ K and are tabulated in Table A.2. Diffusion in hcp Mg can occur along the basal plane, $D_{\parallel}$, or perpendicular to the basal plane, $D_{\perp}$. Both these values are noted along with the average diffusivity value, $D_{avg.}$, which is then utilized to compute the diffusion rate. Arrhenius type experimental relations for self-diffusion in Mg have been reported by Shewmon[20] as well as Combronde and Brebec[21] in the temperature range 468—635°C and 500 –630°C, respectively, with the form:

$$\boldsymbol{D = D_0 \, exp\left(\frac{-E_a}{RT}\right)} \qquad \textbf{2.5}$$

This expression has been extrapolated to a temperature of 300 K to obtain the self-diffusion coefficient at room temperature. Several first-principles DFT results are further available that provide diffusion coefficients in the temperature range of ca. 227–727 ˚C.[22,23] Applicability of the Arrhenius equation is assumed based on the diffusivity—temperature dataset; linear regression analysis of ln (D) versus T is performed to obtain the Arrhenius constants, D_0 and E_a for these datasets. Subsequently, the diffusivity at 26.8 ˚C is obtained from the regression correlation.

2.5. References

[1] B. Liu, J.-G. Zhang, W. Xu, *Joule* **2018**, *2*, 833.

[2] D. Aurbach, Y. Cohen, M. Moshkovich, *Electrochem. Solid-State Lett.* **2001**, *4*, A113.

[3] J. Muldoon, C. B. Bucur, A. G. Oliver, T. Sugimoto, M. Matsui, H. S. Kim, G. D. Allred, J. Zajicek, Y. Kotani, *Energy Environ. Sci.* **2012**, *5*, 5941.

[4] H. D. Yoo, I. Shterenberg, Y. Gofer, G. Gershinsky, N. Pour, D. Aurbach, *Energy Environ. Sci.* **2013**, *6*, 2265.

[5] C. B. Bucur, T. Gregory, A. G. Oliver, J. Muldoon, *J. Phys. Chem. Lett.* **2015**, *6*, 3578.

[6] M. Jäckle, K. Helmbrecht, M. Smits, D. Stottmeister, A. Groß, *Energy Environ. Sci.* **2018**, *11*, 3400.

[7] P. Canepa, G. Sai Gautam, D. C. Hannah, R. Malik, M. Liu, K. G. Gallagher, K. A. Persson, G. Ceder, *Chem. Rev.* **2017**, *117*, 4287.

[8] J. L. Andrews, A. Mukherjee, H. D. Yoo, A. Parija, P. M. Marley, S. Fakra, D. Prendergast, J. Cabana, R. F. Klie, S. Banerjee, *Chem* **2018**, *4*, 564.

[9] L. R. De Jesus, J. L. Andrews, A. Parija, S. Banerjee, **2018**, *16*, 37.

[10] M. Matsui, *J. Power Sources* **2011**, *196*, 7048.

[11] S. DeWitt, N. Hahn, K. Zavadil, K. Thornton, *J. Electrochem. Soc.* **2016**, *163*, A513.

[12] C. Ling, D. Banerjee, M. Matsui, *Electrochim. Acta* **2012**, *76*, 270.

[13] M. Jäckle, A. Groß, *J. Chem. Phys.* **2014**, *141*, 174710.

[14] C. Monroe, J. Newman, *J. Electrochem. Soc.* **2005**, *152*, A396.

[15] F. Hao, A. Verma, P. P. Mukherjee, *ACS Appl. Mater. Interfaces* **2018**, *10*, 26320.

[16] R. Akolkar, *J. Power Sources* **2013**, *232*, 23.

[17] K. N. Wood, E. Kazyak, A. F. Chadwick, K. H. Chen, J. G. Zhang, K. Thornton, N. P. Dasgupta, *ACS Cent. Sci.* **2016**, *2*, 790.

[18] W. C. Oliver, G. M. Pharr, *J. Mater. Res.* **1992**, *7*, 1564.

[19] G. K. P. Dathar, D. Sheppard, K. J. Stevenson, G. Henkelman, *Chem. Mater.* **2011**, *23*, 4032.

[20] P. G. Shewmon, *Trans.Metall.Soc.AIME* **1956**, *206*, 918.

[21] J. Combronde, G. Brebec, *Acta Metall.* **1971**, *19*, 1393.

[22] S. Ganeshan, L. G. Hector, Z. K. Liu, *Comput. Mater. Sci.* **2010**, *50*, 301.

[23] L. J. Zhang, T. I. Spiridonova, S. E. Kulkova, R. Yang, Q. M. Hu, *Comput. Mater. Sci.* **2017**, *128*, 236.

[24] G. Henkelman, B. P. Uberuaga, H. Jónsson, *J. Chem. Phys.* **2000**, *113*, 9901.

3. MAPPING MECHANISMS AND GROWTH REGIMES OF MAGNESIUM ELECTRODEPOSITION AT HIGH CURRENT DENSITIES*

3.1. Overview

The utilization of metallic anodes holds promise for unlocking high gravimetric and volumetric energy densities and is pivotal to the adoption of 'beyond Li' battery chemistries. Much of the promise of magnesium batteries stems from claims regarding their lower predilection for dendrite growth. Whilst considerable effort has been invested in the design of novel electrolytes and cathodes, detailed studies of Mg plating are scarce. Using galvanostatic electrodeposition of metallic Mg from Grignard reagents in symmetric Mg-Mg cells, we establish a phase map characterized by disparate morphologies spanning the range from fractal aggregates of 2D nanoplatelets to highly anisotropic dendrites with singular growth fronts and nanowires entangled in the form of mats. The effects of electrolyte concentration, applied current density, and coordinating ligands have been explored. The study demonstrates a complex range of electrodeposited morphologies including canonical dendrites with shear moduli conducive to penetration through typical polymeric separators. We further demonstrate a strategy for mitigating Mg dendrite formation based on the addition of molecular Lewis bases that promote nanowire growth through selective surface coordination.

*[R. Davidson, A. Verma, D. Santos, F. Hao, C. D. Fincher, D. Zhao, V. Attari, P. Schofield, J. Van Buskirk, A. Fraticelli-Cartagena, T. E. G. Alivio, R. Arroyave, K. Xie, M. Pharr, P. P. Mukherjee, S. Banerjee, Mater. Horizons 2020, 7, 843.] - Reproduced by permission of The Royal Society of Chemistry

3.2. Broader Context

Limitations of current batteries represent perhaps the largest roadblock to the continued advancement of renewable energy technologies. Supplanting the graphite used in Li-ion batteries with metallic anodes holds promise for significantly enhanced capacity and energy density but requires mitigating the proclivity of lithium to deposit as dendrites. The ‘beyond Li’ paradigm of energy storage has attracted consideration attention with much of its promise derived from the utilization of metallic anodes that are safer in comparison to lithium. Here, we explore electrodeposition of magnesium under varying electric fields, concentrations, and added ligands. Distinctive growth mechanisms are differentiated including fractal and dendritic growth regimes, which are rationalized based on the dynamical interplay between electrochemical reaction and self-diffusion rates. Mg dendrites are found to be substantially harder than their lithium counterparts, which further underscores the need for stiffer separators.

3.3. Introduction

Lithium-ion batteries are currently the dominant electrochemical energy storage technology with accessible gravimetric and volumetric energy densities approaching 250 W·h/kg and 600 W·h/L, respectively.[1,2] Current Li-ion batteries pair transition metal oxide cathodes with graphite anodes;[3] supplanting the latter with metallic lithium would yield theoretical capacities as high as 3,860 mAh/g.[4] However, Li metal has a high propensity for dendrite formation; the plating of lithium as anisotropic fractal structures that can bridge across liquid and solid electrolytes, thereby short-circuiting the cell, represents a major safety hazard. Consequently, the paucity of scalable methods to

achieve reproducible electroplating of metallic lithium has emerged as a substantial roadblock to accessing improved storage capacities.[5,6] Dendrite formation has been the scourge even when utilizing graphite anodes wherein under specific temperature, voltage, and electrolyte decomposition conditions, dendritic growth regimes become more favorable as compared to insertion reactions. Indeed, numerous high-profile incidents have underscored the importance of understanding the accumulative impact of low-probability, stochastic processes in electrochemical energy storage systems wherein fundamental processes operate across multiple decades of time and length scales. Developing experimental conditions that replicate such local far-from-equilibrium behavior has thus emerged as an urgent imperative. Considerable effort has been invested in the development of "beyond Li" intercalation systems that derive a considerable portion of their promise from the potential to utilize their respective metallic anodes. Sodium, magnesium, calcium, and zinc are considered to deposit with much lower propensities for dendrite formation as compared to lithium owing to their more facile self-diffusion, which thereby results in the plating of relatively homogeneous deposits.[7–9]

Magnesium batteries are considered a promising alternative given the divalent charge of Mg, which has been proposed as a means of achieving higher energy densities since most cathode materials are limited in terms of their available redox sites and not accessible redox states. In addition, magnesium holds promise for enabling use of metal anodes as a result of its supposed "non-dendrite" forming nature.[10–14] Groβ has attributed the low propensity for dendrite formation to small self-diffusion barriers and

vanishingly small Ehrlich—Schwöbel barriers for 3D diffusion. Much research has targeted the development of novel cathode materials that can readily diffuse highly polarizing divalent Mg-ions as well as in the development of electrolytes stable across extended potential windows that allow for effective desolvation of magnesium at electrode interfaces.[12,15–20] Ideas regarding the permeability or lack thereof of divalent Mg-ions through solid electrolyte interfaces (SEI), which may form through degradation of electrolytes during cycling, have inspired the design of several stable classes of electrolytes.[12,21–23]

Several experimental observations of homogeneous plating as compared to agglomerate formation support the idea of a reduced predilection of magnesium towards formation of dendritic structures.[10,24],[13,14,25,26] Dual-salt electrolytes containing both Li and Mg components have been considered as a means of utilizing the faster kinetics of Li at the cathode whilst avoiding Li dendrite formation through preferential plating of Mg at the anode.[27,28] The faster surface diffusion of Mg-ions along the Mg (0001) plane predicted from first-principles calculations has been put forth as the intrinsic basis for reduced propensity for dendritic growth and is further corroborated by the prediction of low diffusion barriers for diffusion across steps and terraces.[7] Self-diffusion coefficients, Ehrlich-Schwöbel barriers, and anisotropy resulting from the intrinsic crystal structure have emerged as some putative descriptors for comparing the dendrite-forming nature of different anode materials.[26,29–32] While reports of reduced propensity for dendrite growth in magnesium are well founded, it is worth noting that electrodeposition processes often occur far from equilibrium wherein otherwise reliable

descriptors can be thwarted by other vectors.[33] Inhomogeneities in magnesium deposition are not unprecedented[34–36] and capacity fading analogous to the problems discussed with lithium has been observed.[37],[38] Recently Bitenc and co-workers showed highly uneven deposition in $MgCl_2$-$AlCl_3$-DME electrolyte systems.[36] Groβ and co-workers have pointed out that surface self-diffusion in itself cannot explain the deposition characteristics; the applied current density is an equally important measure, which determines the incoming reactant flux.[39–41] Yet, comprehensive investigations of non-equilibrium phase spaces and Mg electrometallurgy are scarce even though reports of fractal Mg microstructures within alloys are abundant in the metallurgy literature.[42,43]

Fractal and dendritic magnesium deposits have indeed been observed upon the electrodeposition of Grignard reagents[12] in Mg—Mg symmetric cells monitored *in situ* with videomicroscopy under galvanostatic conditions. In this article, overpotentials required for electrocrystallization of Mg at varying concentrations and current densities are explored, and distinctive growth morphologies are delineated including unambiguous fractal and dendritic growth regimes. Deposition is seen to be underpinned by diffusion-limited aggregation (DLA) mechanisms across much of the examined reaction space.[6,44–51] The Mg deposits have been extensively explored across different length scales utilizing a combination of electron and X-ray microscopy. The experimental observations are explained with reference to an analytical framework contrasting the Mg^{2+} diffusive transport and reaction rates wherein exacerbated electrodeposition instabilities are anticipated beyond the “Sand’s time” limit at elevated current

densities.[52] Furthermore, phase-field modeling studies have been used to unravel the mechanistic underpinnings of the observed electrodeposited morphologies.

3.4. Results and Discussion

3.4.1. Formation and Characterization of Fractal Mg Structures: Developing a Phenomenological Map of Deposition Regimes

Electrodeposition of metallic Mg from MeMgCl and EtMgCl in tetrahydrofuran (THF) has previously been shown to yield continuous thin film and nanowire array morphologies; the latter has been proposed to result from a modified faces, steps, and kinks mechanism governed primarily by the deposition rate.[53] While these electrolytes have limited stability windows, they have been extensively used for Mg electrodeposition and serve as effective model systems as compared to multicomponent electrolytes. The utilization of a symmetric cell geometry to examine electrocrystallization of Mg as will be discussed here mitigates the influence of convoluting factors such as insertion reactions, electrolyte decomposition at the cathode, and dissolution of the cathode as a result of parasitic reactions. The use of Mg ribbon electrodes further allows for direct observation of intrinsic phenomena without potential confounding factors such as electrocatalytic processes at transition metal electrodes. Nevertheless, similar results are obtained for Pt, stainless steel, A36 steel, and galvanized steel. Application of a voltage in a parallel-plate geometry yields a variety of morphologies of Mg spanning the range from aggregated polycrystalline quasi-spherical deposits to dendrites spanning millimeters in length, aggregated platelets, and nanowires, depending on the current density, concentration, and presence of coordinating ligands

(*vide infra*). **Videos B.1.—B.8.** illustrate time-lapse images of Mg deposition as a function of varying concentration of MeMgCl (Videos B.1—B.5) and concentration of added dodecanethiol (Videos B.6—B.8).

Figure 3.1A shows a phenomenological map illustrating the different observed growth regimes for electroplating of Mg, indicating considerable complexity as well as clear dendritic growth windows in the multidimensional space. The plot charts out correlations between processing conditions and mesoscale texture and microstructure evolving from the interplay between thermodynamics and kinetics of Mg electrodeposition. Intriguingly, this richness of electrodeposited Mg morphologies does not appear to have been previously reported in the literature even for these common electrolytes. Generally, upon increase in concentration of the electrolyte, an increase in the grain size of the deposit is observed resulting in a transition from highly fractal growths formed from aggregation of hexagonal platelets to aggregates of quasi-spherical deposits and finally converging towards stabilization of highly crystalline dendritic deposits with singular dominant growth fronts. Such morphologies represent anisotropic growth regimes, which could detrimentally impact battery performance; mapping such mechanisms is imperative in order to systematically tune the nature of electrodeposited films and to enable identification of consistent, controllable, and stable plating windows. Figure 3.1 depicts, as will be discussed below, that the inclusion of dodecanethiol yields nanowire morphologies in the form of mats, which may offer a route to the design of cyclable high-surface-area metal anodes. In the sections below, we will discuss this phase space across multiple length scales while delineating observations from

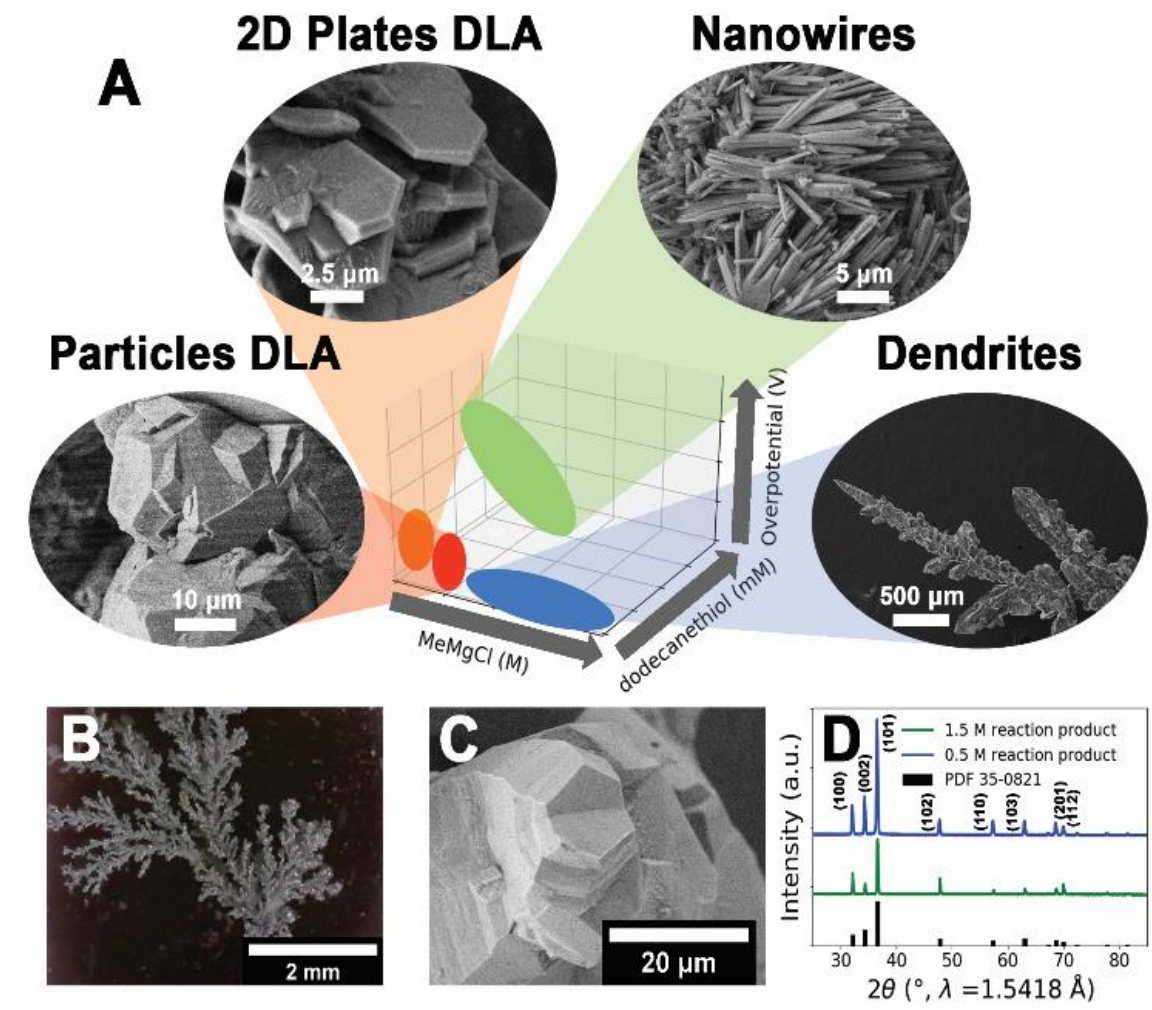

Figure 3.1. Fractal Growth of Electrodeposited Mg. A) Phenomenological map depicting several differentiated growth regimes as a function of reaction variables. 2D diffusion-limited-aggregation-type growth, regions with spherical diffusion-limited aggregation growth, dendritic growth, and nanowire growth are distinguishable across this parameter space. Characterization of Mg deposits obtained at a constant current density of 0.921 mA/cm^2 from a 0.5 M solution of MeMgCl in THF. B) Digital photograph of a magnesium fractal deposit; C) SEM image showing a high-magnification view of the fractal surface; clear hexagonal habits can be discerned. D) powder XRD patterns acquired for detached Mg deposits grown from 0.5 and 1.5M MeMgCl in THF.

monitoring the evolution of mesoscale morphologies, resulting microstructure, and

crystal structure for each distinctive regime.

Mesoscale and higher length scale plating morphologies have been monitored using videomicroscopy (Videos B.1—B.8). Figure 3.1B depicts a typical fractal deposit formed from the electrodeposition of Mg from a 0.5 M solution of MeMgCl in THF at a constant current density of 0.921 mA/cm^2. The deposits span several millimeters in length, are highly branched, and grow from the edges of the Mg ribbon. Figure 3.1C shows a SEM image of the same deposits depicted in Figure 3.1B. SEM images of the fractal deposits indicate aggregates of hexagonal platelets characteristic of the intrinsic habit of hcp Mg. Crystallographic information has further been derived from high-resolution TEM and XRD in order to understand the electrocrystallization process.

Powder XRD patterns of all deposits exhibit sharp reflections that can be readily indexed to PDF 35-0821, corresponding to metallic magnesium as is shown in **Figure 3.1D** for the fractal and dendritic deposits. XPS spectra have further been acquired for fractal deposits to examine the elemental composition of their surfaces. Samples were exposed briefly to ambient environments during loading of the substrates within the instrument. **Figure B.1A** shows a survey scan, whereas high-resolution scans for Mg 2p, O 1s, C 1s, and Cl 2p are shown in Figures B.1B-E, respectively. The Mg 2p high-resolution XPS spectrum exhibits the presence of zero-valent Mg at 49.5 eV. Some samples additionally show a smaller second peak at 52.6 eV, which can be ascribed to surficial Mg-Cl known to exist as a key passivating species in the electrodeposition of Grignard reagents,[54] as well as a feature centered at 55.9 eV arising from the Fe 3p spectrum of impurities resulting from the steel electrode clips. As the clips were not

submerged in solution during the reaction, the influence of Fe on the characteristics of deposits was considered to be negligible and is an artifact of washing the electrodes following the reaction (the Fe signal is not observed in samples where just the electrodes are washed). The oxygen 1s XPS spectrum shows a prominent peak centered at 531.4 eV, which can be assigned to $Mg(OH)_2$. A weak shoulder at 529.9 eV is additionally observed likely arising from MgO and at 533.5 eV ascribed to the presence of surface-bound ether species given the strong complexation of THF and ethers to magnesium.[55,56] High resolution scans of the C 1s region show adventitious carbon as well as smaller peaks at 288.2 eV and 289.4 eV, which can be assigned to carboxylates and carbonates, respectively.[57]

Figures B.2A—C indicate projections of 3D tomography maps constructed using soft-X-ray microscopy at the Mg K-edge. **Videos B.9 and B.10** show the resulting aligned tilt series and the 3D reconstruction, respectively, in terms of the transmission intensity (left) and optical density (right). The fractal aggregate structures are observed to be solid with faceted surfaces.

3.4.2. *In situ* Observations of Dendrite Growth under Varying Deposition Conditions

Studies of fractal growth in metallic copper and zinc deposits have shown that various experimental parameters affecting the reactivity or diffusion of the electrolyte allow for tuning of the crystallinity as well as the compactness of the plated deposits.[58–61] Bazant noted that considerations such as the anisotropy of crystal structures or the high activity of light metals add complexity but do not fundamentally alter the influence

of these parameters.[48] Magnesium electrodeposition from Grignard's agents in THF solution has been first monitored as a function of the applied current density for an overall duration of 8 h from 0.5 M THF solutions of MeMgCl. Digital photographs indicating the formation of fractal structures at 2, 4, 6, and 8 h time points are depicted in **Figure 3.2**. Increasing the current density increases the extent of deposition and yields more heavily branched deposits. This observation as well as the lack of extended crystalline order within the deposits suggests the operation of a diffusion-limited aggregation (DLA) mechanism, as has been observed for dendritic lithium growth.[48,62]

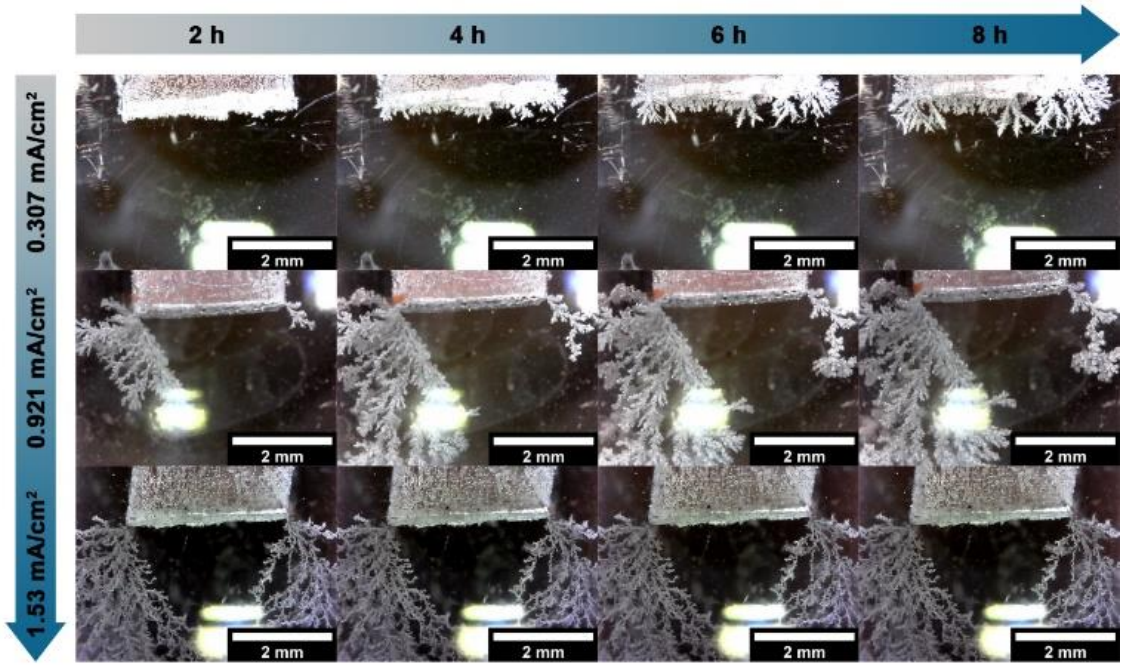

Figure 3.2. *In Situ* Videomicroscopy Observations of Fractal Growth as a Function of Applied Current Density. Digital photographs have been acquired at 2, 4, 6, and 8 h time points for deposition from 0.5 M THF solutions of MeMgCl solutions under different applied current densities (0.307, 0.921, and 1.54 mA/cm^2).

Higher certainty of reduction of metal ions at a given site (oftentimes quantified using a "sticking coefficient"[63,64]) resulting from the increased driving force for deposition at higher current densities results in more extensive fractal growth. The flux and reaction

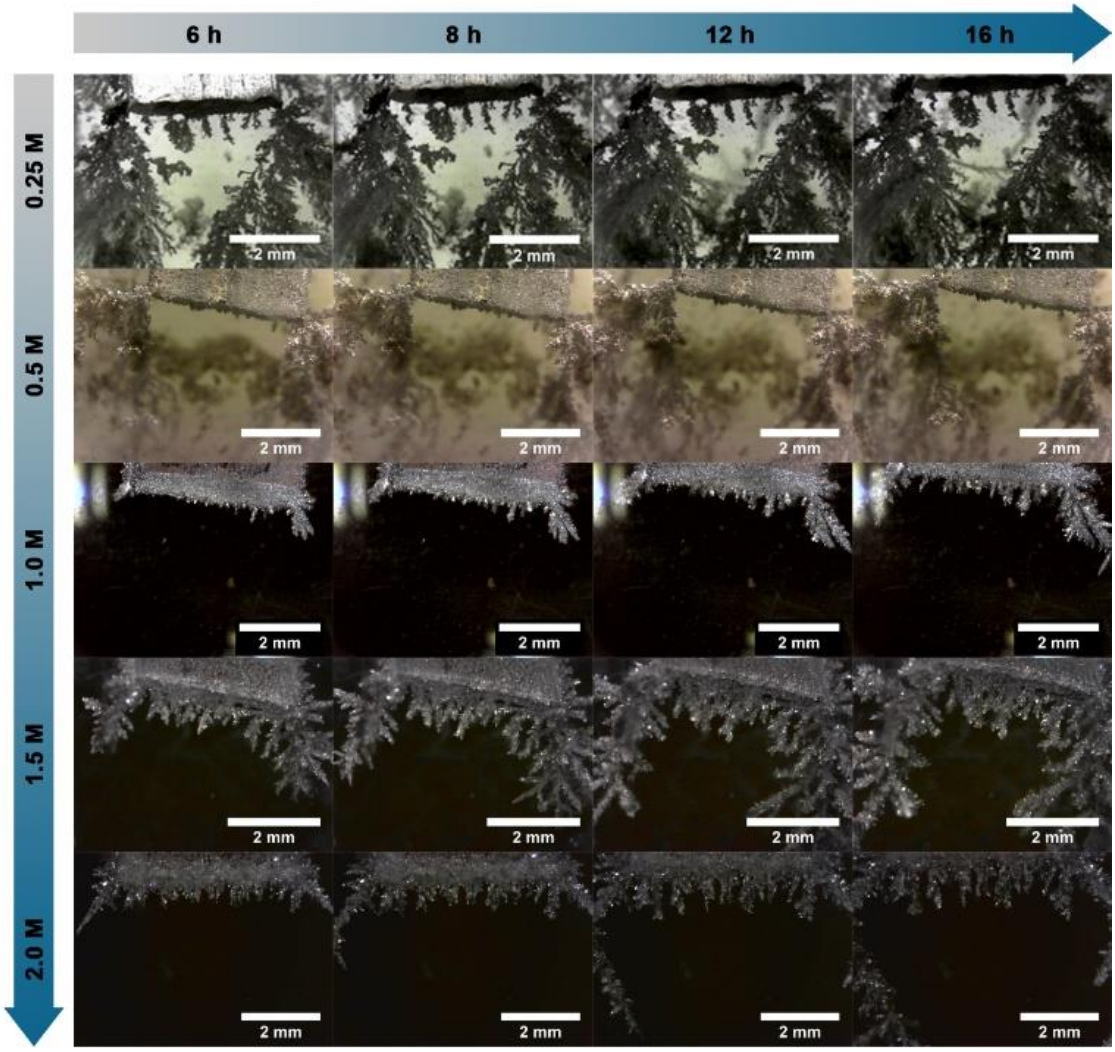

Figure 3.3. *In Situ* Videomicroscopy Observations of Fractal Growth as a Function of Electrolyte Concentration. Digital images acquired at 6, 8, 12, and 16 h time intervals for 0.25, 0.5, 1, 1.5, and 2.0 M concentrations of MeMgCl in THF at a constant current density of 0.921 mA/cm^2.

rates under these conditions overcome the relatively fast self-diffusion predicted for Mg.[7] **Table 3.1** shows the resulting weights of the fractal product and overpotentials required to maintain the constant current conditions. Generally, there is an increase in the overpotential with increasing current density; the resulting mass of fractal deposits is furthermore increased. The analytically predicted total Mg deposition is also tabulated as anticipated from Faraday's law; detailed analysis is presented in the latter half of this article. The conditions correspond to relatively high current densities, but it is worth noting that proposed fast charging applications will indeed necessitate high current fluxes. Corresponding voltage over time plots are shown in **Figure B.3**.

The growth regimes have been additionally monitored as a function of electrolyte concentration. Time lapse digital photographs acquired at 6, 8, 12, and 16 h intervals are shown in **Figure 3.3** for different electrolyte concentrations in THF. Videos exhibiting the progression of dendrite growth as a function of time are shown in Videos B.1—B.5 (Appendix B) and the characteristics of the deposited products are noted in Table 3.1. Corresponding voltage *versus* time plots are shown in **Figure B.4**. Increasing MeMgCl concentration growth.[48,62] Higher certainty of reduction of metal ions at a given site (oftentimes quantified using a "sticking coefficient"[63,64]) resulting from the increased driving force for deposition at higher current densities results in more extensive fractal growth. The flux and reaction rates under these conditions overcome the relatively fast self-diffusion predicted for Mg.[7] **Table 3.1** shows the resulting weights of the fractal

Table 3.1. Resulting weights of fractal deposits and measured voltages

Variation of Applied Current Density

Current Density (mA/cm^2)	Predicted total deposition mass of Mg (mg)	Measured mass of dendritic Mg (mg)	V·h	Volts (average)	E (V/mm)
0.307	3.63	6.8 ± 0.2	100.7	12.6	0.220
0.921	10.9	6.2 ± 1.3	158.7	19.8	0.347
1.54	18.1	14.2 ± 5.0	222.7	27.8	0.487

Variation of Electrolyte Concentration

MeMgCl Concentration (M)	Predicted total deposition mass of Mg (mg)	Measured mass of dendritic Mg (mg)	V·h	Volts (average)	E (V/mm)
0.25	32.64	21.6 ± 9.0	568.0	23.7	0.414
0.50	32.64	27.8 ± 14.3	466.3	19.4	0.340
1.0	32.64	9.1 ± 1.6	37.7	1.6	0.027
1.5	32.64	13.9 ± 3.9	10.3	0.4	0.008
2.0	32.64	12.1 ± 6.8	7.0	0.3	0.005

product and overpotentials required to maintain the constant current conditions. Generally, there is an increase in the overpotential with increasing current density; the resulting mass of fractal deposits is furthermore increased. The analytically predicted total Mg deposition is also tabulated as anticipated from Faraday's law; detailed analysis is presented in the latter half of this article. The conditions correspond to results in the

formation of thicker, less branched deposits, which is thought to be reflective of modification in the growth mechanism. In addition, the microstructure of the deposits is modified upon going from 0.25 to 0.5 M with the 0.25 M reactions yielding fractals constituted from much smaller grains as can be seen more clearly in **Figure 3.4**. The overpotential generally decreases with increasing concentration for all samples as a result of the higher solution conductivity. Typically, electrolyte ionic conductivity

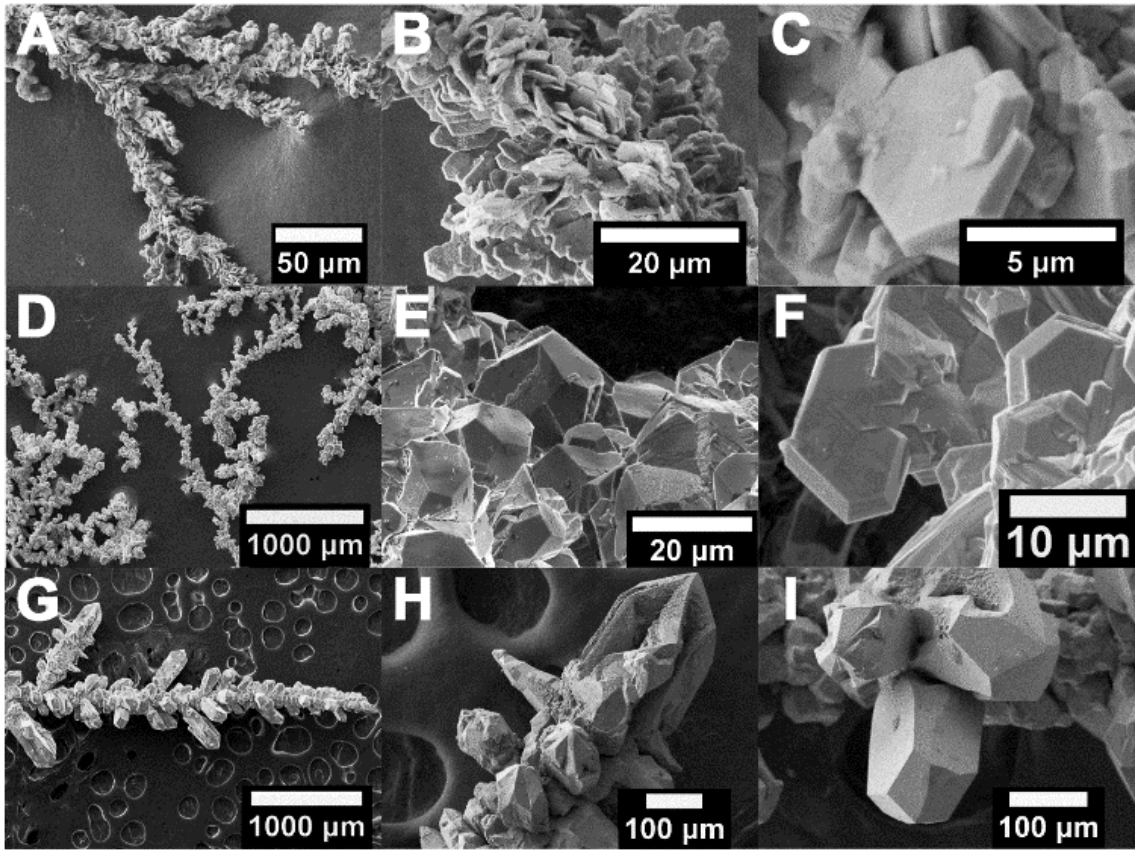

Figure 3.4. Fractal to Dendrite Transformation. SEM images acquired at varying magnifications for deposits obtained at a constant current density of 0.921 mA/cm^2 for A—C) 0.25 M; D—F) 0.5 M; and G—I) 1.5 M solutions of MeMgCl in THF. The top two rows exhibit fractal growth, whereas the bottom row corresponds to a dendritic growth regime.

exhibits a non-monotonic trend with concentration, increasing until an optimal concentration is reached, beyond which it is diminished.[65] For MeMgCl in THF, a steady decrease in overpotential is observed even up to concentrations of 2 M.

The morphologies observed upon non-equilibrium, fractal growth are governed by a balance between local surface dynamics, long-range diffusion, nucleation probabilities, and anisotropic growth rates along different crystallographic directions.[66] Figure 3.4 shows SEM images acquired at different magnifications for deposits obtained from 0.25, 0.5, and 1.5 M solutions of MeMgCl in THF (at a constant current density of

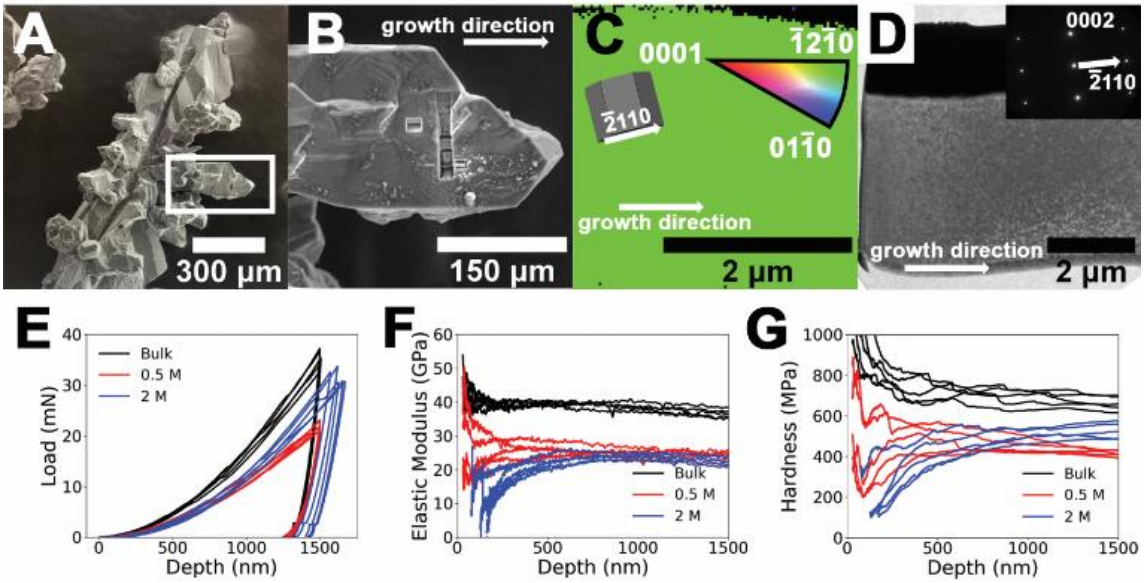

Figure 3.5. Microstructural characterization of Mg dendrites. A) SEM image of a Mg dendrite electrodeposited under 0.921 mA/cm2 applied constant current in a 1.5 M MeMgCl for 24 h; B) Higher magnification SEM image of (A) illustrating regions from which EBSD and TEM specimens have been extracted using FIB; C) EBSD IPF map and 3D crystallographic schematic of the Mg dendrite; D) Bright-field TEM image of the Mg dendrite and corresponding SAED pattern. Representative nanoindentation E) load-depth curves, F) elastic modulus versus depth, and G) hardness versus depth for Mg electrodeposits grown from 0.5 M and 2 M MeMgCl solutions under 0.921 mA/cm^2 applied constant current for 24 h.

0.921 mA/cm^2), which allow for different types of microstructures constituting the fractal morphologies to be differentiated. **Figure 3.5** shows more extensive crystallographic and nanomechanical characterization of the deposits.

Three distinctive growth regimes can be distinguished with considerable differences in the mode of aggregation and directionality of growth. The deposits are constituted from hexagonal platelets as fundamental building blocks, preserving the symmetry of the underlying crystal lattice. Energy minimized Wulff reconstructed surfaces are discernible (Figs. 3.4C, F, and I), which suggest that the low self-diffusion barriers in this system indeed allow for thermodynamic shapes to be stabilized. However, the mesoscale orientation and attachment of the shapes are highly variable as a function of the concentration and current density. At low concentrations of 0.25 M MeMgCl and high overpotentials, nucleation of new particles dominates over growth of incipient nuclei resulting in fractals comprising aggregates of numerous thin hexagonal platelets on the order of around 3—6 μm in diameter. An increase in concentration of MeMgCl results in a decrease in overpotential and greater availability of ions at reactive sites. Consequently, the growth rates are accelerated and the individual crystallites are substantially larger with a more spherical appearance (with end-to-end dimensions of 30—60 μm, albeit still with some clearly defined hexagonal facets) resulting in a considerably altered fractal morphology as seen in Figures 3.4D—F.[67] As described below, growth under these conditions corresponds to a diffusion-limited regime; as a result, the observed morphologies are characteristic of diffusion-limited aggregation. At a still higher concentration of 1.0 M MeMgCl, Figure 3.3 suggests a notable alteration of

the deposition mechanism. SEM images of deposits obtained from 1.5 M THF solutions of MeMgCl (Figures 3.4G—I) indicate that increasing concentration brings about a transition from fractal growth to stabilization of dendrites. The deposits exhibit a singular dominant growth tip, albeit with somewhat irregular branches (Figures 3.4G—I). Video B.4 and Figure B.5 depict lower magnification views of the growth tip (delineated by red arrows in Figure B.5). It is worth noting that such growth is distinctly different from the root-growing, needle-like growth observed in lithium.[48,52] Dendritic growth with the observed dominance of a finite number of growth fronts requires the influence of anisotropy, which may be derived in this case from the intrinsic asymmetry of the hcp crystal structure or, extrinsically, as a result of preferential passivation owing to electrolyte decomposition.[66,68,69] With diminishing diffusion limitations, the effects of anisotropy are clearly discernible at both the micron- and mesoscale levels.

Thin platelet growth is furthermore observed upon the addition of oleylamine (0.121 M) to the 0.5 M THF solution of MeMgCl at a current density of 0.921 mA/cm^2, as shown in **Figures 3.6A-C**. Oleylamine, a Lewis basic ligand that weakly coordinates to Mg-ions, is thought to buffer the monomer supersaturation and allows for nucleation-dominated growth.[70,71] Surface passivation necessitates diffusion of monomer ions through the capping layer and likely also alters self-diffusion rates. XPS spectra for deposits formed through addition of oleylamine are shown in **Figure B.6** and are very similar to that of spectra observed for dendrites formed without the addition of oleylamine with the addition of a characteristic N 1s signal and a shoulder centered around 283.5 eV for the C 1s.

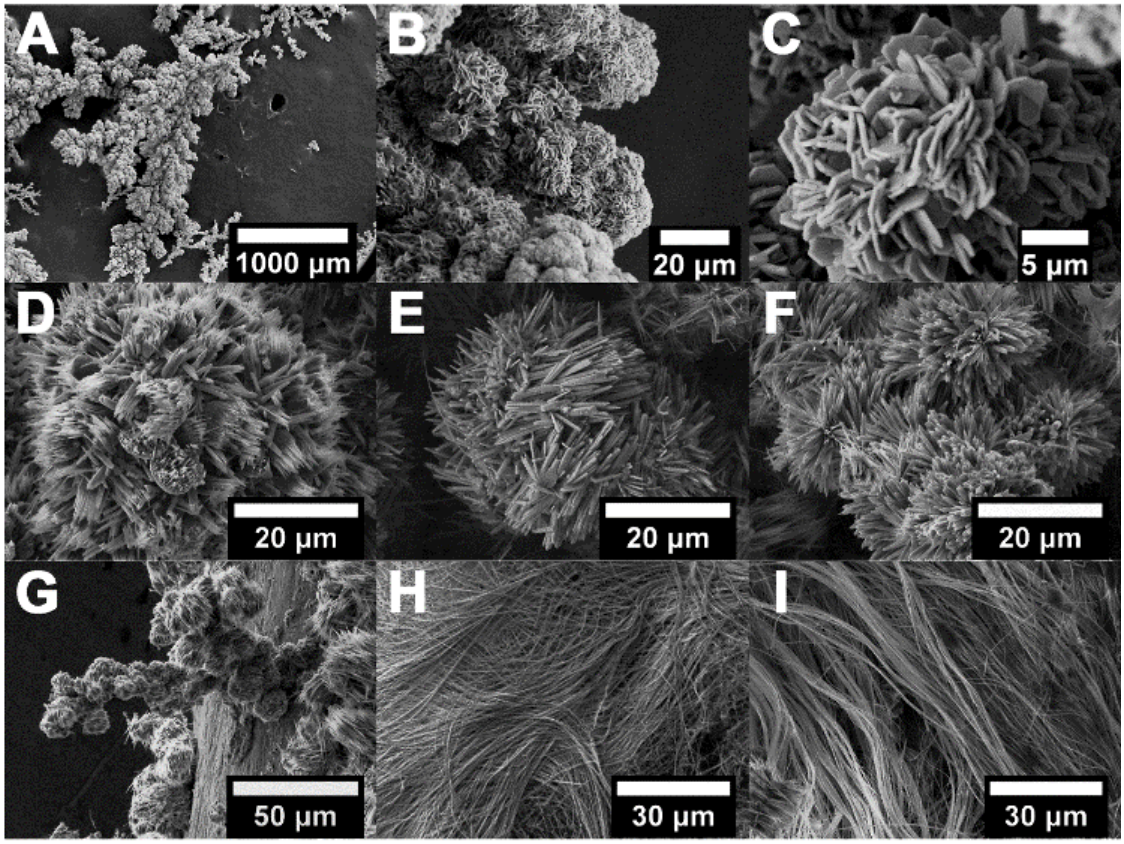

Figure 3.6. Ligand Modification of Mg Morphologies. SEM images of electrodeposited Mg obtained through addition of A-C) oleylamine (0.121 M) or D-I) varying concentrations of dodecanethiol. Spherical clusters of shorter wires have been observed upon addition of D) 0.0626 M, E) 0.125 M, and F) 0.188 M dodecanethiol. These form extended structures as can be observed in (G), which shows a representative example from a reaction containing 0.0626 M dodecanethiol. In addition to clusters, extended 1D wires are observed upon addition of higher concentrations of dodecanethiol as observed upon the addition of H) 0.125 M and I) 0.188 M dodecanethiol.

3.4.3. Characterization of Mg Dendrites

The microstructure and the growth direction of the Mg dendrites electrodeposited from 1.5 M MeMgCl solutions in THF under 0.921 mA/cm^2 constant current densities have been examined by electron backscatter diffraction (EBSD) and transmission

electron microscopy (TEM) (Figure 3.5). The dendrites obtained under these conditions span hundreds of microns in width and millimeters in length. Each dendrite comprises a number of Mg crystals with well-defined crystal facets (Fig. 3.5A). The EBSD and TEM samples have been prepared from an individual branch of a Mg dendrite as shown in Figure 3.5B, obtained from the region in Figure 3.5A highlighted with the white rectangle; the lengths of the lift-out specimens are parallel to the growth direction of the dendrite. The EBSD map, based on the growth direction of the inverse pole figure (IPF) map and IPF triangular reference, displays a uniform green color, indicating that the examined part of the Mg dendrite is single crystalline. The EBSD map reveals a growth direction of $< 11\bar{2}0 >$ (Fig. 3.5C). The single crystalline nature and growth direction of the Mg dendrites have been further corroborated by TEM observations in Figure 3.5D. The corresponding selected area electron diffraction (SAED) pattern (Fig. 3.5D, inset) confirms the $< 11\bar{2}0 >$ growth direction. This growth preference can be rationalized considering that the most dense packing of atoms in hexagonal close-packed Mg is along $< 11\bar{2}0 >$.

As seen in Figure 3.5E-G, indentation measurements have been used to derive elastic and plastic properties for bulk Mg as well as Mg dendrites electrodeposited from 0.5 and 2 M concentrations of MeMgCl in THF. Indentation of bulk Mg in Figure 3.5F yields an elastic modulus of 39.4 ± 0.9 GPa, similar to previously reported values of ca. 40—45 GPa in the literature.[72,73] In contrast, the 0.5 and 2 M electrodeposited Mg deposits exhibit elastic moduli of 23.8 ± 1.6 and 22.5 ± 1.8 GPa, respectively. In other

words, the electrodeposited Mg structures possess an elastic modulus nearly 60% that of bulk Mg. Optical observation of the indents (**Figure B.7**) does not reveal excessive pile-up. Furthermore, consistent and flat E^2/H values at substantial depths as well as the frame stiffnesses'[74] favorable comparison with that of the calibration material (fused silica) provides further verification of the validity of these results. Possible origins of the reduced elastic moduli observed for the dendrites include the presence of porosity, impurities in the electrodeposited Mg, and/or the influence of the grain size and orientation of the electrodeposited Mg.

Analysis of plastic properties suggests that the electrodeposition parameters furthermore influence the resulting mechanical properties of the Mg deposits. As seen in Figure 3.5G, the indentation of bulk Mg yields a hardness of 665 ± 33 MPa. Assuming a Tabor factor of 2.8, the yield strength of the bulk Mg can be estimated to be ~ 235 MPa.[73,75,76] At an indentation depth of 1500 nm, the Mg electrodeposited from 0.5 and 2 M MeMgCl in THF displayed hardness values of 525 ± 38 MPa and 415 ± 18 MPa (corresponding to yield strengths of ~190 and 150 MPa), respectively. The origins of the differences in plastic properties from bulk Mg remain unclear but again may be related to impurities (e.g., precipitates) or specifics of the microstructure (e.g., grain sizes, dislocation densities) that form during electrodeposition under different conditions.

A popular model for predicting conditions to prevent dendrite formation is that of Newman and Monroe, who considered electrode stability of electrode (lithium)/separator (or solid electrolyte) interfaces using linear elasticity theory. According to their model, dendrites can be suppressed by a separator or solid electrolyte that has a shear modulus

approximately twice that of the electrode itself.[77] Taking the elastic modulus for the dendritic Mg as 25 GPa and the Poisson's ratio as 0.35,[78] the shear modulus of a dendrite can be calculated as $\mu = E/[2(1+\nu)] = 10.0$ GPa. As a result, the Newman and Monroe[77] model predicts that a separator or solid state electrolyte with a shear modulus of more than ~20 GPa will be necessary to prevent the formation of Mg dendrites within a battery. Since polymer separators typically have moduli on the order of 1 GPa and a Poisson's ratio of 0.46,[79] their shear modulus of ~340 MPa is much too small to prevent the propagation of Mg dendrites. However, stiff ceramic solid-state electrolytes with large shear moduli (>25 GPa) may suppress dendrites and thereby warrant further investigation. Notably, both of these electrodeposited Mg morphologies possess significantly larger elastic moduli and hardness values as compared to Li (modulus of ~9 GPa and bulk indentation hardness of 4.5 MPa).[80,81] As a result, mechanically suppressing dendritic growth may prove substantially more challenging than that of Li.

3.4.4. Ligand Modification of Electrodeposition Morphologies

The addition of dodecanethiol yields a pronounced change in appearance, a gray powder is obtained at low concentrations of dodecanethiol, whereas an entangled fibrous mat is recovered at high concentrations. Figures 3.6D—I show a pronounced modification of the morphology upon the addition of dodecanethiol at different concentrations. Powder XRD patterns for deposits grown with addition of dodecanethiol can be indexed to metallic Mg (PDF 35-0821, **Fig. B.8**). XPS spectra of the nanowires formed through the addition of 0.125 M dodecanethiol are shown in **Figure B.9** and show similar features to that of the dendrites formed without addition of the alkyl thiol,

with the addition of a S 2p band and a shoulder at around 283.5 eV for the C 1s spectrum. An initial reaction between MeMgCl and dodecanethiol produces a thiolate species and $MgCl^+$; as such the dynamics of deposition is substantially altered. Selective adsorption of the thiolate molecules on specific growth facets and the ability of the Lewis basic ligands to buffer the monomer supersaturation substantially reduces the effective monomer flux.[70,82,83] Under these conditions, the self-diffusion characteristics are comparable to the flux rate; consequently, arrays of faceted nanowires with lateral dimensions of 250—800 nm are observed. Nanowires appear in two primary forms; spherical clusters of shorter wires around 10—20 μm in length are observed upon addition of 0.0626 M, 0.125 M, and 0.188 M dodecanethiol as shown in Figures 3.6D—F, respectively. As shown in Figure 3.6G, such nanowires furthermore form mesoscale patterns through aggregation of the spheres. Still higher concentrations of dodecanethiol result in the stabilization of long Mg nanowires on the order of many tens to hundreds of micrometers in length (Figs. 3.6H and I); the nanowires form entangled mats without the higher order aggregation observed at lower dodecanethiol concentrations. This method of achieving the controlled deposition of nanowire arrays furthermore provides a route to nanotextured metallic anode films directly integrated onto the current collector. The results demonstrate the ability to prepare a disparate range of highly textured Mg anode films from electroplating of Grignard's reagents. Cycling of nanowire arrays is expected to yield improved reaction kinetics and a reduced local overpotential owing to the greater availability of deposition sites, thereby reducing the predilection for dendrite

formation. The utilization of such anodes in conjunction with dual salt electrolytes portends intriguing battery architectures designed to mitigate dendrite formation.[27,28]

3.4.5. Plating Phase Maps and Mechanistic Underpinnings

The morphology of electrodeposited Mg is governed by the interplay of electrochemistry, ion transport, nucleation, and crystal growth. Specifically, the balance between ion transport in the electrolyte, Mg surface diffusion on the plating electrode, and the electrochemical reaction rate dictate the observed morphologies. At applied current rates, i_{app} (A/m^2), exceeding the limiting current density, i_{lim}, for the electrochemical system under observation, diffusional transport in the electrolyte can become the limiting mechanism, resulting in the depletion of Mg^{2+} ions from the proximity of the plating electrode. As such, transformation from smooth to dendritic structures is correlated with this scarcity of Mg^{2+} occurring at Sand's time, τ_{Sand}, given by

$$\boldsymbol{\tau_{Sand} = \frac{\pi D (z c_o F)^2}{4\left(i_{app} t_a\right)^2} \Rightarrow D = \frac{4\left(i_{app} t_a\right)^2 \cdot \tau_{sand}}{\pi (z c_o F)^2}} \qquad \textbf{3.1}$$

Here, z is the cationic charge number, c_0 is the bulk salt concentration in the electrolyte (mol/m^3), F is Faraday's constant (C/mol), D is the binary diffusion coefficient (m^2/s) and t_a is the anionic transference number. Determination of Sand's time can help in accurate quantification of electrolyte diffusivity, which is generally a monotonically decreasing function of concentration owing to concentrated solution effects and hence cannot be taken as constant. Further electrodeposition beyond Sand's time results in preferential growth of dendritic structures. For our experiments, the Sand's time

parameter values can be directly correlated to the amount of dendritic magnesium, *m*, tabulated in Table 3.1 as per Faraday's law:

$$\boldsymbol{I \cdot (\tau_{total} - \tau_{sand}) = \frac{zFm_{den}}{M}} \qquad \textbf{3.2}$$

where I is the applied current (A), τ_{total} is the total temporal duration of the experiment (s), m_{den} is the amount of dendritic magnesium and M is the molar mass of magnesium. Table 3.1 reports the mass of electroplated dendritic Mg deposits for constant current electroplating at 0.921 mA/cm^2 over a 24 h total time period for varying electrolyte concentrations. Consequently, equivalent Sand's time can be computed for each of the experimental conditions reported in Table 3.1. This further enables the estimation of the electrolyte diffusion coefficient, which is required in order to compute the limiting current density.

Limiting current density is estimated from the computed diffusivity as per:

$$\boldsymbol{i_{lim} = \frac{2zc_oFD}{t_aL}} \qquad \textbf{3.3}$$

Here, *L* is the inter-electrode distance (5.715 cm in the system under consideration). The computed diffusivities and limiting current densities are reported in **Table 3.2**, and the corresponding variation with electrolyte concentration is also shown explicitly in Figures 3.7B and C. As pointed out earlier, the diffusivity shows a decreasing trend with concentration. However, the limiting current density has a non-monotonic trend owing to the competing effects of increasing salt concentration and decreasing diffusivity. Notably, the regimes evaluated here are consistently above this limiting current density, which enables mapping of non-equilibrium deposition regimes.

It is notable that while the calculations here pertain to global conditions, diffusion limitations can further play an important role in mediating localized heterogeneous deposition. Electrode interfacial inhomogeneities arising from inadequate electrolyte wetting, a heterogeneous solid electrolyte interphase (SEI), and rough electrode surfaces can create localized reaction zones governed by local diffusion considerations. While poor electrolyte wetting is generally a result of electrolyte-electrode mismatch in terms of interfacial wettability or low concentration electrolyte

Table 3.2. Calculated values for mean diffusivity and limiting current densities for reactions with varying concentrations of MeMgCl in THF based on Sand's time calculations.

Concentration (M)	**Mean Diffusivity (m^2/s)**	**Mean limiting current density (mA/cm^2)**
0.25	1.43×10^{-9}	0.22
0.5	2.41×10^{-10}	0.05
1.0	1.93×10^{-10}	0.13
1.5	4.95×10^{-11}	0.06
2.0	3.14×10^{-10}	0.07

operation, spatial variability of the chemical constituents in a multicomponent SEI can result in a non-uniform Mg-ion flux. Surface perturbations can furthermore serve as preferential deposition sites as a result of the warping of the electric field adjacent to surface protrusions, evidenced by the preferred formation of Mg dendrites near the edges in Figures 3.2 and 3.3. Given that this is an open system, a similar effect is observed

with disk electrodes (**Fig. B.10**) where fields are localized and concentration gradients are amplified at the edges. The subsequent steep increase in local reaction rates can far surpass Mg self-diffusion on the electrode surface.[35] In particular, electrolyte diffusion limitations at high currents beget dendritic Mg morphologies with the specific surface diffusion rates dictating fractal-like or needle-like growth regimes as mapped in **Figure 3.7**. The addition of ligand molecules buffers the electrolyte concentration and alters the effective diffusivity, whilst promoting preferential growth morphologies as a result of selective binding to specific facets. Consequently, the dynamic interplay between the electrochemical Damkohler number *(Da)* contrasting the reaction and self-diffusion rates[84] and the electrochemical Biot number *(Bi)* contrasting the reaction and electrolyte transport rates governs the morphologies of electrodeposited Mg stabilized at high current densities.[85]

Further insight into the growth of dendritic structures has been derived from phase-field modeling calculations. The quaternary phase diagram in **Figure B.11A** illustrates the equilibrium relationship between the different components of the system under consideration.[86] A plane is defined to illustrate zero charge conditions and the respective tie lines depict the equilibria varying between Mg(M)-THF at negative electrode potentials and Mg(M)-MeMgCl at positive electrode potentials. $MgCl_2$ species known to form passivation layers on surfaces of Mg electrodes are further considered.[87] The dynamical model is initiated by seeding a nucleation event at the electrolyte-electrode surface situated at the bottom center of the domain. Figure B.11B shows a

dendrite evolved from an initial seed. Figures 3.7C-E shows progression of dendrite growth as a function of time. Figure B.11C indicates the extracted information from the overview microstructure along the blue arrow. The three extracted curves correspond to the phase-field order parameter (ζ), Mg^{2+} concentration and electrostatic potential (ψ). The local variations of Mg^{2+} concentration and electrostatic potential at the dendrite tip

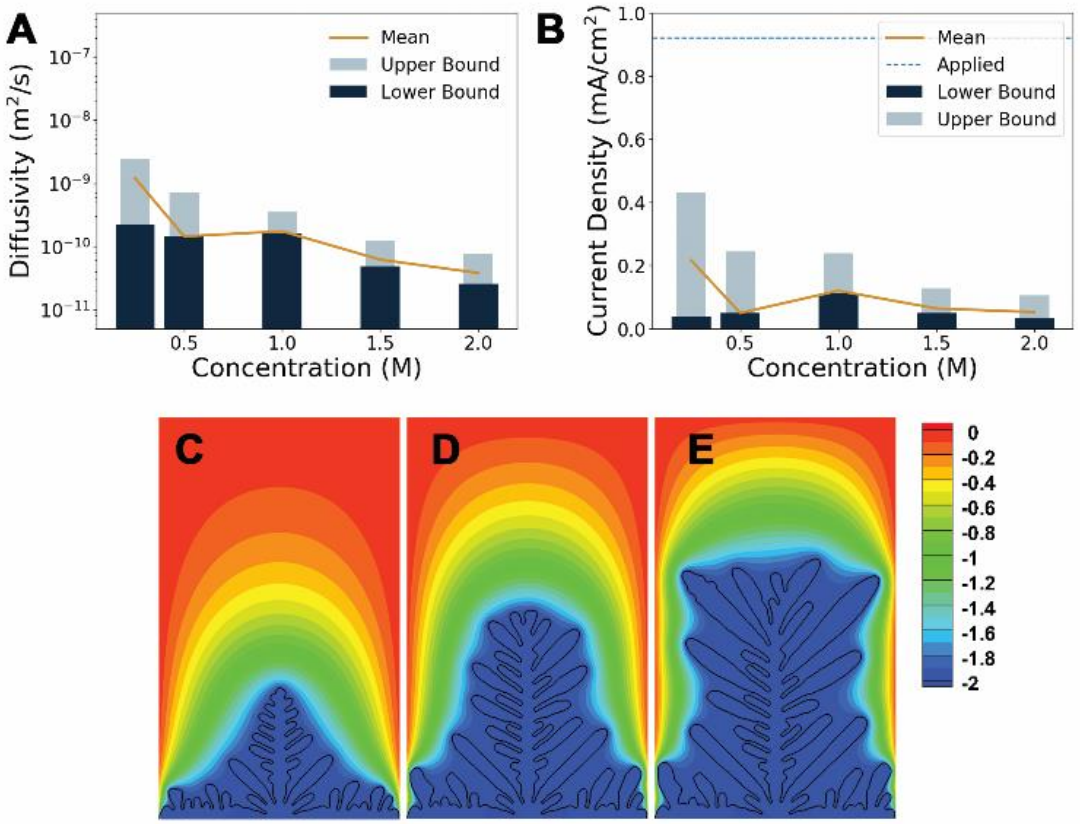

Figure 3.7. A) Variation of diffusion coefficient with bulk electrolyte concentration. Electrolyte diffusivity decreases with concentration. B) Variation of limiting current density with electrolyte concentration. Limiting current density shows a non-monotonic trend because of the competing effects of electrolyte concentration and electrolyte diffusivity. C-E) Evolution of dendritic growth from an initial seed located in the bottom center of the domain based on phase field modeling for a dendrite grown in 1 M MeMgCl with three time points representing $\boldsymbol{t^* = 5}$, $\boldsymbol{t^* = 10}$, and $\boldsymbol{t^* = 15}$.

can be clearly observed in the 1D extracted lines. The overall kinetics of growth are dictated by the energetics of the electrode/electrolyte interface and the Mg^{2+} concentration gradient, which in turn is determined by the surface tension and electrostatic potential. Figure B.11C indicates that both concentration and electric potential gradients are larger in the vicinity of the tip, which in turn increases the local overpotential and results in faster growth. Figure B.11D depicts the Butler-Volmer kinetics under three different symmetry factors. A Butler-Volmer symmetric coefficient of α=0.5 was used in this study based on values are reported in the literature for analogous Mg electrolyte complexes.[87] The results indicate that the velocity of the deposition interface follows a highly nonlinear behavior, as is indeed observed in Videos B.1—B.5.

3.5. Experimental

3.5.1. Electrodeposition Conditions and Videomicroscopy

Symmetric cells were assembled in an argon-filled glove box (< 0.1 ppm O_2) within three-neck round bottom flasks with two electrode leads run through two of the rubber septa with a separation of 5.715 cm. Both leads held Mg ribbon electrodes (Alfa Aesar, purity of 99.5%) creating symmetric cells. MeMgCl solutions (3 M in anhydrous tetrahydrofuran (THF), Alfa Aesar) were diluted using anhydrous THF (DriSolv. EMD Millipore Co., purity of ≥99.9%). Ligand effects were evaluated through the addition of oleylamine (0.121 M, Sigma Aldrich) or dodecanethiol (0.0626 M, 0.125 M, or 0.188 M, Sigma Aldrich). Electrodeposition was performed under Schlenk conditions in an Ar atmosphere using a programmable power supply (FB1000, Fisher Scientific) and

applying a constant current. A videomicroscope (Plugable Technologies) was used to monitor the reactions.

3.5.2. Structural Characterization of Deposits

Deposits easily were separated from the Mg substrate through gentle washing with THF. Powder X-ray diffraction (XRD) was performed in Bragg—Brentano geometry using a Bruker D8-Focus diffractometer (Cu Kα: λ = 1.5418Å; 40 kV voltage; 25 mA current). X-ray photoelectron spectra (XPS) were obtained using an Omicron DAR 400 XPS/UPS system with a 128-channel micro-channel plate Argus detector using a Mg Kα X-ray source (1253.6 eV). A CN10 electron flood source was utilized to reduce charging. High-resolution scans were collected in constant analyzer energy (CAE) mode with a 100 eV pass energy and a step size of 0.05 eV. Spectral line shapes were fit using the Marquart—Levenberg algorithm for mixed Gaussian-Lorentzian (7:3) line shapes. All spectra were aligned to the C 1s line of adventitious carbon at 284.8 eV.

3.5.3. Electron Microscopy

Scanning electron microscopy images were obtained using a JEOL JSM-7500F operating at an accelerating voltage of 10 kV, emission current of 5 μA, and a probe current of 10 μA. Cross-sectional TEM samples of Mg dendrites were prepared using a FEI Helios Nanolab 460F1 Dual-Focused Ion Beam (FIB). The crystal structure and the growth direction of the Mg dendrites were identified using electron backscatter diffraction (EBSD, Tescan FERA-3 scanning electron microscope (SEM) with an accelerating voltage of 20 kV) and bright-field transmission electron microscopy (TEM, FEI Tecnai G2 F20 Super-Twin FE-TEM operated at 200 kV).

3.5.4. 3D X-ray Tomography

Soft X-ray microscopy images were recorded at the SM (101D-1) beamline of the Canadian Light Source (CLS). The sample was mounted on a computer-controlled (*x, y, θ*) tilt-stage, which facilitates spectrotomographic measurements. Tomography data was acquired at the Mg K-edge from +70° to -35° in increments of 5°. Data analysis was performed using TomoJ, a plug-in to the image analysis software, ImageJ.[88] The images were first aligned using Fourier cross-correlation methods, then further refined using 3D landmarks. In the latter, an algorithm locates regions that can be tracked within the series without the aid of fiducial markers.[89] Conversion to optical density was carried out using aXis2000 (http://unicorn.mcmaster.ca/aXis2000.html). A 3D reconstruction was performed on the aligned tilt-series using an algebraic reconstruction technique (ART), accessible through TomoJ.[90] A total of 10 iterations were carried out with a relaxation coefficient of 0.08.

3.5.5. Nanomechanical Characterization of Deposits.

Strips of pristine Mg substrate (never used for electrodeposition) as well as the 0.5 and 2 M electrodeposits were cast into separate epoxy stubs. These embedded samples were consecutively mechanically polished using 9, 3, 1, and 0.05 μm diamond suspensions. After polishing, the elastic modulus and hardness of the samples were measured using a Nanomechanics iMicro indenter equipped with an InForce 50 actuator and a diamond Berkovich tip. The standard approach of Oliver and Pharr was used to estimate the elastic modulus and hardness.[91] Indentation implemented a test with constant $\dot{P}/P = 0.2\ 1/\mathrm{s}$, with continuous stiffness oscillation of 2 nm. Twelve

indentation tests were used for each sample as the basis for the reported mechanical measurements.

3.5.6. Model Formulation

3.5.6.1. Electrolyte Diffusion Limitations

The amount of dendritic magnesium from experiments can be directly correlated to the time between onset of Sand's time limitation and end of experimental runtime. Consequently, the electrolyte diffusion coefficient and symmetric cell system limiting current densities can be evaluated to explain the formation of magnesium dendrites. Cationic transference numbers reported in the literature for EtMgCl in THF, ranging from 0.058 at 0.25 M to 0.018 at 0.4 M, have been used to develop the model.[92] Low mobilities of dimeric species and ion-ion interactions at high concentrations are thought to be the origin of the diminution of the transference number at high concentrations.

3.5.6.2. Phase-field modelling of dendritic growth

The model described here was developed based on the earlier work of Guyer et. al[93], Bazant[94], Chen et al[95], and Yurkiv et al[96]. Primary deposition occurs through the reaction of M^{n+} cations in the electrolyte solution ($M^{n+}A^{n-}$) with electrons e^- at the surface of the electrode. In an isothermal and isobaric state, the total free energy of a heterogeneous system with constant volume V is given by:

$$\boldsymbol{F^{tot}(\zeta, c_i, \nabla c_i, \psi) = \int_V \left[f^{chem} + f^{int} + f^{elec} + f^{noise}\right] dV} \qquad \textbf{3.4}$$

where f^{chem}, f^{int}, f^{elec} and f^{noise} are the chemical, interfacial, electrical, and Langevin noise contributions respectively, given as:

$$\boldsymbol{f^{chem} = g(\bar{c}) + RT[\bar{c}_+ \ln(\bar{c}_+) + \bar{c}_- \ln(\bar{c}_-)]} \quad \textbf{3.5}$$

$$\boldsymbol{f^{int} = \frac{1}{2}\nabla c\kappa.\nabla c} \quad \textbf{3.6}$$

$$\boldsymbol{f^{elec} = \mathcal{F}\sum_i z_i c_i \psi} \quad \textbf{3.7}$$

$$\boldsymbol{f^{noise} = Ah'(\zeta)\chi} \quad \textbf{3.8}$$

where $g(\bar{c}) = W\bar{c}^2(1-\bar{c}^2) = W\zeta^2(1-\zeta^2)$ is a double well potential function with W being the barrier height of transformation in between the equilibrium states of the electrode and electrolyte. The second term in Eq. 3.5 is the entropic contribution of mixing ions where R is the ideal gas constant, and T is the operating temperature. f^{int} describes the interfacial contributions due to heterogeneous nature of the electrode-electrolyte interface where the anisotropic characteristics of this interface was taken into account by:

$$\boldsymbol{\kappa(\theta) = \kappa_0(1 + \delta\cos[j\theta - \theta_0])} \quad \textbf{3.9}$$

where δ and j are the strength and mode of anisotropy, respectively; κ_0 is the interface energy gradient, θ and θ_0 are related to the angle between the normal vector of the surface and the reference axis. f^{elec} is the electrostatic energy density, where $\mathcal{F}$ and z_i are the Faraday's constant and valence of species i, respectively. An additional phase-field variable was used to distinguish the states of the electrolyte ($\zeta = 0$) and electrode ($\zeta = 1$), which continuously changes in the interface region. f^{noise} denotes the Langevin noise, which was applied to the

interface region by using χ, which is a quasi-random number between [-1,1], and A is the amplitude of the fluctuation. The evolution of the non-conserved, conserved, and electrostatic fields were prescribed by the following equations, respectively:

$$\frac{\partial \zeta}{\partial t} = -L_\sigma(g'(\zeta) - \kappa(\theta)\nabla^2\zeta) - \Gamma \quad \textbf{3.10}$$

$$\frac{\partial c_+}{\partial t} = \nabla\left[D^{eff}\nabla c_+ + \frac{D^{eff}c_+}{RT}n\mathcal{F}\nabla\psi\right] - \frac{c_s}{c_0}\frac{\partial \zeta}{\partial t} \quad \textbf{3.11}$$

$$\nabla\left[\sigma^{eff}\nabla\psi\right] = n\mathcal{F}c_s\frac{\partial \zeta}{\partial t} \quad \textbf{3.12}$$

where L_σ is the interface mobility, and Γ is the electrodeposition rate defined by:

$$\Gamma = L_\eta i_0 h'(\zeta)\left\{e^{\frac{(1-\alpha)n\mathcal{F}\eta_a}{RT}} - c_+ e^{\frac{(\alpha)n\mathcal{F}\eta_a}{RT}}\right\} \quad \textbf{3.13}$$

where L_η is the reaction related kinetic coefficient, i_0 is the exchange current density, h' is the derivative of the interpolation function $h(\zeta) = \zeta^3(10 - 15\zeta + 6\zeta^2)$, α is the anodic/cathodic symmetric charge-transfer coefficient (assumed to be 0.5 in this study ($0 < \alpha < 1$)), and η_a is the overpotential. D^{eff} and σ^{eff} are the interdiffusion and conductivity, respectively defined over the domain by means of the interpolation function $h(\zeta)$. The source term in Eq. 3.12 is related to reaction rate.

3.5.6.2.1. Numerical integration of the phase field model.

A metallic Mg electrode in contact with a 1 M MeMgCl solution in THF was selected as the reference state. For the equilibrium numerical simulations, the Mg electrode was located at the bottom of the simulation cell and an artificial nucleation

event was introduced. The partial molar volumes of Mg^{2+}, MeMgCl, and THF are approximated to be the same. Equations 3.10-3.12 were solved using a finite difference solver in a uniform grid with equal mesh size using a parallel in-house Fortran code. Boundary conditions used for Eqs. 3.10-3.12 are listed in Table B.1. Only half of the cell was considered in order to reduce the computational cost; the domain cell size was set at 300×500.

3.6. Conclusions

The promise and excitement of magnesium batteries derives in large portion from the idea that they are immune to dendrite formation. Whilst considerable effort has been invested in the design of novel electrolytes and cathode materials, multivariate studies of Mg electrodeposition are scarce particularly under conditions emulative of high local concentration and potential gradients. Galvanostatic electrodeposition of metallic Mg from Grignard reagents in symmetric cells reveals a complex phase map with varying morphologies of plated deposits including fractal aggregates and highly anisotropic dendrites with singular growth fronts. Based on electron microscopy, X-ray tomography, and optical tomography observations, the deposits are highly faceted primarily zerovalent magnesium with some surface passivation. The growth morphologies have been examined as a function of current density, concentration, and added coordinating ligands. Increase of the current density amplifies the extent of branching, indicating an increase in the electrochemical reaction rate; increases in concentration induce a transition from a fractal to a dendritic growth regime. Remarkably, the dendrites show extended single crystalline domains along the $< 11\bar{2}0 >$ growth direction. At lower

concentrations, smaller grains comprising agglomerated thin hexagonal platelets are observed. In contrast, at higher concentrations more spherical deposits with faceted hexagonal surficial features are seen. At the highest concentrations, canonical dendritic deposits with a strongly anisotropic growth direction are observed. Addition of coordinating ligands greatly alters the growth mechanisms suppressing dendrite growth and instead stabilizing single-crystalline high-aspect-ratio nanowires by altering the extent of supersaturation and the nature of the electrode/electrolyte interface.

Dendritic electrodeposition is a result of electrolyte transport limitations, with surface self-diffusion rates dictating morphological variation from needle-like to fractal-like morphologies. Synergistic analytical and phase-field modeling further establish the proclivity of Mg to form dendrites at high current densities; variations in electrolyte diffusivity variation with concentrations have further been delineated. Whilst data on long-term cycling performance of Mg full cells is scarce and it remains to be observed the extent to which dendrite formation will emerge as a limitation, it is worth noting that electrochemical reaction rates can readily surpass self-diffusion rates as a result of local inhomogeneities; as such, the results herein are expected to be relevant to systems even wherein averages current densities are substantially lower. The hardness of Mg dendrites delineated here, with shear moduli approaching 10 GPa, is substantially greater than Li dendrites, and further suggests the need for caution in the design of separators.

3.7. References

[1] N. Nitta, F. Wu, J. T. Lee, G. Yushin, *Mater. Today* **2015**, *18*, 252.

[2] E. A. Olivetti, G. Ceder, G. G. Gaustad, X. Fu, *Joule* **2017**, *1*, 229.

[3] J. W. Choi, D. Aurbach, *Nat. Rev. Mater.* **2016**, *1*, 16013.

[4] B. Liu, J.-G. Zhang, W. Xu, *Joule* **2018**, *2*, 833.

[5] D. Aurbach, E. Zinigrad, Y. Cohen, H. Teller, *Solid State Ionics* **2002**, *148*, 405.

[6] K. J. Harry, D. T. Hallinan, D. Y. Parkinson, A. A. MacDowell, N. P. Balsara, *Nat. Mater.* **2014**, *13*, 69.

[7] M. Jäckle, K. Helmbrecht, M. Smits, D. Stottmeister, A. Groß, *Energy Environ. Sci.* **2018**, *11*, 3400.

[8] G. Henkelman, B. P. Uberuaga, H. Jónsson, *J. Chem. Phys.* **2000**, *113*, 9901.

[9] L. C. Merrill, J. L. Schaefer, *Front. Chem.* **2019**, *7*, 194.

[10] D. Aurbach, Y. Cohen, M. Moshkovich, *Electrochem. Solid-State Lett.* **2001**, *4*, A113.

[11] J. O. Besenhard, M. Winter, *ChemPhysChem* **2002**, *3*, 155.

[12] C. B. Bucur, T. Gregory, A. G. Oliver, J. Muldoon, *J. Phys. Chem. Lett.* **2015**, *6*, 3578.

[13] C. Ling, D. Banerjee, M. Matsui, *Electrochim. Acta* **2012**, *76*, 270.

[14] M. Matsui, *J. Power Sources* **2011**, *196*, 7048.

[15] J. Muldoon, C. B. Bucur, T. Gregory, *Chem. Rev.* **2014**, *114*, 11683.

[16] Q. Fu, A. Sarapulova, V. Trouillet, L. Zhu, F. Fauth, S. Mangold, E. Welter, S. Indris, M. Knapp, S. Dsoke, N. Bramnik, H. Ehrenberg, *J. Am. Chem. Soc.* **2019**, *141*, 2305.

[17] A. Parija, Y. Liang, J. L. Andrews, L. R. De Jesus, D. Prendergast, S. Banerjee,

Chem. Mater. **2016**, *28*, 5611.

[18] B. Zhou, H. Shi, R. Cao, X. Zhang, Z. Jiang, *Phys. Chem. Chem. Phys.* **2014**, *16*, 18578.

[19] E. Levi, YGofer, D. Aurbach, *Chem. Mater.* **2010**, *22*, 860.

[20] H. D. Yoo, Y. Liang, H. Dong, J. Lin, H. Wang, Y. Liu, L. Ma, T. Wu, Y. Li, Q. Ru, Y. Jing, Q. An, W. Zhou, J. Guo, J. Lu, S. T. Pantelides, X. Qian, Y. Yao, *Nat. Commun.* **2017**, *8*, 339.

[21] D. Aurbach, Y. Gofer, A. Schechter, O. Chusid, H. Gizbar, Y. Cohen, M. Moshkovich, R. Turgeman, *J. Power Sources* **2001**, *97–98*, 269.

[22] J. Muldoon, C. B. Bucur, T. Gregory, *Angew. Chemie - Int. Ed.* **2017**, *56*, 12064.

[23] T. Gao, S. Hou, K. Huynh, F. Wang, N. Eidson, X. Fan, F. Han, C. Luo, M. Mao, X. Li, C. Wang, *ACS Appl. Mater. Interfaces* **2018**, *10*, 14767.

[24] Q. S. Zhao, Y. N. Nuli, Y. S. Guo, J. Yang, J. L. Wang, *Electrochim. Acta* **2011**, *56*, 6530.

[25] S. DeWitt, N. Hahn, K. Zavadil, K. Thornton, *J. Electrochem. Soc.* **2016**, *163*, A513.

[26] M. Jäckle, A. Groß, *J. Chem. Phys.* **2014**, *141*, 174710.

[27] J. Tian, D. Cao, X. Zhou, J. Hu, M. Huang, C. Li, *ACS Nano* **2018**, *12*, 3424.

[28] Y. Zhang, J. Xie, Y. Han, C. Li, *Adv. Funct. Mater.* **2015**, *25*, 7300.

[29] P. G. Shewmon, *Trans.Metall.Soc.AIME* **1956**, *206*, 918.

[30] J. Combronde, G. Brebec, *Acta Metall.* **1971**, *19*, 1393.

[31] S. Ganeshan, L. G. Hector, Z. K. Liu, *Comput. Mater. Sci.* **2010**, *50*, 301.

[32] L. J. Zhang, T. I. Spiridonova, S. E. Kulkova, R. Yang, Q. M. Hu, *Comput. Mater. Sci.* **2017**, *128*, 236.

[33] A. Parija, G. R. Waetzig, J. L. Andrews, S. Banerjee, *J. Phys. Chem. C* **2018**, *122*, 25709.

[34] T. D. Gregory, R. J. Hoffman, R. C. Winterton, *J. Electrochem. Soc.* **1990**, *137*, 775.

[35] R. Davidson, A. Verma, D. Santos, F. Hao, C. Fincher, S. Xiang, J. Van Buskirk, K. Xie, M. Pharr, P. P. Mukherjee, S. Banerjee, *ACS Energy Lett.* **2019**, *4*, 375.

[36] J. Bitenc, K. Pirnat, E. Žagar, A. Randon-Vitanova, R. Dominko, *J. Power Sources* **2019**, *430*, 90.

[37] C. Liebenow, *J. Appl. Electrochem.* **1997**, *27*, 221.

[38] M. S. Ding, T. Diemant, R. J. Behm, S. Passerini, G. A. Giffin, *J. Electrochem. Soc.* **2018**, *165*, A1983.

[39] H. Brune, *Surf. Sci. Rep.* **1998**, *31*, 125.

[40] J. W. Evans, P. A. Thiel, M. C. Bartelt, *Surf. Sci. Rep.* **2006**, *61*, 1.

[41] A. Groß, *Theoretical Surface Science - A Microscopic Perspective*, Springer, Berlin, **2009**.

[42] K. Pettersen, O. Lohne, N. Ryum, *Metall. Trans. A* **1990**, *21*, 221.

[43] D. Dubé, A. Couture, Y. Carbonneau, M. Fiset, R. Angers, R. Tremblay, *Int. J. Cast Met. Res.* **1998**, *11*, 139.

[44] K. N. Wood, E. Kazyak, A. F. Chadwick, K. H. Chen, J. G. Zhang, K. Thornton, N. P. Dasgupta, *ACS Cent. Sci.* **2016**, *2*, 790.

[45] K. Nishikawa, T. Mori, T. Nishida, Y. Fukunaka, M. Rosso, T. Homma, *J. Electrochem. Soc.* **2010**, *157*, A1212.

[46] W.-S. Kim, W.-Y. Yoon, *Electrochim. Acta* **2004**, *50*, 541.

[47] A. J. Ilott, M. Mohammadi, H. J. Chang, C. P. Grey, A. Jerschow, *Proc. Natl. Acad. Sci. U. S. A.* **2016**, *113*, 10779.

[48] P. Bai, J. Li, F. R. Brushett, M. Z. Bazant, *Energy Environ. Sci.* **2016**, *9*, 3221.

[49] J. Song, *J. Power Sources* **2002**, *111*, 255.

[50] G. Bieker, M. Winter, P. Bieker, *Phys. Chem. Chem. Phys. Phys. Chem. Chem. Phys* **2015**, *8670*, 8670.

[51] J. C. Burns, L. J. Krause, D.-B. Le, L. D. Jensen, A. J. Smith, D. Xiong, J. R. Dahn, *J. Electrochem. Soc.* **2011**, *158*, A1417.

[52] F. Hao, A. Verma, P. P. Mukherjee, *ACS Appl. Mater. Interfaces* **2018**, *10*, 26320.

[53] L. Viyannalage, V. Lee, R. V. Dennis, D. Kapoor, C. D. Haines, S. Banerjee, *Chem. Commun.* **2012**, *48*, 5169.

[54] D. Aurbach, *Electrochem. Solid-State Lett.* **1999**, *3*, 31.

[55] C. Fotea, J. Callaway, M. R. Alexander, *Surf. Interface Anal.* **2006**, *38*, 1363.

[56] H. Kuwata, M. Matsui, N. Imanishi, *J. Electrochem. Soc.* **2017**, *164*, A3229.

[57] Y. Gofer, R. Turgeman, H. Cohen, D. Aurbach, *Langmuir* **2003**, *19*, 2344.

[58] R. M. Bradley, R. C. Ball, *Nature* **1984**, *309*, 225.

[59] V. Fleury, M. Rosso, J.-N. N. Chazalviel, B. Sapoval, *Phys. Rev. A* **1991**, *44*, 6693.

[60] Y. Sawada, A. Dougherty, J. P. Gollub, *Phys. Rev. Lett.* **1986**, *56*, 1260.

[61] D. Grier, E. Ben-Jacob, R. Clarke, L. M. Sander, *Phys. Rev. Lett.* **1986**, *56*, 1264.

[62] R. F. Voss, *Phys. Rev. B* **1984**, *30*, 334.

[63] P. Meakin, *Phys. Rev. Lett.* **1983**, *51*, 1119.

[64] A. Ghosh, R. Batabyal, G. P. Das, B. N. Dev, *AIP Adv.* **2016**, *6*, 015301.

[65] L. O. Valøen, J. N. Reimers, *J. Electrochem. Soc.* **2005**, *152*, A882.

[66] D. P. Barkey, in *Adv. Electrochem. Sci. Eng. Vol. 7*, Wiley-VCH Verlag GmbH, Weinheim, FRG, **2001**, pp. 151–191.

[67] O. Zik, E. Moses, *Phys. Rev. E - Stat. Physics, Plasmas, Fluids, Relat. Interdiscip. Top.* **1996**, *53*, 1760.

[68] E. Ben-Jacob, P. Garik, *Nature* **1990**, *343*, 523.

[69] W. Shao, G. Zangari, *J. Phys. Chem. C* **2009**, *113*, 10097.

[70] K. R. Kort, S. Banerjee, *Small* **2015**, *11*, 329.

[71] J. Cho, ab Ho Jin, D. G. Sellers, ab F. David Watson, D. Hee Son, S. Banerjee, *J. Mater. Chem. C* **2017**, *5*, 8810.

[72] M. P. Staiger, A. M. Pietak, J. Huadmai, G. Dias, *Biomaterials* **2006**, *27*, 1728.

[73] M. Avedesian, H. Baker, Eds. , *ASM Specialty Handbook: Magnesium and Magnesium Alloys*, ASM International, **1999**.

[74] W. C. Oliver, G. M. Pharr, *J. Mater. Res.* **2004**, *19*, 3.

[75] M. Rashad, F. Pan, A. Tang, M. Asif, M. Aamir, *J. Alloys Compd.* **2014**, *603*, 111.

[76] E. Mostaed, M. Vedani, M. Hashempour, M. Bestetti, *Biomatter* **2014**, *4*, e28283.

[77] C. Monroe, J. Newman, *J. Electrochem. Soc.* **2005**, *152*, A396.

[78] J. R. Davis, Ed. , *Metals Handbook Desk Edition*, Materials Park, OH, **2003**.

[79] C. T. Love, *J. Electrochem. Energy Convers. Storage* **2016**, *13*, 031004.

[80] W. S. LePage, Y. Chen, E. Kazyak, K.-H. Chen, A. J. Sanchez, A. Poli, E. M. Arruda, M. D. Thouless, N. P. Dasgupta, *J. Electrochem. Soc.* **2019**, *166*, A89.

[81] A. Masias, N. Felten, R. Garcia-Mendez, J. Wolfenstine, J. Sakamoto, *J. Mater. Sci.* **2019**, *54*, 2585.

[82] A. Puzder, A. J. Williamson, N. Zaitseva, G. Galli, L. Manna, A. P. Alivisatos, *Nano Lett.* **2004**, *4*, 2361.

[83] S. A. Morin, M. J. Bierman, J. Tong, S. Jin, *Science (80-.).* **2010**, *328*, 476.

[84] F. Hao, A. Verma, P. P. Mukherjee, *ACS Appl. Mater. Interfaces* **2018**, *10*, 26320.

[85] F. Hao, A. Verma, P. P. Mukherjee, *Energy Storage Mater.* **2019**, *20*, 1.

[86] J. E. Guyer, W. J. Boettinger, J. A. Warren, G. B. McFadden, *Phys. Rev. E* **2004**, *69*, 021603.

[87] Y. Viestfrid, M. D. Levi, Y. Gofer, D. Aurbach, *J. Electroanal. Chem.* **2005**, *576*, 183.

[88] C. MessaoudiI, T. Boudier, C. Sorzano, S. Marco, *BMC Bioinformatics* **2007**, *8*, 288.

[89] C. Sorzano, C. Messaoudi, M. Eibauer, J. Bilbao-Castro, R. Hegerl, S. Nickell, S. Marco, J. Carazo, *BMC Bioinformatics* **2009**, *10*, 124.

[90] G. T. Herman, A. Lent, S. W. Rowland, *J. Theor. Biol.* **1973**, *42*, 1.

[91] W. C. Oliver, G. M. Pharr, *J. Mater. Res.* **1992**, *7*, 1564.

[92] A. Benmayza, M. Ramanathan, T. S. Arthur, M. Matsui, F. Mizuno, J. Guo, P.-A.

Glans, J. Prakash, *J. Phys. Chem. C* **2013**, *117*, 26881.

[93] J. E. Guyer, W. J. Boettinger, J. A. Warren, G. B. McFadden, *Phys. Rev. E* **2004**, *69*, 021604.

[94] M. Z. Bazant, *Acc. Chem. Res.* **2013**, *46*, 1144.

[95] L. Chen, H. W. Zhang, L. Y. Liang, Z. Liu, Y. Qi, P. Lu, J. Chen, L.-Q. Chen, *J. Power Sources* **2015**, *300*, 376.

[96] V. Yurkiv, T. Foroozan, A. Ramasubramanian, R. Shahbazian-Yassar, F. Mashayek, *Electrochim. Acta* **2018**, *265*, 609.

4. MAGNESIUM NANOCOMPOSITE COATINGS FOR PROTECTION OF A LIGHTWEIGHT AL ALLOY: MODES OF CORROSION PROTECTION AND MECHANISMS OF FAILURE*

4.1. Overview

In light of the increased emphasis on lightweighting of vehicular components and continued use of high-performance aluminum alloys in the aerospace industry, designing alternatives to carcinogenic chromium-based corrosion control systems has emerged as an urgent imperative. The high activity of aluminum and the heterogeneous surface structure of Al alloys renders effective corrosion inhibition a formidable challenge. Here, we demonstrate the effective corrosion protection of AA7075 alloys by Mg/polyetherimide nanocomposite coatings prepared by dispersing solution-grown Mg nanocrystals within a polyamic acid matrix followed by imidization on the substrate. The active nanocrystal filler and nanocomposite have been characterized using powder X-ray diffraction, Fourier transform infrared spectroscopy, and cross-sectional electron microscopy. Electrochemical impedance spectroscopy and open circuit potential (OCP) responses of coatings have been evaluated over the course of 100 days of exposure to a 3.5 wt.% aqueous solution of NaCl. These results suggest that the nanocomposite coatings endow efficacious cathodic and barrier protection to the underlying alloy substrate. The Mg/PEI nanocomposite coatings endow immediate cathodic protection to AA7075 substrates upon salt water immersion with rapid mobilization of the active

filler. The nanocomposites represent a vital addition to the sparse set of chrome-free options for corrosion protection of lightweight alloys.

4.2. Introduction

Despite the well-documented carcinogenicity of hexavalent chromium, chromium-based coatings continue to be extensively used in the aerospace industry owing to their superior corrosion resistance and resilience across a broad range of aggressive environments.[1–5] The excellent corrosion protection afforded by chrome-based coatings derives from the facile deposition of insoluble oxides and polyanionic deposits, which are readily precipitated at exposed surfaces as a result of their low K_{sp} values; in addition, chromate ions compete with aggressive chloride ions in terms of binding constants at metal surfaces, thereby inhibiting both anodic and cathodic half-reactions mediating corrosion. The formation of a passivating oxide layer provides some degree of protection to high-performance lightweight aluminum alloys; however, the oxide films thus formed are stable only within a limited pH window (ca. 4—9) beyond which Pourbaix diagrams suggest the preferential formation of Al^{3+} or $Al(OH)_4^-$ as prominent corrosion products.[4,6] The incorporation of alloying elements and intermetallic precipitates to enhance mechanical properties further renders such alloys more susceptible to corrosion by establishing chemical potential gradients across their surfaces, thereby resulting in localized corrosion. Owing to the high activity of aluminum, chrome-based coatings represent one of the few alternatives for inhibition of corrosion.[7,8] Despite considerable research spanning over three decades, chrome-free coatings have yet to meet required specifications, particularly in challenging

environments. As a notable example of the deficiencies of chrome-free coatings, in 2005, the US F-22 fighter jet fleet of 187 aircrafts incorporating such a coating had 534 reports of actionable corrosion, necessitating an estimated $228 million in repairs.[1,9]

The increasing adoption of Al alloys for lightweighting in the automotive industry has provided new impetus to the search for novel sustainable coating solutions[5,10] that eschew carcinogens and have a lower environmental impact.[11–16] Premature failure of strength-critical parts as a result of corrosion poses a risk to passenger safety. Furthermore, the diminished durability of components as a result of corrosion increases their cradle-to-grave environmental impact. Finding effective alternatives to chromium-based coatings has thus emerged as an urgent imperative. Whilst several avenues have been explored spanning the range from design of novel metal matrix composites to polymeric films and multicomponent nanocomposites,[5,17,18] fundamental elucidation of the modes of corrosion protection and mechanisms of failure remain understudied, thereby stymying the rational mechanism-informed design of sustainable chrome-free coatings.

Magnesium is the only viable structural metal that can be used to provide sacrificial, cathodic protection (-2.37 V *vs*. SHE) to aluminum in light of the high activity of the Al/Al^{3+} redox couple (-1.66 V *vs*. SHE).[19] A fundamental materials descriptor for a coating to inhibit corrosion of Al alloys is thus a more negative reduction potential value than -1.66 V, which thereby constrains the available palette of materials to predominantly s-block elements, several of which are highly flammable and soft. Magnesium exhibits high reactivity but can be passivated; it furthermore has an elastic

modulus of 27.5 ±4.1 GPa and a hardness recently estimated for Mg nanostructures as 662 ±77 MPa.[20] Bierwagen and co-workers have demonstrated the feasibility of cathodic protection of Al alloys using Mg composites.[21,22] Their design incorporates a Mg-rich epoxy primer (typically incorporating multiple modes of cross-linking) with pigment volume concentrations (PVCs) approaching 50 % (ca. 70 wt.%) used in conjunction with a polymeric top coat.[21,23] Given that the particles utilized within the primer are around 50 μm in size, the coatings are typically much greater than 100 μm in thickness, which creates challenges in protection of intricately structured components and architectures such as now accessible from additive manufacturing methods.[24,25] Additional challenges with such coatings derive from the high activity of magnesium, which results in rapid depletion of the active material and creates issues with the safe handling of powders. The main mode of failure observed in these coatings is blistering caused by the production of hydrogen upon formation of magnesium hydroxide as per:

$$\mathbf{Mg\ (s) + 2H_2O\ (l) = Mg(OH)_2\ (s) + H_2\ (g)} \qquad \mathbf{4.1}^{[21,26]}$$

Further investigations have revealed that the concentration of atmospheric CO_2 plays a major role in determining the identity of the corrosion product.[27–30] Under ambient conditions, hydrated magnesium carbonate is stabilized, and is thought to offer additional passivation by serving as a barrier coating. Environments with relatively high humidity or immersion in aqueous solutions of NaCl with limited CO_2 solubility result in a greater propensity for the formation of $Mg(OH)_2$ and H_2 gas as per Eq. 4.1, resulting in blistering and increased potential for hydrogen embrittlement.[31] Consequently, the preferential formation of hydrated magnesium carbonate products[32] and delayed

kinetics of magnesium activation[33] are thought to be imperative for effective corrosion protection of Al alloys by Mg nanocomposite coatings. In this work, we report the corrosion protection of AA7075 alloys by a polyetherimide (PEI) nanocomposite containing dispersed Mg nanocrystals. The utilization of ultra-small Mg nanocrystals in conjunction with a highly formable and well-adhered, water-impervious continuous phase allows for the combination of sacrificial cathodic protection and barrier protection modalities within the same coating. Mechanisms of corrosion inhibition and modes of failure have been explored through electrochemical impedance spectroscopy (EIS) and open circuit potential (OCP) measurements monitored over the course of 100 days coupled with ASTM B117 salt spray exposure testing and post-mortem cross-sectional analysis of EIS samples by scanning electron microscopy (SEM).

4.3. Results and Discussion

Mg nanocrystals have been prepared by the Reike reduction of Grignard's reagents by lithium naphthalide as described in previous work.[34] The surfaces of the nanocrystals are passivated with a THF layer (complexation of magnesium species by THF is strong, and plays a major role in determining the identity of electroactive species),[35] which allows them to be safely handled under the processing conditions described above without being combusted in air.[22] Indeed, the nanocomposite coatings have been aerosolized during spray coating and cured in an air ambient at temperatures as high as 250°C. SEM and TEM images and of the Mg nanocrystals used within the nanocomposite coatings are shown in **Figure 4.1A** and **Figure 4.1B** respectively. The nanocrystals have a platelet like morphology ranging from ca. 100-500 nm in terms of

their largest dimensions with an average of 273 nm.[34] A particle size distribution plot is shown in **Figure C.1 (Appendix C)**. A powder XRD pattern of the Mg nanocrystals shown in **Figure 4.1C** can be indexed to PDF 35-0821 corresponding to metallic magnesium with no other discernible crystalline phases. The structure has further been refined to the *P*63/*mmc* hexagonal space group (**Fig. 4.1C**). The refined lattice parameters for the hexagonal unit cell are found to be a = 3.214553(66) Å and c = 5.21868(18) Å with a unit cell volume of V = 46.702(2) Å^3 and a calculated density of 1.728 g·cm^{-3}. The Mg nanocrystals have been dispersed in NMP through ultrasonication to facilitate their intimate mixing with the polyamic acid continuous phase.[36] The Mg nanocrystal/polyamic acid dispersion in NMP is spray-coated onto the AA7075 substrates and subsequently imidized by annealing at 250 °C to obtain the Mg/PEI nanocomposite coating, as schematically illustrated in **Figure 4.1D**. A PEI top-coat with a thickness of 10 μm is further applied to the coating. PEI is known to adhere well to low-alloy steel substrates and provides excellent barrier protection;[36,37] the application of this matrix to Al alloys is less explored. Two different Mg loadings, 17 and 50 wt.%, have been examined. Relatively thick films with overall thicknesses in the range of 40—50 μm have been evaluated to allow for incorporation of high contents of sacrificial corrosion inhibitors. Fourier-transform infrared spectroscopy (FTIR) has been utilized to confirm the structure of PEI within each of the composites as shown in **Figure C.2**. FTIR spectra of PEI, 17 wt.% Mg/PEI, and 50 wt.% Mg/PEI coatings in Figure C.3[36] show carbonyl stretching frequencies from the imide moiety at 1770 cm^{-1} and 1698 cm^{-1}; C-N stretching modes of the imide are observed at 1351 cm^{-1}. The band observed at

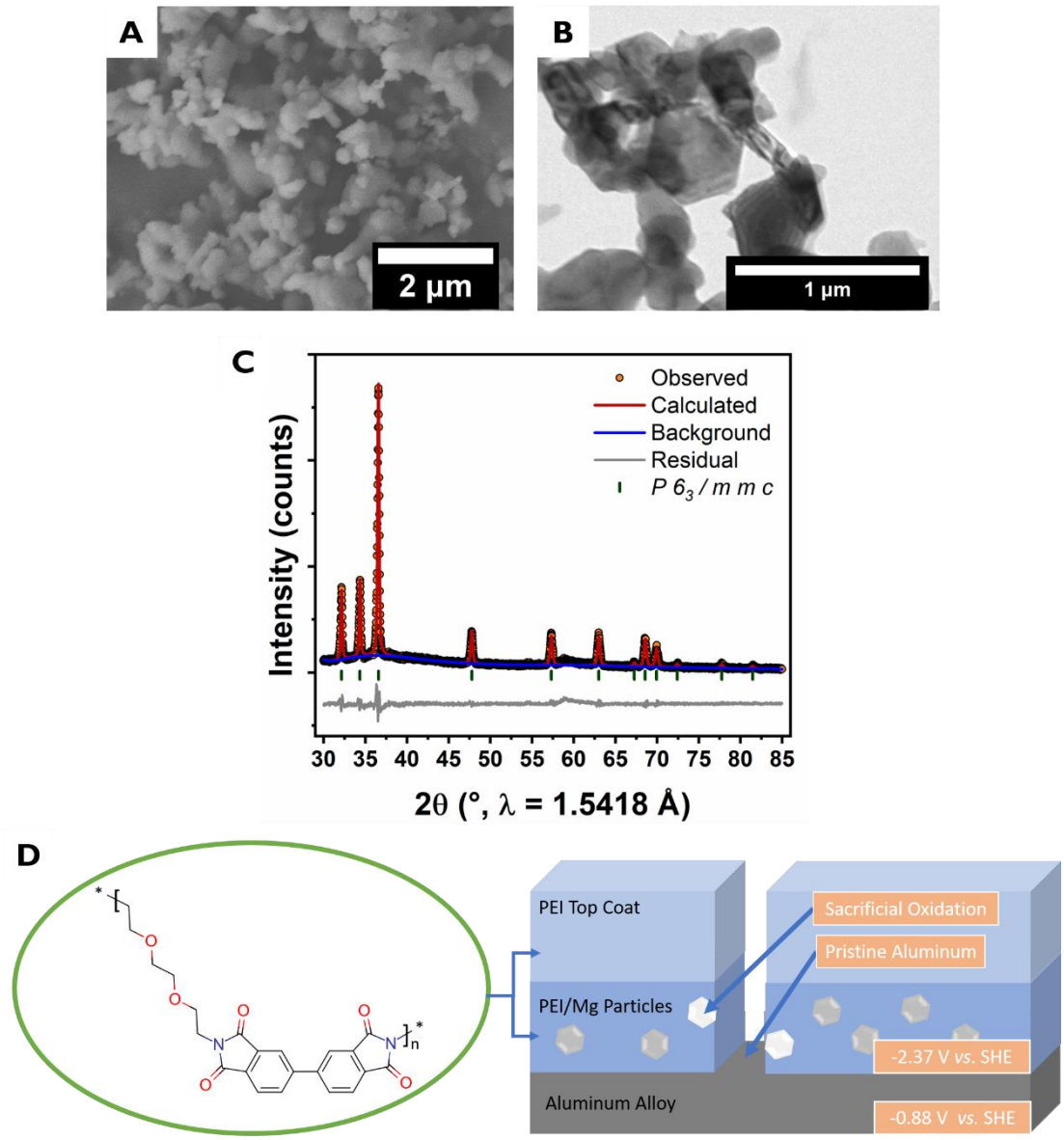

Figure 4.1. A) SEM image, B) TEM image, and C) X-ray diffraction pattern with Rietveld refinement. Collected X-ray diffraction pattern (black-outlined orange circles) is fitted to the calculated *P*63/*mmc* hexagonal space group (solid red line). The implemented Chebychev polynomial background fit (dark blue) and refinement residual (light grey) are also displayed. Lattice parameters were calculated to be: a = 3.214553(66) Å and c = 5.21868(18) Å with a unit cell volume of V = 46.702(2) Å^3 and a calculated density of 1.728 g·cm^{-3}. The goodness of fit parameters for the Rietveld refinement are calculated to be: $\chi 2$ = 2.785, wRp = 11.02%, and Rp = 8.11%. D) Schematic illustration of nanocomposite coating and its mode of action.

736 cm^{-1} likely corresponds to deformation of the imide ring. A band for the aromatic ring breathing mode is observed at 1491 cm^{-1}.[38]

Table 4.1 summarizes the results of ASTM adhesion tests. Despite the relatively high thicknesses (40—50 μm), the nanocomposite coatings are well adhered to the AA7075 substrates. The pull-off pressures are on the order of 0.65—0.95 MPa. Cross-cut testing shows some damage at the intersections of cross-cut points for the PEI coating and 50 wt.% Mg/PEI coating. The 17 wt.% coating showed greater damage with some areas showing loss of coating along the cut lines. It should be noted however, that most of the damage occurs during the initial cut rather than during application and removal of tape. All coatings showed excellent scrape resistance as per ASTM D2197-13 with no discernible break-through even with the maximum applied loading weight of 10 kg. High-magnification scanning electron microscopy images of the Mg/PEI and PEI interface of 17 wt.% and 50 wt.% Mg/PEI coatings are shown in **Figure C.3**. These again demonstrate the homogeneous dispersion of Mg nanocrystals with the polymer network.

Figure 4.2 shows digital photographs of coated samples exposed to salt spray conditions following ASTM B117 for 12 days. The PEI sample without Mg nanocrystals shows clear evidence for corrosion of the exposed etched areas. In contrast, the 17 wt.% Mg/PEI coating (**Fig. 4.2B**) shows evidence of activation and sacrificial cathodic protection afforded by the Mg nanocrystals, discernible as white precipitates on the coating surface. The cross-etched areas show evidence of corrosion of the underlying substrate. In stark contrast, the 50 wt.% Mg/PEI nanocomposite coating (**Fig. 4.2C**)

Table 4.1. Summary of ASTM adhesion testing for PEI and Mg/PEI nanocomposite coatings on AA7075 substrates.

Sample	ASTM D4541-09	ASTM D3359 (Cross-Cut)	ASTM D2197-13 (Scrape)
	Pull-off Pressure (MPa)	ASTM rating (0-5B)	>10 kg
PEI	0.98 ± 0.26	4B	
17 wt.% Mg/PEI	0.65 ± 0.12	3B	
50 wt.% Mg/PEI	0.88 ± 0.08	4B	

shows extensive activation of the embedded Mg nanocrystals. In contrast to the PEI (Fig. 4.2A) and the 17 wt.% Mg/PEI coating (Fig. 4.2B), no corrosion of the AA7075 substrate is observed in the cross-cut area for the 50 wt.% Mg/PEI coating. The remarkable protection of the AA7075 surface afforded by 50 wt.% Mg nanocrystal

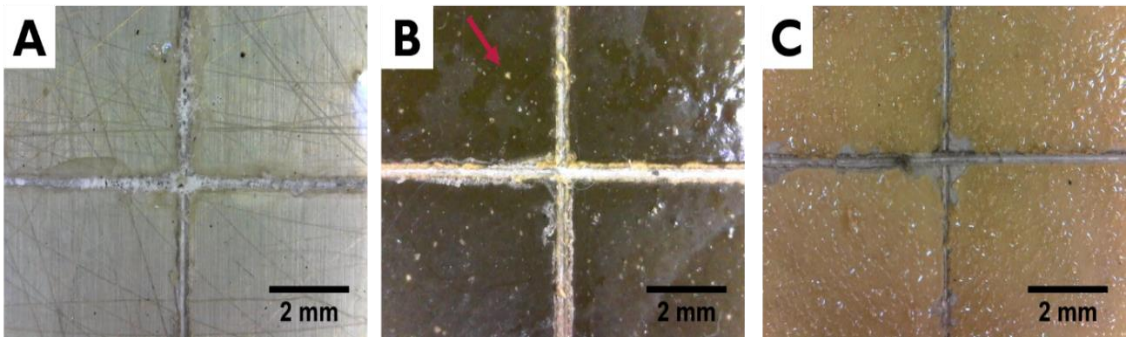

Figure 4.2. Digital photographs of A) PEI; B) 17 wt.% Mg/PEI; and C) 50 wt.% Mg/PEI on AA7075 after exposure to B117 salt spray testing for 12 days. The red arrow in (B) delineates corrosion product formed by activation of the Mg nanocrystals embedded within the nanocomposite coating.

loadings suggests successful electrochemical coupling of the alloy surface and Mg nanocrystals within the composite.

OCP measurements provide an effective means of evaluating the extent of cathodic protection afforded by sacrificial coatings.[39–41] **Figure 4.3** contrasts the evolution of the OCP for 17 and 50 wt.% Mg/PEI nanocomposite coatings with that of the bare AA7075 substrate (ca. -0.88 V *versus* SCE) and PEI.[42] As described in our previous work, the PEI coating initially shows a high open circuit voltage (ca. -0.5 V) relative to the bare AA7075 substrate indicating the presence of excellent barrier protection; however, following the first day, the OCP rapidly decreases (ca. -1.0 V) below that of the bare substrate demonstrating the rapid penetration of electrolyte through the polymer. However, the OCP then increases through day 20 to around -0.5 V and fluctuates between -0.5 V and -0.6 V for the remainder of the study. This is correlated with the formation of a passivating layer which is continually broken down and rebuilt through pitting processes.[42] Upon initial immersion, the OCP values for both nanocomposite coatings are notably more cathodic than the OCP value for bare AA7075. A cathodic polarization of ca. 350 mV and ca. 290 mV is measured for the 17 and 50 wt.% Mg/PEI nanocomposite coatings, respectively, attesting to their ability to provide sacrificial protection to the AA7075 substrate. The rapid cathodic polarization of the alloy substrate by the Mg nanocrystals is quite distinctive from the behavior observed for Zn-rich coatings, wherein initially the OCP is more anodic than that of steel substrate and then fluctuates before reaching a stable mixed potential value. The observed fluctuation in the latter case can be ascribed to the presence of native ZnO,

which must be dissolved in order to activate the Zn particles.[40,41,43] Mg nanocrystals also exhibit a native passivation layer; however, the passivation layer appears to be readily dissolved upon penetration of the electrolyte within the coating as a result of the high reactivity of magnesium in the presence of ionic species. After the first day of immersion, the OCP for both coatings is shifted to more anodic values indicating formation of magnesium corrosion products as a result of the sacrificial corrosion process. Effective cathodic protection is observed to be maintained for 5 and 20 days in the case of 17 and 50 wt.% Mg/PEI nanocomposite coatings, respectively. The longer lifetime of cathodic protection for the latter coatings is directly correlated to the higher loading of Mg nanocrystals within the coating. After cessation of sacrificial cathodic reactions, the OCP for 17 wt.% Mg/PEI increases to relatively more anodic potentials as compared to AA7075, reaching values close to -0.7 V *versus* SCE. This behavior suggests that the corrosion products formed during the cathodic protection process inhibit the overall corrosion process. However, after 20 days of immersion in a 3.5% aqueous solution of NaCl, the OCP values again decrease to values similar to that of AA7075 and are then somewhat further decreased as a function of elapsed time. This behavior can be attributed to re-activation of corrosion processes owing to continuous degradation and leaching of the corrosion products as a result of attack by corrodent species. Based on the OCP values, the corrosion processes can include anodic dissolution of aluminum, dissolution of Mg nanoplatelets (where anodic and cathodic reactions occur on their surfaces), and/or galvanic coupling between the substrate and the Mg particles. The 50 wt.% Mg/PEI coating shows somewhat different behavior.

After 20 days of immersion, the OCP shifted to more anodic potentials just below the OCP of the aluminum substrate. It then remains nearly constant for the remaining immersion time, suggesting that sacrificial protection might be still active, but aluminum dissolution can also be expected.

Based on the OCP results in **Figure 4.3**, it is worth noting that both the 17 and 50 wt.% Mg/PEI nanocomposite coatings provide effective cathodic protection even though these coatings contain significantly lower concentrations of Mg particles and are much thinner in comparison to Mg-rich primers described previously in the literature (which have Mg loadings of ca. 70 wt.% and coating thicknesses on the order of 70 μm).[21,23] The enhanced protection accessible at lower loadings is likely a result of improved

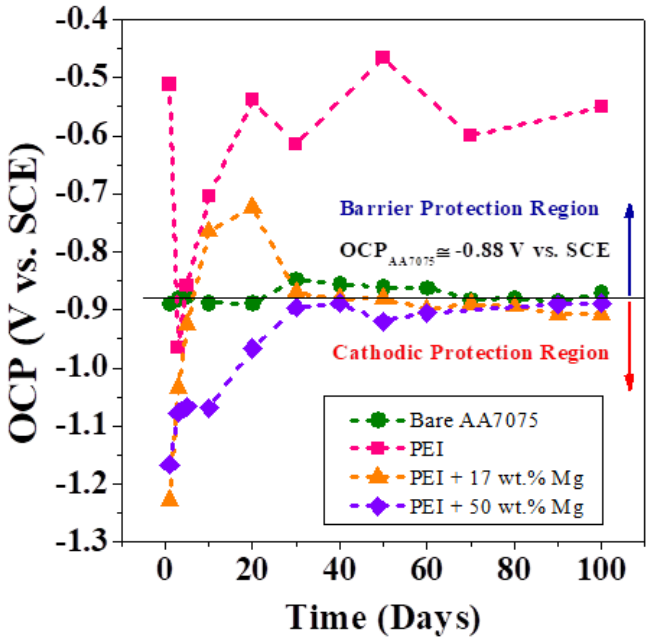

Figure 4.3. Evolution of the OCP of Mg/PEI nanocomposite coatings immersed in aerated aqueous solutions of 3.5 wt.% NaCl for 100 days at room temperature.

dispersion of Mg nanocrystals and the formation of a percolative network within the polymeric matrix, which allows for the effective utilization of the enmeshed Mg nanocrystals in sacrificial cathodic processes.[36]

In order to further examine the underlying mechanisms of corrosion protection, EIS measurements have been performed for the Mg/PEI nanocomposite coatings immersed in a 3.5 wt.% aqueous solution of NaCl for 100 days. Bode and Nyquist representations of the EIS data are plotted in **Figure 4.4** for the 17 and 50 wt.% Mg/PEI nanocomposite films. **Figure 4.4A** shows that the 17 wt.% Mg/PEI coating exhibits a $|Z|_{0.01\ Hz}$ value greater than $2\times10^7\ \Omega\cdot cm^2$ for the first day of immersion, which is almost four orders of magnitude higher than the corresponding value measured for the bare AA7075 substrate. Indeed, the higher impedance reflects the barrier properties of the PEI matrix even though Figure 4.3 indicates that cathodic protection is immediately activated upon salt water immersion. After 3 days of immersion, the impedance is increased to ca. $6\times10^7\ \Omega\cdot cm^2$ and remains relatively constant up to 10 days. The increased impedance can be ascribed to the formation of Mg corrosion products as a result of the sacrificial corrosion of the Mg nanocrystals embedded within the PEI matrix. The corrosion products initially provide some barrier protection to the substrate. After 20 days of immersion, the $|Z|_{0.01\ Hz}$ values start to rapidly decrease. This trend is explicable based on the re-activation process noted above, wherein aggressive ions degrade and leach the corrosion products (for example, by formation and subsequent dissolution of $MgCl_2$ by the attack of Cl^- ions on the hydrated carbonate corrosion products that are initially stabilized) and promote further corrosion processes at the

coating interface. The phase angle diagram for the 17 wt.% Mg/PEI nanocomposite coating is characterized by three distinctive time constants over the immersion period. Based on previous assignments by Battocchi *et al*.,[23] the time constant at high frequency can be ascribed to properties of the continuous PEI matrix, whereas the intermediate frequency time constant likely corresponds to the dissolution of the Mg particles. The origin of the time constant in the low frequency region is unclear but is likely the mass transport of H^+ and OH^- ions as a result of cathodic reactions operational at the AA7075 substrate.

A similar evolution of the EIS response has been observed for the 50 wt.% Mg/PEI nanocomposite coating albeit with some notable differences. Although the $|Z|_{0.01\ Hz}$ value for this coating upon initial immersion time is similar to the value for 17 wt.% Mg/PEI coating (ca. $1\times10^7\ \Omega\cdot cm^2$), it decreases dramatically after one day of immersion to ca. $1\times10^6\ \Omega\cdot cm^2$, which is about one order of magnitude lower as compared to the corresponding value for the 17 wt.% Mg/PEI nanocomposite after 3 days of immersion. The rapid diminution of the $|Z|_{0.01\ Hz}$ value is directly ascribable to the considerably higher loading of Mg nanocrystals in the 50 wt.% Mg/PEI coating, which results in immediate galvanic corrosion of the embedded Mg as a result of electrochemical coupling with the Al substrate. The $|Z|_{0.01\ Hz}$ value then remains constant through 20 days of immersion suggesting the formation of a relatively greater amount of corrosion product for the 50 wt.% Mg/PEI nanocomposite coatings, which thereby affords a greater extent of passivation. Similar to observations for the 17 wt.% Mg/PEI nanocomposite coating, the impedance steadily decreases after 50 days. Based on the

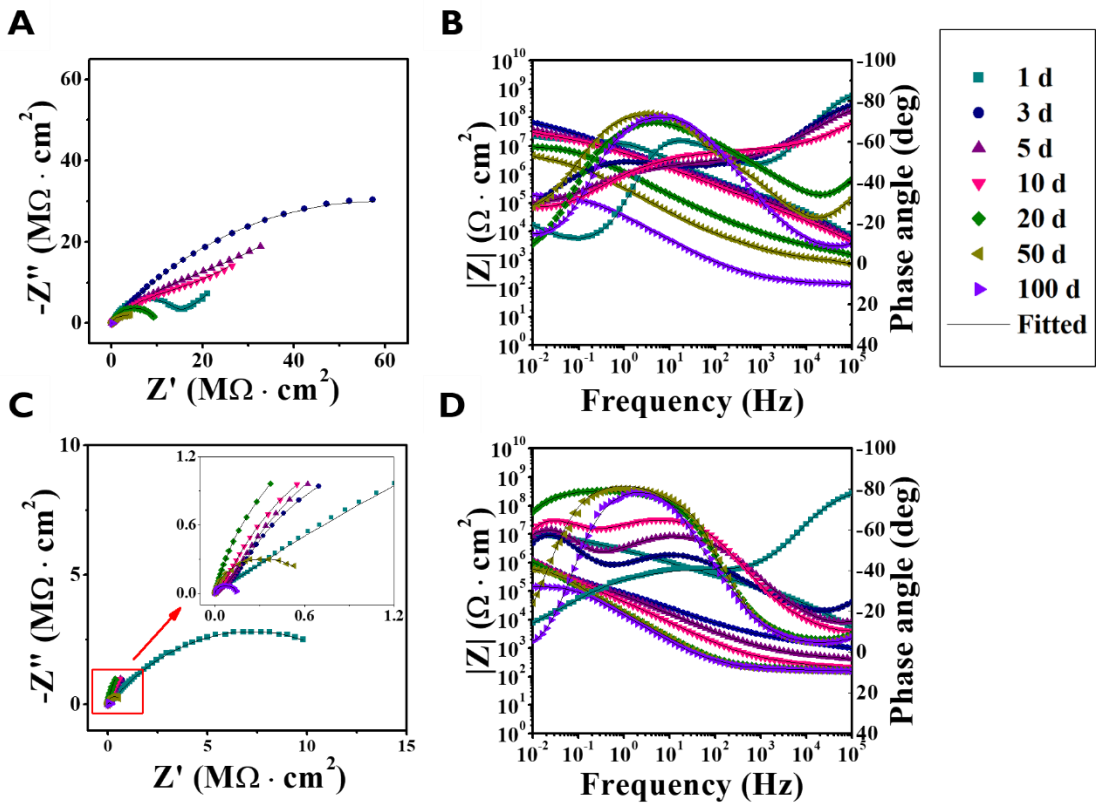

Figure 4.4. Nyquist (left) and Bode (right) plot representations of EIS data for A,B) 17 wt.% Mg/PEI and C,D) 50 wt.% Mg/PEI nanocomposite coatings immersed in 3.5 wt.% NaCl solution for 100 days.

evolution of the OCP noted in Figure 3 and the high concentration of embedded Mg, the decrease in impedance can be related to re-activation of the Mg particles, either as a result of galvanic corrosion or anodic dissolution. Some Al dissolution is also possible in this time period.

Battocchi *et al*. have proposed the equivalent circuit model sketched in **Figure 4.5A** to describe the EIS response of Mg-rich primers.[23] In this equivalent circuit, R_s represents the electrolyte resistance; Q_c and R_c correspond to the capacitance and

resistance of the coating system, respectively; C_{dl} and R_{ct} represent the double layer capacitance and the charge transfer resistance derived from the sacrificial corrosion process, respectively; and Q_{lf} and R_{lf} correspond to the capacitance and the resistance associated with the time constant at lower frequencies noted above.

The evolution of the different circuit elements upon immersion in a 3.5 wt.% aqueous solution of NaCl for 100 days is shown in **Figures 4.5B—D**. The R_c components derived for both coatings are decreased over time owing to penetration of the electrolyte into the coating and dissolution of Mg nanoplatelets and corrosion products, which increases the porosity of the coating. In other words, the ion transport resistance of the coatings is gradually diminished[44] as a result of the sacrificial cathodic corrosion processes and the ensuing loss of filler particles from the nanocomposite matrix. The R_c values derived for the 50 wt.% Mg/PEI coatings (ca. 8×10^1—5×10^4 $\Omega\cdot cm^2$) are smaller than values for 17 wt.% Mg/PEI (ca. 2×10^2—2×10^5 $\Omega\cdot cm^2$) owing to the higher Mg concentration in the former, which engenders greater initial porosity. In addition, the higher sacrificial protection action observed for the former leaves behind a higher density of pores as Mg is dissolved, resulting in a relatively greater decrease in the resistance of the coating system. The R_{ct} value of the 17 wt.% Mg/PEI coating somewhat increases after the third day of immersion and then remains almost constant for up 10 days owing to the formation of passivating Mg corrosion products. The R_{ct} values are then sharply decreased after 20 days of immersion as a result of aluminum dissolution and re-activation of the Mg particles. The observed evolution of the R_{ct} is furthermore consistent with the evolution of the double layer capacitance, which shows a

decrease during the first 3 days of immersion, then an almost constant value, and subsequently, a rapid increase after 20 days of immersion owing to the an increase of the electrochemically active surface area as a result of the degradation of corrosion products, further reactivation of Mg nanocrystals, and corrosion processes.

The R_{ct} and Q_{dl} values derived from equivalent circuit modeling of the EIS response measured for the 50 wt.% Mg/PEI nanocomposite coating show a similar trend as compared to the 17 wt.% Mg/PEI nanocomposite coating. However, these values are stable for a longer period of time owing to the higher amounts of corrosion products

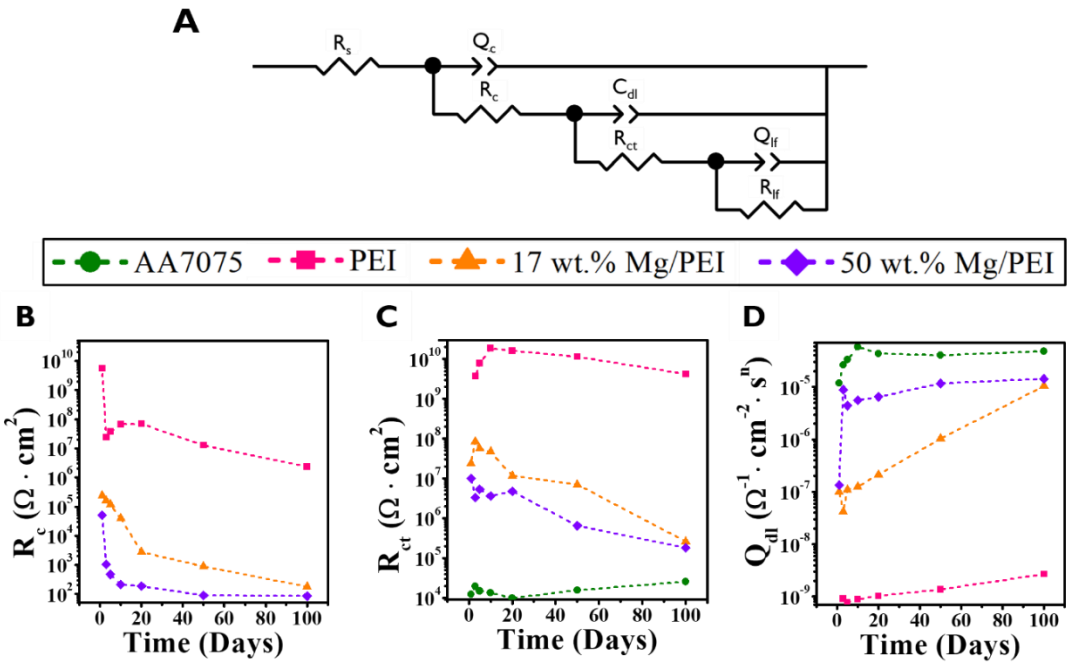

Figure 4.5. A) Equivalent circuit used to model the EIS response of Mg/PEI nanocomposite coatings. Evolution of the equivalent circuit elements derived from fitting of EIS spectra of Mg/PEI nanocomposite coatings upon immersion in a 3.5 wt.% aqueous solution of NaCl over a period of 100 days: B) coating resistance (Rc); C) charge transfer resistance (Rct); D) double layer capacitance (Qdl).

generated as a result of sacrificial cathodic processes within the coating, which results in relatively prolonged corrosion protection and delays the eventual re-activation and initiation of Al dissolution.

Cross-sectional SEM and EDS analysis of as-prepared coated samples (without exposure to saline environments) as well as samples immersed in a 3.5 wt.% aqueous solution of NaCl for 100 days (as part of the EIS measurements described above) are shown in **Figure 4.6** for both the 17 (Figs. 4.6A-H) and 50 wt.% Mg/PEI (I-P) nanocomposite coatings on AA7075. EDS mapping of carbon, aluminum, and magnesium are shown alongside cross-sectional SEM images to visualize the spatial localization of the different components before and after brine exposure. For the unexposed 17 wt.% Mg/PEI coating (**Figs. 4.6A—D**), the Mg signal is clearly localized within a well-defined region between the PEI layer and the AA7075 substrate (**Fig. 4.6D**). The EDS maps suggest the homogeneous dispersion of Mg nanocrystals within the matrix. Following exposure to salt water for 100 days (**Figs. 4.6E—H**), substantial Mg is detected at the coating surface, which corroborates the activation, sacrificial corrosion, and mobility of Mg-species and suggests the formation of corrosion products within the coating and at the coating surface. The 50 wt.% Mg/PEI coating showed signs of delamination upon 100 days of exposure (**Fig. 4.6M**). The more rapid activation and oxidation of Mg nanocrystals at high loadings likely results in a greater extent of $Mg(OH)_2$ formation and hydrogen evolution as per Eq. 4.1. The use of surface modifiers, either surface functionalization of the Mg nanocrystals or encapsulation of nanocrystals within porous frameworks, can potentially facilitate controlled kinetics of Mg activation,

thereby mitigating hydrogen evolution and allowing for homogeneous precipitation of corrosion products. It is noteworthy that previous measurements of corrosion inhibition of AA 7075 substrates used dilute Harrison's solution (0.05 wt.%. NaCl and 0.35 wt.% $(NH_4)_2SO_4$) for 1.6 h.[23] The nanocomposite coatings herein have been challenged with

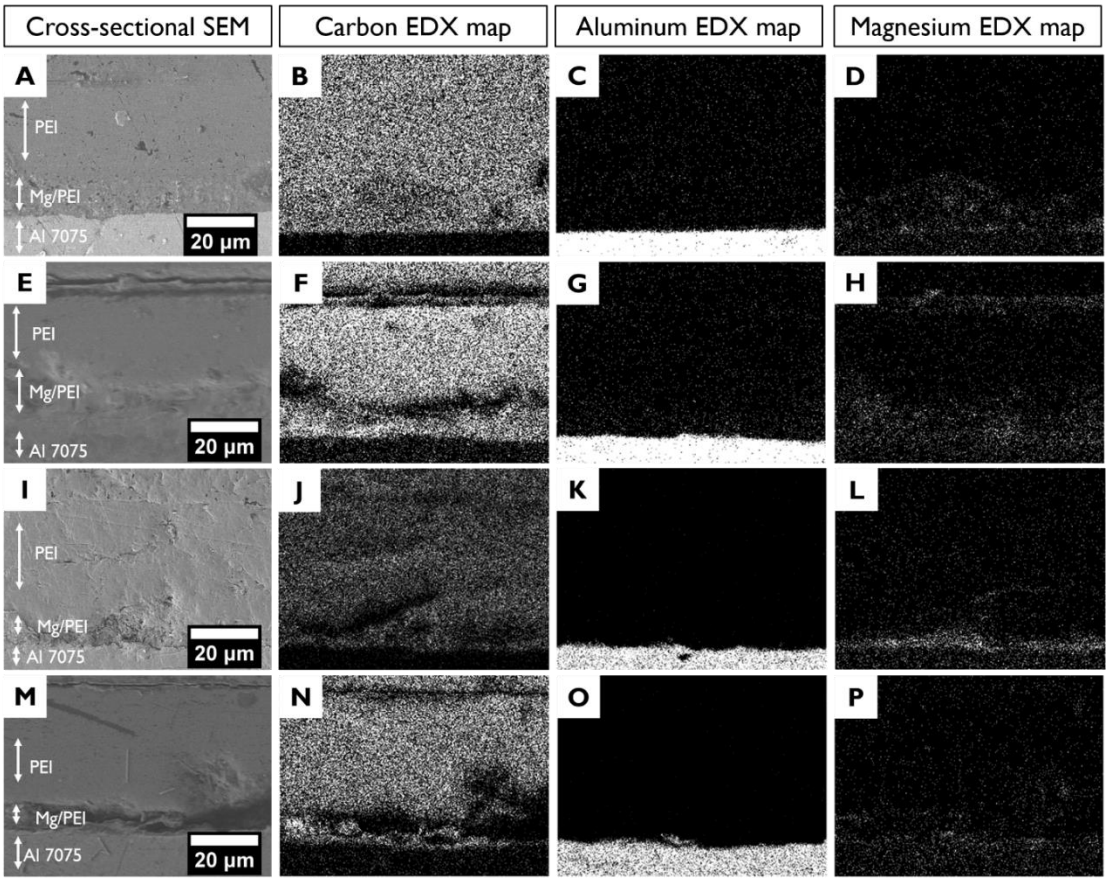

Figure 4.6. Cross-sectional SEM and EDS analysis of A—D) an unexposed 17 wt.% Mg/PEI nanocomposite coating; E-H) a 17 wt.% Mg/PEI nanocomposite coating exposed to a 3.5 wt.% aqueous solution of NaCl for 100 days; I—L) an unexposed 50 wt.% Mg/PEI nanocomposite coating; M—P) a 50 wt.% Mg/PEI nanocomposite coating exposed to a 3.5 wt.% aqueous solution of NaCl for 100 days. In each series of panels, the left column shows the cross-sectional SEM image, whereas the second, third, and fourth columns correspond to EDS maps acquired for carbon (B, F, J, N); Al (C, J, K, O); and Mg (D, H, L, P).

much higher concentrations of salt solution (3.5 wt.% NaCl), and demonstrate considerably prolonged cathodic protection. The efficacious cathodic protection afforded by the Mg/PEI nanocomposite coatings and rapid mobilization of embedded Mg under aggressive environments suggests that the Mg/PEI nanocomposites can serve as useful modular elements of a corrosion control system.

4.4. Conclusions

In summary, Mg/PEI nanocomposite coatings prepared by incorporation of Mg nanocrystals within a polyamic acid matrix followed by imidization upon application show good adhesion to AA7075 substrates and are observed to endow two primary modes of corrosion inhibition. First, cathodic protection is afforded at lower particle loadings and reduced coating thicknesses as compared to conventional Mg-rich primers that utilize substantially larger Mg particles. The utilization of Mg nanocrystals within a polymer composite allows for the highly negative reduction potential of the Mg^{2+}/Mg redox couple, noted above as a key materials descriptor, to be effectively utilized while circumventing the inherent challenges of using continuous metallic Mg films. OCP testing of Mg/PEI coatings indicate that nanocomposite coatings with 17 and 50 wt.% loadings of Mg nanocrystals offer 5 and 20 days of sustained cathodic protection, respectively. Notably, these metrics have been obtained in accelerated testing environments that are represent amongst the most severe conditions to which protective coatings of high-strength Al alloys have been subjected. EIS, OCP, and salt-spray exposure tests suggest that the Mg/PEI nanocomposite coatings endow immediate cathodic protection to AA7075 substrates upon salt water immersion; the higher activity

of Mg and the formation of a permeable passivation layer facilitates much more rapid mobilization of the active filler as compared to Zn inclusions. Secondly, corrosion products formed by reaction of Mg nanocrystalline inclusions along with the cross-linked PEI network provide outstanding barrier protection, delaying attack of the underlying base metal substrate by corrosive species as demonstrated by the high impedance observed in EIS measurements.

Analogous modes of corrosion protection are anticipated for most aluminum alloys. Considering, high-strength aluminum alloys of the 2000 and 7000 series, which are most susceptible to corrosion, the 2000 series has Cu as the primary alloying element, whereas in the 7000 series, the alloying element is Zn.[7] Both alloying elements are less active than Mg, and thus Mg is expected to provide sacrificial cathodic protection to both types of alloys. Notably Bierwagen's group has demonstrated the utility of Mg nanocomposite coatings for 2000 series Al alloys.[21,22,33,39,45] While the mechanisms of protection elucidated here are expected to be generalizable to most Al alloy systems, the target metrics for corrosion performance depend on the specific alloy under consideration and the exposure environment. Higher concentrations of Mg nanocrystals facilitate more extensive and prolonged corrosion protection but can be susceptible to blistering or partial delamination as a result of hydrogen evolution under aggressive conditions resulting from the rapid activation of Mg nanocrystals. This represents the primary mechanisms of failure for these coatings as has similarly been observed by Bierwagen.[22,33] The Mg/PEI nanocomposites represent a valuable addition to the scarce options available for protection of lightweight Al alloys. Future work will

focus on delaying the kinetics of Mg activation through surface modification of the nanocrystals as well as the incorporation of the Mg/PEI coating modules within corrosion control systems additionally incorporating anodic passivation and a non-wettable top coat.[46] Under conditions that induce stress corrosion cracking, mechanical properties of the specific alloy, governed in substantial measure by the alloying elements and their influence on the microstructure, are expected to play a significant role. Examining the utility and generalizability of Mg nanocomposite coatings under conditions that promote stress corrosion cracking will furthermore be the focus of future work.

4.5. Experimental Section

4.5.1. Synthesis of Mg nanocrystals

Mg nanocrystals were prepared through reduction of MeMgCl by lithium naphthalide in tetrahydrofuran (THF) as described in our previous work.[34] The nanocrystals were collected in powder form by first decanting the majority of the solution after the powder was allowed to settle and then sequentially washing three times with THF and centrifuging solvent to separate . Caution should be taken in this step, as any remaining reagent will react in air producing methane. Mg powders were then stored under an argon ambient in an Ar-filled glove box. Phase purity of the prepared materials was determined by powder X-ray diffraction (XRD) using a Bruker D8-Focus diffractometer (Cu Kα: $\lambda = 1.5418$Å; operated at 40 kV and 25 mA) in Bragg—Brentano geometry.). Rietveld refinement of the collected diffraction data was performed using the EXPGUI user interface of GSAS I.[47] All atoms were fixed to special positions as a

result of the hexagonal structure. Profile terms, lattice parameters, and thermal parameters were refined from the laboratory diffraction data. The morphology of the Mg nanocrystals was evaluated by SEM using a JEOL JSM-7500F instrument operating at a probe current of 10 μA, accelerating voltage of 10 kV, and an emission current of 5 μA. The particle size distribution was calculated using the ImageJ software by measuring 350 individual particles using the Measure and Label plugin.

4.5.2. Synthesis of polyamic acid and Mg/polyamic acid dispersions

Polyamic acid was prepared through polymerization of 3,3',4,4'-biphenyltetracarboxylic dianhydride (17.2194 g) with 2,2'-(ethylenedioxy) *bis*(ethylamine) (5.9075 g) and *m*-phenylenediamine (1.8650 g) (all from Sigma Aldrich) in *N*-methyl-2-pyrrolidone (NMP, Honeywell Research Chemicals), as described in previous work.[36],[37] Given the limited solubility of 3,3',4,4'-biphenyltetracarboxylic dianhydride at low temperatures, the two diamines were first heated in NMP (100 mL) to 70°C in a round-bottom flask under a stream of N_2 gas and the dianhydride was then titrated over the course of ca. 5 min under vigorous stirring. The clear, yellow polymer was stirred for 8 h overnight under a N_2 ambient. The Mg nanocrystals were incorporated through ultrasonication in the as-prepared polyamic acid solution in NMP. The desired amount of Mg nanocrystals sought to be incorporated within the coatings was ultrasonicated in NMP for 30 min and subsequently added to 5 mL of the polyamic acid dispersion in NMP. The Mg/polyamic acid dispersions were then immediately coated onto AA7075 substrates after preparation.

4.5.3. Substrates and application of coatings to AA7075 surfaces

Clad AA7075-T6 substrates (Aerotech Alloys, with thickness of 0.02 in.) containing zinc, magnesium, copper, silicon, manganese, iron, titanium, and chromium in addition to aluminum were used as substrates. The surfaces of the AA7075 substrates were lightly abraded with P150 and P400 grit sand paper and washed with hexanes and acetone. Substrates were heated to a temperature of 150 °C on a hot plate during the deposition of magnesium/polyamic acid coatings to aid in evaporation of the solvent. The Mg/polyamic acid dispersions were spray coated onto the AA7075 substrates using a TCP Global spray gun equipped with a 1.00 mm diameter nozzle at a pressure of 45 psi coupled with an external air compressor. The deposited films were cured at 250°C for 5 min resulting in imidization of polyamic acid to form PEI. The coating thickness was monitored using a Byko-test 8500 thickness gauge. For Mg nanocomposite coatings, a top coat of 20 μm of polyamic acid was deposited (and similarly imidized) following the application of the magnesium/polyamic acid layer to mitigate uncontrolled activation and dissolution of Mg nanocrystals. FTIR spectra were recorded using a Bruker Vertex-70 FTIR instrument using a Pike MIRacle single reflection horizontal attenuated total reflectance (ATR) accessory.

4.5.4. Adhesion testing

Three American Society for Testing of Materials (ASTM) standardized test procedures were used to evaluate the adhesion of the nanocomposite coatings to the AA7075 substrates. The pull-off strength was tested using a BYK testing kit following ASTM D4541-09. A 14 mm dolly was glued to the surface of each coating using a two-

part epoxy that was allowed to cure for 24 h. The dolly was removed at a pull off rate of 0.7 MPa/s using a DeFelsko PosiTest AT-A automatic adhesion tester. Scape adhesion was evaluated using a BYK balance beam tester following ASTM D2197-13. Cross-cut testing was performed following ASTM D3359 using a BYK crosshatch paint adhesion testing kit with a 6-edge cross-cutter. Blades were spaced 1 mm apart creating a grid of cuts. The provided adhesive tape was applied and subsequently removed. Coatings were classified with ratings ranging from 0B to 5B. A rating of 5B corresponds to no discernible damage outside of the clean blade cuts, whereas 0B corresponds to significant removal of the coating by the tape with greater than 65 % of the coated area affected by tape removal. A rating of 3B, 4B, and 5B correspond to 15-35 %, 5-15 %, and up to 5 % damage of the coated area after tape removal respectively. More qualitatively, 3B coatings are expected to show damage along the edges of cuts, whereas the 4B coating is expected to only show damage at the cross-section points. All ASTM tests were performed in triplicate for each coating formulation.

4.5.5. Salt Spray Exposure

Samples were tested under salt spray exposure following ASTM B117 using a Q-fog salt spray chamber. The uncoated back face and edges of samples were covered using adhesive tape to prevent preferential corrosion during exposure. A 5 cm × 5 cm cross cut was made on the front face of the coating using a diamond-tipped scribe to define the exposed area. The salt spray chamber was kept at a pressure of 15 psi and a temperature of 35°C. The coatings were subjected to salt spray generated from a 5 wt.% aqueous solution of NaCl. Samples were visually monitored every 24 h for 12 days to

evaluate the progression of damage. The salt spray distribution was monitored using graduated cylinders placed throughout the chamber; consistent volumes of 20—50 mL solution were collected each day.

4.5.6. EIS

The EIS response of AA7075 substrates with Mg nanocomposite coatings was monitored over the course of 100 days continuous immersion in a 3.5 wt.% aqueous solution of NaCl using a Gamry potentiostat/galvanostat/ZRA Reference 1000TM instrument. EIS measurements were performed using a three-electrode cell with the coated AA7075 sample serving as the working electrode, a Pt/Nb mesh as the counter electrode, and a saturated calomel electrode (SCE) as the reference. An O-ring joint clamped to the AA7075 sample surface served to define the electrochemical cell, exposing a 4.67 cm^2 area of the coated substrate to the solution. All experiments were performed within a Faraday cage in order to minimize electromagnetic interference. The OCP of each sample was monitored for 10 min prior to beginning EIS measurements. The EIS response was measured in the frequency range of 100 kHz—10 mHz at 10 points per decade with a sinusoidal perturbation signal of ±10 mV at the OCP of the coating. Each sample was measured in duplicate. The EIS response is interpreted through modeling of equivalent circuits using the EC-lab V10.40 fitting software. Electrochemical data for the bare AA7075 and PEI substrates were presented in our recent work.[42] The OCP data for bare AA7075 and PEI are presented here in order to facilitate comparison with the Mg nanocomposite coatings.

4.5.7. Cross-Sectional SEM

The interface between the nanocomposite coating and the AA7075 substrate immersed in a 3.5 wt.% aqueous solution of NaCl for the EIS studies as well as separately prepared unexposed samples were evaluated using by cross-sectional SEM. The coated substrates were immersed in a two-part epoxy (EpoxiCure 2, Buehler) and diced using a Buehler Isomet 5000 saw to expose the nanocomposite coating/AA7075 interface. The samples were sanded using a Struers LaboPol-5 sample polishing table with 600, 1000, and 1200 grit paper and polished with 9, 6, and 1 μm diamond paste. Higher magnification images of Mg/PEI and PEI layer interfaces were acquired by cryofracturing the samples. The coated substrates were immersed in liquid nitrogen for ca. 5 min and then fractured to expose the Mg/PEI and PEI layer interfaces. All samples were sputtered with 3 nm Pt to prevent charging and subsequently imaged by SEM using a JEOL JSM-7500F instrument operating at an accelerating voltage of 5 kV, an emission current of 10 μA, and a probe current of 10 μA. EDS maps were obtained using an Oxford Instruments energy dispersive X-ray spectroscopy (EDS) detector at an accelerating voltage of 10 kV.

4.5.8. TEM

The morphology of Mg nanocrystals was evaluated using transmission electron microscopy (TEM) using a JEOL-2010 TEM operating with an emission current of 100 mA and an accelerating voltage of 200 kV. Grids were prepared by drop casting solutions of Mg particles in THF onto 400 mesh Cu grids.

4.6. References

[1] O. Gharbi, S. Thomas, C. Smith, N. Birbilis, *npj Mater. Degrad.* **2018**, *2*, 12.

[2] M. W. Kendig, R. G. Buchheit, *Corrosion* **2003**, *59*, 379.

[3] C. Pellerin, S. M. Booker, *Environ. Health Perspect.* **2000**, *108*, 403.

[4] A. E. Hughes, I. S. Cole, T. H. Muster, R. J. Varley, *NPG Asia Mater.* **2010**, *2*, 143.

[5] R. V. Dennis, V. Patil, J. L. Andrews, J. P. Aldinger, G. D. Yadav, S. Banerjee, *Mater. Res. Express* **2015**, *2*, 032001.

[6] G. D. Davis, W. C. Moshier, J. S. Ahearn, H. F. Hough, G. O. Cote, *J. Vac. Sci. Technol. A Vacuum, Surfaces, Film.* **1987**, *5*, 1152.

[7] T. Dursun, C. Soutis, *Mater. Des.* **2014**, *56*, 862.

[8] D. A. Necşulescu, *UPB Sci. Bull. Ser. B Chem. Mater. Sci.* **2011**, *73*, 223.

[9] J. E. Edwards, *Defense Management: DOD Needs to Monitor and Assess Corrective Actions Resulting from Its Corrosion Study of the F-35 Joint Strike Fighter*, **2010**.

[10] D. Sediako, D. Weiss, A. Nabawy, in *Magnes. Technol. 2017* (Eds.: K.N. Solanki, D. Orlov, A. Singh, N.R. Neelameggham), Springer, Cham, **2017**, pp. 639–644.

[11] R. S. Long, E. Boettcher, D. Crawford, *JOM* **2017**, *69*, 2635.

[12] J. M. Luk, H. C. Kim, R. De Kleine, T. J. Wallington, H. L. MacLean, *Environ. Sci. Technol.* **2017**, *51*, 8215.

[13] H. C. Kim, T. J. Wallington, *Environ. Sci. Technol.* **2013**, *47*, 6089.

[14] A. Mayyas, A. Qattawi, M. Omar, D. Shan, *Renew. Sustain. Energy Rev.* **2012**,

16, 1845.

[15] L. A. W. Ellingsen, C. R. Hung, G. Majeau-Bettez, B. Singh, Z. Chen, M. S. Whittingham, A. H. Strømman, *Nat. Nanotechnol.* **2016**, *11*, 1039.

[16] V. K. K. Upadhyayula, D. E. Meyer, V. Gadhamshetty, N. Koratkar, *ACS Sustain. Chem. Eng.* **2017**, *5*, 2656.

[17] M. Y. Rekha, A. Kamboj, C. Srivastava, *Thin Solid Films* **2018**, *653*, 82.

[18] M. Y. Rekha, M. K. Punith Kumar, C. Srivastava, *RSC Adv.* **2016**, *6*, 62083.

[19] S. S. Pathak, S. K. Mendon, M. D. Blanton, J. W. Rawlins, S. S. Pathak, S. K. Mendon, M. D. Blanton, J. W. Rawlins, *Metals (Basel).* **2012**, *2*, 353.

[20] R. Davidson, A. Verma, D. Santos, F. Hao, C. Fincher, S. Xiang, J. Van Buskirk, K. Xie, M. Pharr, P. P. Mukherjee, S. Banerjee, *ACS Energy Lett.* **2019**, *4*, 375.

[21] M. E. Nanna, G. P. Bierwagen-North, P. A. Philadelphia, *JCT Res.* **2004**, *1*, 69.

[22] G. Bierwagen, R. Brown, D. Battocchi, S. Hayes, *Prog. Org. Coatings* **2010**, *67*, 195.

[23] D. Battocchi, A. M. Simões, D. E. Tallman, G. P. Bierwagen, *Corros. Sci.* **2006**, *48*, 1292.

[24] G. Yu, D. Gu, D. Dai, M. Xia, C. Ma, Q. Shi, *J. Phys. D. Appl. Phys.* **2016**, *49*, 135501.

[25] A. Ambrosi, M. Pumera, *Chem. Soc. Rev.* **2016**, *45*, 2740.

[26] J. Lin, V. Upadhyay, X. Qi, D. Battocchi, G. P. Bierwagen, *Corrosion* **2016**, *72*, 377.

[27] R. Lindström, L. G. Johansson, G. E. Thompson, P. Skeldon, J. E. Svensson,

Corros. Sci. **2004**, *46*, 1141.

[28] S. S. Pathak, M. D. Blanton, S. K. Mendon, J. W. Rawlins, *Corros. Sci.* **2010**, *52*, 1453.

[29] R. Lindström, J.-E. Svensson, L.-G. Johansson, *J. Electrochem. Soc.* **2002**, *149*, B103.

[30] R. L. Derosa, I. Szabo, G. P. Bierwagen, D. Battocchi, *Prog. Org. Coatings* **2015**, *78*, 455.

[31] R. G. Song, W. Dietzel, B. J. Zhang, W. J. Liu, M. K. Tseng, A. Atrens, *Acta Mater.* **2004**, *52*, 4727.

[32] S. S. Pathak, M. D. Blanton, S. K. Mendon, J. W. Rawlins, *Corros. Sci.* **2010**, *52*, 3782.

[33] B. J. E. Merten, D. Battocchi, G. P. Bierwagen, *Prog. Org. Coatings* **2015**, *78*, 446.

[34] L. Viyannalage, V. Lee, R. V. Dennis, D. Kapoor, C. D. Haines, S. Banerjee, *Chem. Commun.* **2012**, *48*, 5169.

[35] R. M. Peltzer, O. Eisenstein, A. Nova, M. Cascella, *J. Phys. Chem. B* **2017**, *121*, 4226.

[36] R. V. Dennis, L. T. Viyannalage, J. P. Aldinger, T. K. Rout, S. Banerjee, *Ind. Eng. Chem. Res.* **2014**, *53*, 18873.

[37] R. V Dennis, L. T. Viyannalage, A. V. Gaikwad, T. K. Rout, S. Banerjee, *Am. Ceram. Soc. Bull.* **2013**, *92*, 18.

[38] C. A. Pryde, *J. Polym. Sci. Part A Polym. Chem.* **1989**, *27*, 711.

[39] G. Bierwagen, D. Battocchi, A. Simões, A. Stamness, D. Tallman, *Prog. Org. Coatings* **2007**, *59*, 172.

[40] Y. Cubides, H. Castaneda, *Corros. Sci.* **2016**, *109*, 145.

[41] Y. Cubides, S. S. Su, H. Castaneda, *Corrosion* **2016**, *72*, 1397.

[42] R. D. Davidson, Y. Cubides, C. Fincher, P. Stein, C. McLain, B.-X. Xu, M. Pharr, H. Castaneda, S. Banerjee, *ACS Appl. Nano Mater.* **2019**, *2*, 3100.

[43] C. M. Abreu, M. Izquierdo, M. Keddam, X. R. Nóvoa, H. Takenouti, *Electrochim. Acta* **1996**, *41*, 2405.

[44] C.-F. Chen, P. Barai, P. P. Mukherjee, *J. Electrochem. Soc.* **2014**, *161*, A2138.

[45] A. Simões, D. Battocchi, D. Tallman, G. Bierwagen, *Prog. Org. Coatings* **2008**, *63*, 260.

[46] T. E. O'Loughlin, R. V Dennis, N. A. Fleer, T. E. G. Alivio, S. Ruus, J. Wood, S. Gupta, S. Banerjee, *Energy and Fuels* **2017**, *31*, 9337.

[47] B. H. Toby, *J. Appl. Cryst* **2001**, *34*.

5. TORTUOSITY BUT NOT PERCOLATION: DESIGN OF EXFOLIATED GRAPHITE NANOCOMPOSITE COATINGS FOR THE EXTENDED CORROSION PROTECTION OF ALUMINUM ALLOYS*

5.1. Overview

Increased adoption of engineered aluminum alloys in vehicular components is imperative for automotive lightweighting but such alloys are oftentimes prone to degradation upon exposure to corrosive environments. The design of coatings to inhibit corrosion of aluminum alloys has emerged as a critical need but given the electropositive nature of the substrates, only a sparse few options are available. In this article, we explore the corrosion resistance afforded to aluminum alloy AA7075 substrates by unfunctionalized exfoliated graphite nanocomposite coatings as a function of the exfoliated graphite loading. Detailed mechanistic understanding is developed through monitoring progression of the open circuit potential and electrochemical impedance response of the substrates over 100 days of immersion in a saline environment along with post-mortem cross-sectional scanning electron microscopy and energy dispersive X-ray spectroscopy analysis of sectioned interfaces. Electrochemical studies along with nanoindendation, AC conductivity measurements, and salt spray exposure studies allow for a direct evaluation of the role of exfoliated graphite in inhibiting/accelerating corrosion. Indeed, we identify two distinctive regimes: excellent long-term corrosion resistance is obtained at low exfoliated graphite loadings within a polyetherimide matrix as a result of a substantial enhancement in the tortuosity of ion transport pathways for

*Reprinted (adapted) with permission from ([R. D. Davidson, Y. Cubides, C. Fincher, P. Stein, C. McLain, B. X. Xu, M. Pharr, H. Castaneda, S. Banerjee, *ACS Appl. Nano Mater.* **2019**, *2*, 3100.).

diffusion of corrosive species; however, further inclusion of exfoliated graphite results in formation of a percolative network that gives rise to accelerated galvanic corrosion of the underlying substrate. Finite element modeling shows that a broad distribution of particle sizes of graphene inclusions is particularly favorable for enhancing tortuosity. Cross-sectional scanning electron microscopy analysis of a 5 wt.% exfoliated graphite nanocomposite coating after salt water exposure for 100 days indicates complete retention of coating integrity and an uncompromised interface with the metal surface, which is in stark comparison to the bare polyetherimide matrix, which is plagued by extensive delamination and shows significant interfacial accumulation of corrosion products. Higher graphene loadings beyond the percolation threshold show evidence for severe galvanic corrosion with corrosion products distributed along the thickness of the coating. The results provide evidence that exfoliated graphite can offer performance that is equivalent to that of pristine and functionalized graphene in terms of inhibiting corrosion and suggest an approach for enhancing barrier protection through increased resistance to pore transport enabled by the excellent dispersion of exfoliated graphite sheets within polymeric matrices.

5.2. Introduction

The strong impetus for reducing fuel consumption along with increasingly stringent global emissions standards have spurred a worldwide push towards lightweighting of vehicles.[1–5] Lightweighting of vehicular components is most often targeted through (a) the replacement of steel by magnesium and aluminum alloys, engineered polymers, or carbon fiber composites or (b) through the design of porous

monolithic forms (increasingly accessible from additive manufacturing methods) that provide load-bearing capabilities and mechanical resilience comparable to fully dense fabricated parts but with much greater economy of material consumption.[6,7] In contrast to vehicular transportation, the use of light-weight metal alloys is much more prevalent in other sectors where they are designed to meet demanding structural specifications. For instance, high-strength aluminum alloys have served for over 80 years as the primary structural material used in aircraft construction.[8] While aluminum metal itself is prone to corrosion at low and high pH values, the addition of other metals, as required to stabilize high-strength alloys further exacerbates this problem by giving rise to a complex microstructure with a diverse range of intermetallic inclusions and precipitates that render the resulting alloy vulnerable to local corrosion. Indeed, corrosion cells are readily established across the surface of a heterogeneous alloy upon exposure to an electrolyte environment. Failure of vehicular structural components because of corrosion can give rise to serious passenger safety issues. The need to replace failing parts furthermore decreases service life and thereby increases the cradle-to-grave environmental impact of engineered alloys.[2,3] Chromium-based conversion coatings provide excellent corrosion protection of aluminum and have been the mainstay for corrosion protection in the aerospace industry; however, it is well established that hexavalent chromium effluents released at various points in the production, use, and as disposal of such coatings are highly toxic as well as carcinogenic.[9] Indeed, concerns regarding the ecological toxicity and human health impact of hexavalent chrome have led to strict regulation of its use in commercial products.[10,11] With increasing use of

aluminum alloys for vehicular applications, the development of sustainable chrome-free coatings has emerged as an urgent imperative. The -1.66 V value of the Al^{3+}/Al redox couple (*versus* SHE) implies that zinc and trivalent chrome commonly used to protect steel substrates are ineffective at providing sacrificial cathodic protection to aluminum alloys. Magnesium-based nanocomposite coatings have instead been developed to provide sacrificial protection to aluminum alloy substrates and are effective under certain environments,[12–14] but are plagued by issues such as the typically high reactivity of Mg particles, the complexity of preparing surface-passivated Mg pigments that can be safely handled, and the need for relatively thick coatings spanning scores of microns. In this article, we demonstrate an alternative approach wherein unfunctionalized exfoliated graphite (UFG) nanocomposite coatings with sub-30 μm thickness dispersed within a polyetherimide matrix show excellent corrosion inhibition of AA7075 substrates upon prolonged exposure to saline environments. A detailed mechanistic elucidation of the origins of corrosion protection afforded by such coatings has been performed using open circuit potential measurements, electrochemical impedance spectroscopy, salt spray exposure testing, and post-mortem analysis of interfacial layers between the coating and substrate. The measurements suggest the excellent ability of exfoliated graphite to enhance the resistance to transport of corrosive species through barrier protection and increased tortuosity, but emphasize the need to prevent galvanic corrosion, which can be activated when a percolative network of UFG is constituted within the polymeric matrix.

Graphene has received significant attention as a means of designing more sustainable coatings for corrosion inhibition. The efficacy and mechanism of corrosion

inhibition provided by graphene remains somewhat controversial; the debate derives in part from the diversity of materials delineated as graphene coatings (ranging from monolayer graphene grown by chemical vapor deposition and transferred onto metal substrates to exfoliated graphene, graphene oxide dispersed within polymeric matrices and cast as nanocomposite coatings, electroplated graphene/metal thin films, and tubular graphene derived by Nguyen and co-workers through thermal annealing)[15–17] and the differences in their mode of interfacial interaction with the surfaces sought to be protected.[11,18] Notably, given challenges inherent to the industrial production of pinhole-free monolayer graphene, much of the literature has focused on related materials that are much more readily accessible. Whilst the electronic structure and thus transport properties of such materials are strongly dependent on the layer thickness, the barrier protection derived from ion-impervious 2D sheets are anticipated to be largely preserved even for functionalized derivatives and thicker platelets that are not monolayer graphene.

Galvanic corrosion is a common mode of failure for graphene-based coatings. While the value of the electrode potential of graphene, or for that matter, graphite, varies as a function of the surface chemistry, the reported value of +0.150 V reported for pure graphite *versus* SCE[19] is substantially higher as compared to pure aluminum (-0.76 V *versus* SCE; corrosion potential of AA7075-T6 is -0.765 V *versus* SCE);[20] consequently, galvanic corrosion of the latter is possible upon direct coupling.[21] Zettl and co-workers have shown that the corrosion of Cu is initially diminished by the presence of graphene layers deposited directly onto the substrates owing to the impermeability of graphene.[22] However, in the presence of defects, the permeated

electrolyte establishes a corrosion cell between the graphene layer and the underlying copper substrate, bringing about accelerated galvanic corrosion of the underlying metal. Recent studies indicate that the accumulation of chloride ions at the edges of graphene facilitates metal oxidation and dissolution.[23] However, this picture is complicated by the strong interfacial hybridization of graphene to several transition metals, which results in substantial charge transfer and can give rise to potential barriers at the interface that can endow corrosion protection.[24–26] An alternative strand of research has focused on the corrosion protection endowed by graphene nanocomposites wherein few-layered chemically derived graphene flakes are embedded within a polymeric coating. As an impermeable 2D material,[27] inclusion of graphene adds substantial tortuosity to pathways for diffusion of species participating in the redox reactions of corrosion. Functionalization of graphene and/or incorporation of graphene in non-conductive polymers results in a considerable enhancement of the tortuosity of ion diffusion pathways and a substantially increased pore transport resistance while preventing direct electrochemical coupling with the substrate.[28–33]

The utilization of graphene as a filler within a polymeric system necessitates its effective dispersion within the host matrix, which can be achieved through surface functionalization, selection of a compatible polymer, achieving high loadings in solvents prior to mixing, or application of shear forces.[11,34] Graphene has a tendency to agglomerate and restack within composites when chemical compatibility is poor; the resulting larger agglomerations form phase segregated domains that are much less effective at increasing the tortuosity of pathways for ion transport.[35] Achieving higher

loadings of graphene in coatings is potentially beneficial for corrosion protection provided that electrochemical coupling resulting in galvanic corrosion can be avoided. Yang and co-workers have shown improved corrosion inhibition performance with higher loadings of graphene, which is attributed in part to the greater tendency of graphene to align at higher loadings, which extends the effective diffusion path that needs to be traversed by corrosive species from the surface to the substrate.[36] In addition to dispersibility at high loadings, several studies of graphene nanocomposite coatings have shown a dependence of functional performance on graphene flake size,[37] positioning within the polymer,[38,39] and the use of high-surface-area 'crumpled' graphene.[40]

With a view towards the stabilization of few-layered nanosheets that can enhance the tortuosity of ion diffusion pathways, we eschew harsh oxidation methods that can introduce vacancies and holes and instead utilize unfunctionalized exfoliated graphite (UFG) derived from non-oxidative methods as our filler material. While characterized by a wide size distribution of layer thicknesses, unfunctionalized exfoliated graphite represents perhaps the most facile route to an industrially viable graphitic coating for corrosion inhibition given its ease of preparation and retention of crystallinity. Specifically, solvent-assisted exfoliation of graphite allows for retention of the conjugated π-framework without creation of porosity, thereby enabling π—π interactions with the host polymeric matrix to be utilized to achieve effective dispersion at high loadings. In previous work, we have shown the remarkable corrosion resistance afforded by UFG/polyetherimide (PEI) composites for the protection of mild steel.[11,36] UFG is

incorporated *in situ* during condensation of the anhydride with two different amines to form polyamic acid; subsequently, polyamic acid is imidized to form PEI by thermal annealing after casting the films onto the metal substrates. The nanocomposite coatings show excellent corrosion performance based on Tafel analysis and extended exposure testing.[13,41] A life cycle assessment independently performed by Koratkar and co-workers has indicated that these coatings have a substantially lower cradle-to-grave environmental impact as compared to hot-dipped galvanized steel.[37]

In this article, we examine the corrosion protection afforded to aluminum alloy AA7075 substrates by UFG/PEI nanocomposites as a function of the exfoliated graphite loading. A detailed mechanistic study based on extensive electrochemical characterization allows for two distinct regimes to be distinguished: Excellent corrosion protection, which is competitive with or superior to graphene-based coatings, is obtained at relatively low loadings of UFG, but higher UFG loadings result in establishment of a percolative network that promotes galvanic corrosion. The electrochemical impedance response of the coatings immersed in salt water is monitored for 100 days yielding unprecedented mechanistic insight into the origins of the corrosion protection derived from the nanocomposite coatings. Consequently, these studies indicate that effective coatings must provide extensive tortuosity of diffusion paths for ionic species but ensure that an extended percolative network is not stabilized across extended length scales.

5.3. Experimental

5.3.1. Synthesis of UFG

UFG was prepared by exfoliation of graphite in *N*-methyl-2-pyrrolidone (NMP, Honeywell Research Chemicals).[36] In order to prepare different loadings of UFG dispersions, 5, 10, and 20 mg/mL of graphite (Bay carbon, SP-1 graphite powder) was ultrasonicated for 6 h and shaken every hour to avoid settling of larger unexfoliated graphite particles. The prepared UFG was examined by Raman spectroscopy and scanning electron microscopy (SEM). Size distribution statistics were obtained through combined atomic force microscopy (AFM) and SEM analysis. Given the large distribution of sizes obtained from the exfoliation process, the dimensions of larger particles on the order of tens of micrometers in width and 2.5 ± 2.1 μm thick and smaller particles on the order of a few hundred nanometers wide and 9—16 nm thick were analyzed separately, and statistics on the estimated proportions of large and small particles are additionally provided. Distributions of lateral dimensions of large and small particles were obtained with the help of the ImageJ-plugin analyzing numerous SEM images at different magnifications. An image contrast threshold was defined and the dimensions of the larger particles were estimated with the help of Image-J. Thicknesses of larger particles were determined from cross-sectional imaging of the particles in SEM; thicknesses of smaller particles were evaluated by AFM using a Bruker Dimension Icon AFM. Gwyddion software was used for image analysis.

5.3.2. Preparation of UFG/Polyamic Acid Dispersions

Polyamic acid was prepared by the polymerization of 3,3',4,4'-biphenyltetracarboxylic dianhydride with 2,2'-(ethylenedioxy)*bis*(ethylamine) and *m*-phenylenediamine in NMP. In brief, the two diamines dissolved in NMP were heated to 70°C under a stream of nitrogen within a round-bottom flask. The dianhydride was slowly added over the course of 5 min with rapid stirring. The resulting clear, yellow solution was further stirred under a stream of nitrogen for 8 h. In order to prepare UFG/PEI dispersions, the two diamines were added to UFG dispersions in NMP, followed by addition of the dianhydride as noted above.[13,42] Where required, additional UFG solution was added post-synthesis to achieve the intended UFG/polymer loadings.

5.3.3. AA7075 Substrate and Surface Preparation

Clad AA7075-T6 substrates were obtained from Aerotech Alloys. The nominal composition of AA7075-T6 is listed in **Table D.1**. Prior to application of the coatings, the AA7075 substrates were abraded with P150 and P400 grit sandpaper and washed with hexanes followed by acetone.

5.3.4. UFG/PEI Coatings

The UFG/polyamic acid dispersions were spray coated onto the cleaned AA7075 substrates using a TCP Global spray gun with an output pressure of 45 psi and a nozzle diameter of 1.00 mm. Substrates were held at a temperature of 250°C during application of the coating and were subsequently cured for an additional 5 min. The thickness of the coatings was monitored using a Byko-test 8500 thickness gauge. All coatings were applied at a thickness of 20—30 μm.

5.3.5. Optical Microscopy and Raman Spectroscopy

Raman spectra were acquired using a Jobin-Yvon Horiba Labram HR instrument coupled with an Olympus BX41 optical microscope. A 514.5 nm Ar-ion laser was used as the excitation source. Each of the prepared exfoliated graphite solutions were drop cast onto heated silicon substrates for analysis. Optical images were acquired using the Olympus BX41 optical microscope.

5.3.6. AC Conductivity Measurements

AC conductivity measurements were performed using a Gamry potentiostat/galvanostat/ZRA Reference 1000TM in the frequency range from 100 kHz to 10 mHz at an amplitude of 10 mV. The samples were sandwiched between two circular stainless steel electrodes, and the entire cell configuration was tightened with a screw. All samples were tested under dry conditions at room temperature. Coatings were measured as prepared while UFG was analyzed by creating films drop cast onto AA7075 substrates.

5.3.7. Adhesion Testing

Adhesion testing was performed using three American Society for Testing of Materials (ASTM) standardized methods. As per ASTM D3359, a cross-cut test was performed using a test kit procured from BYK. Cross-cuts were made with 1 mm spacing between blades, and the adhesive tape was subsequently applied and removed. A classification of 0—5B was assigned to each of the coatings tested as per the specifications of the testing protocol. A rating of 5B corresponds to no discernible removal of the coating, whereas a designation of 0B is reflective of significant damage.

ASTM D4541-09 was used to evaluate the pull-off strength of the coatings. A 14 mm diameter dolly was applied to the surface of the coating using a two-part epoxy and allowed to cure for 24 h. The pucks were removed at a pull-off rate of 0.7 MPa/s using a PosiTest AT-A automatic adhesion tester manufactured by DeFelsko. ASTM D2197-16 was performed to evaluate scrape adhesion using a balance beam scrape adhesion tester. Samples were aligned under the scraping loop that supported the specified applied load. The samples were then slid along a linear path of 3 in. and monitored for damage. All adhesion testing was repeated in triplicate for each type of coating.

5.3.8. Nanoindentation Experiments

The elastic modulus and hardness of the films were measured using a Nanomechanics iMicro nanoindenter with an InForce 50 actuator and diamond Berkovich tip. Elastic analysis follows the procedure of Oliver—Pharr,[43] wherein the contact stiffness, S, was related to the elastic modulus, E, through the universal stiffness equation:

$$\boldsymbol{S = \beta \frac{2}{\sqrt{\pi}} E_r \sqrt{A}} \qquad \textbf{5.1}$$

where β is a geometric constant that depends on the indenter geometry (taken as 1 in this work), and A is the area of the elastic contact. Meanwhile, E_r is the effective modulus given as follows:

$$\boldsymbol{E_r = \left(\frac{1-\nu_i}{E_i} + \frac{1-\nu}{E}\right)^{-1}} \qquad \textbf{5.2}$$

where E_i and ν_i represent the elastic modulus and Poisson's ratio of the indenter, whereas E and ν represent the elastic modulus and Poisson's ratio of the indented sample. The hardness was estimated from the contact area as

$$\boldsymbol{H = \frac{P_{max}}{A}} \qquad \textbf{5.3}$$

where P_{max} is the peak indentation load. Both the frame stiffness and the depth-area relationship were empirically determined based upon the indentation response of a fused silica standard sample. Tests were conducted on each sample using a constant loading rate over a load setting of 0.05, 0.1, 0.2, and 0.3 s^{-1}.

5.3.9. Salt Spray Exposure

Samples were exposed to salt spray conditions following procedures outlined in the ASTM B117 standard. The pressure of the chamber was kept at 15 psi. During exposure, the distribution of the spray was monitored using graduated cylinders distributed throughout the chamber. The collection volume for all cylinders was consistently between 20 and 50 mL per day. The back of the samples and edges were protected with tape to prevent preferential corrosion of uncoated sections. A 5 cm × 5 cm cross-sectional cut was made in each of the coatings using a diamond-tipped scribe. As specified in the standard, the samples were exposed to a spray generated from a 5 wt.% aqueous solution of NaCl in a chamber held at 35°C for the entirety of the testing cycle. Samples were monitored at 24 h intervals for 12 days.

5.3.10. Electrochemical Impedance Spectroscopy (EIS)

EIS measurements were performed to characterize the electrochemical response and degradation of the different systems under consideration up to a period of 100 days

in an aerated aqueous solution of 3.5 wt.% NaCl at room temperature. The measurements were performed in a conventional three-electrode cell using the coated sample as the working electrode, a saturated calomel electrode (SCE) as the reference electrode, and a Pt/Nb mesh as the counter electrode. A cylindrical glass vessel was utilized as the electrochemical cell exposing an area of 4.67 cm^2 on the working electrode; an O-ring and a metallic clamp were used to hold together the working electrode and the glass vessel. Electrochemical data was collected using a Gamry potentiostat/galvanostat/ZRA Reference 1000TM instrument surrounded by a Faraday cage to minimize electromagnetic interference. The open circuit potential (OCP) was measured for 10 min before each EIS measurement. The EIS measurements were carried out at the OCP in the frequency range of 100 kHz—10 mHz at 10 points per decade using a sinusoidal perturbation signal of ±10 mV. The electrochemical measurements were conducted on duplicate samples. The EIS spectra were fitted to appropriate equivalent circuit models using the EC-lab V10.40 fitting software.

5.3.11. Cryo-fracture, Cross-sectional Analysis

Coatings were cryo-fractured through immersion in liquid nitrogen for 5 min and then fractured and imaged using a JEOL JSM-7500F SEM without Pt coating to allow for localization of charging to be observed. The coatings were imaged at an accelerating voltage of 1 kV, an emission current of 10 μA, and a probe current of 8 μA.

5.3.12. Transmission Electron Microscopy (TEM)

TEM was performed on a JEOL JEM-2010 instrument at an accelerating voltage of 200 kV. Prior to TEM measurements, a solution of the 10 wt.% UFG/PEI polymer

composite was drop-cast onto a Formvar-coated 400 mesh copper TEM grid that was heated to remove excess solvent.

5.3.13. Cross-sectional Analysis of the Coating/Substrate Interface

Cross-sections of a set of unexposed coatings as well as all those exposed for 100 days as part of the EIS study were prepared by immersing the coatings in epoxy (EpoxiCure 2, Buehler) and subsequently cutting the samples to expose the metal/coating interface using a Buehler Isomet 5000 system. The cross-sectional samples were sanded using 600, 1000, and 1200 grit paper and polished successively with 9, 6, and 1 μm diamond paste prior to imaging. The samples were subsequently sputtered with ca. 3 nm of Pt and imaged using a JEOL JSM-7500F SEM equipped with an Oxford Instruments energy dispersive X-ray spectroscopy (EDS) detector. EDS maps were obtained for each of the interfaces using an acceleration voltage of 10 kV, an emission current of 10 μA, and a probe current of 8 μA.

5.3.14. Finite Element Modeling of Diffusivity

A computational first-order homogenization scheme based on the Finite Element method was utilized to model effects of particle size distribution on effective diffusivity for composite coatings. Approximating the density of UFG by that of graphite, $\rho = 2.2$ g/cm^3, together with the density of PEI, $\rho = 1.27$ g/cm^3, the mass fractions of 5, 10, and 17 wt.% were converted into corresponding volume fractions of 2.8, 5.4, 8.9 vol.%, respectively. Using a random sequential addition algorithm, UFG flakes, represented by thin hexahedral slabs, within sample cells of dimensions 200 μm × 200 μm × 200 μm

were placed within the matrix until reaching the desired volume fractions. Flake size distributions used in this approach are provided in **Tables D.2** and **3**.

The effective diffusivity tensors were determined through solving a Laplace problem across the composite. For each of the three space directions, linear concentration/potential conditions have been prescribed on the sample surface. Effective diffusivity tensors can then be determined using the average flux vectors and concentration/voltage gradients in the specimen. In order to reduce the impact of the random microstructure, these calculations have been performed for 5 random samples each. The effective diffusivity then results from the trace of the average diffusivity tensor. For the diffusion calculations, we assumed the UFG to have a diffusivity near zero and assumed a unit diffusivity for the PEI matrix. The resulting effective diffusivity hence gives the relative change in diffusivity with respect to the diffusivity of the pristine PEI matrix.

5.4. Results and Discussion

5.4.1. Characterization of UFG and UFG/PEI Nanocomposite Coatings on AA7075

Challenges related to the dispersion of few-layered graphene at high loadings within solvents and polymeric matrices represent a significant constraint to the design of high-performance graphene inks and composites.[34,44,45] Exfoliation of unfunctionalized graphene monolayers in solution has been accomplished by Hernandez *et al*. but is limited to concentrations of ca. 1 wt.% in NMP.[46] Exfoliated graphene prepared in this manner is characterized by extended π-conjugated domains without a high concentration of pores and damaged regions observed in graphene oxide.[47] Given that such pores in

oxidatively functionalized graphene can potentially mediate undesirable ionic diffusion,[48] exfoliated UFG has been selected as the filler of choice for corrosion-resistant composites. Attempting to achieve higher-concentration UFG dispersions inevitably results in a greater abundance of thicker few-layered graphitic platelets. While the effective dispersion of individual sheets within the polymeric matrix is most desirable to maximize tortuosity, low-solid-content dispersions do not yield robust pinhole free coatings given the large solvent volume that has to be removed during curing. Surfactants can be utilized to aid dispersibility at higher concentrations but often give rise to deleterious porosity. In order to balance the above constraints, extended ultrasonication has been used to obtain dispersions with relatively high loadings of 5, 10, and 20 mg/L of UFG without the addition of surfactants and without further fractionation, thereby yielding a mixture of larger few-layered platelets and thinner exfoliated flakes. This method allows for inclusion of a substantial proportion of exfoliated few-layered nanosheets enabling high-solid-loading dispersions in NMP while inevitably yielding a proportion of larger graphitic particles. **Figure D.1** (Appendix D) shows SEM images of UFG obtained from the 5, 10, and 20 mg/mL solutions illustrating the presence of both larger graphitic particles and exfoliated sheets. Size distribution histograms are shown in **Figure D.2** and the relevant statistics are summarized in **Table D.4**. The graphitic particles range in lateral dimensions from a few hundred nanometers to tens of micrometers. Based on AFM analysis, smaller particles are around 9—16 nm in thickness. Cross-sectional views of the larger graphitic particles indicate thicknesses of 2.5 ± 2.1 μm. At lower loadings of graphite, the smaller particles constitute a greater

proportion of the suspended solids, as illustrated by Table D.4. These high-solid-loading NMP dispersions allow for preparation of UFG/polyamic acid formulations that yield pinhole-free continuous films upon spray-coating while limiting the amount of NMP that has to be used within the formulations.

Raman spectroscopy data collected for the larger graphitic platelets and thinner exfoliated sheets from 5, 10, and 20 mg/mL UFG dispersions are shown in **Figure D.3**. The vertical dashed lines demarcate the positions of the D-band at ca. 1,350 cm^{-1}, G-band at ca. 1,580 cm^{-1}, and 2D band at ca. 2,700 cm^{-1}.[49] The position of the G-band indicates that the recovered materials are few-layered graphene. The thinner exfoliated sheets show prominent D-bands as a result of edge effects.

Figure 5.1 schematically illustrates the preparation of UFG/polyamic acid nanocomposites and their casting onto abraded AA7075 substrates whereupon imidization is accomplished *in situ* through thermal annealing to obtain the UFG/PEI nanocomposite coating. The stochastic inclusion of *m*-phenylenediamine units within polyamic acid inhibits crystallization and thus yields an amorphous, pliant, and formable polymer matrix. The excellent dispersion of UFG within polyamic acid has been extensively characterized in our previous work,[11,18,36] and is facilitated by the *in situ* synthesis of the polymer around the exfoliated graphite platelets; π—π interactions of the basal planes of the exfoliated graphite framework with the conjugated anhydride result in the growing polymer framework encasing the filler UFG nanoplatelets. UFG/polyamic acid formulations have been prepared with 5, 10, and 17 wt.% UFG loadings, which as delineated in Figure 5.1 corresponds to two different regimes (*vide*

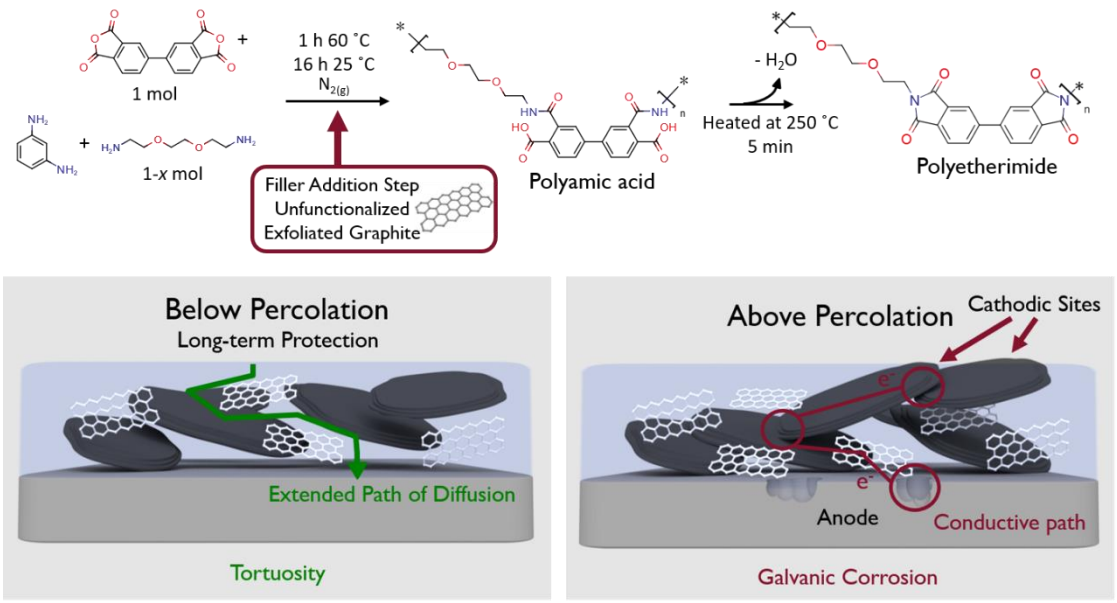

Figure 5.1. Schematic illustration of the preparation of nanocomposite exfoliated graphite coatings based on *in situ* synthesis of polyamic acid in the presence of UFG followed by imidization during curing. Two distinct regimes can be distinguished as a function of the UFG loading: A) the incorporation of UFG imbues considerable additional barrier protection at low loadings (of ca. 5 wt.% UFG) as a result of increased tortuosity of ion transport pathways, whereas at higher loadings (ca. 10 wt.% and higher), B) galvanic corrosion is initiated owing to the coupling of the percolative UFG network with the underlying Al substrate.

infra): the 5 wt.% UFG/PEI sample corresponds to well-dispersed UFG below the percolation threshold, where physical isolation of UFG flakes is maintained and the coatings provide tortuous and extended pathways for diffusion of corrodant species through the polymeric network, whereas the 10 and 17 wt.% UFG/PEI samples correspond to stabilization of continuous percolative, conductive networks across the polymer matrix. The connectivity of exfoliated graphite inclusions within the coating has a profound influence on the activation of galvanic corrosion mechanisms as will be discussed in subsequent sections, providing a tortuous pathway inhibiting the diffusion

of corrodant species at low loadings but activating galvanic corrosion at high loadings when the percolation threshold is reached.

Figure D.4 shows optical microscopy images of the coated AA7075 surfaces. The inclusion of increasing amounts of UFG in the coatings brings about in a decrease in transparency of the coatings. The 5 and 10 wt.% UFG/PEI coatings show similar dispersion, whereas in the 17 wt.% UFG/PEI coating, some larger graphitic agglomerates are observed to segregate at the surfaces. **Figure D.5** shows the same coatings at lower magnifications. **Figure D.6** shows SEM images of cryo-fractured 10 wt.% UFG/PEI nanocomposite coatings (Figs. D.6 A—D) demonstrating homogeneous dispersion of the UFG inclusions without evidence for local charging indicative of phase segregation; Figures D.6E—H furthermore exhibit transmission electron microscopy (TEM) images of 10 wt.% UFG/PEI films cast onto a copper grid. The UFG inclusions can be distinguished based on their greater electron density contrast. Figures D.6E and F demonstrate the large distribution of sizes of the exfoliated graphite platelets present within the nanocomposite coatings. Larger sheets can be imaged at lower magnifications (Figure D.6E); whereas the smaller sheets are observed only at higher magnifications (Fig. D.6F). The electron microscopy images attest to the excellent dispersion of the graphitic platelets within the polymeric matrix. Further support for the homogeneous dispersion of UFG inclusions within the coatings comes from cross-sectional SEM images that will be discussed below before and after salt water immersion.

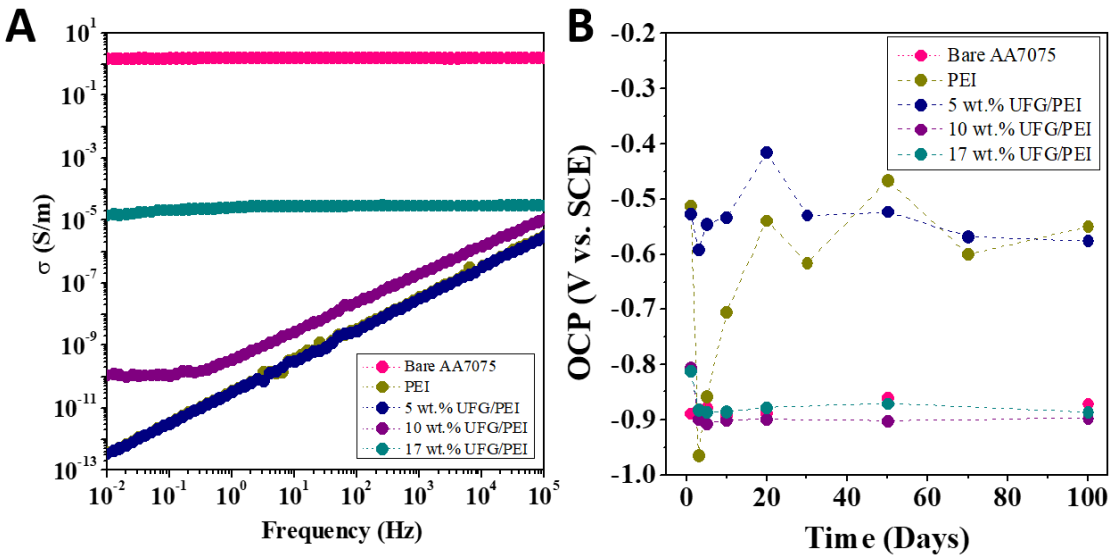

Figure 5.2. A) AC conductivity measurements of bare AA7075, PEI coated onto AA7075, and UFG/PEI coatings on AA 7075 with different UFG loadings and B) evolution of the OCP for UFG/PEI coatings, PEI-coated AA7075, and bare AA7075 immersed in an aerated aqueous solution of 3.5 wt.% NaCl for 100 days at room temperature.

Figure 5.2 shows AC conductivity data acquired as a function of frequency for bare AA7075, a PEI-coated AA7075 substrate, and exfoliated graphite/PEI-coated substrates with different UFG loadings. The conductivity of the as-prepared exfoliated graphite was similarly measured for drop cast films and is shown for comparison in **Figure D.7**. The evolution of AC conductivity in terms of frequency is reflective of the overall electrical conductivity of the composite and is strongly dependent on the extent of dispersion and the dimensions of the conductive filler; as such, it is commonly used to probe the percolation threshold for conductive fillers embedded within dielectric matrices.[50–57] Based on evolution of the AC conductivity in terms of frequency, composite coatings containing conductive particles can be categorized in three

classes.[50] Below the percolation threshold, the composite material behaves as a dielectric, with the AC conductivity linearly increasing as a function of the frequency. In proximity to the percolation threshold, the AC conductivity is independent of the frequency up to a certain characteristic frequency value. Beyond this point, the AC conductivity again linearly increases as a function of the frequency. Finally, above the percolation threshold, the AC conductivity remains constant across the entire frequency range. In Figure 5.2, bare AA7075 not surprisingly behaves as a conductive material (as do the exfoliated graphite films in Fig. D.7), whereas the PEI coating shows characteristic dielectric behavior with an AC conductivity that increases linearly as a function of the frequency. The AC conductivity response of the 5 wt.% UFG/PEI coating is essentially the same as that of the pristine PEI coating, suggesting that the exfoliated graphite content in this coating is below the percolation threshold of the material. Interestingly, when the concentration of UFG is increased to 10 wt.%, the AC conductivity shows a strongly frequency dependent response with a linear variation of the conductivity as a function of frequency above ca. 0.3 Hz but a frequency-invariant response below this value. In other words, a 10 wt.% loading of UFG brings the composite close to its percolative threshold. The 17 wt.% UFG/PEI composite shows a frequency-invariant response characteristic of metallic materials suggesting that the percolation threshold has been reached and that the exfoliated graphite flakes form a continuous electrical network within the polymeric matrix. The data in Figure 5.2 thus underpins the delineation of the distinctive regimes schematically illustrated in Figure

5.1, which as described below strongly influences the corrosion performance of these nanocomposite coatings.

Adhesion testing has been performed on each type of coating using ASTM testing procedures (**Table 5.1**). Evaluation of the coatings by ASTM D3359, the cross-cut test, shows excellent adhesion of the PEI and UFG/PEI nanocomposite coatings to the abraded AA7075 substrates with all of the coatings earning a rating of 5B, corresponding to no measurable loss of the coating upon peeling of the adhesive tape. Additionally, the ASTM D2197-13 scrape test shows no break in the coatings at the maximum loading of 10 kg. Pull-off testing has also been performed as per ASTM D4541-09. The point of failure for all coatings is the contact between the coating and metal; pull-off pressures for each of the coatings are listed in Table 5.1. These results demonstrate that the adhesive properties are dominated by the interfacial bonding between PEI and the abraded AA7075 substrate and are not substantially altered by inclusion of UFG.

In contrast, the mechanical properties measured by nanoindentation indicate that the addition of exfoliated graphite indeed influences the elastic and plastic properties of the resulting nanocomposite. As seen in Table 5.1, the elastic modulus of PEI has been measured to be 5.17 GPa, which is similar to the 2.775 GPa value reported by Khatam and Ravi-Chandar for a PEI strip[58] and the modulus measured using ASTM Standard D638 for PEI resin.[59] Interestingly, in the nanocomposite coating, the addition of exfoliated graphite first leads to a decrease in the elastic modulus and hardness. However, with increasing exfoliated graphite incorporation, the elastic modulus and

Table 5.1. Summary of adhesion testing and mechanical properties measured for PEI and UFG/PEI nanocomposite coatings on AA7075

	ASTM D4541-09 (Pull Off)	**ASTM D3359 (Tape)**	**ASTM D2197-13 (Scrape)**	**Nanoindentation**	
Sample	Average Pull-off pressure (MPa)	5B	>10 kg	Elastic Modulus (GPa)	Hardness (MPa)
PEI	0.73 ± 0.02			5.17 ± 0.10	422 ± 15
5 wt.% UFG/PEI	0.76 ± 0.13			4.92 ± 0.32	401 ± 20
10 wt.% UFG/PEI	0.77 ± 0.07			4.45 ± 0.30	395 ± 10
17 wt.% UFG/PEI	0.67 ± 0.10			5.44 ± 0.31	463 ± 30

hardness are substantially increased, surpassing that of the host matrix. The observed non-monotonic behavior highlights the complex mechanical interaction between the exfoliated graphite and PEI. At low UFG loadings, the exfoliated graphite inclusions

disrupt cross-linking of the polyamic acid chains resulting in a polymeric matrix that is softer than the host matrix alone. However, at higher UFG loadings, the rule of mixtures prevails and the filler brings about an increase in the elastic modulus and hardness of the composite coatings. Values of elastic moduli in Table 5.1 are averages of the measured moduli from all loading rates for the specified coating. The elastic moduli measured at each specific loading rate for each coating are shown in **Figure D.8**.

5.4.2. Evaluation of the Corrosion Protection Endowed by Nanocomposite Coatings

As an initial qualitative means of evaluating the corrosion protection afforded to the AA7075 substrates by PEI and UFG/PEI nanocomposite coatings, coated samples with cross-sectional cuts have been exposed to a salt spray chamber for 12 days. **Figure 5.3** shows digital photographs of the coatings after 12 days of exposure. The areas at some distance from the cross-sectional cut are unaffected by salt spray exposure, attesting to the excellent barrier properties of the coatings. For the coating comprising just PEI, accumulation of corrosion products is confined to the exposed region of the metal surface. Indeed, the PEI coating functions solely as a barrier, and thus when the barrier is compromised, corrosion is initiated at the exposed metal surface. In contrast, the UFG/PEI composites show the corrosion product spreading outwards from the cross -sectional cut; the amount of the product and the extent of its accumulation scales roughly proportionately to the graphene loading. Creation of a scratch within these coatings allows for contact between the graphene, the electrolyte medium, and the exposed aluminum substrate, thereby establishing a corrosion cell. Given the relative

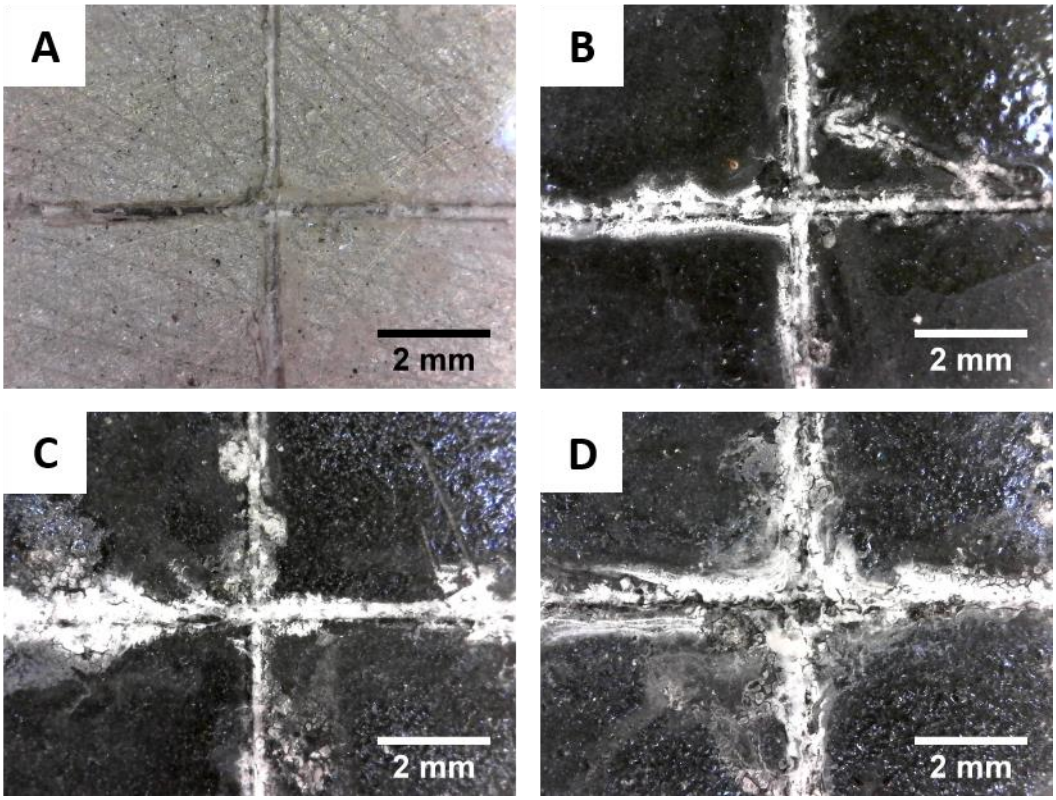

Figure 5.3. Digital photographs of the cross-sectional cuts after 12 days of salt spray exposure for A) PEI-coated AA7075 as well as B) 5; C) 10; and D) 17 wt.% UFG/PEI coatings.

differentials of reduction potentials noted above, exfoliated graphite thus promotes the galvanic corrosion of the AA7075 substrate (Fig. 5.1). Consequently, the mitigation of galvanic couples between conductive exfoliated graphite and the aluminum substrate is imperative in order to utilize the potential strongly enhanced tortuosity of diffusion pathways accessible upon incorporation of exfoliated graphite.

The evolution of the OCP for the UFG/PEI coatings, PEI coated onto AA7075, and bare AA7075 immersed in a 3.5 wt.% aqueous solution of NaCl for 100 days is shown in Figure 5.2. The bare AA7075 substrate exhibits OCP values close to -0.88 mV

versus SCE during the first few days of salt water immersion. These OCP values are associated with active corrosion processes that involve the breakdown of the native oxide film as a result of attack by reactive Cl^- ions in the electrolyte and the initiation of charge transfer processes at the metal/electrolyte interface.[60,61] After ca. 20 days of immersion, the OCP values of AA7075 are shifted to more anodic values, which suggests the formation of passivating corrosion products at the metal surface that decelerate the corrosion process. In contrast, the measured OCP for the PEI coating is -0.50 V *versus* SCE for the first day of immersion indicating negligible or absent corrosion processes immediately after immersion. However, the OCP value for the PEI-coated AA7075 substrate is dramatically decreased to more negative values after ca. 24 h of salt water immersion, approaching values comparable to those measured for bare AA7075. The observed shift can be ascribed to the diffusion of water and ionic species through the coating, which results in the initiation of corrosion processes at the metal/coating interface. However, after 5 days of immersion, the OCP values for PEI are increased to more positive values indicating the entrapment of corrosion products underneath the coating, which results in the formation of a passivation layer. Indeed, a gradual increase of the OCP values is observed over 20 days of salt water immersion. Subsequently, the OCP values fluctuate between approximately -0.45 and -0.60 V *versus* SCE. This fluctuation is likely derived from the initiation of pitting corrosion processes wherein pit formation and repassivation occur alternately at active zones on the metal surface. Interestingly, the OCP values for the 5 wt.% UFG/PEI coating are suggestive of significantly improved stability against corrosion. As shown in Figure 5.2, the OCP

values remain constant around -0.55 V *versus* SCE during the entire period of immersion, which indicates that the coating is effective in protecting the metallic substrate from attack by the corrosive medium and thus corrosion processes are not initiated at the coating/metal interface. However, further addition of graphene to the PEI coating appears to be somewhat detrimental in terms of corrosion inhibition; Figure 5.2 shows that the OCP values for the 10 and 17 wt.% UFG/PEI coatings are slightly more negative as compared to the OCP values for bare AA7075, suggesting greater corrosion activity at the aluminum surface in the presence of relatively high amounts of exfoliated graphite. The values do not increase upon prolonged exposure, which suggests that high amounts of exfoliated graphite inclusions (≥10 wt.%) accelerate the corrosion process without allowing for formation of an effective passivation layer owing to the formation of galvanic cells.

Electrochemical impedance spectroscopy (EIS) has been used to investigate the evolution of the electrochemical response of the different coatings and the bare AA7075 substrate upon immersion in a 3.5 wt.% aqueous solution of NaCl for up to 100 days. **Figure 5.4** plots Nyquist and Bode representations of EIS data measured for bare AA7075 and PEI-coated AA7075 at different immersion times. In Figure 5.4A, it can be seen that during the first 10 days of immersion, the Nyquist plot for the bare AA7075 substrate is characterized by a capacitive loop from high to intermediate frequencies, which is related to the charge transfer processes at the metal/electrolyte interface; an inductive loop is furthermore observed at the low frequencies and is associated with adsorbed intermediate species (charge transfer process) present during the breakdown of

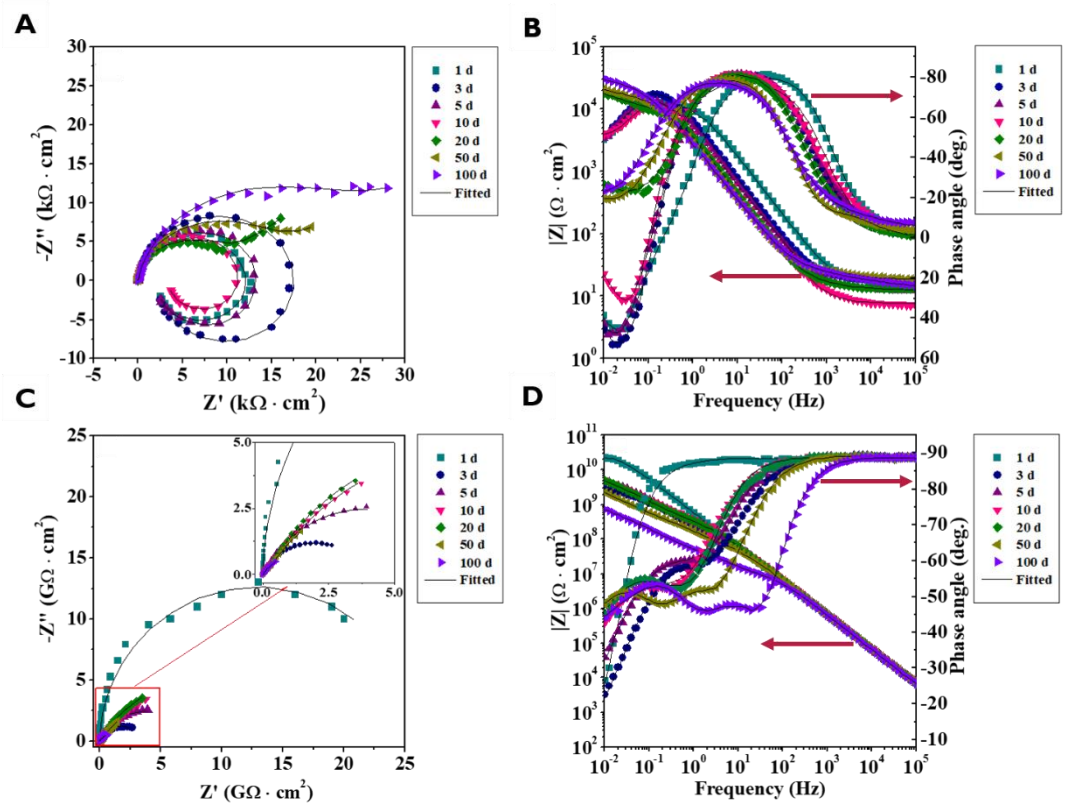

Figure 5.4. EIS spectra monitored for A, B) AA7075 and C, D) PEI-coated AA7075 immersed in a 3.5 wt.% aqueous solution of NaCl for up to 100 days.

the passivating film and the initiation of pitting corrosion.[62],[63] These features can also be identified in the phase angle plot shown in Figure 5.4B where the capacitive response corresponds to the region from 10^{3} to 10^{-1} Hz and is characterized by a negative peak value, whereas the inductive response is observed at the lowest frequencies and exhibits a positive peak value. After 20 days of immersion, the Nyquist representation (Figure 5.4A) shows that the inductive loop at low frequencies is no longer present and a diffusion tail is instead observed in this frequency range. The appearance of this feature at low frequencies is indicative of a diffusion-controlled corrosion process such that the

formation of corrosion products at the metal/electrolyte interface is limited by the diffusion of reacting species towards and away from the metal surface. The appearance of the diffusion tail after 20 days of immersion is consistent with the increase of the OCP to more positive values at this time (Figure 5.2) and indicates that the corrosion products formed at the surface are somewhat passivating and can modestly impede the corrosion process and limit charge transfer.

EIS data for the PEI-coated AA7075 substrate is shown in Figure 5.4C. The Nyquist representation exhibits a large capacitive loop during the first day of immersion covering the entire measured frequency range; such an extended loop derives from the dielectric properties of the organic coating and its resistance to the diffusion of water and ionic species. Notably, the magnitude of the impedance at the lowest frequency ($|Z|_{0.01Hz}$) approaches a value higher than 10^{10} $\Omega \cdot cm^2$. Since$|Z|_{0.01Hz}$ provides an estimation of the effective resistance of the coating system, the high value suggests that the PEI coating provides good barrier protection against aggressive species immediately upon immersion. However, a stark change is observed within 24 h; the $|Z|_{0.01Hz}$ value is decreased by almost one order of magnitude upon salt water immersion for 3 days. Furthermore, the phase angle plot shows that after 3 days of immersion, a second time constant at a lower frequency of ca. 0.4 Hz is observed, which can be ascribed to the initiation of pitting corrosion at the metal/coating interface. Indeed, this data is consistent with the drastic decrease of the OCP value at this immersion time shown in Figure 5.2. However, upon prolonged immersion, the $|Z|_{0.01Hz}$ value in Figure 5.4D as well as the radii of the semicircle in the Nyquist plot of Figure 5.4C are monotonically

increased up until 20 days of immersion as a result of the formation and growth of corrosion products at active sites. These corrosion products are entrapped within the PEI coating and impede the migration of ionic species from and towards the incipient pits formed on the substrate. In other words, the local accumulation of corrosion products at the pit sites delay further propagation of the pit.[64] Further exposure to the electrolyte solution brings about a continuous decrease of $|Z|_{0.01Hz}$, which reaches a value $<10^9$ $\Omega \cdot cm^2$ at 100 days when the immersion test is concluded. In addition, a third time constant at intermediate frequencies (ca. 0.1—25 Hz) can be distinguished after 50 days of immersion. This response can be attributed to the accumulation of corrosion products at the pit sites. As the corrosion products build up at the pit sites, internal tensile stresses start to develop at the coating/metal interface. These internal stresses weaken the adhesion between the metal and the coating, resulting eventually in local delamination of the coating at the active sites.[64] The continuing partial delamination of the coating from the metal substrate underpins the overall reduction in the corrosion resistance of the system as a function of time.

Figures 5.5A and **B** plot EIS data acquired for AA7075 substrates with a 5 wt.% UFG/PEI coating. A singular time constant is observed during the entire immersion time. In addition, the EIS signal shows an almost ideal capacitive behavior with $|Z|_{0.01Hz}$ values ranging between ca. 3×10^{10} $\Omega \cdot cm^2$ for the first day of immersion to 1.1×10^{10} $\Omega \cdot cm^2$ upon 100 days of salt water immersion. The slight decrease of $|Z|_{0.01Hz}$ values corresponds to the slow diffusion of water and ionic species, which have to navigate a path made much more tortuous by the inclusion of graphene, into the coating. Indeed,

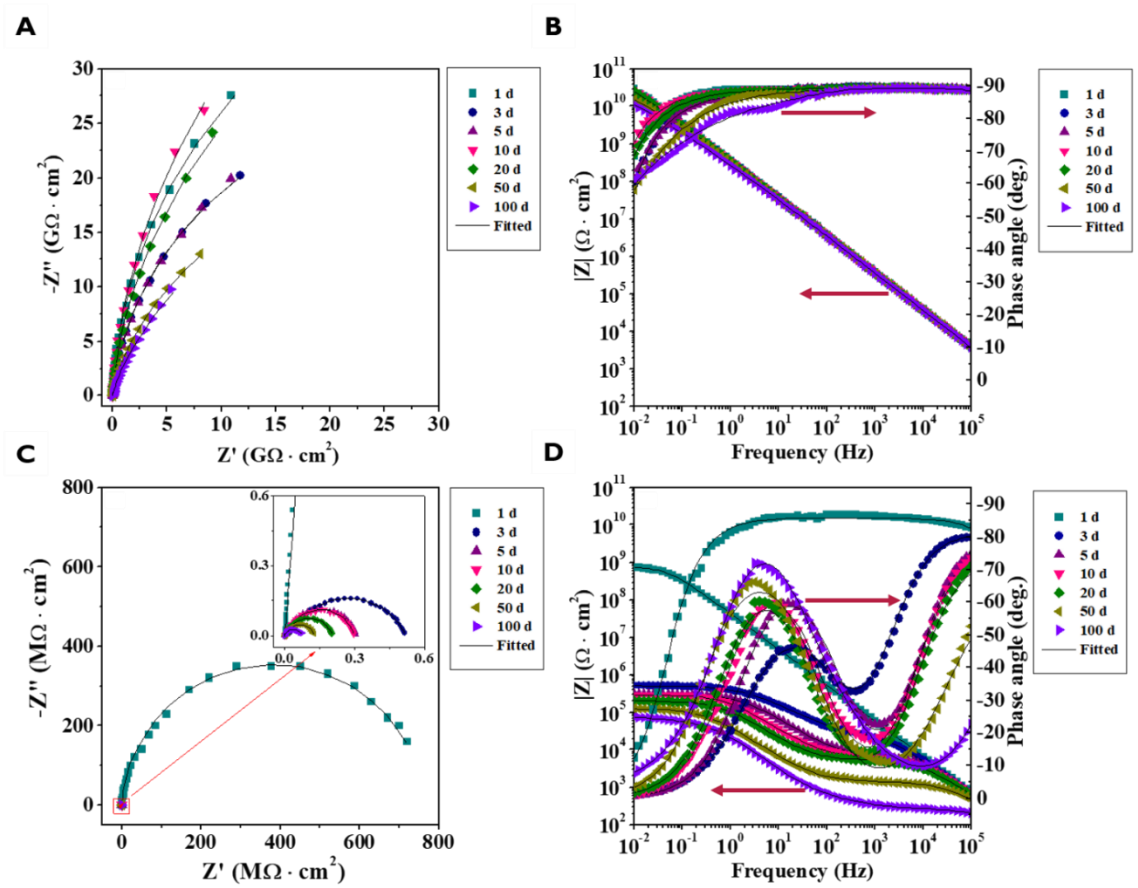

Figure 5.5. EIS spectra monitored for A, B) 5 wt. % UFG/PEI and C, D) 10 wt.% UFG/PEI on AA7075 immersed in a 3.5 wt.% aqueous solution of NaCl for up to 100 days.

the results suggest that the 5 wt.% UFG/PEI coating shows excellent barrier protection without any signatures of corrosion processes being operational at the coating/metal interface over the entire duration of the testing period. The substantial enhancement in the barrier properties of the nanocomposite as compared to PEI alone can be ascribed to several reasons. At these loadings (below percolation as per Fig. 5.2), 2D sheets of few-layered graphene serve as excellent water-impermeable[27] and ion-impervious inclusions and greatly reduce the concentration of microscopic defects and pores within the

polymeric matrix. As such, the exfoliated graphite inclusions substantially increase the effective pathlengths for the diffusion of water and chloride ions towards the metal surface.[32,41,65,66] The increase in tortuosity is reflected in a substantially enhanced pore transport resistance. The strong interaction between the π-conjugated basal planes of exfoliated graphite and the aromatic groups of PEI further ensures excellent adhesion without development of porosity at the filler/matrix interface as is often the case with less compatible fillers. The high elastic modulus of graphene and the strong interfacial adhesion ensures that the composite as a whole is able to withstand strains developed during local corrosion without delamination (Fig. D.8).[36,41]

Figures 5.5C and D plot analogous EIS data acquired for an AA7075 substrate coated with 10 wt.% UFG/PEI. **Figure D.9** shows corresponding data measured for the 17 wt.% UFG/PEI coating. Interestingly, the excellent corrosion inhibition of UFG/PEI nanocomposites at low concentrations of exfoliated graphite is severely compromised when the exfoliated graphite concentration is increased above the percolation threshold. During the first day of salt water immersion, the EIS signal for both coatings is characterized by a singular time constant (Figs. 5.5D and D.9B) suggesting that similar to the 5 wt.% UFG/PEI sample, no corrosion processes are occurring at the metal/coating interface. However, the $|Z|_{0.01Hz}$ values for the 10 and 17 wt.% UFG/PEI coatings (Figs. 5.5D and D.9B) are approximately one and two orders of magnitude lower than that of the 5 wt.% UFG/PEI coating (Fig. 5.5B), which connotes decreased efficacy of barrier protection upon increased graphene incorporation. Upon 3 days of salt water immersion, a drastic decrease of the $|Z|_{0.01Hz}$ values is observed for both the

coatings with high loadings of exfoliated graphite, decreasing to values $<10^6\ \Omega \cdot cm^2$. Furthermore, Figures 5.5D and D.9B indicate the appearance of another time constant in the range between intermediate and low frequencies (10^2 Hz to 10^{-1} Hz), which is ascribed to the initiation of corrosion processes at the coating/metal interface. This latter behavior persists till the end of the exposure period and along with the successive diminution of $|Z|_{0.01Hz}$ values with prolonged immersion suggests that the corrosion process proceeds under charge transfer control during the entire time period. It is additionally worth noting that the EIS data for these two coatings do not show the diffusion tail observed for bare AA7075 or the third time constant observed for the PEI coating that are indicative of the accumulation of corrosion products at the metal surface. Instead, it appears that electrochemical activity proceeds for the entire 100 days and the 10 and 17 wt.% UFG/PEI coatings promote continuous dissolution of the corrosion products without formation of a passivation layer. The aggressive corrosion observed in the presence of these coatings above percolation threshold can be ascribed to galvanic coupling established between exfoliated graphite and the metal substrate.[22,67–69] Since graphite has a substantially more positive corrosion potential (+0.150 V)[19] as compared to AA7075-T6 (-0.765 V)[20], cathodic reactions are likely to occur at the exfoliated graphite, whereas anodic dissolution reactions are anticipated for the Al alloy substrates when the two are electrochemically coupled. The establishment of a percolative exfoliated graphite network renders the underlying aluminum substrate particularly vulnerable to galvanic corrosion since local oxidative processes at specific pit sites can then be balanced by reductive processes at exfoliated graphite sites located at a

substantial distance from the coating/metal interface within the bulk of the coating. Furthermore, the incipient corrosion products are unable to achieve local passivation since the substrate is coupled to an extended exfoliated graphite network and as such corrosion continues unabated as oxidized Al^{3+} species can traverse through the film and be reduced at the surfaces of exfoliated graphite particles. Such corrosion acceleration as a result of galvanic coupling has been observed for bare graphene films and is strongly dependent on the electrical conductivity of the exfoliated graphite coating and its ease of degradation such as to form a corrosion cell.[22,33,66,70]

In order to provide a more quantitative perspective of the performance of the coatings, the equivalent electrical circuits (EECs) sketched in **Figure 5.6A** have been used to fit the EIS data plotted in Figures 5.4 and 5.5. **Table D.5** summarizes which of the equivalent circuits shown in Figure 5.6A have been used to model the EIS over specific time intervals across the duration of exposure. The equivalent circuit shown in Figure 5.6A(i) has been used to model the EIS response for bare AA7075 over the first 10 days of salt water immersion. In this circuit, R_s corresponds to the electrolyte resistance; Q_{dl} and R_{ct} denote the double layer capacitance and the charge transfer resistance, respectively, of the pitting corrosion process taking place at the aluminum surface; and R_L and L represent the resistance and the inductance, respectively, associated with adsorption of intermediate species at the metal surface during the initiation of the pitting corrosion process.[62] For longer immersion times, beyond 20 days of salt water immersion, the inductance response is no longer observed and thus a Warburg impedance (W) component is added to describe the diffusion-controlled

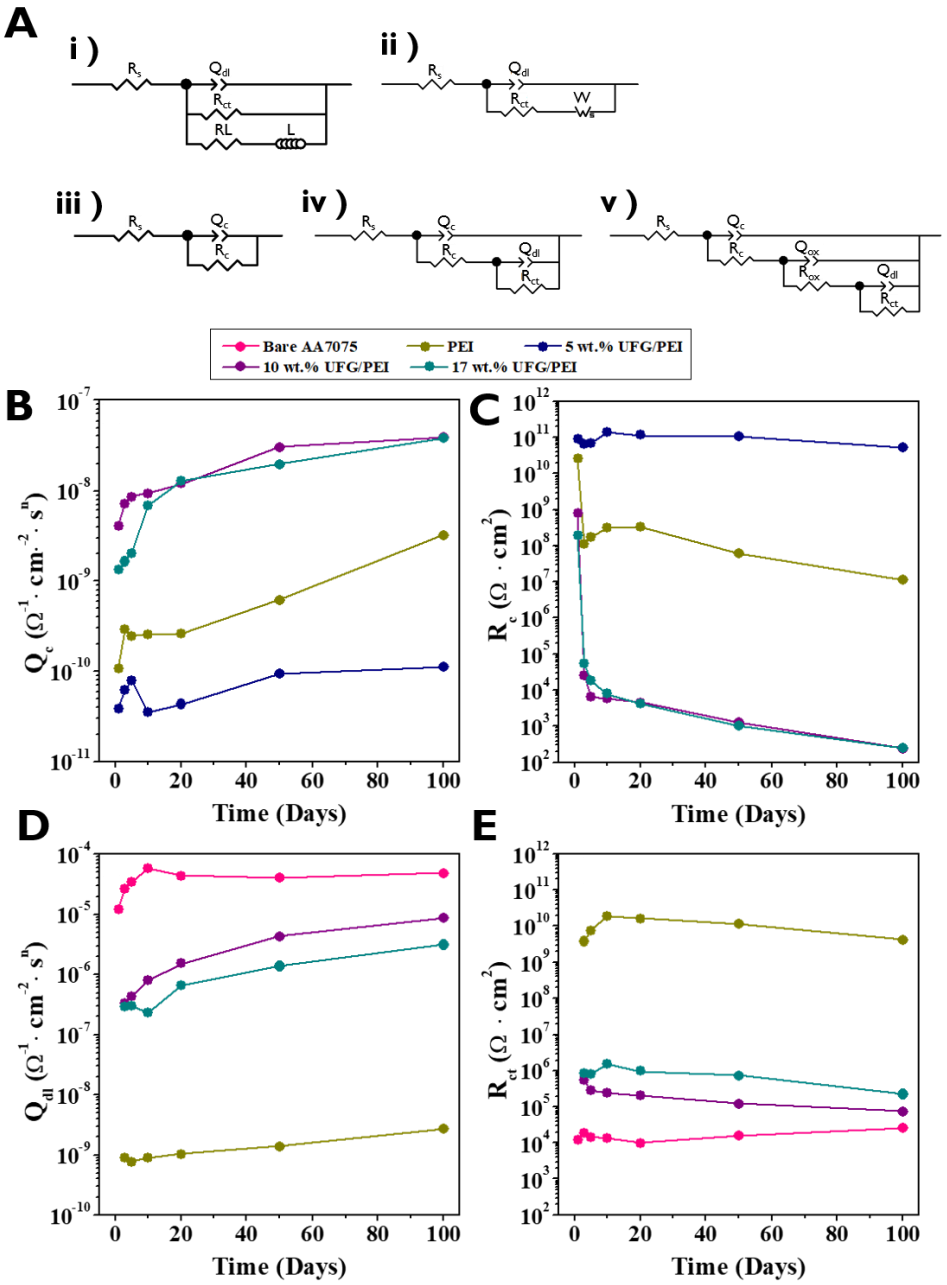

Figure 5.6. A) Equivalent electrical circuits used to model the EIS response for bare AA7075, PEI, and UFG/PEI coatings immersed in a 3.5 wt.% aqueous solution of NaCl for 100 days. Evolution of equivalent circuit elements derived from fitting of EIS spectra of AA7075 and exfoliated graphite/PEI coatings; B) coating capacitance (Q_c), C) coating resistance (R_c), D) double layer capacitance (Q_{dl}), and E) charge-transfer resistance (R_{ct}).

process derived from the accumulation of corrosion products at the metal surface (Fig. 5.6A(ii)). The EIS response for the pristine PEI coating has been fitted using the equivalent circuits sketched in Figure 5.6A(iii)-(v); circuit (iii) has been used for the first day of immersion, circuit (iv) for 3—20 days of immersion, and circuit (v) for 50—100 days of immersion (Table D.5). In these circuit diagrams, Q_c and R_c represent the capacitance and resistance of the pristine PEI coating, respectively; Q_{dl} and R_{ct} represent the double layer capacitance and charge transfer resistance, respectively, as delineated above for bare AA7075; and Q_{ox} and R_{ox} describe the capacitance and the resistance, respectively, of the corrosion products that are locally accumulated at the coating/electrolyte interface (and bring about local stresses and delamination as discussed above). The equivalent circuit in Figure 5.6A(iii) suffices to fit the EIS response of the 5 wt.% UFG/PEI coating for the entire immersion time, since no corrosion processes are operational at the metal/electrolyte interface, and only modest diffusion of water and ionic species within the polymeric matrix is observed. Circuits (iii) and (iv) have been used to fit the EIS response measured for 10 and 17 wt.% UFG/PEI coatings; only the former is necessary for the first day of immersion, whereas the latter captures the continuing corrosion for the remaining duration of salt water immersion. For all the equivalent circuits diagrammed in Fig. 5.6, constant phase elements (CPE) have been used instead of capacitances to take into consideration deviations from ideal capacitive behavior.[71],[72] The impedance of the CPE is defined as:

$$\mathbf{Z_Q = {1}/{Y_0(j\omega^n)}, \cdots} \qquad \mathbf{5.4}$$

where Y_o is the admittance of the constant phase element, j is an imaginary number, ω is the frequency, and n is an empirical exponent in the range between 0 to 1; $n = 0$ corresponds to a resistor, whereas $n = 1$ describes a purely capacitive element.[72,73]

Modeling the EIS response of the different coatings using the equivalent circuits noted above allows for systematic comparison of the magnitude of individual elements as a function of the immersion time. Figure 5.6B plots the time evolution of the coating capacitance (Q_c), which is related to the dielectric properties of the coatings and is a measure of the efficacy of barrier protection that the coatings provide against permeation of water and ionic species. Figure 5.6B indicates that the 5 wt.% UFG/PEI coating exhibits the lowest capacitance values of all of the samples, almost an order of magnitude lower than PEI, during the entire immersion time, thereby indicating that it provides the best barrier protection against diffusion of water and ionic species. In addition, the Q_c values remain most constant across the 100 days of salt water immersion with only a slight increase suggestive of some permeation of the electrolyte within the coating. In contrast, the Q_c values for the PEI coating without exfoliated graphite initially increase during the first 5 days of immersion as a result of water uptake (water permeation is substantially increased in the absence of exfoliated graphite) by the coating. The Q_c value remain essentially constant up to 20 days, suggestive of water saturation. However, after 20 days of immersion, a substantial increase of the Q_c value is observed and can be related to the local delamination of the coating as noted above. The Q_c values for 10 and 17 wt.% UFG/PEI coatings are significantly higher as compared to the 5 wt.% UFG/PEI and PEI coatings, suggesting that high concentrations of exfoliated

graphite compromise the barrier properties of the polymeric matrix, likely by forming phase segregated domains (Figure D.4). For these coatings, the Q_c value again shows a rapid increase over the first 10 days of salt water immersion, followed by a slower increase at longer immersion times. The observed progression suggests rapid diffusion of the electrolyte during the early stages of salt water immersion and continuous deterioration of the coating upon prolonged immersion.

The evolution of the coating resistance (R_c), shown in Figure 5.6C is furthermore concordant with the trends observed for Q_c values of the different coatings. Figure 5.6C shows that the 5 wt.% UFG/PEI coating has the highest resistance value with R_c approaching 10^{11} $\Omega \cdot cm^2$ and holding fairly constant over the entire immersion time. The PEI coating without exfoliated graphite also has a high R_c value for the first day of immersion (ca. 3×10^{10} $\Omega \cdot cm^2$); however, this value rapidly plummets by over two orders of magnitude as a result of the diffusion of electrolyte, which increases the electrical conductivity of the coating and eventually results in delamination of the coating from the metal surface. The R_c values for the 10 and 17 wt.% UFG/PEI coatings during the first day of immersion are significantly lower as compared to the 5 wt.% UFG/PEI coating (ca. 8×10^8 and 2×10^8 $\Omega \cdot cm^2$, respectively). A drastic decrease of R_c by almost five orders of magnitude is observed upon prolonged immersion of these higher exfoliated-graphite-content substrates in salt water.

The Q_{dl} and R_{ct} circuit elements delineated in Figure 5.6A (i-ii, and iv-v) are related to the charge transfer process at the coating/metal interface. No such process is observed for 5 wt.% UFG/PEI. Q_{dl} is associated with the distribution of ionic charges at

the metal/coating interface, and is proportional to the electrochemically active area at the interface.[74] Bare AA7075 shows the highest Q_{dl} values, which reflects current leakage and the high accessible surface area for activation of corrosion processes in the absence of a protective coating. For the PEI-coated sample, relatively small and constant Q_{dl} values are observed upon initial immersion (Figure 5.6D). However, these values are increased upon 50 days of immersion as a result of the delamination of the coating from the metal substrate, which exposes a larger area for subsequent corrosive attack. The Q_{dl} values for 10 and 17 wt.% UFG/PEI coatings are more than two orders of magnitude higher than the corresponding values for the PEI coating (Figure 5.6D). The significant enhancement in electrochemically active sites is suggestive of the operation of galvanic corrosion processes, which accelerate the anodic dissolution of the aluminum substrate. Notably, the Q_{dl} values continuously increase as a function of the immersion time, which supports the notion stated above that as a result of the galvanically coupled corrosion, a passivating layer of solid corrosion products is not formed at the metal/coating interface. The charge transfer resistance (R_{ct}) values plotted in Figure 5.6E are in good agreement with the Q_{dl} trends for the different coatings. PEI exhibits the highest charge transfer resistance, which increases during the first few days of immersion owing to the accumulation of corrosion products at the pit sites, and subsequently decreases as a result of delamination of the coating from the substrate. The evolution of R_{ct} for the 10 and 17 wt.% UFG/PEI coatings corroborate the proposed galvanically accelerated active corrosion hypothesis noted above with no evidence for an increase of charge transfer resistance anticipated when a passivating layer is formed at the coating/metal interface.

Taken together, analysis of impedance data acquired over 100 days of salt water exposure provides unprecedented mechanistic insight into the corrosion protection/acceleration endowed by UFG/PEI coatings to aluminum substrates. Below the percolation threshold, the exfoliated graphite inclusions provide substantially increased tortuosity of diffusion pathways and yield an excellent barrier film that protects the aluminum substrate from attack by ionic species. In contrast, PEI without graphene is much more susceptible to permeation of water and ionic species. Remarkably, above the percolation threshold, continuous charge-transfer-controlled electrochemical activity continues to occur at the electrolyte/metal interface and corrosion proceeds without stabilization of the interfacial passivating layer observed for bare AA7075.

The inhibition efficiency (%IE) is often calculated to determine the relative decrease in corrosion rate provided by different coatings in comparison to the corrosion rate for a specified baseline and can be calculated using the following expression:[75,76]

$$\%\boldsymbol{IE} = \left(\frac{\boldsymbol{R_p - R_p^0}}{\boldsymbol{R_p}}\right) \times \mathbf{100} \qquad \mathbf{5.5}$$

where R_p and R_p^0 are the polarization resistances for the coating under consideration and the baseline coating, respectively. The higher the value of R_p, the greater the effectiveness of the coating in mitigating corrosion processes at the metal substrate. R_p has been defined as the impedance value at 0 Hz ($Z_{\omega \to 0} = R_s - R_p \approx R_p$) that describes the total corrosion resistance of the system.[77,78] Following this definition, the R_p and R_p^0 values can be calculated as follows:

$$\frac{1}{R_p^0} = \frac{1}{R_{ct}^0} + \frac{1}{R_L^0} \rightarrow \boldsymbol{R_p^0 = \frac{R_{ct}^0 * R_L^0}{R_{ct}^0 + R_L^0}} \quad \textbf{5.6}$$

$$\frac{1}{R_p} = \frac{1}{R_c} \rightarrow \boldsymbol{R_p = R_c} \quad \textbf{5.7}$$

where R_c is the resistance of the coating, R_{ct}^0 is the charge transfer resistance of the aluminum substrate, and R_L^0 is the resistance associated with the adsorption of intermediate species on bare aluminum. These values have been calculated based on the equivalent circuits shown in Figure 5.6A. Polarization resistance values for each coating and bare AA7075 at each time point are plotted in **Figure D.10A**. Examining the polarization resistance values alone, substantial differences in performance for each of the coatings can be distinguished. The 5 wt.% UFG/PEI coating retains the highest corrosion resistance across the duration of the study with PEI in second place with an order of magnitude lower R_p. The values for polarization resistance for the 10 and 17 wt.% UFG/PEI coatings are consistently lower as compared to the baseline PEI coating. Additionally, the polarization resistance rapidly decreases for the 10 and 17 wt.% UFG/PEI coatings going from being around one to being five orders of magnitude lower than observed for the PEI coating. Using AA7075 as a baseline for comparison (i.e., as R_p^0), an inhibition efficiency of 99.99% was maintained for the 5 wt.% coating over the course of the 100 days immersion in a 3.5 wt.% aqueous solution of NaCl. Using the polarization resistance of PEI as R_p^0, we have calculated the inhibition efficiency derived from the incorporation of exfoliated graphite particles below the percolation threshold. The evolution of inhibition efficiency with PEI taken to be R_p^0 is plotted for the 5 wt.% UFG/PEI coating in Figure D.10B as a function of time. Even with respect to PEI, the

addition of UFG brings about a substantial improvement. The relative inhibition efficiency starts out low since unmodified PEI acts as a good barrier coating during the initial 24 h; a substantial enhancement of the inhibition efficiency is observed with time and illustrates the role of UFG in increase tortuosity of ion and water transport, whereas PEI alone progressively deteriorates and is delaminated owing to the accumulation of corrosion products. No meaningful numbers for corrosion efficiency can be derived for the 10 and 17 wt.% UFG/PEI coatings given the activation of galvanic corrosion, which causes these coatings to have a lower polarization resistance value as compared to PEI.

Figure 5.7 shows cross-sectional SEM images of the aluminum/coating interface for the PEI coating and 5, 10, and 17 wt.% UFG/PEI coatings before and after 100 days of immersion in salt water. The labels in the figure indicate the interfaces and materials being imaged in each case. **Figure D.11** shows additional cross-sectional SEM images of the aluminum/coating interface for the exposed surfaces shown in Figure 5.7B,D,F,H at lower magnifications demonstrating that the features shown in Figure 5.7 are representative for each sample. The PEI coating shows accumulation of corrosion products at the interface as well as notable delamination as surmised above from the observed modulation of the OCP (Fig. 5.2) and Q_c circuit element values (Fig. 5.6). As discussed above, preferential deposition of corrosion product at the most active sites can give rise to inhomogeneous stress at the interface, resulting in localized delamination of the coating. Consistent with the electrochemical characterization discussed above, the 5 wt.% UFG/PEI coating is essentially unchanged following salt water exposure without any discernible delamination or accumulation of corrosion product across the entire

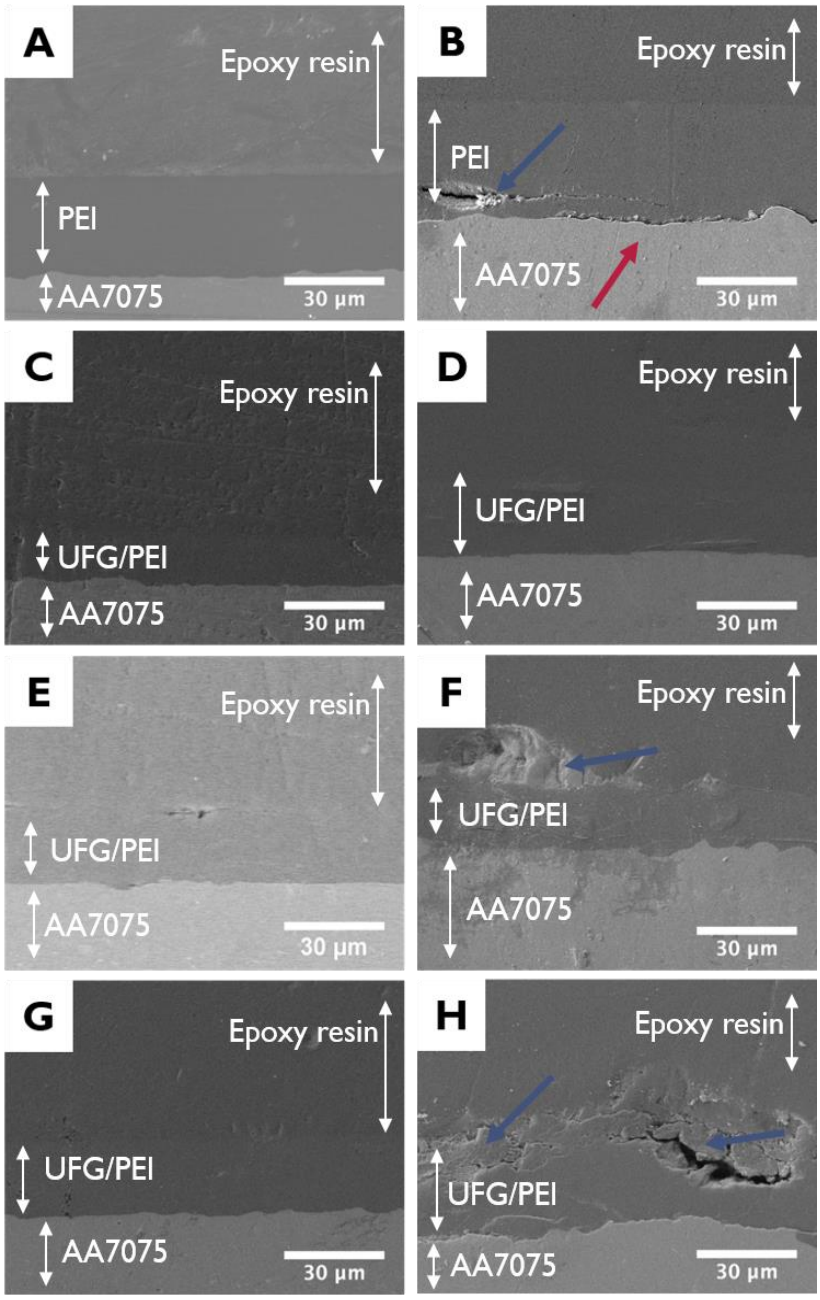

Figure 5.7. Cross-sectional SEM images of coatings on AA7075: A, B) PEI; C, D) 5 wt.% UFG/PEI; E, F) 10 wt.% UFG/PEI; and G, H) 17 wt.% UFG/PEI coatings shown before and after exposure to a 3.5 wt.% aqueous solution of NaCl for 100 days. The red arrow in B delineates a delaminated region and blue arrows indicate regions with corrosion product. The AA7075 substrate, UFG/PEI nanocomposite coating, corrosion product, and epoxy resin used to section the samples can be distinguished.

cross-sectional area. **Figure D.12** provides additional images of the 5 wt.% UFG/PEI coating following immersion in 3.5 wt.% NaCl at three separate locations across the interfaces further demonstrating that the coating integrity remains uncompromised over this time period. In stark contrast, the 10 and 17 wt.% UFG/PEI coatings show signs of corrosion of the aluminum as well as the accumulation of corrosion product at the surface of the coating. **Figure 5.8** exhibits Al compositional maps acquired across the interfaces for the four coated samples using EDS. While the Al-signal is localized at the substrate for the 5 wt.% UFG/PEI coating, diffusion of Al species across the polymer with deposition on the coating surface is observed for the 10 and 17 wt.% UFG/PEI coatings. This observation is consistent with the mechanism proposed above wherein as a result of galvanic coupling of aluminum to the percolative graphene network, cathodic reduction of Al^{3+} species can occur throughout the exfoliated graphite network or sparingly soluble oxidized aluminum species can be deposited onto the coating surface.

An idealized model has been developed to evaluate the influence of embedding conductive particles of varying dimensions within a dielectric matrix and its effect therein in altering the tortuosity. A computational first-order homogenization scheme based on the Finite Element method has been implemented. The employed flake size distributions are given in the Tables D.2 and D.3, and exemplary snapshots of the resulting particle distributions are shown in **Figure D.13**.

Table 5.2 lists the effective (normalized) diffusivity as a function of mass fraction and size distribution. From **Table 5.2** it is apparent that the size distribution of the inclusions has a significant impact on the effective diffusivity of the considered

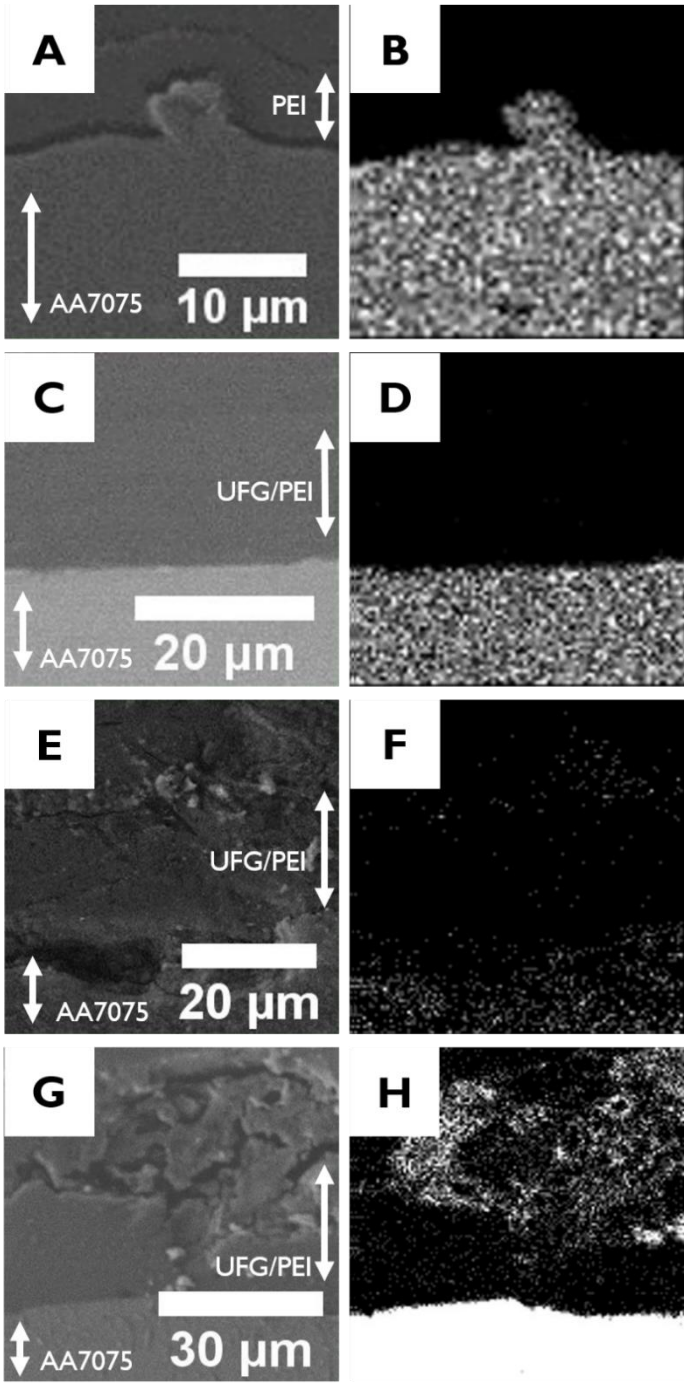

Figure 5.8. SEM images and corresponding Al elemental distribution maps measured by EDS for each of the coatings exposed to a 3.5 wt.% aqueous solution of NaCl for 100 days. A, B) PEI-coated AA7075; C, D) 5 wt.% UFG/PEI; E, F) 10 wt.% UFG/PEI; G, H) 17 wt.% UFG/PEI.

samples. The use of uniformly sized particles results in the diffusivity being nearly unchanged between the 5 and 10 wt.% samples. This is due to the fact that the latter contains nearly twice the amount of particles as compared to the former specimen, albeit with a slightly smaller particle size. Comparing these data with the results calculated from the heterogeneous particle size distributions, it is clear that a pronounced decrease in diffusivity (and hence an increase in tortuosity) is observed for non-uniform particle size distributions in this range of particle loadings. Based on these observations, the use of a heterogeneous particle size distribution is greatly favorable for enhancing the tortuosity and hence the corrosion resistance imparted by a PEI/UFG coating.

Table 5.2. Effective (normalized) diffusivity as a function of mass fraction and size distribution (with standard deviation).

Weight percent (%)	5	10	17
Uniform size	0.916 ± 0.004	0.920 ± 0.003	0.736 ± 0.016
Size distribution	0.894 ± 0.021	0.785 ± 0.053	0.705 ± 0.077

5.5. Conclusions

In summary, exfoliated graphite /PEI coatings have been examined for their ability to inhibit the corrosion of an aerospace alloy, AA7075, as a function of the exfoliated graphite loading upon protracted exposure to saline environments. Two distinct regimes are distinguished: at low exfoliated graphite loadings, below the

percolation threshold, the composite coatings endow long-term corrosion protection as a result of the substantially enhanced barrier properties realized by inclusion and dispersion of exfoliated graphite within the polymeric matrix. In contrast, at high exfoliated graphite loadings, above the percolation threshold, the large differential in redox potentials of the AA7075 substrate and the exfoliated graphite network results in galvanic corrosion of the former (Fig. 5.1). A loading of 5 wt.% exfoliated graphite within PEI provides excellent corrosion resistance for aluminum AA7075 surfaces with a $|Z|_{0.01Hz}$ maintained in the range of 1.1—3×10^{10} $\Omega\cdot cm^2$ over the course of 100 days of submersion in a 3.5 wt.% aqueous solution of NaCl. Constituting the polymeric matrix around the dispersed graphene platelets and the strong π—π interactions between the basal planes of exfoliated graphite and the aromatic rings of the anhydride precursor ensures a dense nanocomposite with excellent dispersion of the filler. The exfoliated graphite inclusions greatly increase the tortuosity of water permeation and ion diffusion pathways from the surface to the substrate as compared to a PEI film of comparable thickness that does not include exfoliated graphite. The latter unmodified polymeric film does endow some corrosion protection by trapping corrosion products at the interface but is nevertheless prone to delamination and continued corrosion. The presence of a broad distribution of exfoliated graphite particle sizes is shown by finite element modeling to endow increased tortuosity and thereby enhanced ion transport resistance.

When the exfoliated graphite loading is above the threshold value needed to achieve percolation, the challenges with corrosion protection of electropositive metals are manifested in full measure. Indeed, loadings of 10 and 17 wt.% exfoliated graphite in

PEI accelerate corrosion as a result of pronounced differential in redox potentials. Oxidation at the substrate, Al^{3+} diffusion, and deposition across the exfoliated graphite network and at the surface is observed without stabilization of a passivating interfacial layer. Such coatings with percolative networks of exfoliated graphite could potentially be used for anodic protection upon application of a voltage. Detailed impedance studies allow for evaluation of capacitance and resistance elements across 100 days of salt water exposure corroborating the distinctive mechanisms observed as a function of exfoliated graphite platelet loadings. The materials developed here thus provide an excellent addition to the sparse repertoire of composites that are viable for the protection of engineered aluminum alloys. Future work will focus on inclusion of electroactive layers such as surface-passivated Mg nanoparticles to additionally impart cathodic protection[12,13] as well as application of recently developed omniphobic composite coatings to limit fluid interactions.[79]

5.6. References

[1] H. C. Kim, T. J. Wallington, *Environ. Sci. Technol.* **2013**, *47*, 6089.

[2] H. C. Kim, T. J. Wallington, J. L. Sullivan, G. A. Keoleian, *Environ. Sci. Technol.* **2015**, *49*, 10209.

[3] J. M. Luk, H. C. Kim, R. De Kleine, T. J. Wallington, H. L. MacLean, *Environ. Sci. Technol.* **2017**, *51*, 8215.

[4] A. Mayyas, A. Qattawi, M. Omar, D. Shan, *Renew. Sustain. Energy Rev.* **2012**, *16*, 1845.

[5] L. A. W. Ellingsen, C. R. Hung, G. Majeau-Bettez, B. Singh, Z. Chen, M. S. Whittingham, A. H. Strømman, *Nat. Nanotechnol.* **2016**, *11*, 1039.

[6] R. Huang, M. Riddle, D. Graziano, J. Warren, S. Das, S. Nimbalkar, J. Cresko, E. Masanet, *J. Clean. Prod.* **2016**, *135*, 1559.

[7] R. S. Long, E. Boettcher, D. Crawford, *JOM* **2017**, *69*, 2635.

[8] T. Dursun, C. Soutis, *Mater. Des.* **2014**, *56*, 862.

[9] A. E. Hughes, I. S. Cole, T. H. Muster, R. J. Varley, *NPG Asia Mater.* **2010**, *2*, 143.

[10] J. W. Bibber, *J. Appl. Surf. Finish.* **2007**, *2*, 273.

[11] R. V. Dennis, V. Patil, J. L. Andrews, J. P. Aldinger, G. D. Yadav, S. Banerjee, *Mater. Res. Express* **2015**, *2*, 032001.

[12] G. Bierwagen, R. Brown, D. Battocchi, S. Hayes, *Prog. Org. Coatings* **2010**, *67*, 195.

[13] R. V. Dennis, L. T. Viyannalage, J. P. Aldinger, T. K. Rout, S. Banerjee, *Ind. Eng. Chem. Res.* **2014**, *53*, 18873.

[14] R. D. Davidson, Y. Cubides, J. L. Andrews, C. M. McLain, H. Castaneda, S. Banerjee, *Phys. status solidi* **2019**, *216*, 1800817.

[15] M. Y. Rekha, A. Kamboj, C. Srivastava, *Thin Solid Films* **2018**, *653*, 82.

[16] M. Y. Rekha, M. K. Punith Kumar, C. Srivastava, *RSC Adv.* **2016**, *6*, 62083.

[17] A. T. Nguyen, W.-C. Lai, B. D. To, D. D. Nguyen, Y.-P. Hsieh, M. Hofmann, H.-C. Kan, C.-C. Hsu, *ACS Appl. Mater. Interfaces* **2017**, *9*, 22911.

[18] R. V. Dennis, N. A. Fleer, R. D. Davidson, S. Banerjee, in *Graphene Technol.*

From Lab. to Fabr., Wiley-VCH Verlag GmbH & Co. KGaA, Weinheim, Germany, **2016**, pp. 155–176.

[19] F. Bellucci, *Corrosion* **1991**, *47*, 808.

[20] T. D. Burleigh, R. C. Rennick, F. S. Bovard, *Corrosion* **1993**, *49*, 683.

[21] C. Cui, A. T. O. Lim, J. Huang, *Nat. Nanotechnol.* **2017**, *12*, 834.

[22] M. Schriver, W. Regan, W. J. Gannett, A. M. Zaniewski, M. F. Crommie, A. Zettl, *ACS Nano* **2013**, *7*, 5763.

[23] J. Lee, D. Berman, *Carbon* **2018**, *126*, 225.

[24] Y.-P. Hsieh, M. Hofmann, K.-W. Chang, J. G. Jhu, Y.-Y. Li, K. Y. Chen, C. C. Yang, W.-S. Chang, L.-C. Chen, *ACS Nano* **2014**, *8*, 443.

[25] D. Prasai, J. C. Tuberquia, R. R. Harl, G. K. Jennings, K. I. Bolotin, *ACS Nano* **2012**, *6*, 1102.

[26] B. J. Schultz, R. V. Dennis, V. Lee, S. Banerjee, *Nanoscale* **2014**, *6*, 3444.

[27] D. Zhang, D. Z.-R. Wang, R. Creswell, C. Lu, J. Liou, I. P. Herman, *Chem. Mater.* **2015**, *27*, 5032.

[28] W. Sun, L. Wang, T. Wu, M. Wang, Z. Yang, Y. Pan, G. Liu, *Chem. Mater.* **2015**, *27*, 2367.

[29] C. Chen, S. Qiu, M. Cui, S. Qin, G. Yan, H. Zhao, L. Wang, Q. Xue, *Carbon* **2017**, *114*, 356.

[30] Y. Li, Z. Yang, H. Qiu, Y. Dai, Q. Zheng, J. Li, J. Yang, *J. Mater. Chem. A* **2014**, *2*, 14139.

[31] S. Qiu, W. Li, W. Zheng, H. Zhao, L. Wang, *ACS Appl. Mater. Interfaces* **2017**, *9*,

34294.

[32] L. Gu, S. Liu, H. Zhao, H. Yu, *ACS Appl. Mater. Interfaces* **2015**, *7*, 17641.

[33] W. Sun, L. Wang, T. Wu, Y. Pan, G. Liu, *Carbon* **2014**, *79*, 605.

[34] H. Kim, A. A. Abdala, C. W. MacOsko, *Macromolecules* **2010**, *43*, 6515.

[35] L. C. Tang, Y. J. Wan, D. Yan, Y. B. Pei, L. Zhao, Y. B. Li, L. Bin Wu, J. X. Jiang, G. Q. Lai, *Carbon* **2013**, *60*, 16.

[36] R. V Dennis, L. T. Viyannalage, A. V. Gaikwad, T. K. Rout, S. Banerjee, *Am. Ceram. Soc. Bull.* **2013**, *92*, 18.

[37] B. Ramezanzadeh, G. Bahlakeh, M. H. Mohamadzadeh Moghadam, R. Miraftab, *Chem. Eng. J.* **2018**, *335*, 737.

[38] F. Yu, L. Camilli, T. Wang, D. M. A. Mackenzie, M. Curioni, R. Akid, P. Bøggild, *Carbon* **2018**, *132*, 78.

[39] S. Kim, T.-H. H. Le, C. S. Park, G. Park, K. H. Kim, S. Kim, O. S. Kwon, G. T. Lim, H. Yoon, *Sci. Rep.* **2017**, *7*, DOI 10.1038/s41598-017-15552-w.

[40] O. C. Compton, S. Kim, C. Pierre, J. M. Torkelson, S. T. Nguyen, *Adv. Mater.* **2010**, *22*, 4759.

[41] V. K. K. Upadhyayula, D. E. Meyer, V. Gadhamshetty, N. Koratkar, *ACS Sustain. Chem. Eng.* **2017**, *5*, 2656.

[42] T. K. Rout, A. V. Gaikwad, T. Dingemans, *A Method of Preparing a Polyetherimide Coating on a Metallic Substrate*, **2010**, WO2011035920A1.

[43] W. C. Oliver, G. M. Pharr, *J. Mater. Res.* **1992**, *7*, 1564.

[44] D.-M. Sun, C. Liu, W.-C. Ren, H.-M. Cheng, *Small* **2013**, *9*, 1188.

[45] E. B. Secor, P. L. Prabhumirashi, K. Puntambekar, M. L. Geier, M. C. Hersam, *J. Phys. Chem. Lett.* **2013**, *4*, 1347.

[46] Y. Hernandez, V. Nicolosi, M. Lotya, F. M. Blighe, Z. Sun, S. De, I. T. McGovern, B. Holland, M. Byrne, Y. K. Gun'Ko, J. J. Boland, P. Niraj, G. Duesberg, S. Krishnamurthy, R. Goodhue, J. Hutchison, V. Scardaci, A. C. Ferrari, J. N. Coleman, *Nat. Nanotechnol.* **2008**, *3*, 563.

[47] L. R. De Jesus, R. V Dennis, S. W. Depner, C. Jaye, D. A. Fischer, S. Banerjee, *J. Phys. Chem. Lett.* **2013**, *4*, 3144.

[48] Y. You, V. Sahajwalla, M. Yoshimura, R. K. Joshi, *Nanoscale* **2016**, *8*, 117.

[49] A. C. Ferrari, J. C. Meyer, V. Scardaci, C. Casiraghi, M. Lazzeri, F. Mauri, S. Piscanec, D. Jiang, K. S. Novoselov, S. Roth, A. K. Geim, *Phys. Rev. Lett.* **2006**, *97*, DOI 10.1103/PhysRevLett.97.187401.

[50] Y. J. Kim, T. S. Shin, H. Do Choi, J. H. Kwon, Y.-C. C. Chung, H. G. Yoon, *Carbon* **2005**, *43*, 23.

[51] P. Fan, L. Wang, J. Yang, F. Chen, M. Zhong, *Nanotechnology* **2012**, *23*, 365702.

[52] F. Gardea, D. C. Lagoudas, *Compos. Part B Eng.* **2014**, *56*, 611.

[53] G. D. Seidel, Y. Bisrat, D. C. Lagoudas, in *Vol. 1 Adv. Aerosp. Technol.*, ASME, **2007**, pp. 245–253.

[54] J. K. W. Sandler, J. E. Kirk, I. A. Kinloch, M. S. P. Shaffer, A. H. Windle, *Polymer (Guildf).* **2003**, *44*, 5893.

[55] P. R. Thakre, Y. Bisrat, D. C. Lagoudas, *J. Appl. Polym. Sci.* **2010**, *116*, 191.

[56] J. Sandler, M. S. . Shaffer, T. Prasse, W. Bauhofer, K. Schulte, A. . Windle,

Polymer (Guildf). **1999**, *40*, 5967.

[57] J. Li, P. C. Ma, W. S. Chow, C. K. To, B. Z. Tang, J. K. J.-K. Kim, *Adv. Funct. Mater.* **2007**, *17*, 3207.

[58] H. Khatam, K. Ravi-Chandar, *Strain* **2013**, *49*, 420.

[59] J. E. Mark, *Polymer Data Handbook*, Oxford University Press, **2009**.

[60] B. L. Treu, S. Joshi, W. R. Pinc, M. J. O'Keefe, W. G. Fahrenholtz, *J. Electrochem. Soc.* **2010**, *157*, C282.

[61] B. D. Mert, R. Solmaz, G. Kardaş, B. Yazıcı, *Prog. Org. Coatings* **2011**, *72*, 748.

[62] R. Aliramezani, K. Raeissi, M. Santamaria, A. Hakimizad, *Surf. Coatings Technol.* **2017**, *329*, 250.

[63] W. Tian, S. Li, B. Wang, J. Liu, M. Yu, *Corros. Sci.* **2016**, *113*, 1.

[64] D. Zhu, W. J. van Ooij, *Corros. Sci.* **2003**, *45*, 2177.

[65] C.-H. Chang, T.-C. Huang, C.-W. Peng, T.-C. Yeh, H.-I. Lu, W.-I. Hung, C.-J. Weng, T.-I. Yang, J.-M. Yeh, *Carbon* **2012**, *50*, 5044.

[66] J. Hu, Y. Ji, Y. Shi, F. Hui, H. Duan, M. Lanza, *Ann. Mater. Sci. Eng.* **2014**, *1*, 1.

[67] H. Hayatdavoudi, M. Rahsepar, *J. Alloys Compd.* **2017**, *727*, 1148.

[68] M. Rashad, F. Pan, Z. Yu, M. Asif, H. Lin, R. Pan, *Prog. Nat. Sci. Mater. Int.* **2015**, *25*, 460.

[69] A. U. Chaudhry, V. Mittal, B. Mishra, *RSC Adv.* **2015**, *5*, 80365.

[70] F. Zhou, Z. Li, G. J. Shenoy, L. Li, H. Liu, *ACS Nano* **2013**, *7*, 6939.

[71] S. V Harb, S. H. Pulcinelli, C. V Santilli, K. M. Knowles, P. Hammer, *ACS Appl. Mater. Interfaces* **2016**, *8*, 16339.

[72] U. Trdan, J. Grum, *Corros. Sci.* **2014**, *82*, 328.

[73] P. Zoltowski, *J. Electroanal. Chem.* **1998**, *443*, 149.

[74] S. Pourhashem, M. R. Vaezi, A. Rashidi, M. R. Bagherzadeh, *Eval. Program Plann.* **2017**, *115*, 78.

[75] J. O. Iroh, W. Su, *Electrochim. Acta* **2000**, *46*, 15.

[76] G. Zhang, C. Chen, M. Lu, C. Chai, Y. Wu, *Mater. Chem. Phys.* **2007**, *105*, 331.

[77] J. R. Scully, *CORROSION* **2000**, *56*, 199.

[78] S. Qin, Y. Cubides, S. Lazar, R. Ly, Y. Song, J. Gerringer, H. Castaneda, J. C. Grunlan, *ACS Appl. Nano Mater.* **2018**, *1*, 5516.

[79] T. E. O'Loughlin, R. V Dennis, N. A. Fleer, T. E. G. Alivio, S. Ruus, J. Wood, S. Gupta, S. Banerjee, *Energy and Fuels* **2017**, *31*, 9337.

6. CONCLUSIONS

Given the heterogeneous nature of electrodeposition reactions, it would seem counterintuitive that magnesium can be plated without dendrite formation despite several claims that have sought to propagate this idea. The complex phase map of dendritic and fractal growth of magnesium presented here makes evident the need for future work investigating operational windows for metallic magnesium anodes and the design of anodes with mesoscale texturation such as to limit dendritic growth. The role of surface adsorbed molecular species in dictating crystal growth further needs to be elucidated under high electric fields given emerging evidence for formation of non-blocking passivating layers. Such passivating layers can alter the surface energy, local chemical potential, and self-diffusion barrier, thereby driving growth along different 3D morphologies.

We have demonstrated that nanostructured magnesium can provide cathodic protection at lower loadings compared to designs incorporating bulk particles; however, the duration of sacrificial protection was somewhat limited under accelerated testing conditions. Deleterious evolution of hydrogen gas may be further avoided by inclusion of species which promote formation of $MgCO_3$ or similarly dense byproducts or by combining cathodic protection with additional modes of passive inhibition which may protect and delay activation of active particles. In particular, encapsulation of electroactive Mg species within polymeric or ceramic shells represents a promising strategy for extended cathodic protection.

Unfunctionalized exfoliated graphite composite coatings demonstrate that graphene indeed serves as an excellent barrier and increase the tortuosity of diffusion pathways through the coating. However, the benefits of tortuosity are lost above the percolation threshold owing galvanic corrosion, which allows for delocalization of cathodic and anodic processes.

Continued improvements may involve encapsulation of exfoliated graphite to enable incorporation of higher volume fractions without achieving percolation and the exploration of densely cross-linked polymeric hosts which exhibit improved thermal properties enabling deployment of the nanocomposite coatings in extreme environments.

APPENDIX A.

SUPPLEMENTARY FIGURES AND TABLES

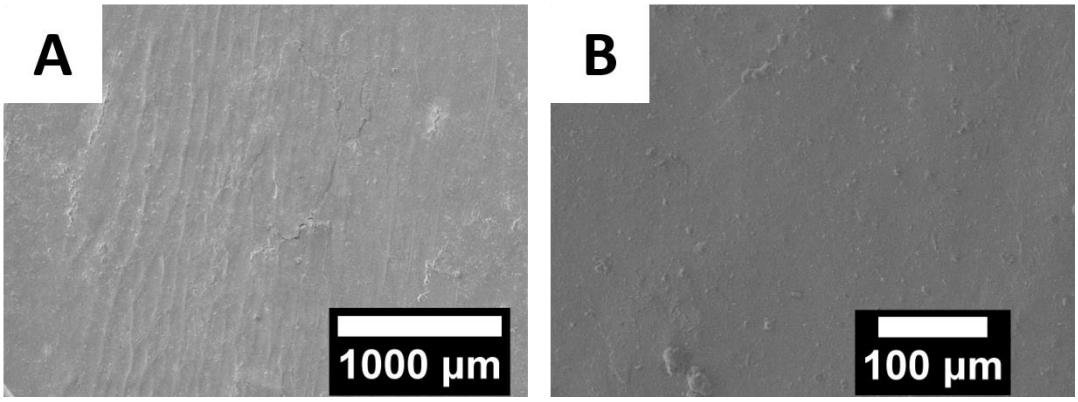

Figure A.1. SEM images of the pristine Mg ribbon at different magnifications.

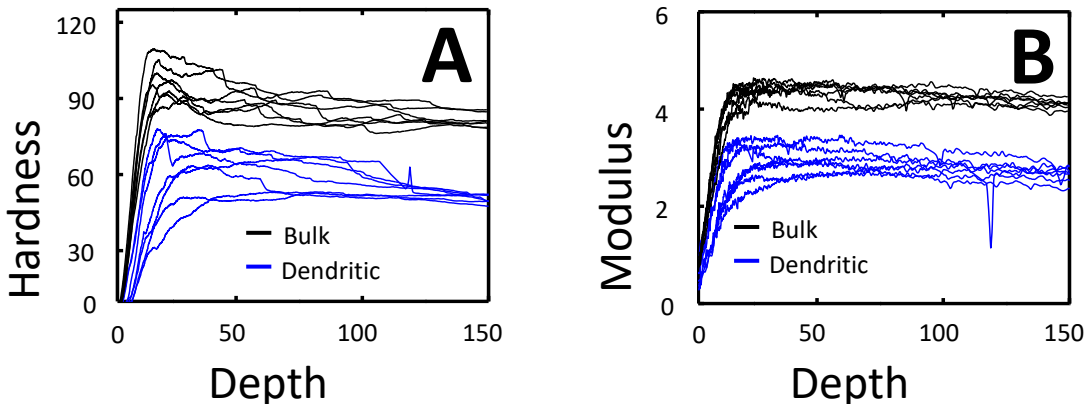

Figure A.2. A) Representative hardness versus depth and B) elastic modulus versus depth curves for bulk and dendritic Mg. For both samples, 7 curves are displayed. After an initial transient at small depths, the flat nature of the modulus versus depth curves is consistent with indentation of a homogeneous material, thereby suggesting a high-fidelity measurement despite the complicated geometry of the dendrites.

Table A.1. Model parameters.

Parameters		**Values**	**Units**
$\boldsymbol{D}$	Lattice cell dimension	5	Å
$\boldsymbol{J_0}$	Average current density	9.2	A/m^2
$\boldsymbol{R}$	Gas constant	8.314	J/mol·K
$\boldsymbol{F}$	Faraday's constant	96,487	C/mol
$\boldsymbol{N_a}$	Avogadro's constant	6.022×10^{23}	1/mol
$\boldsymbol{T}$	Operating temperature	300	K
ν	Vibration frequency	5×10^{12}	1/s
$\boldsymbol{k_B}$	Boltzmann's constant	$1.38x10^{-23}$	$m^2\cdot kg/s^2\cdot K$

Table A.2. Values of self- diffusion coefficient, energy barrier, and rate used in the model. LDA and GGA refer to local density approximation and generalized gradient approximation variants of density functional theory, respectively. Both experimental and theoretical values have been tabulated and are distinguished in parentheses.

References		$D_{\parallel}$ **(m²/s)**	$D_{\perp}$ **(m²/s)**	D_{avg} **(m²/s)**	E_{diff} **(eV)**	k_d **(s⁻¹)**
Shewmon (Expt.)[20]		3.4695×10^{-27}	3.7421×10^{-27}	3.6058×10^{-27}	1.2051	2.8846×10^{-8}
Combronde and Brebec (Expt.)[21]		1.8154×10^{-27}	1.3398×10^{-27}	3.1552×10^{-27}	1.2086	2.5242×10^{-8}
Ganeshan *et. al.* (calculated)[22]	LDA	9.9201×10^{-27}	4.9844×10^{-27}	7.4523×10^{-27}	1.1863	5.9618×10^{-8}
	GGA	2.2919×10^{-24}	1.1162×10^{-24}	1.7041×10^{-24}	1.0459	1.3633×10^{-5}
Zhang *et. al.* (calculated)[23]	LDA / GGA	7.2716×10^{-28}	6.5608×10^{-28}	6.9162×10^{-28}	1.2478	5.5330×10^{-9}
Jäckle *et al.* (calculated)[24]	GGA	2.8840×10^{-7}	-	2.8840×10^{-7}	0.02	2.3072×10^{12}

A.1. Supporting Video Descriptions

Video A.1. Time lapse video of growth at a current density of 0.307 mA/cm^2 from a 0.5 M MeMgCl solution in THF over a period of 24 h shown at 4000x speed.

Video A.2. Time lapse video of growth at a current density of 0.921 mA/cm^2 from a 0.5 M MeMgCl solution in THF over a period of 24 h shown at 4000x speed.

Video A.3. Time lapse video of growth from 1.54 mA/cm^2 from a 0.5 M MeMgCl solution in THF over a period of 24 h shown at 4000x speed.

Video A.4. Tomographic reconstruction of a dendrite formed at 0.921 mA/cm^2 applied current in 0.5 M MeMgCl solution for 24 h.

APPENDIX B.

SUPPLEMENTARY FIGURES AND TABLES

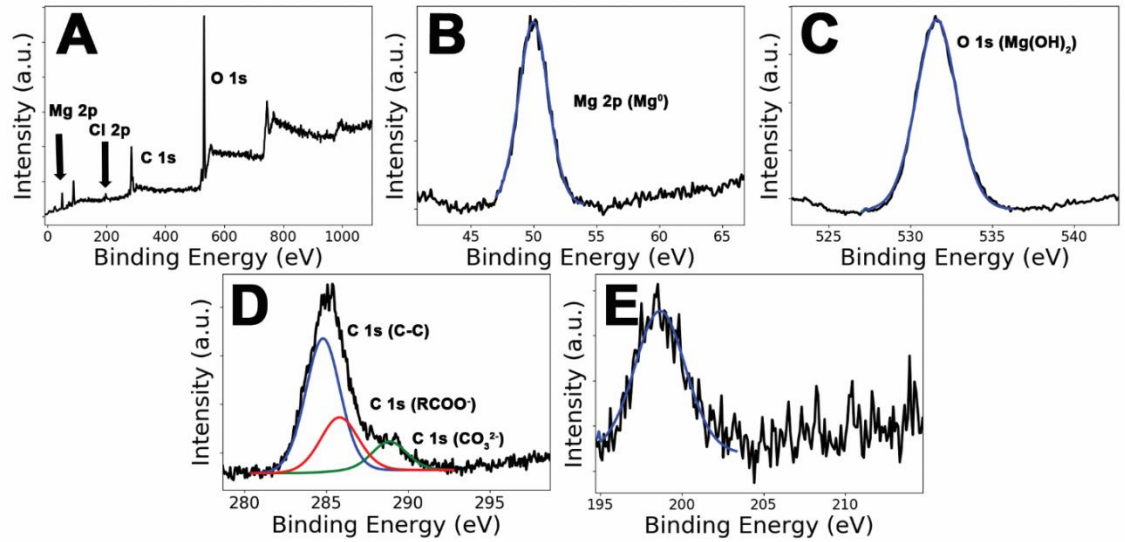

Figure B.1. A) XPS survey scan measured for detached Mg fractal deposits formed at a current density of 0.921 mA/cm2 from a 0.5M solution of MeMgCl in THF; High-resolution XPS spectra measured at B) Mg 2p; C) O 1s; D) C 1s regions; and E) high-resolution Cl 2p XPS spectrum. Spectral assignments are indicated for each of the deconvoluted lines.

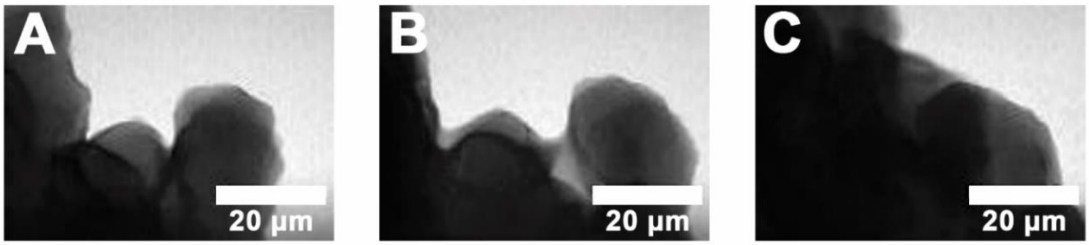

Figure B.2. Projections of 3D tomographic maps from soft-X-ray microscopy at the Mg K-edge acquired at tilt angles of A) 40°, B) 80°, and C) 120°.

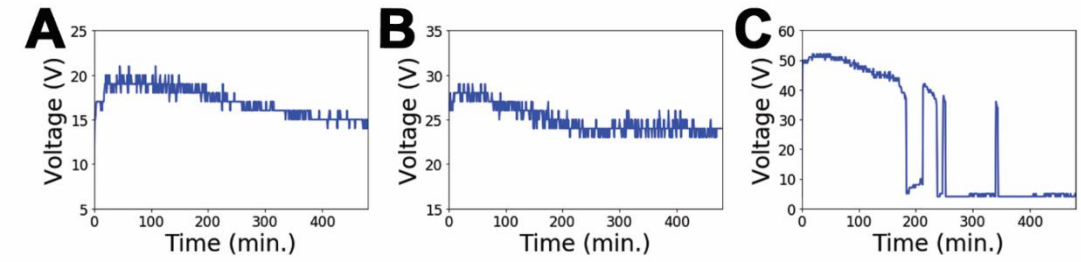

Figure B.3. Plots of voltage *versus* time for the electrodeposition of Mg from MeMgCl as a function of applied current density for electrodeposition reactions at A) 0.307, B) 0.921, and C) 1.54 mA/cm^2 constant current applied for 8 h in 0.5 M MeMgCl solutions in THF.

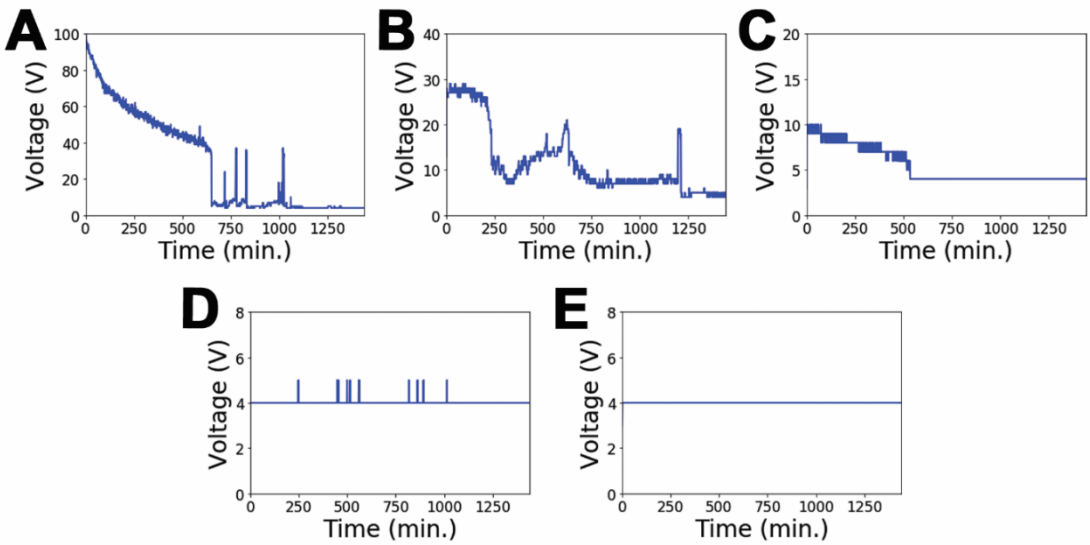

Figure B.4. Plots of voltage *versus* time for the electrodeposition of Mg from MeMgCl as a function of concentration of electrolyte showing plots for reactions run with A) 0.25, B) 0.5, C) 1.0, D) 1.5, E) 2.0 M MeMgCl electrolyte solutions under a constant current of 0.921 mA/cm^2 applied for 24 h.

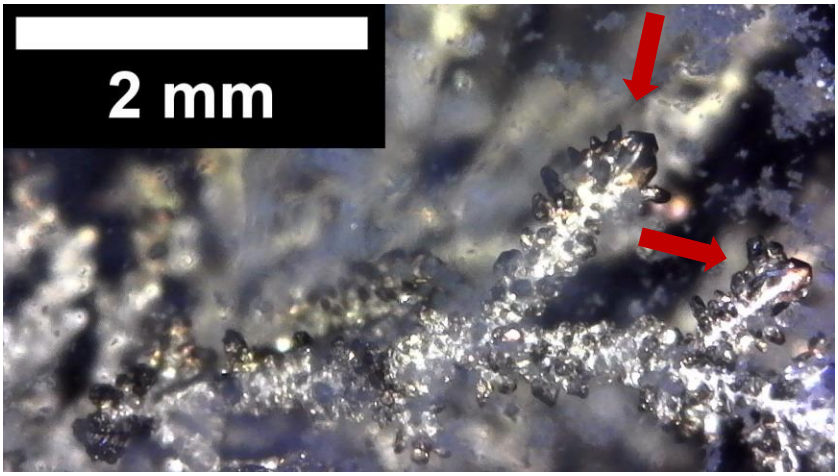

Figure B.5. Digital image of a dendrite deposited under 0.921 mA/cm^2 applied current density in a 1.5 M MeMgCl solution for 24 h.

s

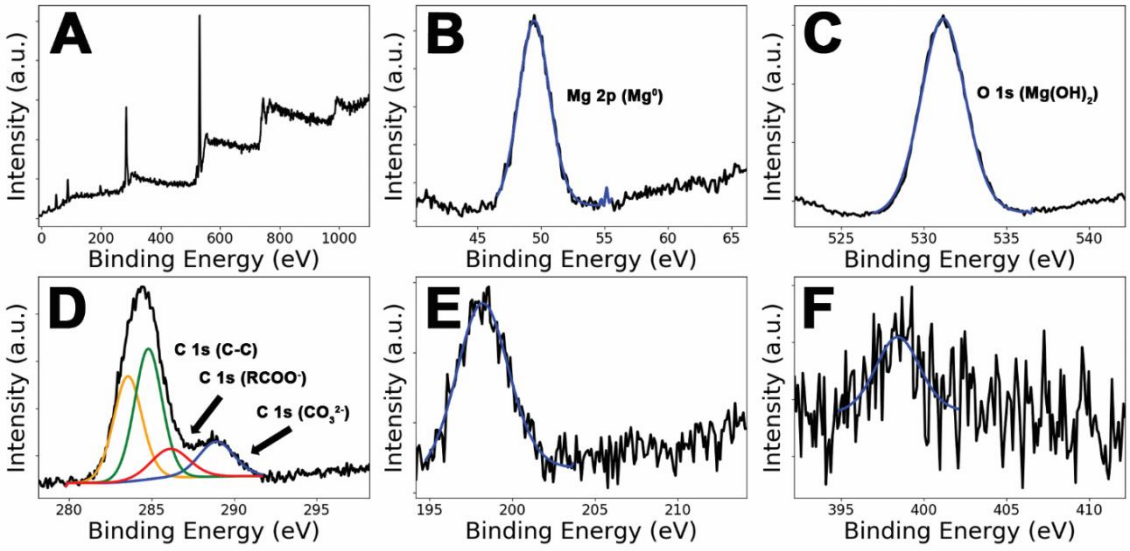

Figure B.6. A) XPS survey scan measured for detached Mg fractal deposits formed at a current density of 0.921 mA/cm^2 from a 0.5M solution of MeMgCl in THF with the addition of oleylamine; High-resolution XPS spectra measured at B) Mg 2p; C) O 1s; D) C 1s regions; E) high-resolution Cl 2p XPS spectrum; and F) N 1s. Spectral assignments are indicated for each of the deconvoluted lines.

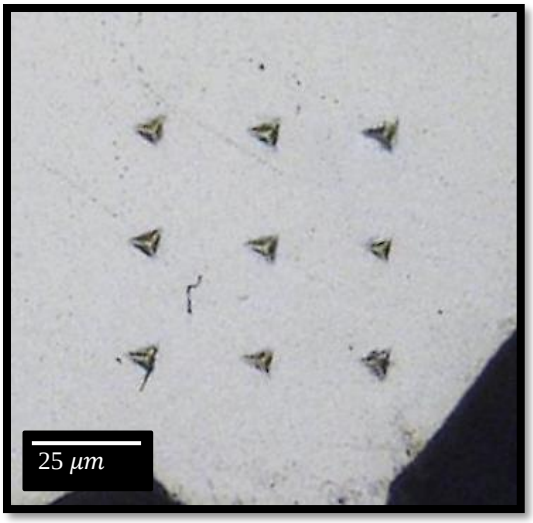

Figure B.7. Optical image acquired for a set of indents in the cross-section of a polished Mg dendrite grown in 0.5 M MeMgCl solutions under 0.921 mA/cm^2 applied constant current for 24 h, displaying insignificant indentation pile-up.

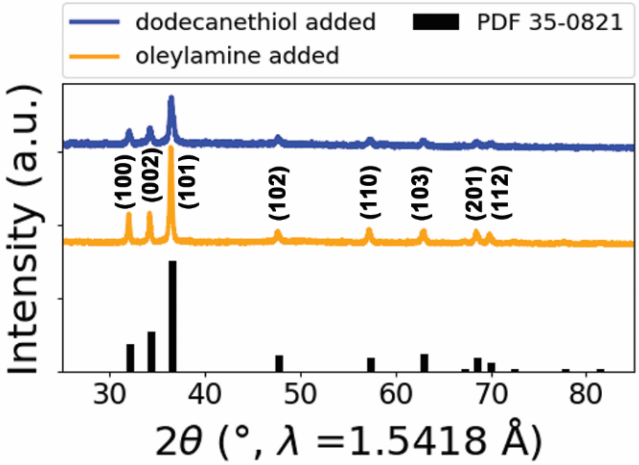

Figure B.8. Powder XRD patterns for Mg deposits electrodeposited at a current density of 0.921 mA/cm^2 from 0.5M MeMgCl electrolyte solutions with the addition of dodecanethiol and oleylamine. The reflections can be indexed to metallic Mg with hexagonal close packing of atoms (PDF 35-0821).

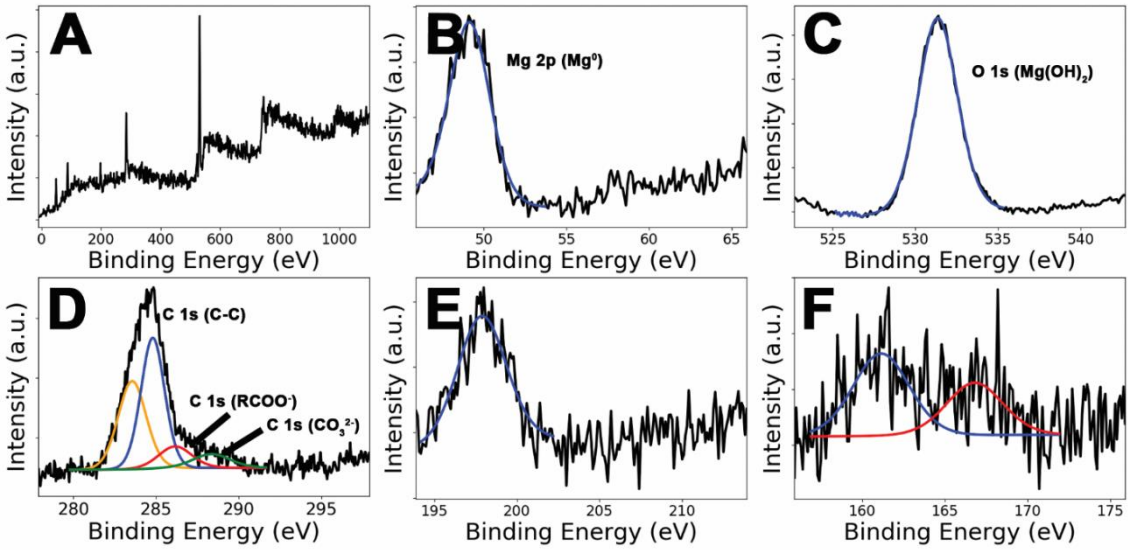

Figure B.9. A) XPS survey scan measured for detached Mg fractal deposits formed at a current density of 0.921 mA/cm^2 from a 0.5M solution of MeMgCl in THF with the addition of dodecanethiol; High-resolution XPS spectra measured at B) Mg 2p; C) O 1s; D) C 1s regions; E) high-resolution Cl 2p XPS spectrum; and F) S 2p. Spectral assignments are indicated for each of the deconvoluted lines.

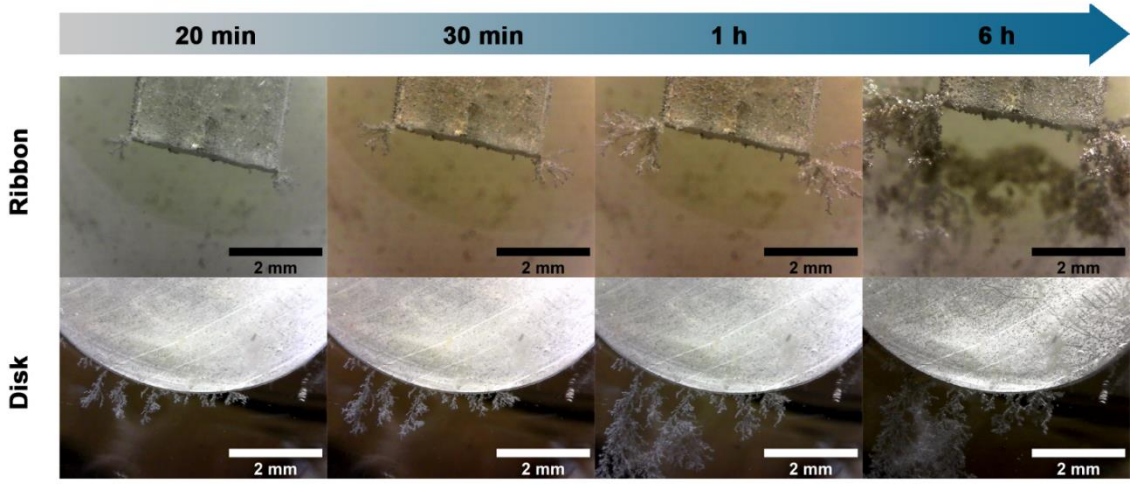

Figure B.10. Digital images of an Mg ribbon and disk electrode as a function of time upon electrodeposition from a 0.5 M MeMgCl solution in THF under a 0.921 mA/cm^2 applied current density held constant for 24 h.

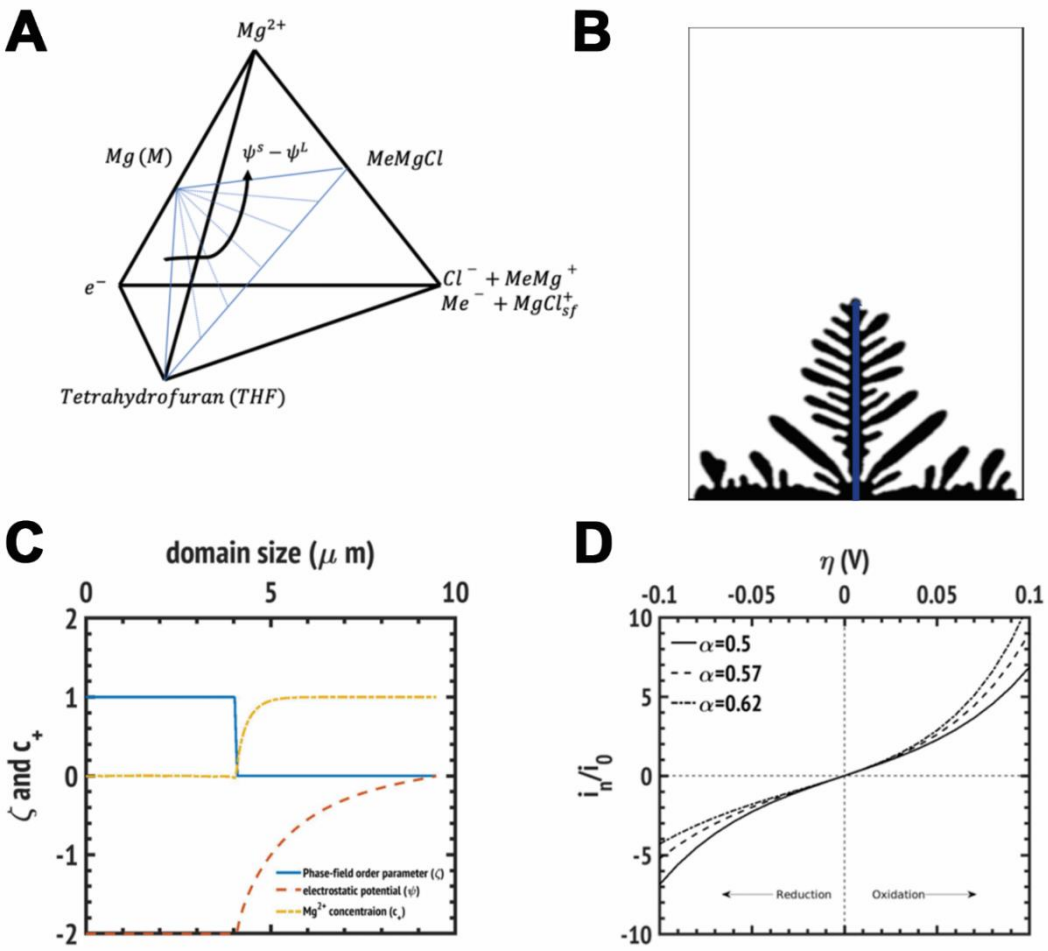

Figure B.11. A) Hypothetical phase diagram[1] and charge-neutral plane for Mg(M)-MeMgCl-THF. B) Dendrite formed following initial seeding at the bottom center of the domain. C) Phase-field order parameters extracted along the blue line in (B). D) Comparison of the nonlinear phase-field model with a Butler-Volmer symmetric coefficient of $\boldsymbol{\alpha}$=0.5 used in this study and Butler-Volmer coefficients reported by Viestfrid and co. workers[2] for (0.25 M complex in THF) and for (0.25 M complex in (0.25 M Bu_2Mg + THF) solutions.

Table B.1. List of boundary conditions used for equations 3.10-3.12

	Eq. (3.10)	**Eq. (3.11)**	**Eq. (3.12)**
Top	$\nabla\zeta = 0$	$c = c^{electrolyte}$	$\boldsymbol{\psi = \psi_{half-cell}}$
Bottom		$c = c^{Mg^{2+}}$	$\boldsymbol{\psi = \psi_{electrode}}$
Left/Right		$\nabla c = 0$	$\boldsymbol{\nabla\psi = 0}$

B.1. Captions for Videos

Video B.1. Time lapse video of growth from 0.921 mA/cm^2 in 0.25 M MeMgCl solution for 24 h reactions shown at 4000x speed.

Video B.2. Time lapse video of growth from 0.921 mA/cm^2 in 0.5 M MeMgCl solution for 24 h reactions shown at 4000x speed.

Video B.3. Time lapse video of growth from 0.921 mA/cm^2 in 1.0 M MeMgCl solution for 24 h reactions shown at 4000x speed.

Video B.4. Time lapse video of growth from 0.921 mA/cm^2 in 1.5 M MeMgCl solution for 24 h reactions shown at 4000x speed.

Video B.5. Time lapse video of growth from 0.921 mA/cm^2 in 2.0 M MeMgCl solution for 24 h reactions shown at 4000x speed.

Video B.6. Time lapse video of growth from 0.921 mA/cm^2 in 0.5 M MeMgCl solution with addition of 0.0626 M dodecanethiol for 24 h reactions shown at 4000x speed.

Video B.7. Time lapse video of growth from 0.921 mA/cm^2 in 0.5 M MeMgCl solution with addition of 0.125 M dodecanethiol for 24 h reactions shown at 4000x speed.

Video B.8. Time lapse video of growth from 0.921 mA/cm^2 in 0.5 M MeMgCl solution with addition of 0.188 M dodecanethiol for 24 h reactions shown at 4000x speed.

Video B.9. The alighted tilt series of soft X-ray microscopy images of a fractal grown at 0.921 mA/cm^2 in 0.5 M MeMgCl for 24 h obtained at the Mg K-edge in transmission (left) and optical density (right).

Video B.10. 3D reconstruction series of soft X-ray microscopy images of a fractal grown at 0.921 mA/cm^2 in 0.5 M MeMgCl for 24 h obtained at the Mg K-edge in transmission (left) and optical density (right).

Video B.11. 3D digital tomography of growth from 0.921 mA/cm^2 in 0.5 M MeMgCl solution for 24 h reactions.

Video B.12. 3D digital tomography of growth from 0.921 mA/cm^2 in 2.0 M MeMgCl solution for 24 h reactions.

APPENDIX C.

SUPPLEMENTARY FIGURES AND TABLES

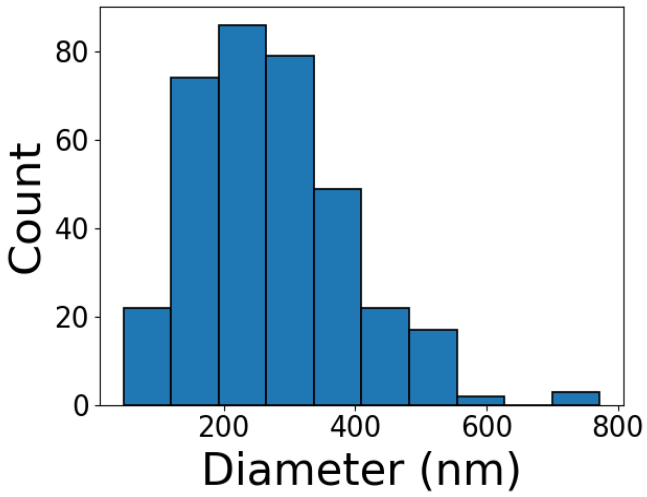

Figure C.1. Particle size distribution of Mg nanocrystals as determined from statistical analysis of SEM images acquired for 350 individual nanocrystals.

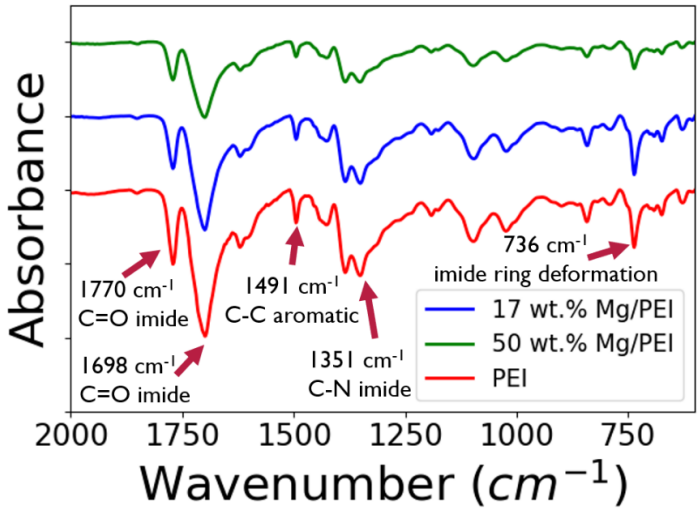

Figure C.2. FTIR spectra of pristine PEI, 17 wt.% Mg/PEI, and 50 wt.% Mg/PEI coatings.

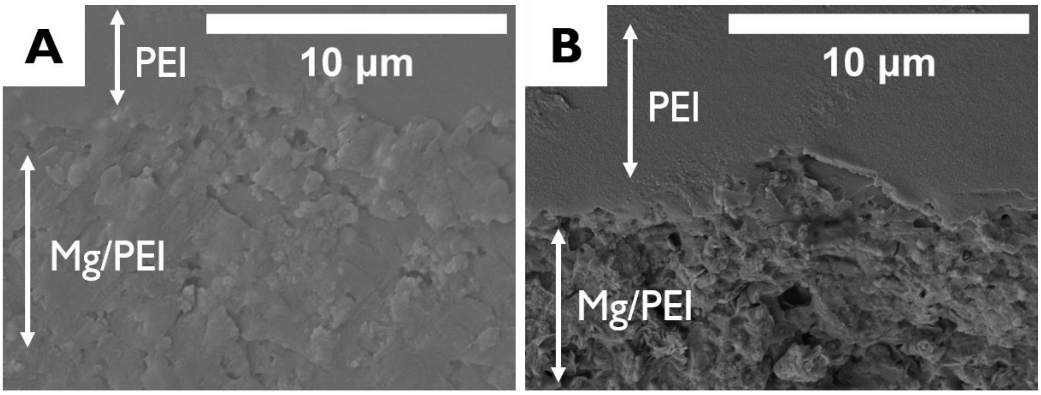

Figure C.3. SEM images of the Mg/PEI and PEI interface for A) 17 wt.% Mg/PEI and B) 50 wt.% Mg/PEI coatings. Both coatings have a top layer of PEI. Relative positions of the Mg/PEI and the PEI layer are labeled.

APPENDIX D.

SUPPLEMENTARY FIGURES AND TABLES

Table D.1 Nominal chemical composition (wt.%) of aluminum alloy AA7075-T6.

	Mg	**Si**	**Cu**	**Cr**	**Mn**	**Zn**	**Fe**	**Ti**	**Al**
7075-T6	2.1–2.9	0–0.4	1.2–2.0	0.18–0.28	0–0.30	5.1–6.1	0–0.5	0–0.2	Balance

Table D.2. Representative UFG flake sizes used in finite element modeling.

Weight percent (%)	**5**	**10**	**17**
Major diameter (μm)	35.8	33.9	53.6
Minor diameter (μm)	2.5	2.5	2.5

Table D.3. UFG flake size distributions for the 5, 10, and 17 wt.% nanocomposite coatings; all particles are modeled as having a thickness of 2.5 μm.

5 wt.% UFG/ PEI	**Average diameter (μm)**	**11.5**	**20.5**	**29.5**	**38.5**	**47.5**	**56.5**	**65.5**	**74.5**	**92.5**
	Volume fraction	0.089	0.217	0.233	0.188	0.123	0.081	0.038	0.018	0.013
10 wt.% UFG/ PEI	Average diameter (μm)	12.0	19.5	27.0	34.5	41.5	49.0	56.5	64.0	71.5
	Volume fraction	0.085	0.215	0.217	0.190	0.119	0.053	0.047	0.046	0.028
17 wt.% UFG/ PEI	Average diameter (μm)	19.5	36.5	53.5	70.5	87.5	104.5	121.5	138.5	172.5
	Volume fraction	0.218	0.283	0.176	0.138	0.084	0.05	0.023	0.02	0.008

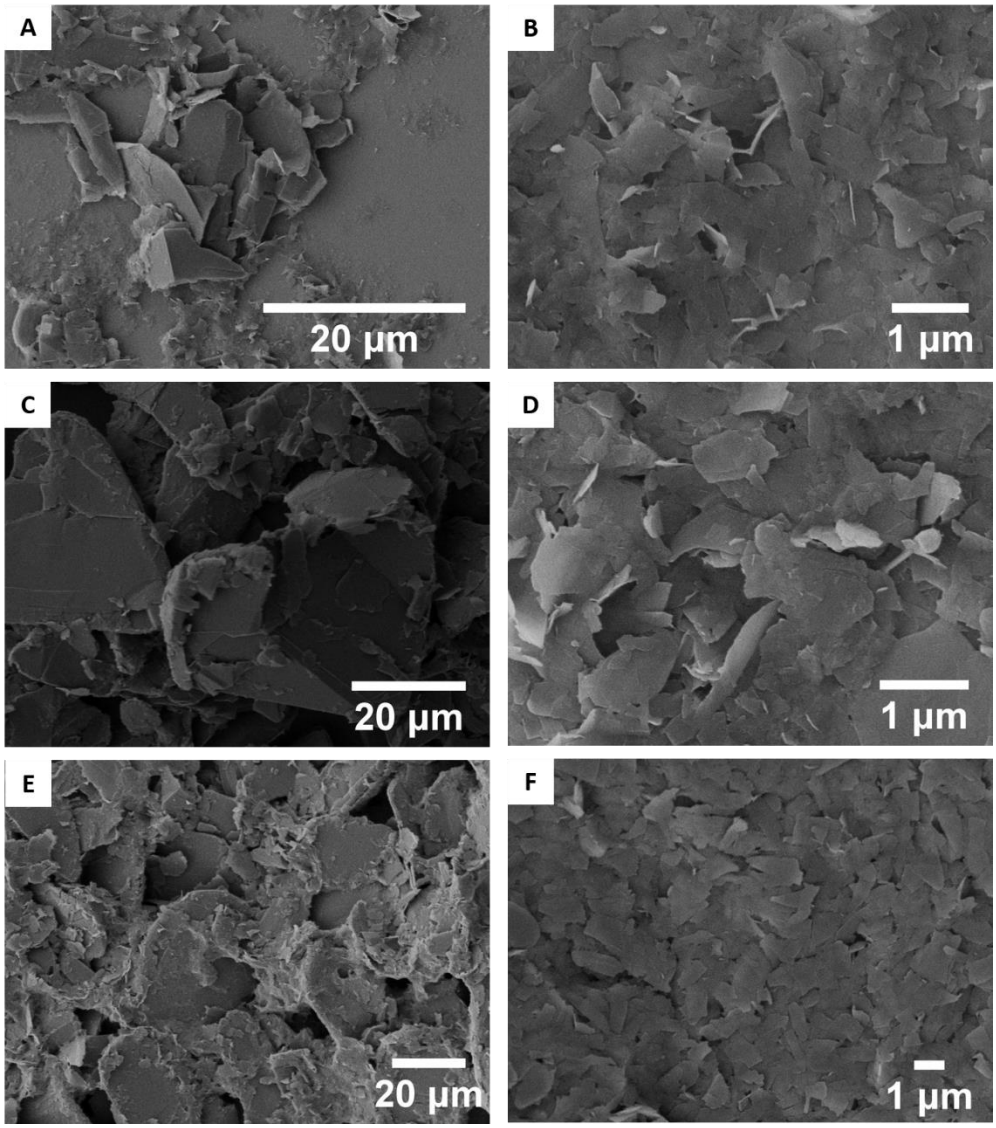

Figure D.1. SEM images acquired for A, C, E) larger few-layered graphite platelets; B, D, F) thinner exfoliated sheets present within A, B) 5; C, D) 10; and E, F) 20 mg/mL dispersions prepared by exfoliation of graphite in NMP.

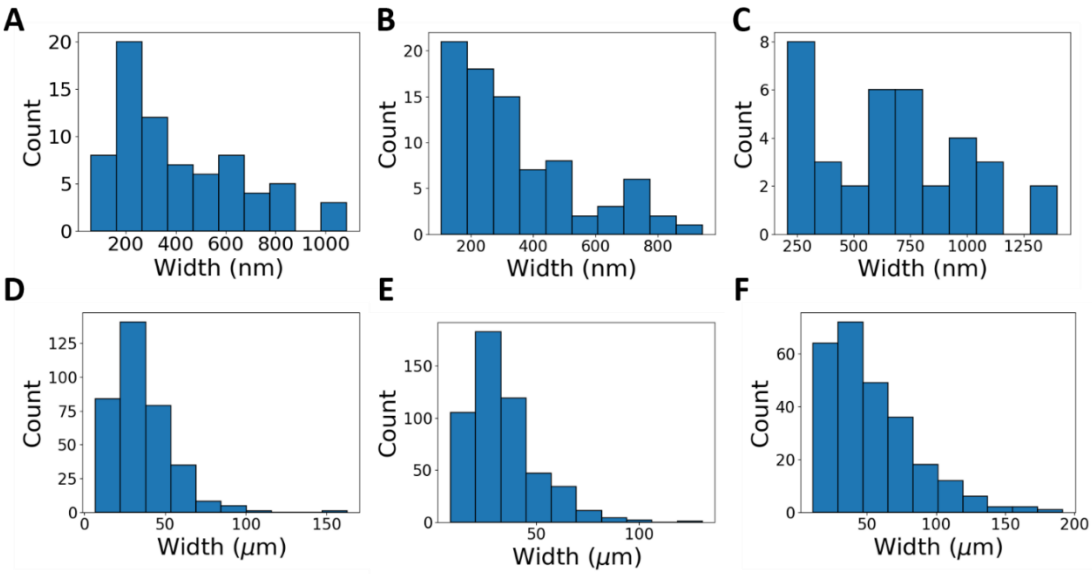

.

Figure D.2. Size distribution histograms for A—C) smaller few-layered graphene and D—F) larger exfoliated graphite particles within A,D) 5, B,E) 10, and C,F) 20 mg/mL UFG dispersions. The lateral dimensions have been determined based on statistical analysis of SEM images.

Table D.4. Average lateral dimensions and thicknesses of exfoliated graphite particles in NMP dispersions at different loadings determined from statistical analysis of AFM and SEM images.

Concentration of UFG in NMP (mg/mL)	**Percent Smaller Particles (%)**	**Average Lateral Dimensions of Smaller Few-Layered Graphene Flakes (nm)**	**Average Thickness of Smaller Exfoliated Graphite Flakes (nm))**	**Percent Larger Particles (%)**	**Average Lateral Dimensions of Larger Exfoliated Graphite Particles (μm)**
5	69.6	343 ± 203	11.58	30.4	35.8 ± 18.3
10	36.7	419 ± 248	9.28	63.3	33.9 ± 16.9
20	45.7	683 ± 327	15.9	54.3	53.6 ± 31.8

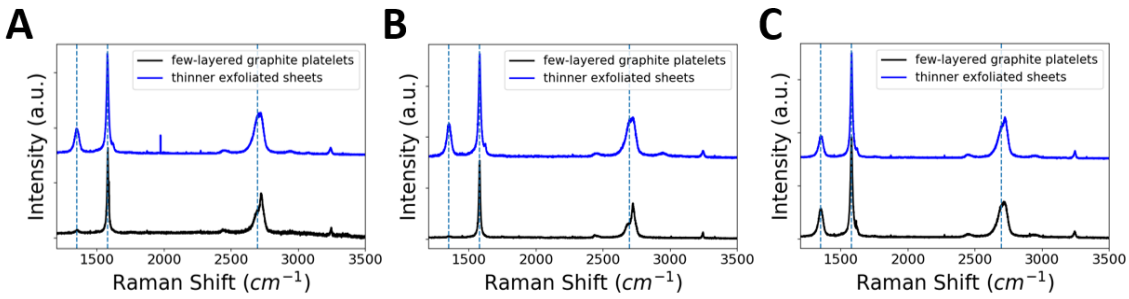

Figure D.3. Raman spectra acquired for few-layered graphite platelets and thinner exfoliated sheets recovered upon exfoliating graphite in NMP at concentrations of A) 5, B) 10, and C) 20 mg/mL at 514.5 nm laser excitation. The vertical dashed lines demarcate the positions of the D-band at ca. 1,350 cm^{-1}, G-band at ca. 1,580 cm^{-1}, and 2D-band at ca. 2,700 cm^{-1}.

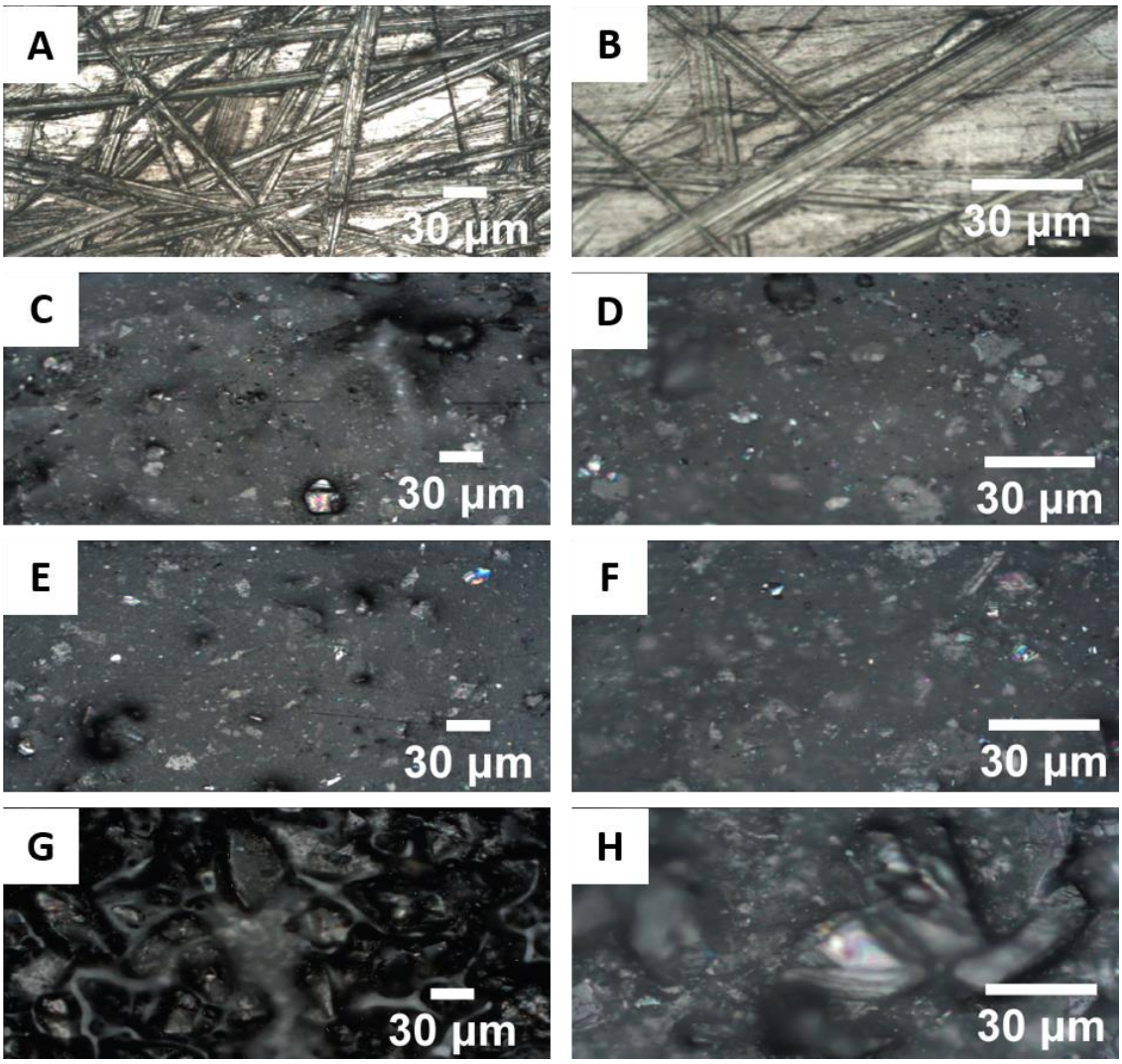

Figure D.4. Optical microscopy images of the surfaces of A,B) PEI-coated AA7075; C,D) 5 wt.% UFG/PEI; E,F) 10 wt.% UFG/PEI; and G,H) 17 wt.% UFG/PEI on AA7075 surfaces. The textured surface of the abraded AA7075 substrate is discernible in (A) and (B) given the transparent nature of the PEI coating. The incorporation of graphene diminishes the optical transparency of the coatings.

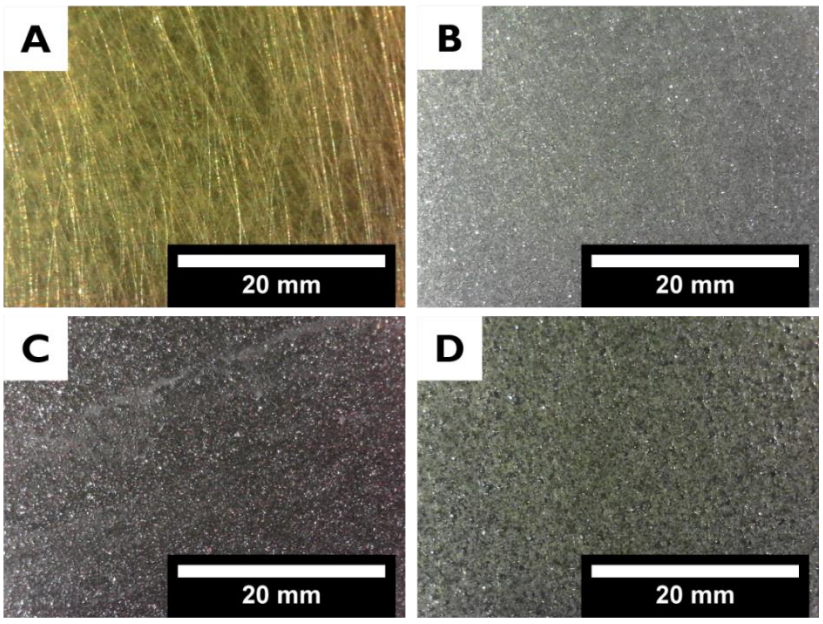

Figure D.5. Optical microscopy images at lower magnifications of the surfaces of A) PEI-coated AA7075, B) 5 wt.% UFG/PEI; C) 10 wt.% UFG/PEI; and D) 17 wt.% UFG/PEI on AA7075 surfaces.

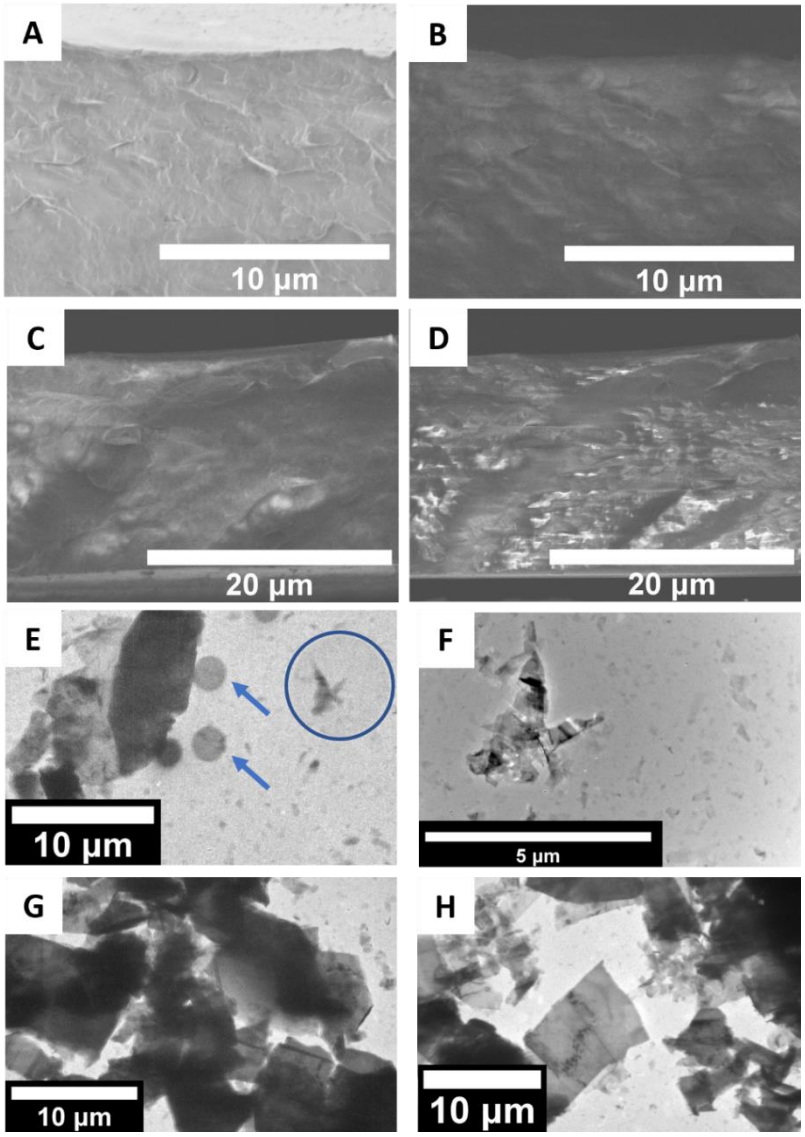

Figure D.6. A-D) Cross-sectional SEM images of cryo-fractured 10 wt.% UFG/PEI nanocomposite coatings acquired across two areas (A,B) and (C,D). Panels A and C illustrate higher-magnification views, whereas panels B and D illustrate the lack of localized charging. E—H) TEM images of 10 wt.% UFG/PEI nanocomposites acquired at varying magnifications. Panel E shows a low-magnification image; a higher magnification view of the area with panel E delineated with a blue circle is shown in Panel F. G,H) Additional low-magnification images acquired for the nanocomposite.

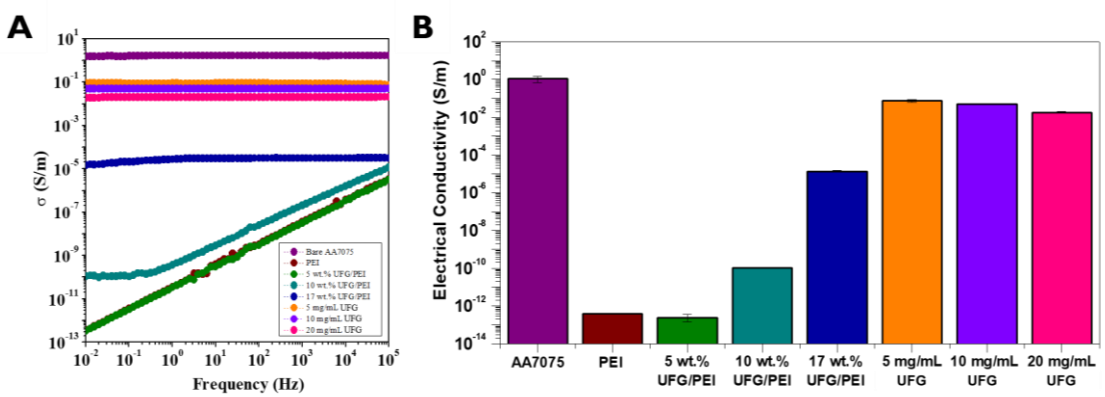

Figure D.7. A) AC conductivity plotted as a function of frequency for bare AA7075, PEI, 5 wt.% UFG/PEI, 10 wt.% UFG PEI, and 17 wt.% UFG/PEI coatings as well as drop-cast thin films of exfoliated graphite obtained from 5, 10, and 20 mg/mL NMP dispersions. B) Conductivity values deduced from the AC conductivity measurements.

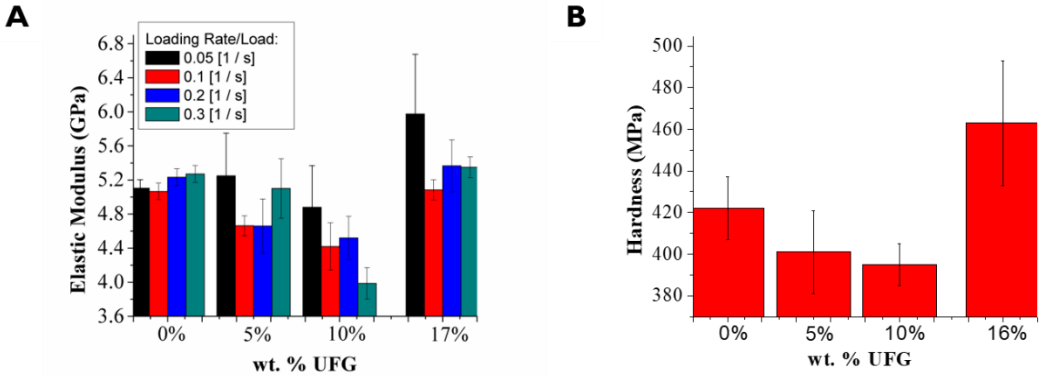

Figure D.8. A) Elastic modulus and B) hardness measured using nanoindentation for each loading of UFG/PEI on AA7075.

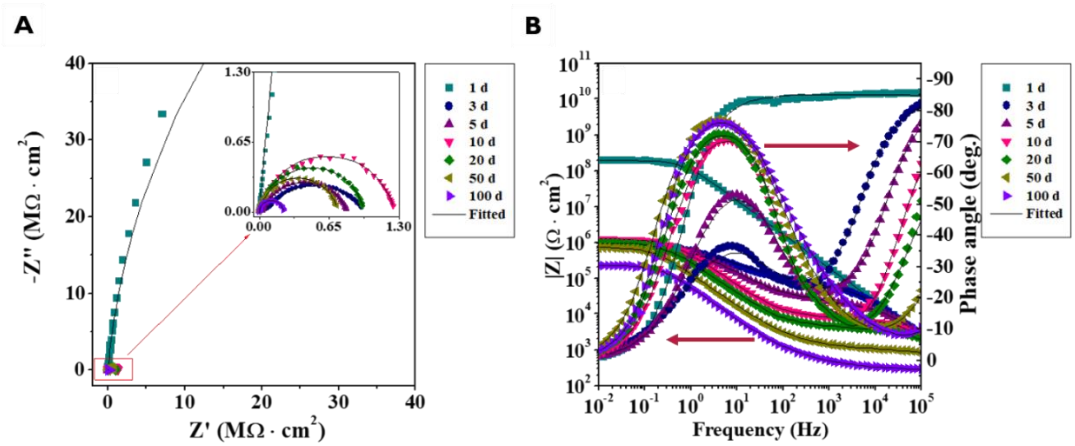

Figure D.9. EIS spectrum monitored for 17 wt. % UFG/PEI on AA7075 immersed in a 3.5 wt.% aqueous solution of NaCl for up to 100 days.

Table D.5. Summary showing the specific equivalent circuit models shown in Figure 8A that were used to model the EIS response for each coating and time period throughout the study.

Circuit	Sample	Days Applicable
i	AA7075	1-10
ii	AA7075	20-100
iii	PEI	1
	5 wt.% UFG/PEI	1-100
	10 wt.% UFG/PEI	1
	17 wt.% UFG/PEI	1
iv	PEI	3-20
	10 wt.% UFG/PEI	3-100
	17 wt.% UFG/PEI	3-100
v	PEI	50-100

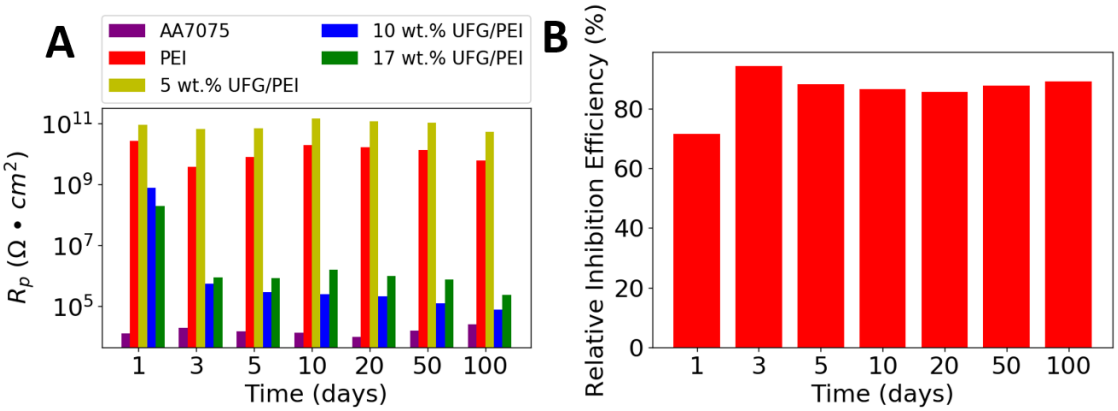

Figure D.10. A) Polarization resistance and B) inhibition efficiency of the 5 wt.% UFG/PEI coating taking PEI as R_p^0 at specific time points during exposure testing.

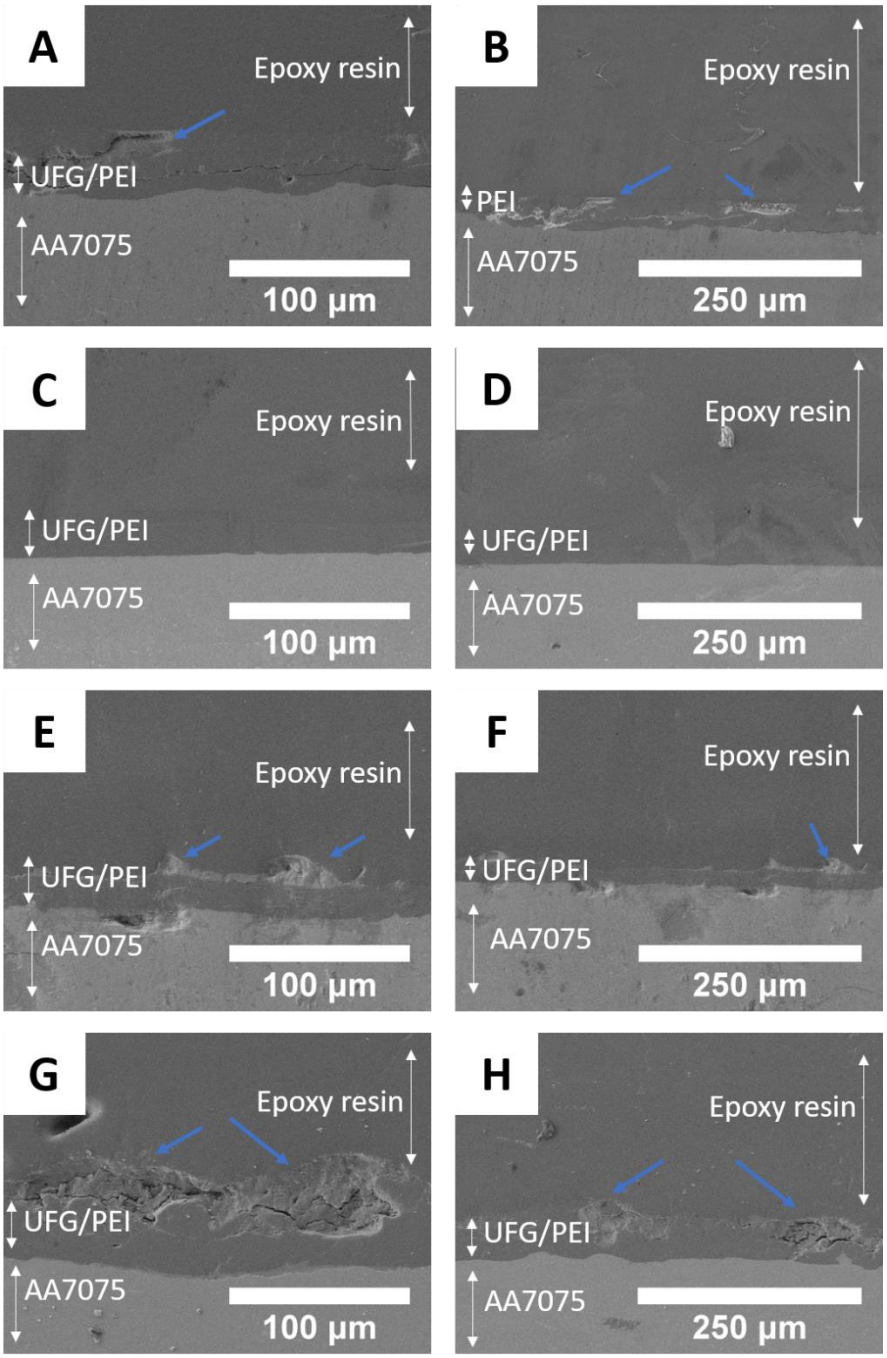

Figure D.11. Additional cross-sectional SEM images of the coating/aluminum interface for A,B) PEI, C,D) 5 wt.% UFG/PEI, E,F) 10 wt.% UFG/PEI, and G,H) 17 wt.% UFG/PEI coatings at lower magnifications following immersion in 3.5 wt.% NaCl for 100 days. Blue arrows identify areas with corrosion product present. The AA7075 substrate, UFG/PEI nanocomposite coating, corrosion product, and epoxy resin used to section the samples can be distinguished.

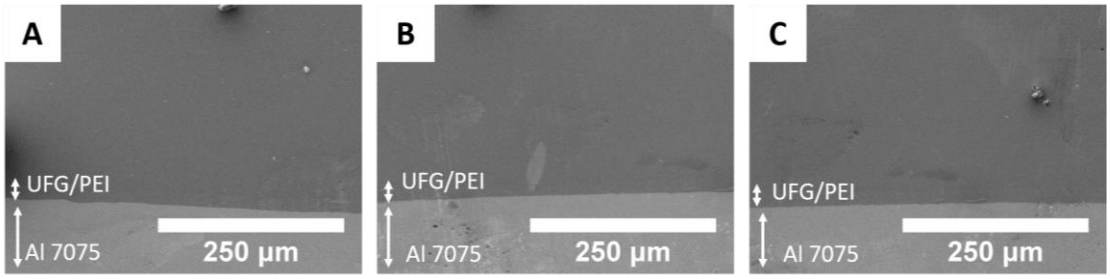

Figure D.12. Cross-sectional SEM images of the coating/aluminum interface acquired at various locations for a 5.wt.% UFG/PEI coating following exposure to 3.5 wt.% aqueous solution of NaCl for 100 days. A clean coating/substrate interface is observed without any discernible accumulation of corrosion products.

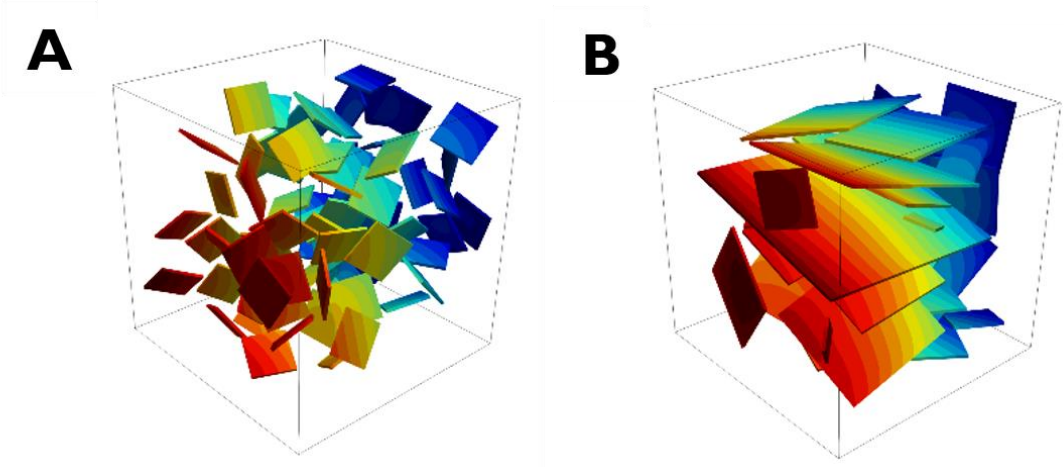

Figure D.13. Randomly generated microstructure for A) uniform particle size and B) widely spaced particle size distribution. Color coding is only used to facilitate distinction of the individual particles.